CRANFIELD INSTITUTE OF TECHNOLOGY

SCHOOL OF MECHANICAL ENGINEERING

Ph.D. THESIS

M. MAHMOOD

HEAT TRANSFER FROM SWIRLING IMPINGING JETS.

Supervisor: J. WARD

April 1980

SUMMARY

This thesis is concerned with the determination of the local and average mass/heat transfers from swirling jets impinging orthogonally onto flat surfaces. Application of swirl alters the flow field of the jet considerably and eventually the maximum velocity in the jet is displaced from the axis resulting in a typical 'double-peak' profile. Further increase of swirl can even result in a recirculation in the inner core of the flow. The turbulence characteristics of the jet are also affected. It is expected that these changes will, in addition, modify the heat transfer behaviour.

Consequently, a study of both single free jets and a square array (of 3 x 3) of jets was undertaken. The range of swirls examined in this study was from zero through to weak and then medium swirl, i.e. the swirl number S was varied from 0 to 0.48. The other parameters varied in the experiments were the nozzle-to-target spacing z/D from 2 to 12, the nozzle pitches x/D (for arrays of jets) which were 3.2, 4.8 and 6.4, and the jet Reynolds number. In the single frce jet tests, two flow rates corresponding to $Re_D = 32,000$ and 60,000 were studied whilst, for the 'multiple' jets, the measurements were confined to the lower of these Reynolds numbers. (Re_D is based on the mean exit velocity in the non-swirling case and the diameter of the nozzle.)

Limited velocity and turbulence measurements were also undertaken on the single jet to characterise the flow and also to compare the behaviour of the present jets with those in previous studies. The flows were similar to those observed previously for swirling jets so that the heat transfer results should be generally applicable.

A 'thin-film' naphthalene sublimation technique was used to measure mass transfers over the target surface. The heat transfer coefficients were then derived using the Chilton-Colburn analogy. A rig was developed to spray a uniform coating of naphthalene on the target surface. This 'thin-film' technique was found to provide repeatable results and the validity of the experiments was further assessed by comparing the results with previously published data for the no swirl case. These were in reasonable agreement.

For the single free jets, the application of swirl was found to continuously reduce the heat transfers. The heat transfers, however, became more uniform. An empirical correlation has also been suggested for the average Nusselt number associated with these single swirling jets and is valid for S = 0.12 to 0.48. In some circumstances in the 'multiple' jet tests (e.g. at close nozzle-

to-target spacings) the average heat transfers increased to a maximum of S = 0.24 (approximately). Further increases in the degree of swirl brought about a subsequent reduction in average heat transfer coefficients until eventually the performance of the swirling jets was poorer than that of the non-swirling flows. This discrepancy in behaviour can be explained in terms of changes in the local heat transfer distributions.

ACKNOWLEDGDMENTS

The author would like to express his sincere and profound thanks to his Project Supervisor, Mr. J. Ward, for his advice, guidance and encouragement throughout the project.

Thanks are also due to Mr.S.B.H.C. Neal of C.E.R.L. Leatherhead, for inviting the initial interest in the thin-film naphthalene sublimation technique.

The author also wishes to thank Professor R.S. Fletcher, Head of the School of Mechanical Engineering, for allowing the use of School facilities in connection with this work.

Acknowledgement is also due to the laboratory and workshop staff in helping out at different stages of the work, especially Mr.C.S. Chapman, Mr.D.C. Beattie, Mr.J.F. Dawe, Mr.L. Relton and Mr.N.Butcher. The Photographic Section of the Institute is also thanked for their cooperation.

The author is also grateful to the Science Research Council and the School of Mechanical Engineering for providing financial support for this project.

Finally, the author wishes to extend his special thanks to Mrs. Yvonne Speller for patiently typing this thesis.

CONTENTS

Page

PART 3

LIST OF FIGURES

LIST OF PLATES

NOMENCLATURE

a	Distance from the nozzle exit to the effective origin.
A_f	Open or free area. Ratio of the total nozzle cross-sectional area to heat transfer (target) area.
A_n	Area associated with the mass transfer, m^2
b	Width of slot nozzle, m
b'	Mass transfer coefficient, m/s.
c_v	Vapour concentration, kg/m^3
C	Degree centigrade.
C_p	Specific heat of air at constant pressure, kJ/kgK.
d	Diameter of the target area over which integration of heat transfer coefficient has been carried out.
D	Diameter of the nozzle, m
E	Hot-wire probe output voltage. $E_1 \ldots E_4$ refer to the measuring planes of the probe.
$\bar{E}$	Time mean average voltage. E_{max} signifies $(\bar{E} + \sqrt{E'^2})$ and, similarly, $E_{min} = (\bar{E} - \sqrt{E'^2})$. E' is the fluctuating component of the voltage.
E_o	Voltage at zero velocity for the hot wire probe.
f	Friction coefficient (Blasius coefficient of friction is 4f , $f = \tau / \frac{1}{2} \rho V^2$)
G	Directional constant for the 'v' direction, (perpendicular to the wire).
G	Ratio of the maximum tangential and axial velocities, i.e. $w_{\overline{m}_o} / u_{\overline{m}_o}$.
G_x	Axial flux of the linear momentum, see Equation 3.3
G_ϕ	Axial flux of the angular momentum, see Equation 3.2
h	Heat transfer coefficient, W/m^2K. 'h_o' is the heat transfer coefficient at the stagnation point. '$\bar{h}$' is the average heat transfer over a surface.
H	Height of the manometer column in the 5-hole probe. $H_1 \ldots H_5$ refer to the individual apertures on the probe.
Hz	Hertz, cycles per second.
k	Thermal conductivity, W/m K

K Directional constant for the 'w' direction (along the wire).

K degrees Kelvin.

ℓ Litres.

m Mass of naphthalene sprayed, mg.

m_{tan} Mass of air flowing in the tangential entry of the swirler.

m_{tot} Total mass of air at the nozzle exit.

N Mass transfer flux, kg/m^2s

p Static pressure, N/m^2.

p_n Vapour pressure of naphthalene, N/m^2.

q Heat transfer per unit area.

r Radius of the target d/2; radial distance from the axis of the jet.

r_p Impingement radius defined by Equation 2.1.

rms Root mean square of the fluctuating quantity.

R_n Gas constant for naphthalene vapour, J/kgK.

s Second.

S Swirl number, $S = 2G_\phi/G_x D$

t Time for the clearance of naphthalene, s

T Temperature.

Tn Temperature at the naphthalene surface.

Tu Turbulence intensity, $Tu = \frac{\sqrt{(\bar{u}'^2 + \bar{v}'^2 + \bar{w}'^2)/3}}{u_e}$

u Axial component of the velocity; 'u_m' is the maximum velocity at a section; 'u_{mo}' is the mean nozzle exit velocity for the non-swirling jet. 'u_e' is the measured nozzle exit velocity at the jet axis for the non-swirling jet.

u' Fluctuating value of u.

u_c Velocity of the cross-flowing stream.

$u_{\overline{mo}}$ Maximum axial velocity at the orifice.

U Effective cooling velocity. $\bar{U}$, U_{max}, U_{min}, etc. are defined in a similar manner as the values of voltage E.

v	Radial component of the velocity.
v'	Fluctuating value of v.
$\bar{V}$	Resultant velocity. $(u^2 + v^2 + w^2)^{\frac{1}{2}}$
w	Tangential component of the velocity. 'w_m' is the maximum velocity at a section.
w'	Fluctuating value of w.
$w_{\overline{mo}}$	Maximum tangential velocity at the orifice.
W	Watts.
x	Nozzle pitch.
x_s	Distance along the target surface from the stagnation point for the impinging slot jets.
x_i	Lateral distance between adjacent nozzles.
x_j	Diagonal distance between nozzles.
z	Nozzle-to-target spacing; distance along the axis of the jet.
z_c	Length of the potential core.

Greek Symbols.

α	Pitch angle in five-hole probe measurements; phase difference between voltages; thermal diffusivities, $k/\rho C_p$.
γ	St/St_m
$\mathfrak{D}$	Mass diffusivity, m^2/s.
ε	Eddy diffusivity (momentum)
ε_H	Eddy diffusivity (heat transfer)
ε_M	Eddy diffusivity (mass transfer)
μ	Dynamic viscosity, kg/ms.
ν	kinematic viscosity or momentum diffusivity, m^2/s.
ρ	Density, kg/m^3.
ρ_a	Density of air, kg/m^3
σ	Standard deviation.
τ	Shear stress.

ϕ Acute angle of the jet inclination, see Figure 2.9; yaw angle in the five-hole probe.

Dimensionless Numbers

j_H j-factor for the heat transfer, $St\,Pr^{2/3}$.

j_M j-factor for the mass transfer, $St_m.Sc^{2/3}$.

Le Lewis number; (thermal diffusivity/mass diffusivity, i.e. $\alpha/\mathcal{D}$).

Nu Nusselt number, hD/k; Similarly $\bar{N}u$ is the average Nusselt number corresponding to $\bar{h}$ and Nu_o is the stagnation point Nusselt number corresponding to h_o.

Nu_x, Nu_d Nusselt number based on the nozzle pitch and the target diameter respectively.

$\overline{Nu}_s/\overline{Nu}_{ns}$ Ratio of Nusselt number for a swirling jet to non-swirling jet.

Pr Prandtl number; (momentum diffusivity/thermal diffusivity, i.e. ν/α).

Pr_t Turbulent Prandtl number, $\varepsilon/\varepsilon_H$.

Re_D Reynolds number, $\rho.u_{mo}.D/\mu$; Similarly, Re_x is based on nozzle pitch and u_{mo}.

Re_{ax} Reynolds number based on the arrival velocity, u_a, and the nozzle pitch, $Re_{ax} = \rho.u_a x/\mu$.

Sc Schmidt number; (momentum diffusivity/mass diffusivity, i.e. $\nu/\mathcal{D}$).

Sc_t Turbulent Schmidt number, $\varepsilon/\varepsilon_M$.

Sh Sherwood number, $b'D/\mathcal{D}$.

St Stanton number, $Nu/Re\,Pr$.

St_m Mass Stanton number, $Sh/Re\,Sc$.

Subscripts

D Diameter of the nozzle.

mo Mean at nozzle exit.

n Mass transfer surface (naphthelene).

CHAPTER 1

INTRODUCTION

The employment of impinging jets can produce high rates of convective heat or mass transfer, see Table 1.1. Moreover, impinging jet systems are also readily controllable so that their use has become wide-spread in recent years in industrial heating, cooling or drying operations. Arrays of either circular or slot jets can be arranged to cover large transfer areas.

Table 1.1

TYPICAL CONVECTIVE HEAT TRANSFER COEFFICIENTS FOR AIR (Ref.1)

Natural Convection	3-15	W/m^2K
Flow parallel to a surface	15-150	W/m^2K
Impinging jets.	75-450	W/m^2K

Jet impingement heat transfer has also received previous attention at Cranfield with the aim of improving the design of 'rapid heating' furnaces. Isothermal models (near ambient temperature) are employed to simulate the furnace chamber and both circular and slot jet arrangements have been studied (Refs.2-7). The work described in the present thesis is part of this programme and is concerned with the effects of swirl on impingement heat transfer rates. It is, thus, relevant at this stage to examine briefly the use of impingement jets in rapid heating furnaces and other important engineering situations.

1.1 JET IMPINGEMENT FURNACES

Both ferrous and non-ferrous metals can be heated in so-called 'rapid heating' furnaces which utilise 'high speed convective heating', see Ref.3. The necessary high rates of convective heat transfer can be obtained by either:-

(a) tangential firing into a chamber which closely surrounds the stock,

or

(b) impingement of jets of combustion products issuing from industrial burners.

In commercial 'jet impingement' systems, the burners are supplied with a pre-mixed near stoichiometric mixture of gas and air, and combustion is completed within the burner tunnel. The issuing combustion products exit at velocities of up to 150 m/s and at temperatures approaching the adiabatic flame temperature. The jet velocity is dictated by the static pressure within the burner (which is converted into dynamic head upon discharge) and the 'flame temperature'.

Figure 1.1 illustrates the essential features of a typical jet impingement furnace consisting of a pre-heat zone which recovers heat from the exit gases, a rapid heating zone utilizing 'jet-impingement', and a soak zone which is required to reduce the temperature gradients in the stock. In the rapid heating zone, the forced convection from the impinging jets is the dominant mode of heat transfer. The particular features of this heating technique in comparison with conventional furnaces (in which radiative heat transfer dominates) can be summarised as follows:- (see Refs.8-12).

1. Convective heating rates are often significantly higher so that the period the stock spends in the hot zone of the furnace is greatly reduced. This makes jet impingement particularly advantageous in applications in which metallurgical problems can arise through severe decarburisation, oxidation, or other phenomena which are dependent on the time spent at high temperature.

2. These high heating rates together with the comparatively low furnace height (dictated by the burner to stock spacing) result in a more compact furnace for a particular throughput.

3. Since the main mode of heat transfer is forced convection from the hot gases, such systems do not primarily rely on re-radiation from furnace walls and these may be readily designed to have a low thermal inertia. Therefore, rapid start-up or shut-down is possible with the consequent benefit of improved temperature control during heating and the possibility of automation.

4. The directional nature of impingement heating permits localised or concentrated heating on a defined zone of limited extent on a component. This can often be desirable in heat treatment processes, e.g. in hardening or toughening tool blanks.

5. Commercial jet-impingement burners are normally supplied with gaseous fuels (such as LPG or natural gas) although oil-fired versions have

been tested experimentally.

6. Available burners have relatively small thermal ratings so that the engineering difficulties associated with the installation of large numbers of burners have limited the size of 'jet-impingement' furnaces. However, when used in small furnaces, they result in a simple construction with low maintenance costs.

1.2 OTHER USES OF JET IMPINGEMENT

Some of the advantages discussed in the previous section, namely the high heat transfer rates which can be 'localised' at specific zones on the impingement surface, together with the precise control and the ease of automation, make 'jet impingement' attractive in other industrial applications.

Impingement dryers have been used extensively in the paper industry for the past two decades. They are used for drying veneer, cardboard, paper and aqueous coatings. Drying of tissue paper and towelling material which should take place 'uniformly' over the surface can also be achieved by selecting an appropriate array of jets. References 13-15 should be consulted for further information on this subject.

In recent years, a development programme has been conducted with the aim of using impingement of air jets for drying ink during printing, see Refs.16-19. These drying operations require high rates of heat and mass transfer because of the high production speeds of modern printing machines and the limited length of the dryer. In some cases, the speed of the printing process is dictated by the rate of drying ink rather than by the printing operation itself.

The impingement cooling of turbine blades and discs is also gaining importance (Refs.20 and 21). Other reported uses include spot cooling of electronic components, cryogenic treatment of tumours, and the cooling of glass and metals. Thermal surface treatment processes as in tempering and toughening of metals and glass, together with localised heat treatment of plastics and glass plates also employ impinging jets.

1.3 SCOPE AND PURPOSE OF THE PRESENT WORK

In some jet impingement burners swirl is imparted to the combustion products and this can markedly alter the flow characteristics of the hot-gas jet (see Refs.22 and 23). As the degree of swirl is progressively increased, the jet spread, the rate of entrainment of the surroundings,

and the rate of decay of the velocity are all increased. The centrifugal forces set-up by the swirling motion produce an adverse pressure gradient along the jet axis. Consequently, even with relatively weak swirl, the maximum axial velocity of the jet is decreased. With a higher degree of swirl, the pressure gradient can overcome the forward kinetic forces and the flow reverses in the central region of the jet. The turbulence and the flow characteristics of a swirling jet are also quite different from those of the non-swirling case. These changes in the fluid dynamics obviously effect the convective heat transfer associated with jet impingement.

Unfortunately, there is a paucity of published data on the heat transfer characteristics of impinging swirling jets. Perry (Ref.24) conducted a preliminary study at Cranfield using a single jet. The size of the target surface in this investigation was relatively small and only extended from $0 \leqslant r/D \leqslant 3$. The present work along with the average heat transfer measurements of Dunn (Ref.25) was undertaken to fill this gap. Dunn's work was concerned with average heat transfers from swirling jets arranged in arrays of square pitch and is discussed later in Section 3.5.

The present thesis describes measurements of the local heat transfer coefficients, both single and multiple (3 x 3) square array), swirling jets impinging on a flat plate. The parameters varied in the study were the degree of swirl, the nozzle-to-plate separation, the pitch of jets and the jet Reynolds number. The range of swirls investigated can only be classified as weak or medium but covered those of practical interest. The upper limit on the swirl number resulted mainly because of the large pressure drop in the swirlers at high swirls. Morover, there appeared to be little justification for studying higher swirls since Dunn (Ref.25) showed that the heat transfers were greatly reduced under these conditions. The variation of nozzle-to-target separation was also limited to a maximum of 12 nozzle diameters because of very low heat transfers at greater spacings (Ref.25). $Z/D = 2$ was considered to be the practical minimum spacing in any installation. The nozzle pitches (x/D) were similar to those studied previously by Dunn for his average heat transfer measurements.

Mass transfer measurements (determination of the sublimation of naphthalene) were undertaken in order to estimate the heat transfer . A 'thin-film' technique was employed instead of the more usual profilometric measurements, and a special spray rig was developed for this purpose as described in Chapter 8. The Chilton-Colburn analogy was employed to infer the heat transfer coefficient.

Limited velocity and turbulence measurements using a hot-wire anemometer were also undertaken as an aid in under-

standing the heat transfer phenomena. Jet velocities were also measured with a five-hole pitot probe with the main aim of characterising the swirling jet. It was considered that a detailed investigation of the flow and turbulence fields lay outside the scope of the present work.

1.4 LAYOUT OF THE THESIS

The thesis has been arranged in three parts. The first of these is a review section and previously published work on jet impingement is discussed. A chapter outlining main feature of swirling flows is also included together with a literature review of flow and heat transfer phenomena associated with swirling jets.

The second part is concerned with the overall description of the experimental rigs and swirlers as used in both the single and multiple jet studies. Details of the jet characterisation, i.e. the five-hole and hot-wire probe measurements are also presented. A full discussion of the velocity and turbulence results concludes this part of the thesis.

The final part is concerned with the heat transfer studies. The introductory Chapter discusses heat transfer analogies and justifies the use of the Chilton-Colburn relationship. A second chapter describes the detailed construction of the naphthalene 'thin-film' spray rig. The measurement procedure and results are discussed in two final chapters.

Appendices have been included to present further details as desired.

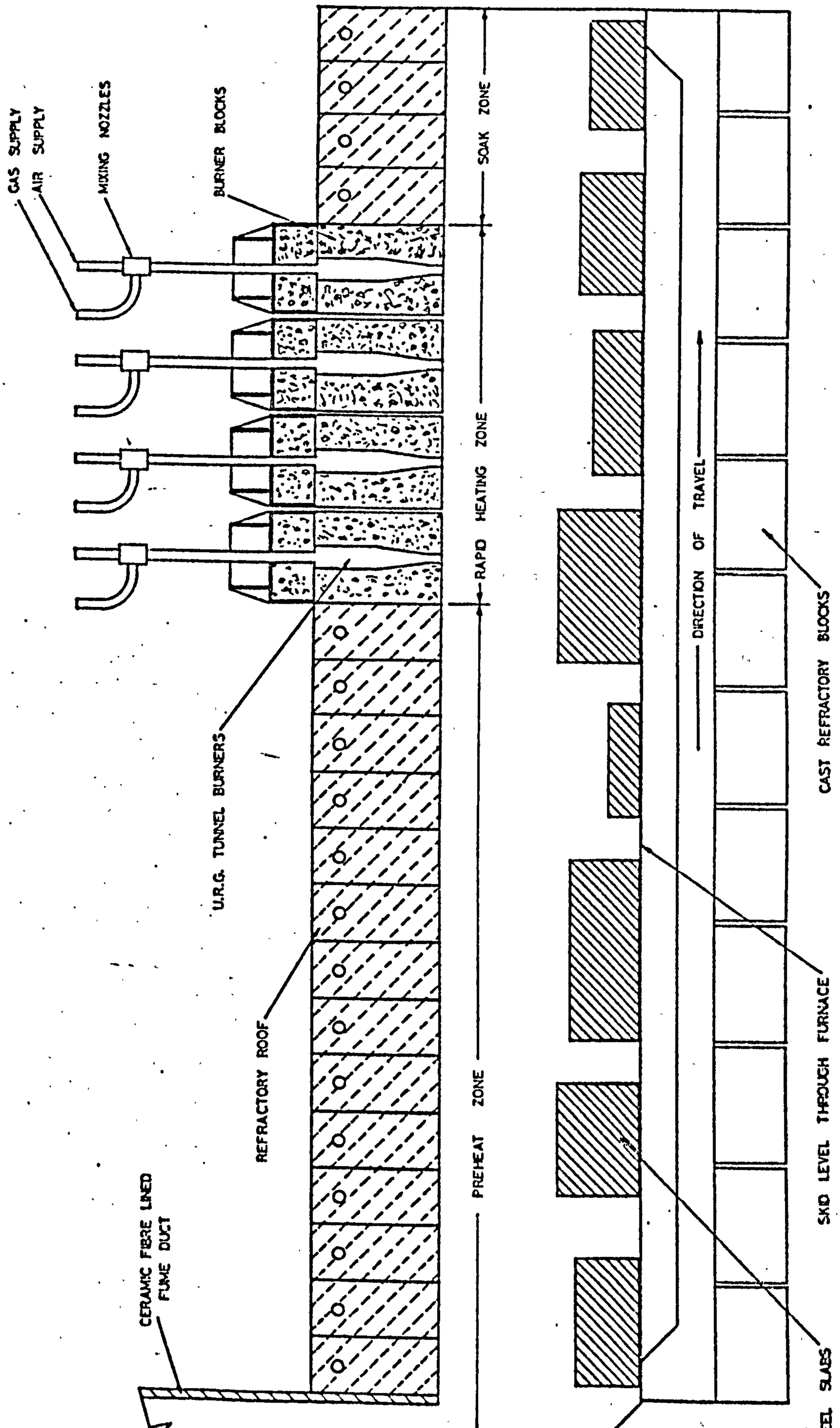

Fig.1.1 TYPICAL JET-IMPINGEMENT FURNACE.

CHAPTER 2

THE FLOW AND HEAT TRANSFER CHARACTERISTICS OF IMPINGING JETS

2.1 INTRODUCTION

As mentioned in the previous chapter, heat transfer from impinging jets has been studied extensively in the past. Most of the investigations have been concerned with free, non-swirling jets issuing from either slot or circular nozzles into initially quiescent surroundings. The effects of crossflows, jet swirl and confinement have only been studied relatively recently. This chapter reviews the main flow and heat transfer characteristics of both single and multiple jets arranged in arrays. Since this thesis is concerned primarily with impingement of swirling jets, the fluid dynamics of these systems are discussed separately in Chapter 3. Previous heat transfer studies due to impingement of jets with swirl are also described in this latter chapter.

Selected individual publications are discussed in the present chapter, and some of these published data have been used for comparison purposes to establish validity of the experimental work described in this thesis.

2.2 FLUID DYNAMICS OF IMPINGING JETS

2.2.1 Single Jets.

Fluid jets can be conveniently classified according to their geometry, i.e. they are usually either two dimensional, long, narrow slot jets or circular axisymmetric jets. Jets can also be classified according to whether they are laminar or turbulent. Most jets in practical use are turbulent or, alternatively, the initially laminar jet soon becomes turbulent due to entrainment of the surroundings. The critical Reynolds number for transition (based on nozzle diameter or slot width and the velocity at the exit section) is approximately 2,000, see Vickers (Ref.26). A jet Reynolds number of 14,000 ensures that the turbulence is fully developed.

Figure 2.1 illustrates schematically the basic flow characteristic of an impinging jet issuing into initially stagnant surroundings in the absence of swirl. The flow-field may be divided into the following four regions:-

(i) A flow establishment region which extends from the exit of the nozzle to the end of the 'potential core'.

(ii) An established flow region in which velocity profiles are similar and the flow is unaffected by the presence of the impingement surface.

(iii) An impingement region in which the flow turns through a right angle. A strong negative pressure gradient exists at the surface of the plate in this region with the surface pressure higher than that of the surrounding fluid.

(iv) A wall jet region in which the fluid flows over the plate to produce a boundary layer which gradually builds up in thickness.

The free and wall jets are mainly influenced by viscous forces whereas, in an impingement region, pressure and momentum forces predominate.

On leaving the nozzle, the jet entrains the surrounding fluid so that the velocity near the boundary of the jet is reduced. The central core is, however, not initially affected by this entrainment process and the velocity within this area is unaltered. This region is referred to as the 'potential core'. At greater distances from the nozzle exit, the potential core progressively decreases in width, although the central velocity is still unaltered. Eventually, entrainment effects extend throughout the jet which becomes fully established. The length of this potential core zone (as measured by previous investigators) can vary from 4.7 to 7.7 nozzle diameter, see Ref.27. This length has been found to be independent of the exit Reynolds number Re_D, for a fully developed turbulent jet. The reported variations in the potential core length can be attributed to differences in the turbulence characteristics (and hence mixing behaviour) of the jet rather than to experimental error.

Beyond the potential core zone, further viscous mixing and entrainment of the surrounding fluid results in continual spreading of the jet. The maximum jet velocity progressively decreases downstream from the jet exit. Figure 2.2 presents the decay of the centreline velocity of slot and circular jets. Mixing is generally more intense for circular jets and the velocity decays (after the potential core) can be related to $1/\sqrt{z}$ and $1/z$ for the slot and circular jets respectively, 'z' being the distance from the nozzle exit along the jet axis.

The influence of the impingement surface is only experienced at a distance of 1.2 jet diameters from the surface for a circular jet (Schrader, Ref.28).

In this region, the velocity decreases, the flow turns through 90 degrees, and the static pressure rises. The centreline velocity of the jet eventually decelerates to 'zero' at the stagnation point.

A boundary layer flow (with origin at the stagnation point) builds up beneath the outer impinging jet flow. This boundary layer has been shown to be of constant thickness over a near stagnation region of 1.2 nozzle diameters by Schrader, after which boundary layer growth occurs. However, later measurements carried out by Hoogendoorn (Ref.29) suggested that for certain cases the thickness of the layer decreased up to a distance of 0.3 nozzle diameters from the stagnation point. Wall jet is subsequently established as the boundary layer builds up along the surface of the plate. This wall jet region may be divided into two parts:- an inner layer where the effect of the wall is present, and an outer layer which is characterised by the features of a free turbulent flow. The velocity at the boundary between these two layers is maximum. Further details of wall jet flow may be seen in Ref.27.

The impingement region can be characterised by the presence of strong negative pressure gradient, and Dawson and Trass (Ref.30) suggested that this region can be empirically determined by:-

$$r_p = 0.284\, z \qquad (2.1)$$

where 'r_p' is the radial extent of impingement region centred on the stagnation point.

The above somewhat brief description serves to illustrate the complexity of the flow-fields associated with impinging jets, especially if the target is placed near to the nozzle exit. Nevertheless, the problem has been given considerable attention, both analytically and experimentally, and Kabari (Ref.6), Hardisty (Refs. 17 and 18), and Gauntner et al (Ref. 27) should be consulted for comprehensive reviews of the subject. Empirical velocity relationships for the different regimes have also been quoted in the literature, see for example Schlunder (Ref.31). Two such typical equations are presented here, and they express the relationship between the maximum velocity of an axisymmetric jet and the velocity at another section. Thus:-

$$\frac{u}{u_m} = \exp\left[-(r/C\,z)^2\right] \qquad (2.2)$$

where 'u_m' is the maximum axial velocity at any section, 'r' is the distance from the axis of the jet, and C is approximately equal to 0.1.

and,

$$\frac{u_m}{u_{mo}} = \left\{1 - \exp\left[-(D/\sqrt{2}\, C_1 z)^2\right]\right\}^{1/2} \qquad (2.3)$$

where 'u_{mo}' is the nozzle exit velocity and C_1 is a constant related to the length of the potential core 'z_c' by:-

$$C_1 = 0.102\ (4D/z_c)$$

Equation (2.2) is valid only for the fully established region discussed previously, while equation (2.3) applies from the exit of the nozzle to the region where the effects of the impingement surface are felt.

2.2.2 Multiple Jet Systems

The flow characteristics of individual jets when arranged in arrays are generally similar to those of single free jets. However, in addition, secondary stagnation zones ensue where the wall jets from the adjacent nozzles interact. The flow can be further complicated at small nozzle pitches and small nozzle-to-plate separations. In large confined arrays, the 'spent air' from upstream jets can affect the flow patterns associated with jets further downstream, especially if the system is confined so that the exhaust is removed from one side. The effects of cross flows are discussed later in Section 2.3.3.

2.2.3 Turbulence

Turbulence levels can considerably affect jet impingement heat transfer, especially in the 'impingement region'. The earliest published measurements of jet turbulence were carried out by Corrsin (Ref. 32). Some of his results have been reproduced in Figure 2.3 The turbulence intensity (based on the maximum velocity at jet exit 'u_{mo}') increases up to an axial distance z/D of 8 and subsequently decreases. However, if 'u_m' (maximum velocity at the section of measurement) is used as a reference, the turbulence intensity does not show any decrease with

increasing 'z/D'. Recently, Boguslawski and Popiel (Ref.33) carried out a detailed study on the flow structure (velocity and turbulence) in the initial flow regions ($z/D \leq 10$) of free round turbulent jets and may be referred to for further details on this subject.

2.3 JET IMPINGEMENT HEAT TRANSFER

Several authors have published reviews of the heat and mass transfer phenomena associated with impinging jets, see for example Arganbright and Resch (Ref.14) in 1971 and Martin (Ref.34) in 1978. In this section, generally accepted characteristics of impingement heat transfer are described briefly. Contributions of selected individual investigators are examined later in Section 2.4.

Jet impingement heat transfer coefficients depend on the jet flow rate, the shape, size and position of the nozzle, and the nozzle-to-plate separation distance. The stagnation region heat transfer is also considerably affected by the turbulence intensity of the jet. Most of the experimental heat transfer data can be correlated by an expression of the form:-

$$Nu = \alpha (Re)^{m} (Pr)^{n} . f(Geometry) \qquad (2.4)$$

where α, m, and n are empirical constants (n = 1/3 usually). The geometrical parameters are usually non-dimensionalised in terms of the diameter (or slot width) of the jet.

In the ensuing discussion, the effects of the geometrical parameters (e.g. jet diameter, nozzle pitch, and nozzle-to-plate distance) are not described separately but are included implicitly in the arguments used to discuss other aspects of impingement heat transfer.

2.3.1 Single Jets

(a) Heat Transfer in the 'Stagnation Region'

Gardon and Cobonpue (Ref.35), using circular jets, and Gardon and Akfirat (Ref.36), employing slot jets, observed stagnation point heat transfers at different Reynolds numbers and various nozzle-to-target spacings (z/D). Although the results for both types of nozzle exhibit similar trends, the range of Reynolds numbers covered in the slot jet studies was greater and this data is, therefore, reproduced in Figure 2.4 as an aid for further discussion.

As illustrated in Figure 2.4, the stagnation Nusselt number increases with jet Reynolds numbers. It may also be observed that at low Reynolds number (i.e. initially laminar jets), the stagnation heat transfer is virtually constant at separations 'z/b' $\leq$ 5 and, subsequently, decreases. This follows the trends shown by the variation of the centreline velocity, see Figure 2.2. For the fully turbulent jets (Re_D > 2000), the stagnation point heat transfer coefficients increase with increasing 'z/b' (nozzle-to-target spacing) upto 7 to 11. At greater spacings, they decrease in a continuous fashion. This variation in 'Nu_o', the Nusselt number at stagnation point, with increasing 'z/b' was explained in a following paper by Gardon and Akfirat (Ref.37). They suggested that the increase in the turbulence intensity of the jet which occurs up to a 'z/b' of 8 or thereabouts, results in an increase in heat transfer coefficients. This increase in turbulence can overcome the effects of a decrease in velocity outside the potential core. The heat transfer, however, subsequently decreases as the intensity of turbulence (based on the maximum exit velocity) and also the velocity of the jet decrease. Gardon and Akfirat substantiated their arguments by observing an increased heat transfer when the turbulence intensity of the jet was increased artifically. They also demonstrated that the artificial increase in turbulence levels at the nozzle exit were only effective when the target plate was placed at z/D $\leq$ 8.

It is also apparent from Figure 2.4 that, at small separation distances (z/D < 8) and Re_D > 5,500, the slot size effects the stagnation point heat transfer. This is again attributed to the differences in turbulence characteristics of the nozzles used.

Several correlations have been suggested to express stagnation heat transfers, e.g. Vallis et al (Ref.38) proposed:-

$$Nu_o = 1.93\ Re_D^{0.58}\ P_r^{0.33}\ (z/D)^{-0.74} \qquad (2.5)$$

This being valid for 10 < z/D < 20 and

$$3880 < Re_D < 23000$$

As mentioned earlier, the stagnation point heat transfer is dependent on the turbulence intensity of the jet and Hoogendoorn (Ref.29) has suggested

a relation between the Nusselt number and turbulence intensity expressed as:-

$$Nu_o/Re_a^{1/2} = 0.65 + 2.02\,(Tu\,Re_a^{1/2}/100) - 2.46(Tu\,Re_a^{1/2}/100)^2 \qquad (2.6)$$

where 'Re_a' is the Reynolds number based on the diameter of the jet and the arrival velocity, and 'Tu' is the turbulence intensity based on the main velocity component.

This equation is limited to $1 \leqslant z/D \leqslant 10$, $20{,}000 \leqslant Re_a \leqslant 90{,}000$, and $9\% \leqslant Tu \leqslant 20\%$. However, it should be emphasised that there was considerable scatter in the results.

The problem of measurement and comparison of stagnation point values can be reduced by studying an impingement region whose diameter may be found by using Equation (2.1). Vallis et al (Ref.38) have given a correlation for the impingement zone which compares fairly well with the results of earlier studies, i.e.:-

$$\overline{Nu} = 0.225\ Re_D^{0.68}\ Pr^{0.33} \qquad (2.7)$$

within the following limits:-

$$10 \leqslant z/D \leqslant 20, \quad 2 \leqslant d/D \leqslant 16, \quad \text{and}$$

$$5675 \leqslant Re_D \leqslant 20{,}680.$$

'D/d' is the ratio between the diameter of the nozzle and the target over which the values of heat transfers are integrated.

(b) Lateral Variations in Heat Transfers.

The local heat transfer coefficients show large lateral variation, especially at small nozzle/target spacings. This is illustrated in Figures 2.5 and 2.6 for a 3.2mm (1/8 inch) wide slot jet at $Re_D = 11{,}000$, as quoted in Ref.36. In general, the heat transfer coefficients decrease rapidly with increasing distance along the transfer surface from the stagnation point. Furthermore, the distributions exhibit secondary peaks at $x_s/b = 6$ (approx.) for $z/b \leqslant 6$. This is due to the laminar to turbulent transition in the boundary layer of the flow.

(c) Average Heat Transfer Coefficient

Average heat transfer coefficients can be determined either by direct measurements or by integration of the local values over the specified region. In the case of the single round nozzle, the average heat transfer coefficient '$\bar{h}$' can be found by evaluating:-

$$\bar{h} = 8/d^2 \int_0^{d/2} h.r\, dr \qquad (2.8)$$

Most of the previous investigations have found that heat transfer over reasonably large areas (e.g. $0 \leqslant r \leqslant 20D$) is independent of the nozzle-to-target spacings up to about 6 jet diameters for circular nozzles, see Refs. (35), (39) and (40). Metzger (Ref.41), however, found that average heat transfer decreased monotonically with increase of nozzle-to-target spacings for their tests on circular nozzles. For slot jets, Metzger and Gardon and Akfirat (Ref.36) found that average heat transfer actually increased up to a 'z/b' of 8. This was particularly so if the averages were determined over small areas (e.g. $0 \leqslant x_s/b \leqslant 4$).

Correlations for the average heat transfer from a single jet should always be checked for the limits of applicability and the integration range. One such correlation for single round jets is expressed as:- (Ref.36)

$$\overline{Nu} = 0.78\ Re_a^{0.55} \qquad (2.9)$$

provided $Re_a \geqslant 1{,}000$ ('Re_a' is the Reynolds number based on the 'arrival velocity' and the nozzle diameter), $z/D \geqslant 12$, and $1 \leqslant d/D \leqslant 24$ ('d' is the target diameter over which the correlation can be applied).

Expressing the correlation in this form avoids the introduction of 'z/D' term since this is implicitly involved in 'u_a' the arrival velocity (see Appendix D).

Martin (Ref.34) has proposed a more generalised correlation which has been referred to in Section 10.4.4, while comparing the present single jet results with the published data.

2.3.2 Multiple Jet Systems

The heat transfer phenomena from arrays of jets are qualitatively similar to those of the single jets. Secondary peaks ensue, however, as the wall jets from adjacent nozzles interact. The effects of these interactions are increased when the jets are closely spaced or are near to the target plate.

The lateral variations of the local heat transfer coefficients from an array of 3.2mm slot jets are shown in Figure 2.7 (Ref.36). Generally, for $z/b < 8$, the identity of each jet is unaffected and the maximum heat transfers are approximately those associated with a similar single jet. The jets interact producing a secondary peak in 'h' at a position midway between the jet axes. As the nozzle-to-plate separation is increased, jet interaction occurs before impingement, resulting in the reduction of the heat transfer coefficients. At the largest separation studied, the jets coalesce and act as a single large jet. The interactions between adjacent jets and their effect on heat transfer are difficult to generalise, and the reader is referred to Martin (Ref.34) for details.

Two typical correlations for multiple round and slot jets from Refs.35 and 36 respectively are quoted:-

$$\overline{Nu}_x = 0.286\ Re_{ax}^{0.625} \qquad (2.10)$$

(Multiple Round Jets)

where '$\overline{Nu}_x$' is the average Nusselt number based on the nozzle pitch 'x', and 'Re_{ax}' is the Reynolds number based on the 'arrival velocity' and nozzle pitch. The correlation is valid for $4 \leqslant z/D \leqslant 128$, $2.4 \leqslant x/D \leqslant 32$, and $1{,}000 \leqslant Re_{xa} \leqslant 300{,}000$.

$$\overline{Nu}_x = 0.36\ Re_{ax}^{0.62} \qquad (2.11)$$

(Multiple Slot Jets)

This relation is valid for $8 \leqslant z/b \leqslant 64$, $2{,}000 \leqslant Re_{ax} \leqslant 600{,}000$, and $16 \leqslant x/b \leqslant 64$.

Other correlations for multiple round jets are presented in Section 2.4, and some of these together with that expressed in Equation 2.10 are presented in Figure 2.8.

2.3.3 Effects of Crossflows.

The 'crossflow' or 'spent air' effect which occurs due to the removal of the exhaust in multiple jet systems generally decreases the stagnation point heat transfer and effectively displaces the regions of high heat transfer downstream in the direction of crossflow due to the jet deflection. The local heat transfers upstream of the impingement region are generally decreased under crossflows, whereas the downstreams are increased. This upstream degradation and the subsequent downstream enhancement in the local heat transfer can be explained by the flow phenomena. Upstream of the jet, the crossflowing stream is decelerated due to the blockage effect. In the downstream zone, however, 'jet impingement' together with the flushing influence of crossflow results in higher heat transfer. The net effect on average heat transfer is to bring about an overall reduction except at small nozzle-to-target spacings (z/D = 1 approx.), see Ref.44.

The detailed effects of the crossflowing stream depend on the usual geometrical parameter as well as the mass velocity ratio ($\rho_c u_c / \rho_j u_j$) between crossflow and the jet so that they are difficult to generalise. Refs.6, 15, 42, 43 and 44 can be consulted for further details.

2.3.4 Jet Inclination

The influence of the inclining of the jet on impingement heat transfer was studied by Perry (Ref.45) in one of the earliest published papers on impingement heat transfer. The heat transfer coefficients were determined by means of a calorimeter flush with the surface of the plate. This calorimeter, whose diameter was less than or equal to the diameter of the nozzle used ($r/D \leqslant 0.5$), was always centred at the point of intersection between the jet axis and surface. With the distance 'z' between the nozzle exit and this point of intersection kept constant, the heat transfer coefficients decreased with decreasing impact angle ϕ, see Figure 2.9. At an angle of ϕ = 15 degrees, the heat transfer coefficient was found to be about 43% lower than the corresponding one for normal impingement (ϕ = 90 degrees).

Korger and Krizek (Ref.46) found that, for the slot jets, the point of maximum heat transfer does not coincide with the point of intersection between jet axis and surface. The point of maximum heat transfer shifts by a length 'Δx' towards that part of the jet being deflected in the acute angle (Figure 2.9).

This length can be determined, for slot jets, approximately by:-

$$\Delta x = C \cot \phi \qquad (2.12)$$

where, $C = 1.4\ (b + 0.11z)$, 'b' is slot width, and 'z' is the nozzle to plate separation.

Korger and Krizek also found that the average heat transfer was practically independent of the jet inclination for a constant distance 'z' within the range $30^{o} \leqslant \phi \leqslant 60^{o}$. This confirmed earlier findings by Perry (Ref.45).

2.4 REVIEW OF SELECTED PUBLICATIONS ON IMPINGEMENT HEAT TRANSFER

Most of the experimental studies on jet impingement heat transfer have been concerned with orthogonal impingement onto a flat surface. In order to limit the length of this present chronological review, only certain of the publications have been selected for inclusion. Furthermore, the studies dealing specifically with the effects of crossflow have been excluded, whilst any published data for impinging swirling jets is discussed in the next chapter.

In 1951, Freidman and Mueller (Ref.47) evaluated average heat transfer rates from an array of air jets impinging orthogonally onto a flat plate. These arrays were provided by several types of distributors consisting mainly of holes (orifices) but some of angled nozzles and slots (both normal and angled). The parameters varied according to the diameter of the orifices (6.3 and 12.7mm), hole pitch (free area 'A_f' varying from 0.7 to 10.4% with respective hole pitches of 10.7 and 2.7), plate separation (z/D = 4.5 to 17), and air flow rates (Re_{ax} = 20,000 to 140,000). The target plate was heated by steam and the heat transfer coefficients were obtained by measuring the amount of condensation. The proposed relationship between heat transfer coefficients and mass velocity 'G_s' for all the tests was:-

$$\bar{h} = C\, G_s^{0.78} \qquad (2.13)$$

where 'C' was a function of the geometrical configuration. For example, C = 0.046 for an array corresponding to 12.7 mm diameter holes, A_f = 0.104 and z/D = 9.5; and C = 0.321 for 12.7 diameter holes, A_f = 0.00628, and z/D = 4.5

They concluded that the optimal performance, considering heat transfer and power consumed, corresponds to the perforated plates (holes) having a free area of 2 to 3 per cent and spaced about 4 to 6 diameters from the target.

Perry (Ref.45) investigated in particular the effects of jet inclination (from 0 to 90 degrees to the horizontal) on the impingement heat transfer from a single round air jet (21.6 and 16.5 mm diameter). The Reynolds number (Re_D) was varied between 11,000 to 30,000 with nozzle-to-plate separation being greater than 8 nozzle diameters. Heat transfers were measured using a 16.5mm calorimeter positioned at the centre of the target plate coinciding with the jet axis. The correlation proposed was of the form:-

$$Nu_L = C\ Re_L^{0.7}\ P_r^{0.33} \qquad (2.14)$$

where the characteristic length in Nusselt and Reynolds numbers is the 'transducer' diameter. The constant 'C' depends on the inclination of the jet (e.g. C = 0.1810 for orthogonal impingement whilst C = 0.122 for the jet inclined at 30 degrees to horizontal).

The lateral variations of the heat transfer coefficient were obtained by moving the plate relative to the jet. The integration of these lateral variations showed that the average heat transfer over the plate was practically independent of the jet inclination.

Thurlow (Ref.48), commenting on the above-mentioned publication, reported that his results on single jets (12.5 and 25.4mm) conducted at Re_D = 22,000 to 60,000 agreed generally with those of Perry (Ref.45). However, he favours the use of nozzle diameter in any correlation for impinging round jets. He also suggested that, for heat transfers at large radial distances from the stagnation point, natural convection should also be taken into consideration, but no values of (r/D) are quoted where natural convection should be accounted for.

Smirnov et al (Ref.49) investigated heat transfers from impinging water jets for Re_D = 50 to 31,000. Six different nozzles with diameters ranging from 2.5 to 36.6mm were used. The heat transfers were measured on a 48mm diameter copper calorimeter. They studied the effect of nozzle-to-target spacing (z/D) more closely, and proposed separate correlations for $z/D \leqslant 0.5$, $0.5 \leqslant z/D \leqslant 10$, and $z/D \geqslant 10$. The correlation for $z/D \leqslant 0.5$ is of almost no practical importance and is, therefore, not presented here. For the other two cases:-

$$\overline{Nu} = C.\ Re_D^{0.64}\ .\ P_r^{0.33}\ \exp(-0.037\ z/D) \qquad (2.15)$$

where $C = 0.034\ D^{0.9}$, where D is in millimeters;
Valid for $0.5 \leqslant z/D \leqslant 10$, $1,600 \leqslant Re_D \leqslant 30,000$ and $0.7 \leqslant Pr \leqslant 10$.

$$\overline{Nu} = C_1(Re_D.Pr)^{0.33} \exp(-0.037\ z/D) \qquad (2.16)$$

where $C_1 = 0.034\ D^{1.3}$, where D is again in millimeters.
Valid for $z/D > 10$; Re_D and Pr are valid for similar ranges as for Equation 2.15.

The dependence of the heat transfer coefficient on the nozzle diameter in the above equations is probably due to the differences in the turbulence characteristics of the impinging jets. As discussed in Section 2.3.1, the region around the stagnation point is particularly affected by the jet turbulence and most of the measurements by Smirnov et al correspond to $r/D < 2.24$, where 'r' is the target radius.

Most of the previous investigators, e.g. Perry (Ref.45), employed relatively 'large' transducers to measure local heat transfers at the stagnation point and along the surface of the plate. The heat transfer coefficients near the stagnation point show particularly large variations, and these transducers were unsuitable for such measurements. Gardon and Cobonpue (Ref.35) successfully measured the local heat transfers on a flat plate by employing a transducer less than 1mm in diameter. Both single jet and multiple jet arrays (square) were studied. The jets of air impinged on a vertical 152 x 152mm electrically heated plate. Local heat transfer variations were measured by moving the plate relative to the jets. Average heat transfer was also determined directly by measuring the total power input to the plate.

They proposed a correlation for stagnation point heat transfer as follows:-

$$Nu_o = 13\sqrt{Re_D}\ .\ (z/D)^{-1} \qquad (2.17)$$

provided $z/D \geqslant 20$ and $Re_D \geqslant 14,000$. The constant was later considered to be 40% too high (Ref.36).

The correlations proposed for average heat transfer from single and multiple jets have already been quoted, see Equations 2.9 and 2.10. The parameters varied in single jet studies were the nozzle diameter (D = 2.3 to 9mm), nozzle-to-plate separation (z/D = 0 to 50), and jet velocity (corresponding to Re_D = 7,000 to 112,000). In the case of multiple jet heat transfers, two square arrays of 5 x 5 and 7 x 7 jets were examined.

The parameters varied in these studies were also nozzle diameter (D = 1.6 to 12.7mm), nozzle-to-plate spacing (z/D up to 128), nozzle pitch (x/D = 2.4 to 32) and jet velocity (Re_a = 1000 to 300,000).

Metzger (Ref.41) was mainly interested in 'spot cooling' by slot jet impingement. Some experiments on circular jets were also carried out. The Reynolds number for the slot jets varied from 3,000 to 8,000 (based on hydraulic diameter and nozzle exit velocity). As discussed earlier in Section 2.3.3, he observed a maximum local stagnation point at z/b = 8, probably due to the increase of the jet turbulence. He also found that the effect of exit velocity profiles on heat transfer is very small. The correlation proposed for the slot jets can be expressed as:-

$$\overline{St}\ Re_{hyd.}^{0.434} \cdot P_r^{0.63} = 0.74\ (x_s/b)^{-0.434} \qquad (2.18)$$

where '$\overline{St}$' is the average Stanton number (on the target, $3 \leqslant x_s/b \leqslant 50$); '$Re_{hyd}$ is the Reynolds number based on the hydraulic diameter of the nozzle exit and $\bar{u}_{mo}$.

The circular jet tests were carried out at a nozzle diameter of 5mm and Re_D = 8,000 to 19,700. He observed that in the case of the circular jets, the heat transfer coefficients show a monotonic decrease with the increase of nozzle-to-plate separation. No specific correlation was proposed, but Equation 2.18 was considered to be applicable (approximately) also for circular jets.

Gardon and Akfirat (Ref.36) reported local and average heat transfer from single and multiple slot jets impinging normally onto a flat plate. The measurements were made by a method similar to that used by Ref.35. The results were similar to those found previously for the circular jets (see also Section 2.3). The proposed correlation for slot jets has already been presented, see Equation 2.11.

The same authors in a subsequent paper (Ref.37) discussed the effects of turbulence on the heat transfer at the stagnation point. They were able to show that the heat transfer increased with the increase in jet turbulence up to z/b = 8. Turbulence could, therefore, explain the discrepancies in local heat transfer values at the stagnation point observed by several researchers. They also explained the phenomena of secondary peaks in the lateral heat transfer variations by proposing that these were caused by laminar to turbulent transitions in the wall jet boundary layer flow.

Hilgeroth (Ref.51) employed direct heat transfer measurements to study circular impinging jets in triangu-

lar arrays (isosceles). He also studied the effect of 'exhaust' air on the impinging jets. The parameters varied were the nozzle diameter (D = 15 to 50mm), nozzle pitches (x/D = 4.5 to 10.5), nozzle-to-plate spacing (z/D = 2 to 6), and air mass flow rates to produce Re_x = 40,000 to 300,000 ('Re_x' is the Reynolds number based on the jet pitch and nozzle exit velocity). The proposed correlation for the average Nusselt number (based on the nozzle pitch) was:-

$$\overline{Nu}_x = 0.124\ (u_c/u_{mo})^{0.75}\ Re_x^{0.75}\ (z/D)^{-0.2} \qquad (2.19)$$

where, 'u_c' is the velocity of the exhaust stream flowing parallel to the plate, whilst 'u_{mo}' is the nozzle exit velocity.

Kercher and Tabakoff (Ref.42) were mainly interested in the 'spent air' effects and evaluated the heat transfer coefficient from a square array of round jets impinging on a flat surface. This surface was constructed from four electrically heated copper plates so that the heat transfer associated with particular rows of jets could be determined. The system was enclosed on three sides and the spent air was exhausted from the fourth side. This exhaust air thus affected the behaviour of the jets. The jet Reynolds number Re_D was varied from 300 to 30,000, and the jet pitches ranged from 3.1 to 12.5 nozzle diameters by varying jet diameters. In these tests, 'z/D' ranged from 1 to 4.8.

The proposed correlation for the average heat transfer from a row of jets was:-

$$\overline{Nu} = C_1\ C_2\ Re_D^m\ (z/D)^{0.091}.\ Pr^{0.33} \qquad (2.20)$$

'C_1' and 'm' were functions of the jet pitch (x/D) and the Reynolds number, and were presented graphically (for example, for $3,000 < Re_D < 30,000$, m is 0.75 and 0.92 at x/D = 4 and 10 respectively; C_1 for these conditions was 0.085 and 0.01). The constant C_2 is a factor which allows for the 'degradation' of the heat transfer due to the flow of 'spent air'. C_2 thus depends on the position of measurement as well as the other geometrical factors (C_2 varies from 1 to 0.5). The correlation also shows an increase in the heat transfer with the increase of nozzle/target spacings (z/D). However, it may be pointed out that the 'z/D's studied were fairly small.

Ward et al (Ref.52) were primarily interested in heat transfer at the nozzle plate surface due to 'return' flows towards the surface. They employed a mass trans-

fer technique and, to demonstrate the applicability of this technique, they initially investigated the average mass/heat transfer from an array of round jets. Their results correlated satisfactorily with other similar studies, and can be correlated as :-

$$Nu_x = 0.2605\ Re_{ax}^{0.638} \qquad (2.21)$$

for the range $1{,}000 \leqslant Re_{ax} < 270{,}000$; $2 \leqslant z/D \leqslant 12$, and $x/D = 6$.

Chance (Ref.15) also used an arrangement similar to that of Kercher and Tabakoff (Ref.42) to study heat transfers from arrays of round jets. The parameters varied were the impingement velocity (Re_D = 3,000 to 50,000), open area (A_f = 0.61 to 8%, A_f being the function of nozzle pitch), jet to surface spacing (z = 2 to 8 nozzle diameters), orifice diameter (D = 0.125 to 0.613 inches), the pattern of the nozzles, and the jet temperature. He concluded that the diameter of the orifice or nozzle provides the most useful reference length in correlating the heat transfer data. The effect of 'z' was dependent on the open area 'A_f', e.g. at A_f = 0.69%, the variation of Nusselt number was independent of z/D whilst, for all larger A_f values, the heat transfer decreased with increased 'z'. This corroborated the findings of Metzger and Korstad (Ref.43) and Freidman and Mueller (Ref.47) but is in conflict with Kercher and Tabakoff (Ref.42). The probable reason for this is the limited region of z/D studied by these later authors.

Chance correlated his results in a similar fashion to Kercher and Tabakoff. The effects of the crossflow and the Reynolds number exponent were also similar. He observed that heat transfer continued to increase with an increase in A_f, as was also reported by Kercher and Tabakoff, whereas Refs. (43) and (47) suggested an optimal A_f of 2 to 3%. The reasons for this difference were attributed to the construction of the experimental set-ups. To obtain increased performance at large open areas, the crossflow interference must be minimized by incorporating well-designed exhaust passages.

Finally, Chance found that jet pattern was not very critical from the point of view of average heat transfer although triangular or square arrays were found to be generally preferable.

Koopman and Sparrow (Ref.50) employed a naphthalene sublimation technique to study the local heat transfer from a row of impinging circular jets. The nozzle-to-target spacings varied from 2 to 10D and jet pitches were either at 4 or 6.67D (Re_D varied from 2,500 to 10,000). The presence of these adjacent jets was found to depress the stagnation point heat transfer.

Baines and Keffer (Ref.53) determined shear stresses along the surface due to impingement of a free slot jet. Their measurements indicated a minimum at the stagnation point with an adjacent local minima. Heat transfers were inferred by using Reynolds analogy. However, comparisons with previously published data showed severe discrepancies. For example, the maximum stagnation point heat transfer observed by Gardon and Akfirat (Ref.36) at z/b = 8 was not apparent and continuous decrease in heat transfer at this point with 'z' was found.

Vallis, Patrick and Wragg (Ref.38) used an electro-chemical technique to determine the heat transfer on a flat plate due to jet impingement. The diameters of the jets employed were 3.0, 6.0 and 9.0mm, and the Reynolds number Re_D varied from 3,880 to 23,000, whilst 'z/D' ranged between 5 and 20. Separate correlations were suggested for the stagnation point, impingement and wall jet region. The equations expressing the stagnation point and impingement heat transfers have already been quoted in Section 2.3.1. The authors concluded that the agreement between previous heat transfer results and their results was good in the region where the fully developed wall jet existed with boundary layer characteristics. However, significant differences, particularly with respect to the exponent on the Reynolds number, existed in the stagnation and impingement region.

Hoogendoorn (Ref.29) was interested in the effects of turbulence on heat transfer and used a liquid crystal technique to determine local heat transfer coefficients due to impinging air jets. The nozzle diameter was fixed at 57mm but two different arrangements were used to vary the turbulence intensity at the exit section. The stagnation point heat transfer were expressed by Equation 2.6, see Section 2.3.1. It should, however, be emphasised that there is considerable scatter in the data and that the equation only fits the results to within ± 8%.

2.5 SUMMARY

It is apparent from the previous discussions that impingement heat transfer has been studied fairly extensively, and correlations obtained by different researchers agree fairly well in the regions where the effects of jet turbulence are not dominant. Therefore, studies carried out at $z/D < 8$ and small target areas (r/D) are more dependent on the particular experimental arrangement (affecting the turbulence characteristics of the jet).

In general, average heat transfer rates are more easily ob-

tainable than the local variations which, nevertheless, are often required. A comparison of the average heat transfer correlation for multiple round jets obtained by several researchers are presented in Figure 2.8, while a similar curve applicable for single jets is presented in Figure 10.28.

PAGE
NUMBERS
CUT OFF
IN
ORIGINAL

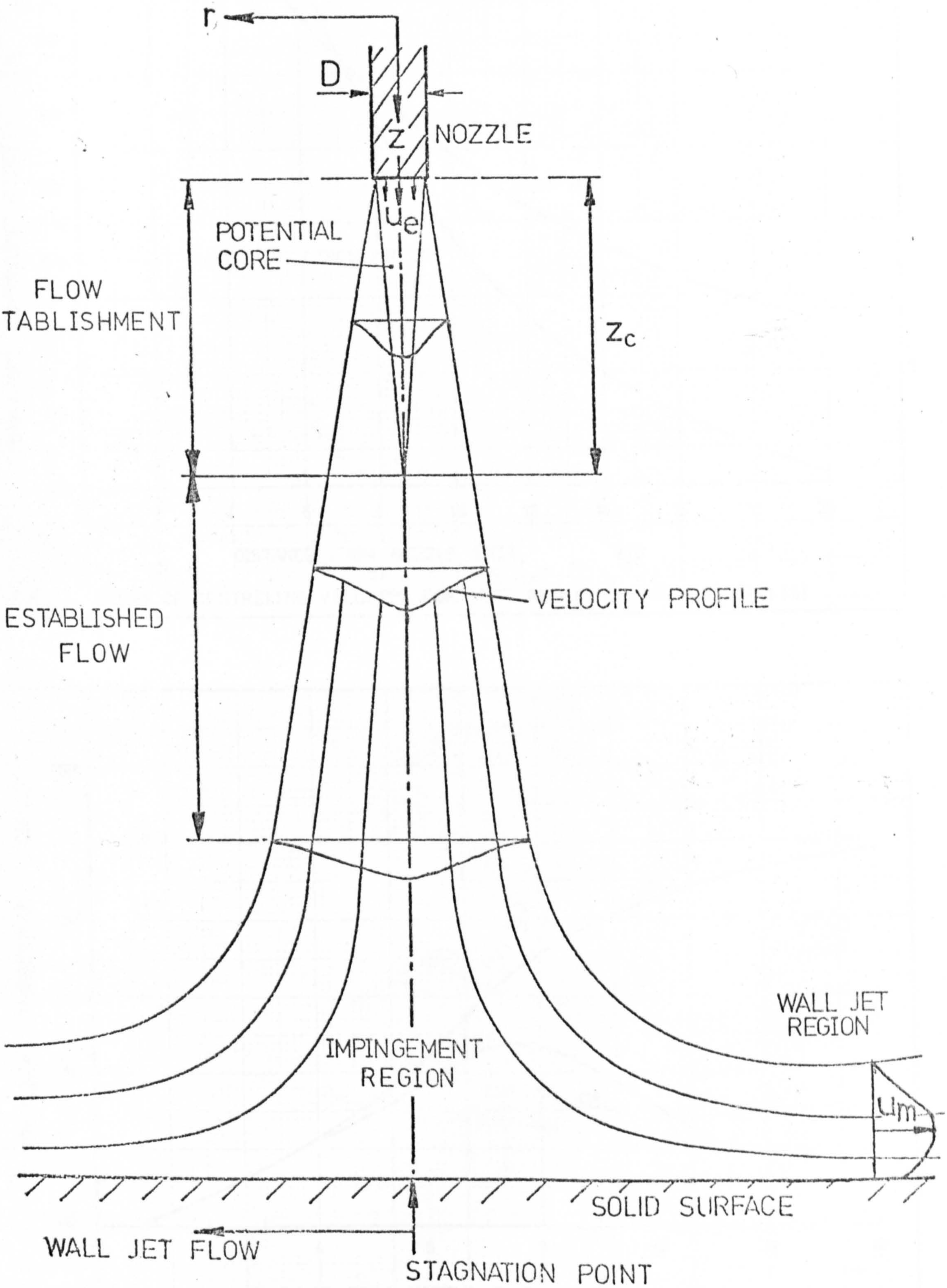

Fig 2.1 FLOW CHARACTERISTICS OF A FREE JET IMPINGING ON A FLAT PLATE.

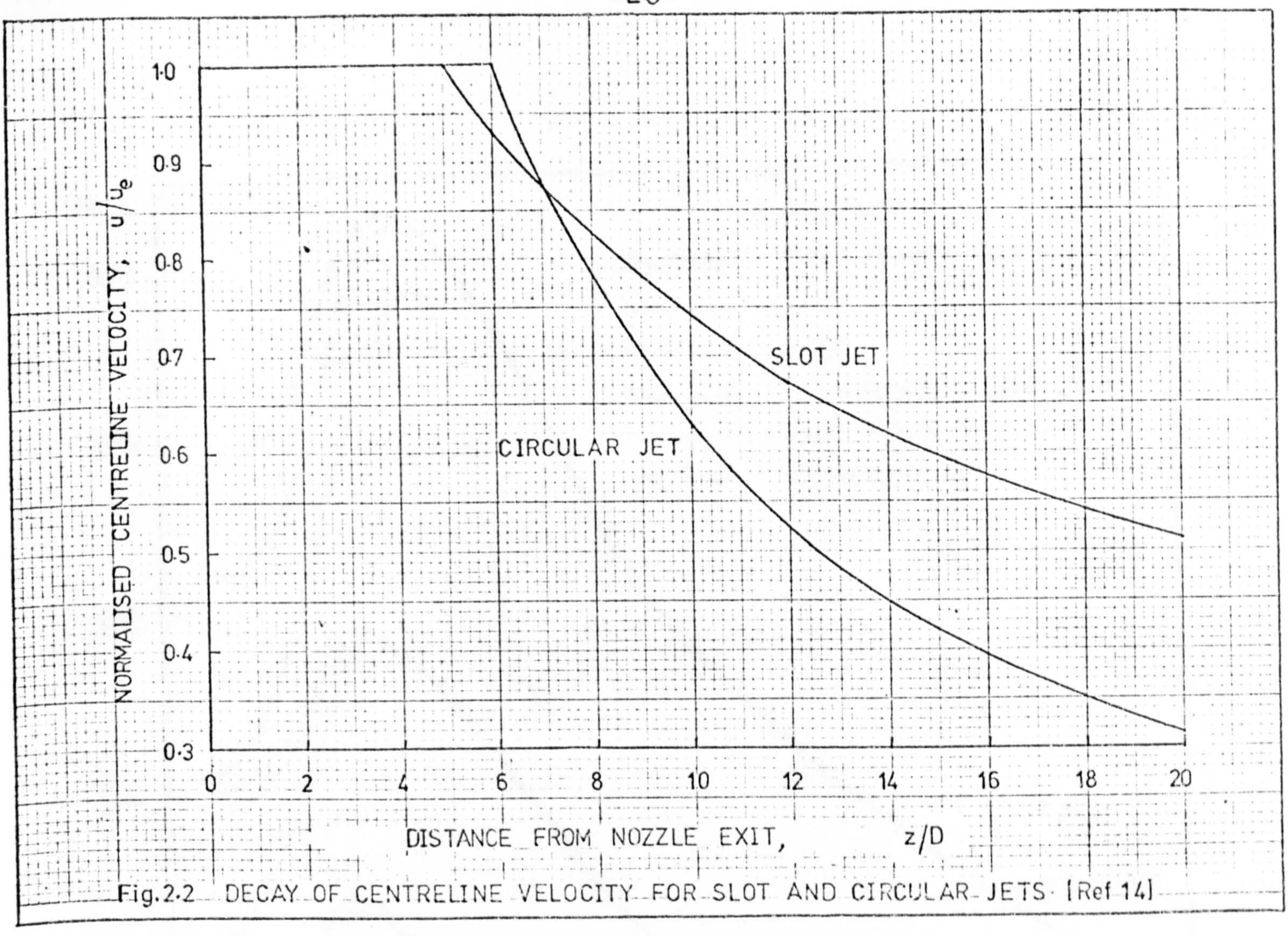

Fig.2·2 DECAY OF CENTRELINE VELOCITY FOR SLOT AND CIRCULAR JETS [Ref 14]

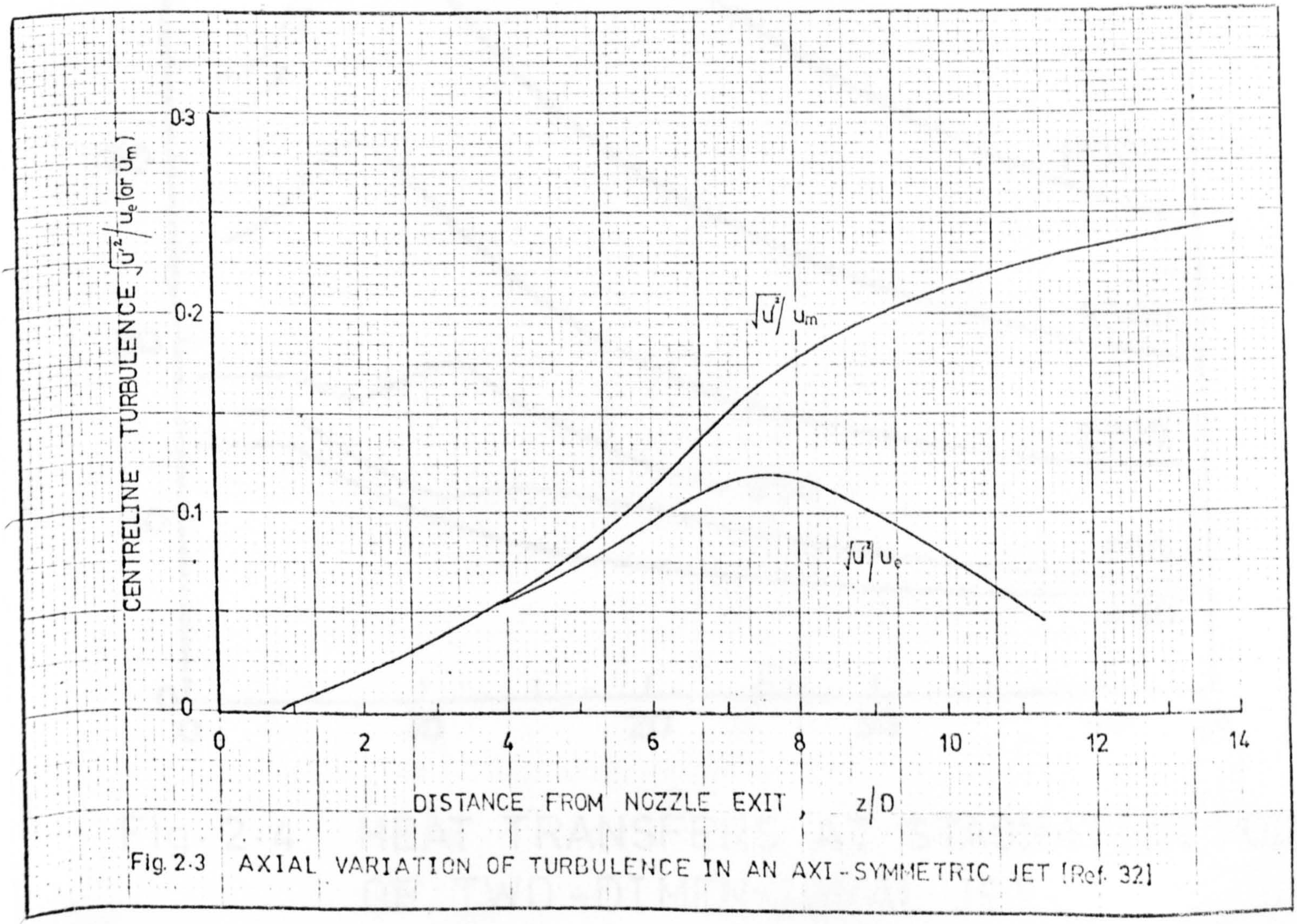

Fig. 2·3 AXIAL VARIATION OF TURBULENCE IN AN AXI-SYMMETRIC JET [Ref. 32]

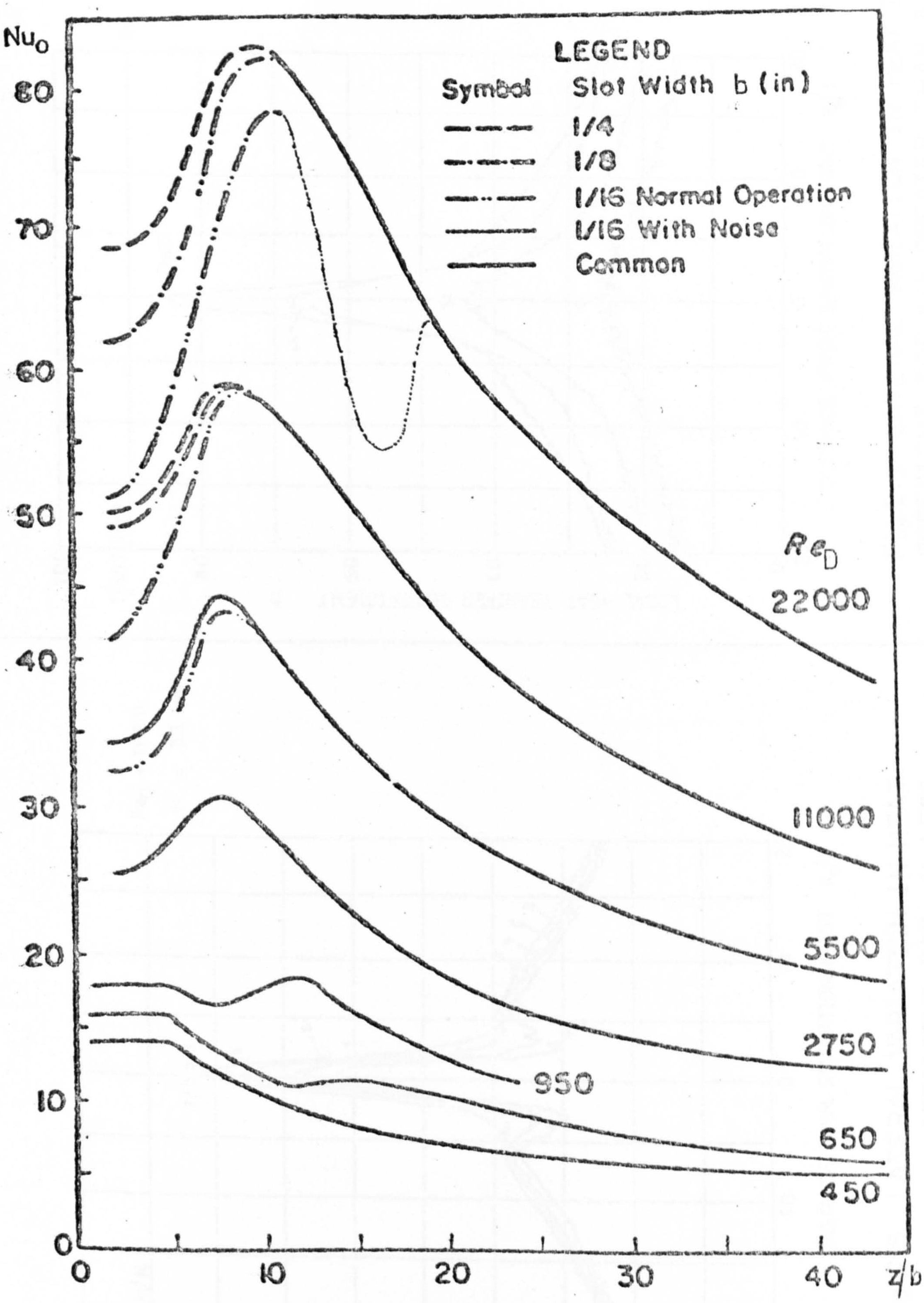

Fig. 2.4 HEAT TRANSFERS AT STAGNATION POINT OF TWO-DIMENSIONAL JET.

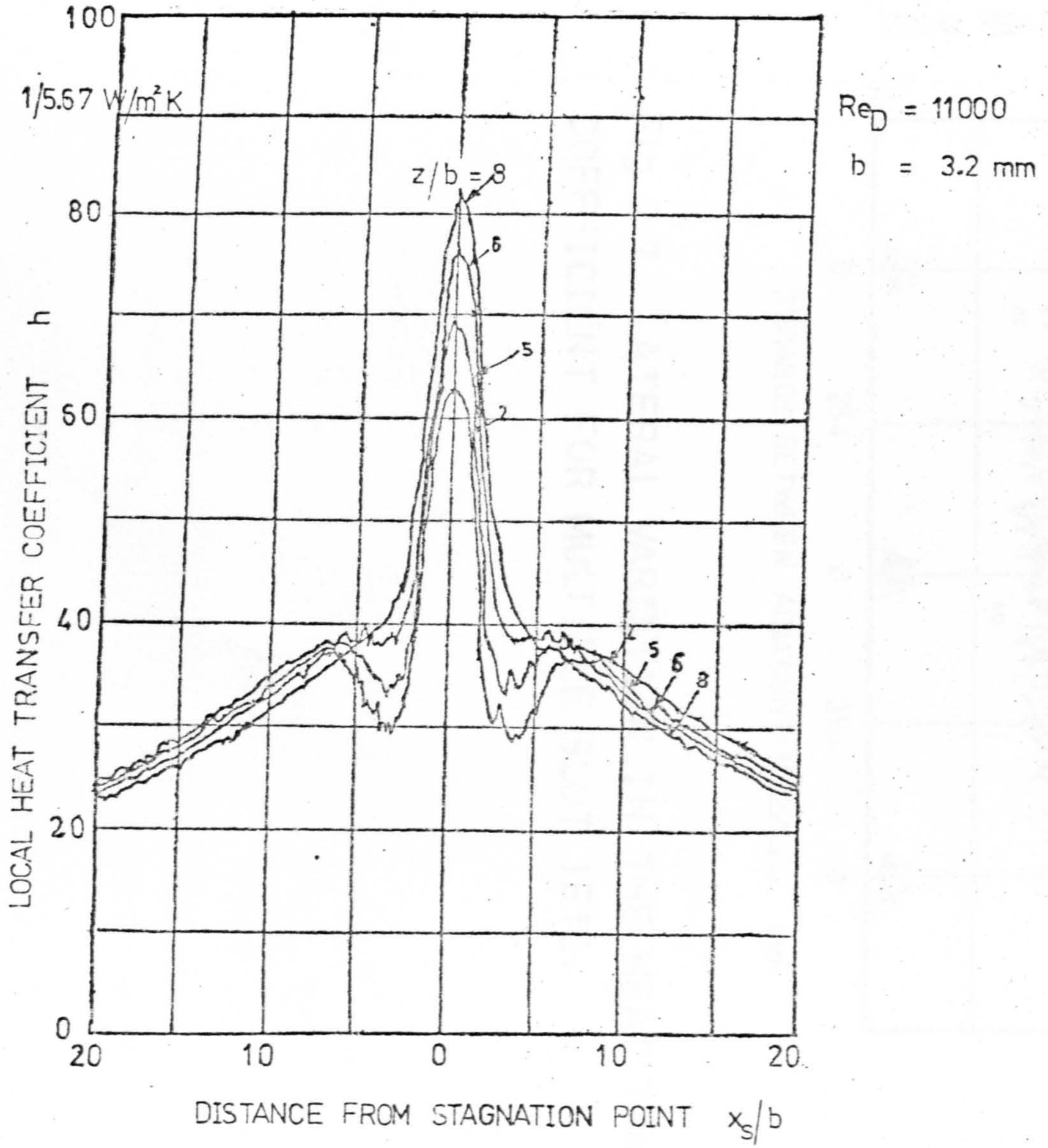

Fig.2.5 LATERAL VARIATION IN HEAT TRANSFER COEEFICIENT FOR z/b LESS THAN 8 [Ref. 36]

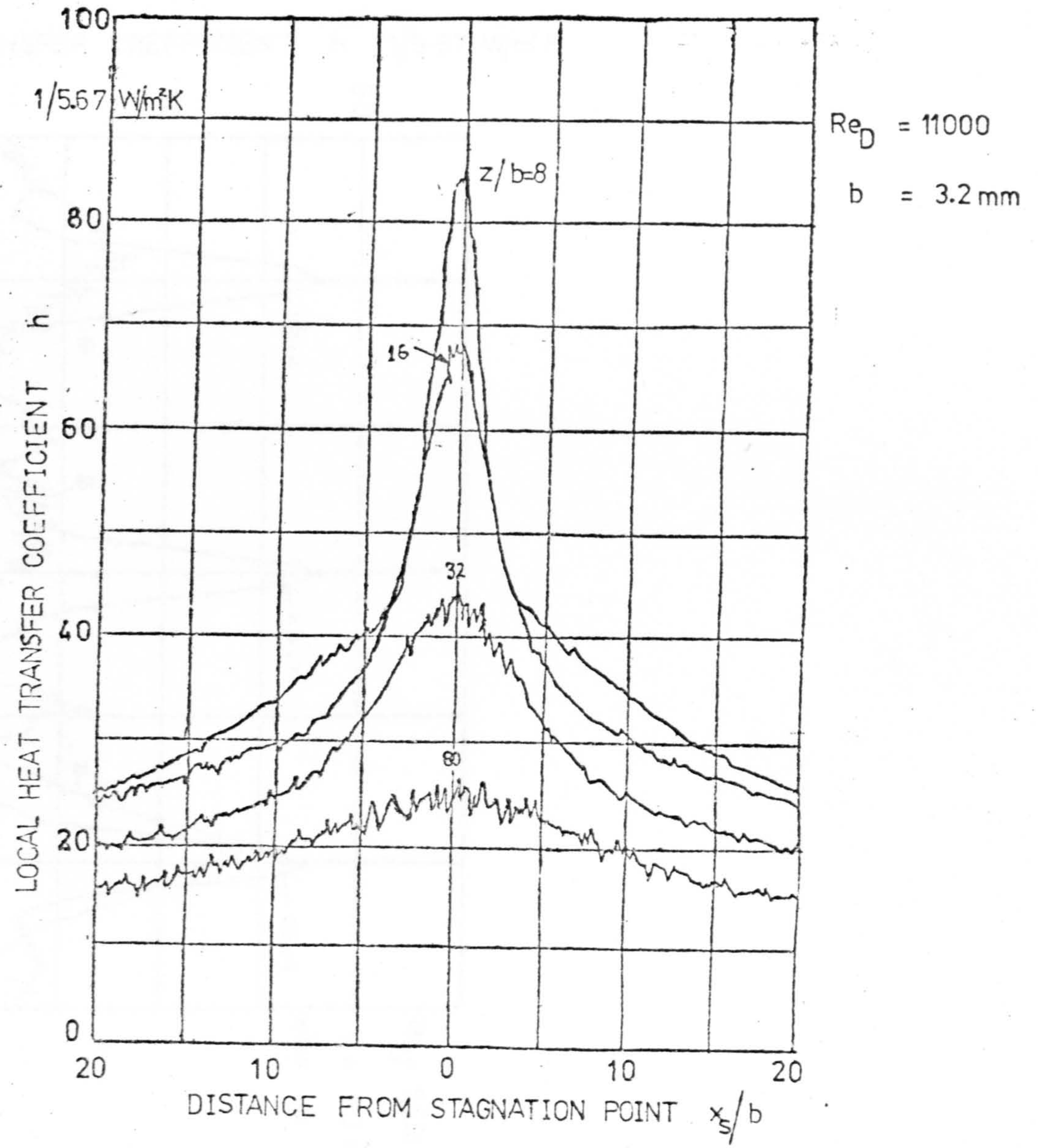

Fig.2.6 LATERAL VARIATION IN HEAT TRANFER COEFFIENT FOR z/b GREATER THAN 8 [Ref. 36]

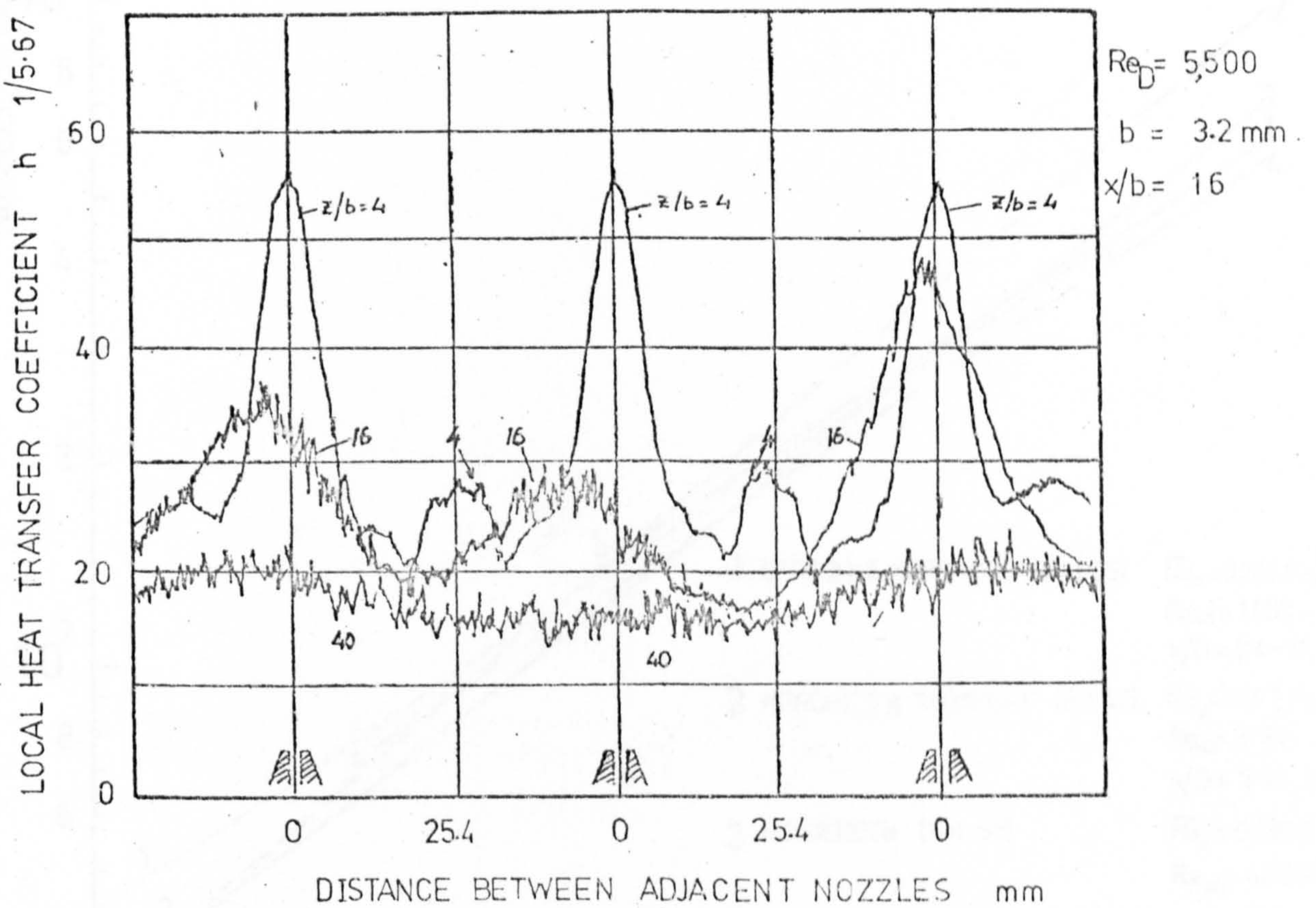

Fig. 2.7 LATERAL VARIATION IN THE HEAT TRANSFER COEFFICIENT FOR MULTIPLE SLOT JETS.

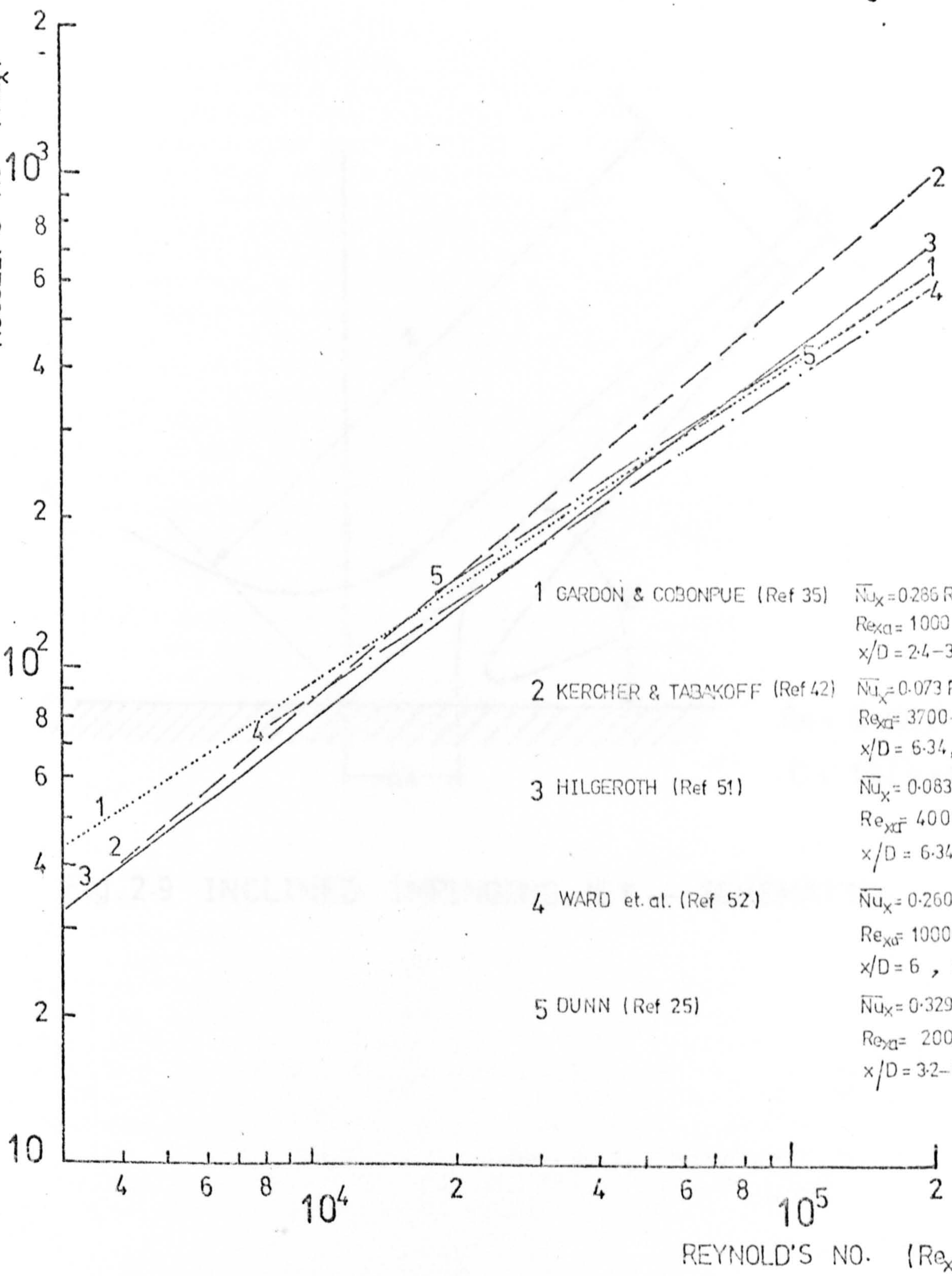

Fig. 2.8 SOME CORRELATIONS OBTAINED BY PREVIOUS WORKERS FOR MULTIPLE AXI-SYMMETRIC IMPINGING JETS.

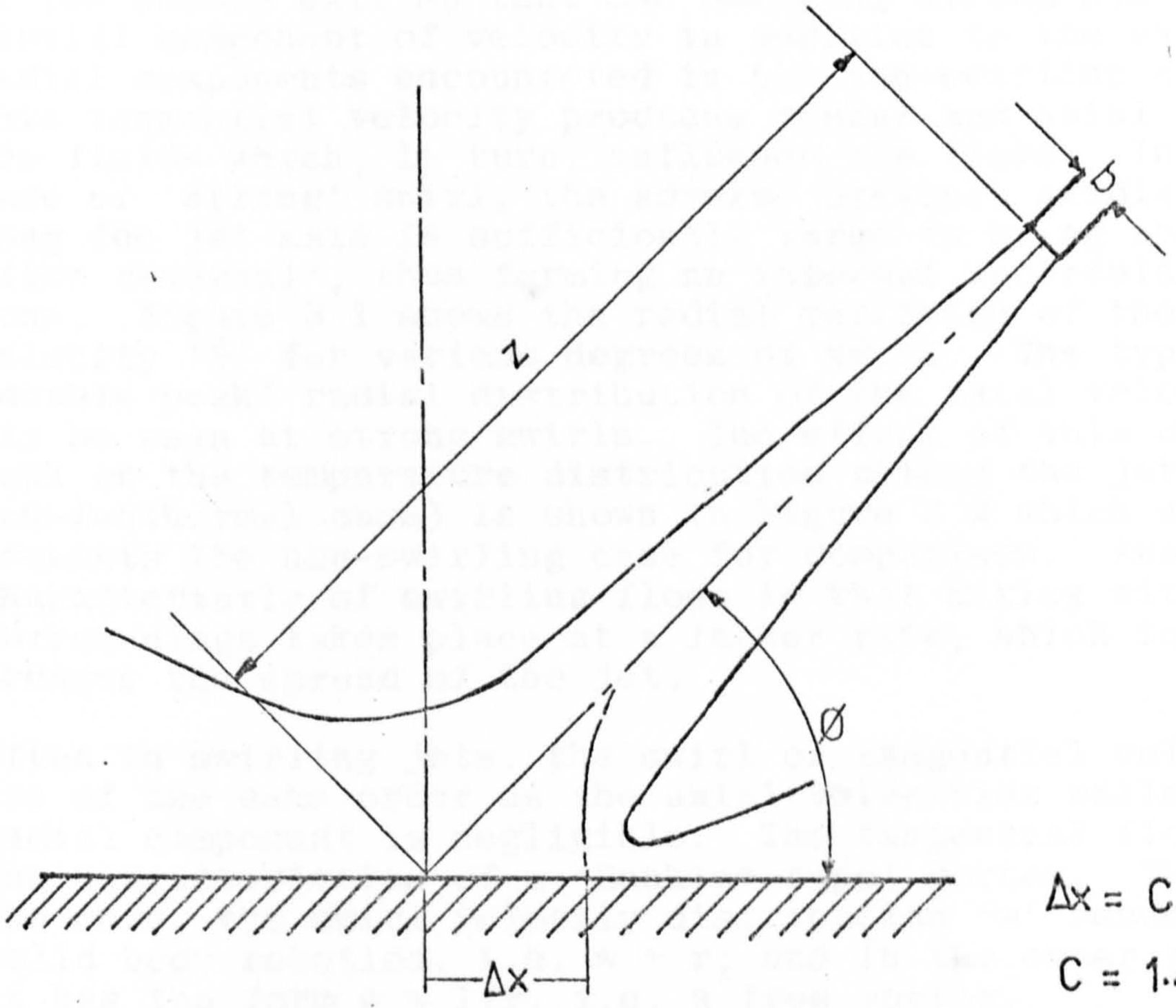

Fig.2·9 INCLINED IMPINGING JET — SCHEMATIC.

CHAPTER 3

THE CHARACTERISTICS OF SWIRLING JETS

3.1 INTRODUCTION

In a turbulent swirling jet, the fluid is rotated upstream of the nozzle exit so that the emerging stream has a tangential component of velocity in addition to the axial and radial components encountered in the non-swirling case. This tangential velocity produces radial and axial pressure fields which, in turn, influence the flows. In the case of 'strong' swirl, the adverse pressure gradient along the jet axis is sufficiently large to bring about 'flow reversal', thus forming an internal recirculation zone. Figure 3.1 shows the radial variation of the resultant velocity '$\bar{V}$' for various degrees of swirl. The typical 'double peak' radial distribution of the axial velocity may be seen at strong swirls. The effect of this double peak on the temperature distribution within the jet (in a non-isothermal case) is shown in Figure 3.2 which also presents the non-swirling case for comparison. Another characteristic of swirling flows is that mixing with the surroundings takes place at a faster rate, which increases the spread of the jet.

Often in swirling jets, the swirl or tangential velocities are of the same order as the axial velocities whilst the radial component is negligible. The tangential flow has the characteristics of a 'Rankine type' vortex. Thus, in the core, the swirl velocity distribution 'w' resembles solid body rotation, i.e. $w \sim r$; and in the outer region it has the form $w \sim 1/r$, i.e. a free vortex.

'Swirl' is often used in combustion systems since, despite the consequent increase in pressure drop, the application of swirl to the burner air supply provides a simple means of controlling the shape, size and rate of heat release of the flame. By variation of the degree of swirl, a long narrow 'lazy' flame can change to a shorter, wider and more compact flame. This can be particularly useful in certain industrial applications, e.g. a high intensity flame impinging on raw materials can be desired during the melting stage of a process with alteration of the flame shape to provide an atmosphere of reasonably uniform temperature in the 'holding' stage (see Ref.54). Swirl can also affect the residence time of the combustion products in the system so that it can be used to control pollution.

3.2 THE GENERATION OF SWIRL

Swirling flows can be generated by:-

(a) Pipe bends - a rather weak swirl is created as the flow moves around a pipe bend.

(b) Incorporation of a spiral insert in a tube.

(c) Rotation of the tube containing the fluid.

(d) Tangential entry of part of or all the fluid into a cylindrical nozzle, and

(e) The use of guide vanes.

Swirling flows obtained by using the first three of these methods have been employed only for experimental purposes. Tangential entry type swirlers are generally used in furnace systems. Vane type swirlers have been applied as flame stabilizers in aircraft gas turbine combustors, and can be used equally well in the burners employed in industrial furnaces.

Previous investigators (Refs. 23 and 55) have reported that both tangential entry and guide vanes are reasonably efficient means (in terms of the pressure drop) of generating weak and medium swirls. Mathur and Maccallum (Ref. 55) and Kilik (Ref.56) also observed that hubless swirlers were difficult to manufacture and gave slightly unsymmetrical flows. In the present study, it was decided to use the tangential entry swirler and the advantages of using this device are discussed in Chapter 4.

3.3 CHARACTERISATION OF SWIRL

Beér and Chigier (Ref.57) demonstrated that, for a tangential entry swirler, once the flow has become established inside the swirler the axial flux of angular momentum 'G_ϕ' and the axial flux of axial momentum 'G_x' are conserved along the axis of the jet. They proposed a similarity criterion called the 'swirl number', 'S', to characterise the jet and defined it as follows:-

$$S = 2\, G_\phi / G_x\, D \qquad (3.1)$$

where 'D' is the diameter of the jet and 'G_ϕ' and 'G_x' are expressed as:-

$$G_\phi = \int_0^{D/2} 2\pi \rho\, u\, w\, r^2\, dr \qquad (3.2)$$

$$G_x = \int_0^{D/2} 2\pi \rho\, u^2\, r\, dr + \int_0^{D/2} 2\pi\, p\, r\, dr \qquad (3.3)$$

'u' and 'w' are the axial and tangential components of velocity, and 'p' is static pressure at any cross-section of the jet.

Chigier and Chervinsky (Ref.58) showed that the axial momentum 'G_x' can also be expressed as:-

$$G_x = \int_0^{D/2} 2\pi \rho r \, (u^2 - \tfrac{1}{2}w^2) \, dr \qquad (3.4)$$

This equation is valid if the term

$$\left[\overline{u'^2} - \left(\frac{\overline{v'^2} + \overline{w'^2}}{2}\right)\right]$$

is small and can be neglected, u', v' and w' being the turbulent fluctuations in the axial, radial and tangential directions.

These expressions for the momenta can thus be evaluated by integrating the velocity and pressure profiles at any section perpendicular to the jet axis.

In the case of vane swirlers, the swirl number can be related to the geometry of the swirler, e.g. in hubless vane swirlers, the swirl number 'S' = 1/3 tan θ, where θ is the vane angle.

Chigier and Chervinsky also showed that the ratio of the maximum values of the axial and tangential velocities at the nozzle exit ($G = w_{mo}/u_{mo}$) can be related to the swirl number, see Figure 3.3. This can provide a simple method of determining 'S', provided '$u_{\overline{mo}}$' and '$w_{\overline{mo}}$' can be measured accurately. This is obviously difficult for small diameter nozzles.

Swirling flows can be roughly classified as:-

$0 < S < 0.3$	weak swirl.
$0.3 < S < 0.6$	medium swirl with a characteristic double peak axial velocity distribution.
$S > 0.6$	strong swirl - flow reversal occurs with the formation of a torroidal vortex in the core.

Finally, it should be mentioned that the swirl number cannot be regarded as the sole universal criterion for

characterising swirling jets since the physical shape of the nozzle and the method of generating swirl can also influence the jet behaviour. However, it is the most significant criterion for swirling jets produced from the geometrically similar generators.

3.4 THE FLUID DYNAMICS OF SWIRLING JETS - A REVIEW OF SELECTED PUBLISHED WORK.

The earliest reference to the use of vane swirlers was published by Watson and Clarke (Ref.59) in 1947. They examined the effects of swirl in a gas turbine combustion chamber. Mathur and Maccallum (Ref.55) have presented an excellent list of references covering all pre-1966 publications on 'swirl'. Syred and Beér (Ref.60) have also published an extensive bibliography concerned with swirling flows in combustion systems. These two references, together with the chapter related to swirling flows in Ref.23, form a suitable basis for studying previous work on swirling jets. Thus, in this review section, only the works of particular relevance to the present study are included.

In a comparatively early study, Hartnett and Eckert (Ref. 61) investigated the effect of jet swirl and observed that the radial velocities were negligible in comparison with the axial and swirl components. They used a tangential entry swirler in their experiments.

Rose (Ref.62) studied the velocity and turbulence fields associated with a swirling jet. A weak swirl was generated by rotating a 13.5mm diameter pipe (1.35m long) at 9500 rpm. The jet Reynolds number was approximately 15,000. Turbulence intensities were measured using a hot-wire anemometer. They found that, when compared to the non-swirling case, the swirling jet spreads more rapidly and entrains the surrounding fluid at a greater rate. Thus, the mean velocity decays more rapidly and there is a greater rate of growth of turbulence intensity.

Chigier and Beér in 1964 (Ref.57) studied the velocity and static pressure distributions in swirling jets issuing from annular, convergent and divergent nozzles. The magnitude and direction of the velocities were measured with a five-hole pitot probe (see Ref.63), while the static pressures were measured with the help of a disc static probe (see Ref.64). The swirl was generated by subjecting all or part of the fluid tangentially, giving swirl numbers from 0 to 1.57. At swirls $S > 0.6$, a recirculation zone was set up near the nozzle exit and the size of this region increased with the increase of swirl. Figure 3.4 shows typical streamlines obtained at a swirl number of $S = 1.57$. They also found that, with an increase in swirl, the angle of spread of the jet is increased and, correspondingly, the decay in the values of

the axial, tangential and radial components of velocity along the jet is greater. The decay rate of the velocities and pressures tend to be in agreement with the form predicted by the theoretical analyses of Loitsyanskii (Ref.65) and Gortler (Ref.66). Thus, the tangential velocity component decay is a function of $(1/z^2)$, whilst the axial and radial velocities decay inversely with z. The pressure field decays even more rapidly and is proportional to $(1/z^4)$.

Kerr and Fraser (Ref.67) studied the flow field in the fully developed region of a jet in which swirl was generated by vanes. They suggested that the swirl number can also be defined as Torque/Thrust x Radius. Swirl numbers greater than 0.8 were difficult to generate with their swirler. Velocity measurements were conducted using a three-dimensional probe developed by Hiett and Powell (Ref.68).

Chigier and Chervinsky (Ref.58) carried out an investigation of the swirling vortex motion in jets. This paper was based on an earlier report by the same authors (Ref. 69). The investigation covered weak as well as moderate and strongly swirling flows. These swirls were generated by a tangential entry swirler, as shown in Figure 3.5. The results indicate that jet similarity is achieved at axial distances as close as two nozzle diameters for the lower swirls. This is appreciably closer to the nozzle exit than for the non-swirling case due to the faster breakdown of the potential core. However, with the strongly swirling jets, where the maximum axial velocity is displaced from the central axis, similarity is only achieved after the velocity maxima have eventually converged on the jet axis. Figure 3.6 presents their radial distributions of the axial and tangential velocities. Ref. 58 also suggested an empirical equation for the axial and tangential velocity profiles, and these are plotted in Figure 3.6 as the thick lines. The equation for the axial profile is similar to that for the non-swirling jets which were discussed in Section 2.2:-

$$u/u_m = \exp\left(-K_u r^2/(z+a)^2\right) \qquad (3.5)$$

where the distribution constant 'K_u' = $92/(1+6S)$ and 'u_m' is the maximum velocity at any section, and 'a' is the 'apparent' origin of the jet.

In a further study, the same authors (Ref.70) also undertook velocity and temperature measurements in a series of free turbulent swirling flames using swirlers similar in geometry to those used in their ambient temperature experiments. The flames were stabilised in the shape of an annular ring at an axial distance of four nozzle diameters from the burner exit. The measurements made in

this region for three different swirls, i.e. S = 0, 0.116 and 0.214, indicate that the decay of the axial and swirl velocities was lower for the flames than for the ambient temperature jets. Figure 3.7 illustrates the temperature field at a swirl of 0.116.

Mathur and Maccallum (Ref.55), as well as comprehensively reviewing the available literature, compared experimentally various designs of vane swirler (both hubless and annular) and estimated their efficiency in terms of the required pressure drop. Their axial and tangential velocity profiles for hubless swirlers are shown in Figure 3.8.

Syred, Beer and Chigier (Ref.71) investigated experimentally the recirculation zones set up on the central axis of a large diameter (17.6cms) burner. Swirl was generated by introducing the combustion air into the burner body via tangential slots. A strong swirl (S = 2.2) was thus produced so that the flame and recirculation zones penetrated more than two nozzle diameters back inside the burner tunnel. The kinetic energy of turbulence encountered in this vortex was as high as 160%. High combustion intensity was thus obtained as the fuel/air reactions were completed at an axial distance of 1.5 diameter.

Pratte and Keffer (Ref.72) studied the spread of a moderately swirling jet (S = 0.3). Swirl was generated by rotating a pipe at 8700 rpm in a manner similar to Rose (Ref. 62). The Reynolds number was approximately 2300, i.e. marginally above that required for fully developed turbulent fluctuations and Reynolds stresses of the velocity field. Most of their observations agreed with those of previous researchers with regard to the spread of the jet, the decay of velocity and pressure.

Concurrently with these experimental investigations, a number of theoretical analyses of swirling flows have been undertaken. Analytical studies mentioned earlier in this section, see Refs. 65 and 66, are only applicable to fully developed weakly swirling jets with no reversal of flow at any station. Lilley (Ref.73) deals with the computation of strongly swirling flows and also quotes other related publications which apply numerical methods.

3.5 HEAT TRANSFER FROM SWIRLING IMPINGING JETS

There are only a few references in the literature concerned with the heat transfer from impinging swirling jets. Martin (Ref.34) in his review of heat and mass transfer from impinging jets quotes that "the insertion of swirl baffles in a single round jet has no significant influence on heat transfer". No other details are given and so it is not possible to determine the range of swirl numbers to which this refers.

Recently, Huang et al (Ref.74) published the results of a numerical study of heat transfer from a partially confined, laminar, swirling, impinging jet. They undertook a parametric study and examined the effects of the variation in the nozzle-to-plate spacing, the plate diameter (r/D), the jet Reynolds number, the degree of swirl, the inlet axial and swirl velocity profiles, and also the application of suction/blowing at the impingement surface. The use of swirl was found to increase the spreading of the jet at a rate dependent on both the swirl number and the inlet swirl velocity profile. At large swirl numbers, torroidal recirculation zones were formed at the stagnation region. these produce an insulation effect and depress the local heat transfer rates. The Stanton number (based on the average heat transfer) over the plate diameter was proportional to $Re_D^{0.56}$ whereas, in the non-swirling case, the appropriate index was 0.5.

In a previous preliminary study at Cranfield, Perry (Ref. 24) examined heat transfer from a single impinging jet of 50.8mm diameter, and varied the degree of swirl and nozzle-to-target spacing. A mass transfer technique (based on the sublimation of naphthalene) was employed together with surface profilometry to determine local heat transfer coefficients. A very high swirl number was claimed, and this was probably due to the unsuitable method used to measure the degree of swirl. Velocity measurements were not carried out to characterise the swirl but rather a single yaw probe on the central axis of the jet was used to measure the 'swirl angle'. The target field was very small and covered only a radius of three nozzle diameters about the stagnation point. He found that the heat transfer for most of the nozzle-to-target spacings (z/D = 3 - 6) increased with weak swirls but decreased with the further increase of swirl. At z/D = 2, the lowest studied, the heat transfer remained constant for the swirl values.

Dunn (Ref.25) measured average mass transfer (also using naphthalene sublimation techniques) from an array (3 x 3) of axi-symmetric swirling jets impinging orthogonally onto a plane surface. The Chilton-Colburn analogy was employed to infer the corresponding heat transfer . The nozzle diameter was fixed at 15.9mm diameter and the Reynolds number, Re_D, for the no-swirl case was 13,800. The airflow which produced this Reynolds number was kept constant in all swirling cases (this simulates a constant air/fuel supply to the burner). Dunn varied the nozzle pitch (x/D), the nozzle-to-target spacing (z/D) and the jet swirl number. It was found that the heat transfer were more dependent on 'z/D' than on 'x/D'. The application of swirl to a jet at a small nozzle-to-target spacing (z/D < 4) can result in an increase in heat transfer with the maximum occurring at swirl numbers between 0.2 and 0.3. Swirl generally caused significant reductions in heat transfer at large z/Ds except at weak swirls.

Since the present studies of multiple jets were carried out on the rig used by Dunn, his results are discussed further in Chapter 10.

3.6 SUMMARY

Overall, it may be seen that the swirling jets behave differently from the non-swirling flow, especially at high swirls where the maxima of the axial velocity are displaced from the axis of the jet. Swirl also produces greater mixing rates and, therefore, the jets spread more rapidly and achieve similarity much earlier. The turbulence characteristics are also very different so that the heat transfer should be correspondingly affected. The swirl number and the shape of the exit velocity profile would have a significant effect on the heat transfer.

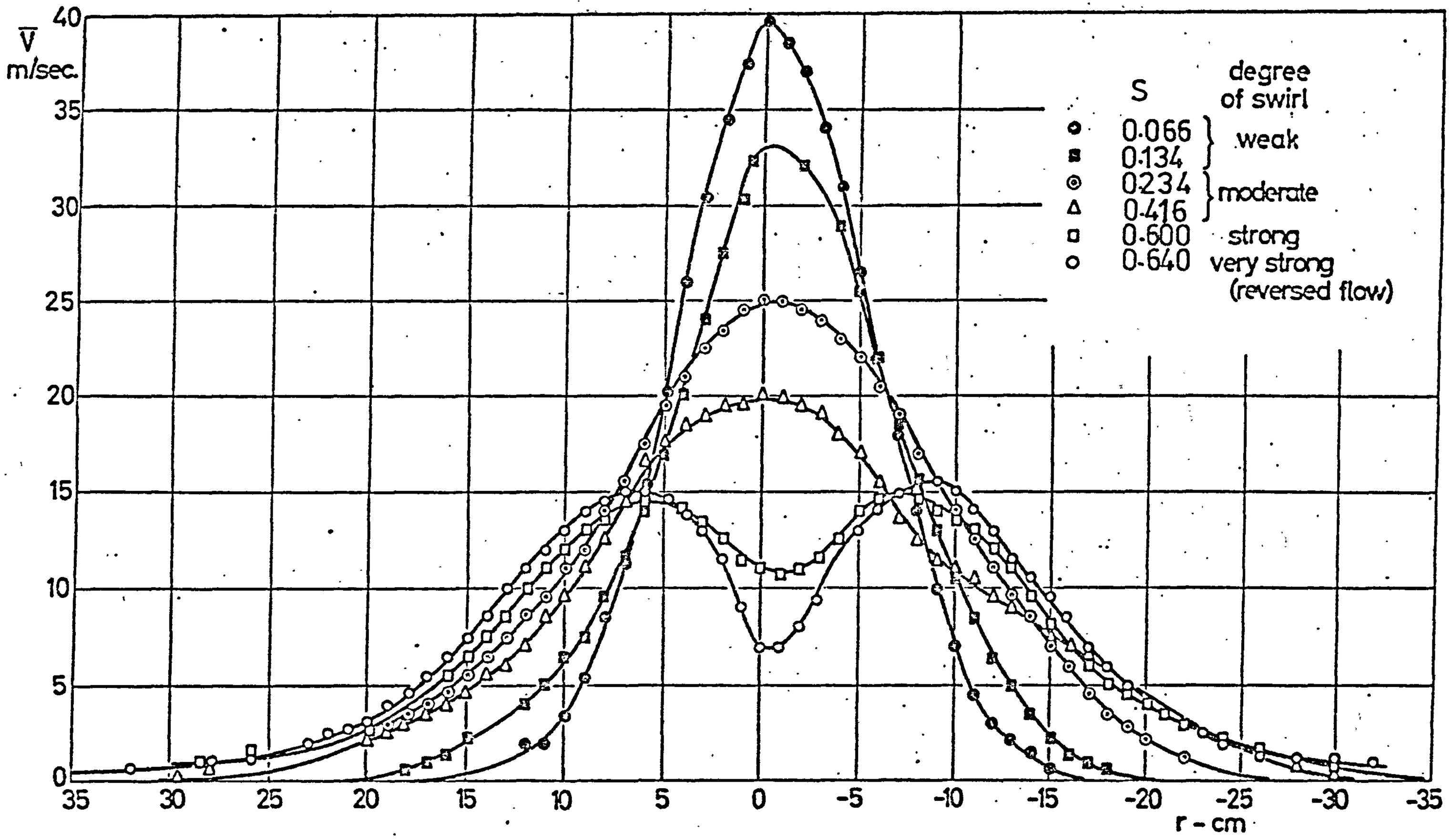

FIG.3.1 RADIAL DISTRIBUTION OF THE VELOCITY VECTOR $z/D = 4.1$ (REF 69)

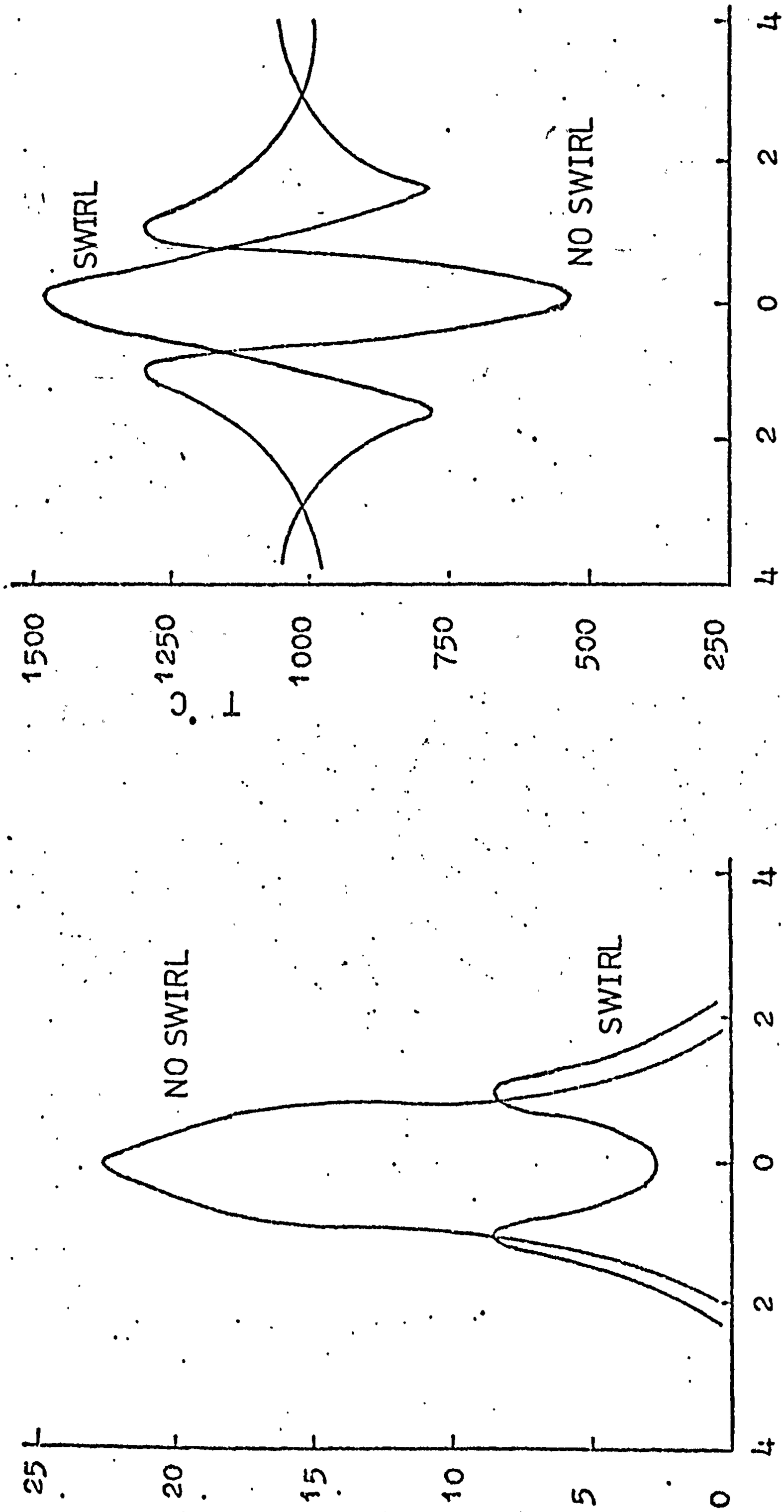

Fig. 3.2 AXIAL VELOCITY & TEMPERATURE DISTRIBUTION IN SWIRLING AND NON-SWIRLING FLAMES (Ref. 54)

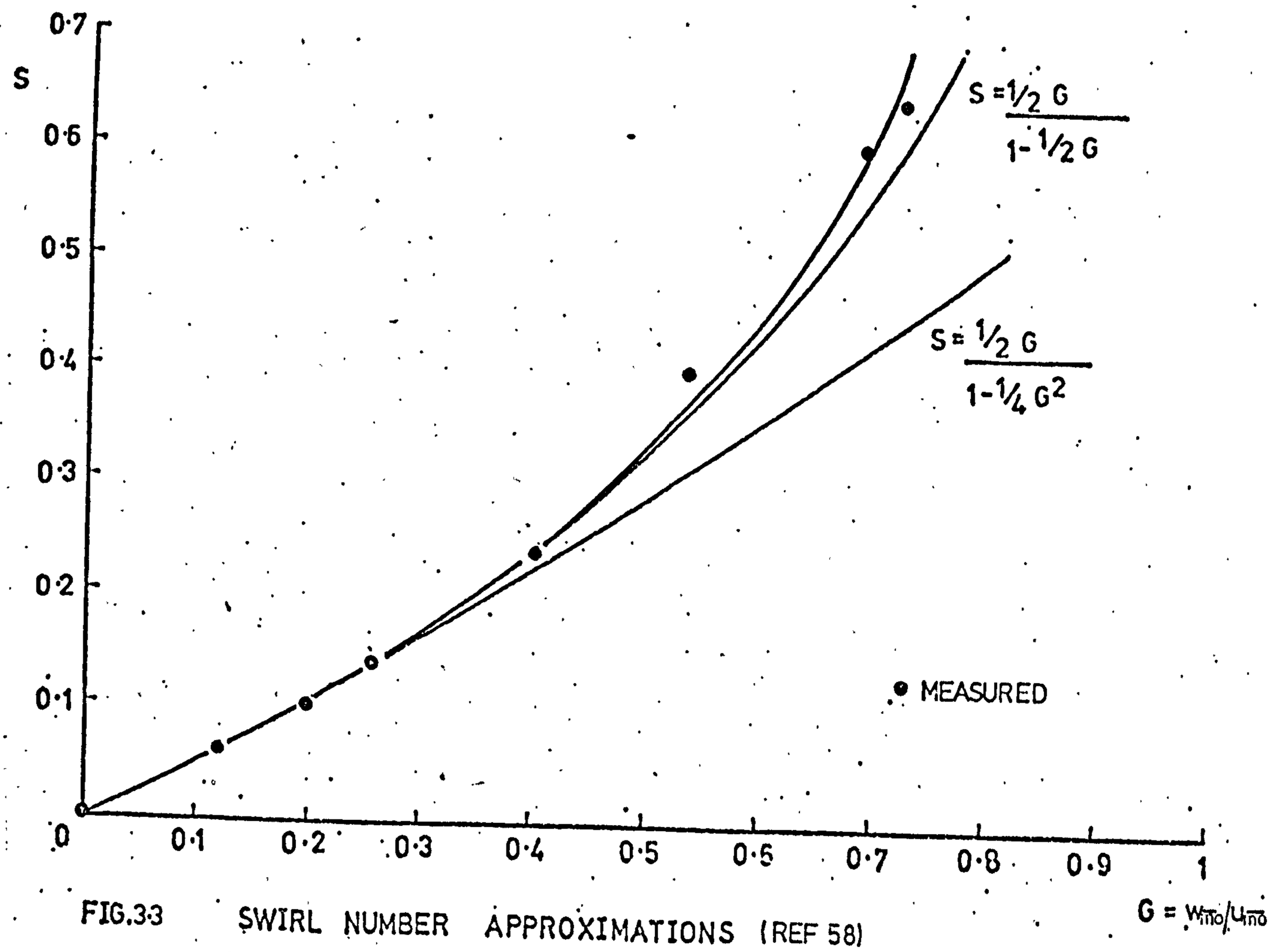

FIG.3·3 SWIRL NUMBER APPROXIMATIONS (REF 58)

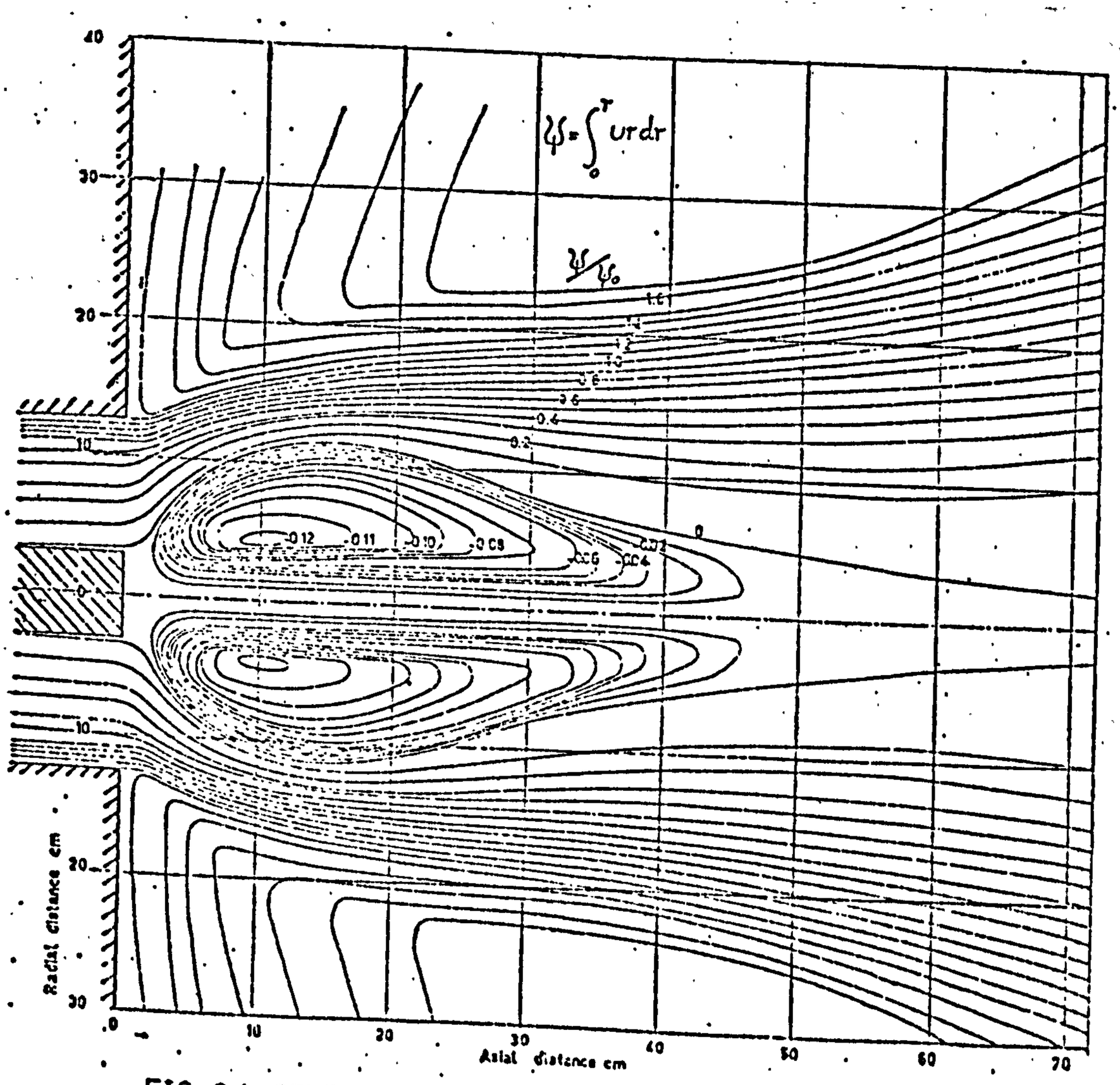

FIG. 3.4 STREAMLINES OF FLOW IN THE VORTEX REGION—S = 1·57 (REF 23)

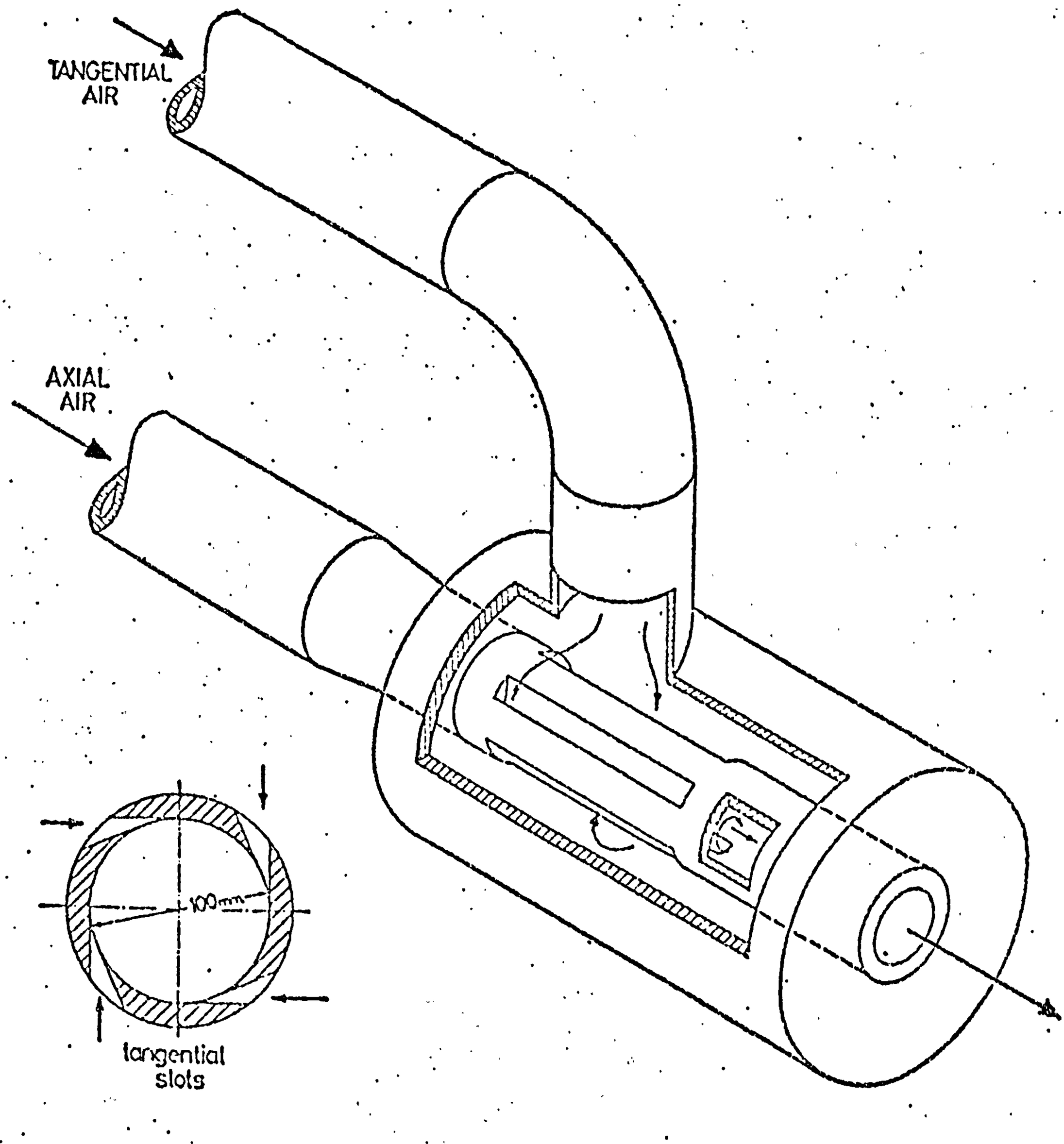

Fig. 3.5 SWIRL GENERATOR [Ref. 58]

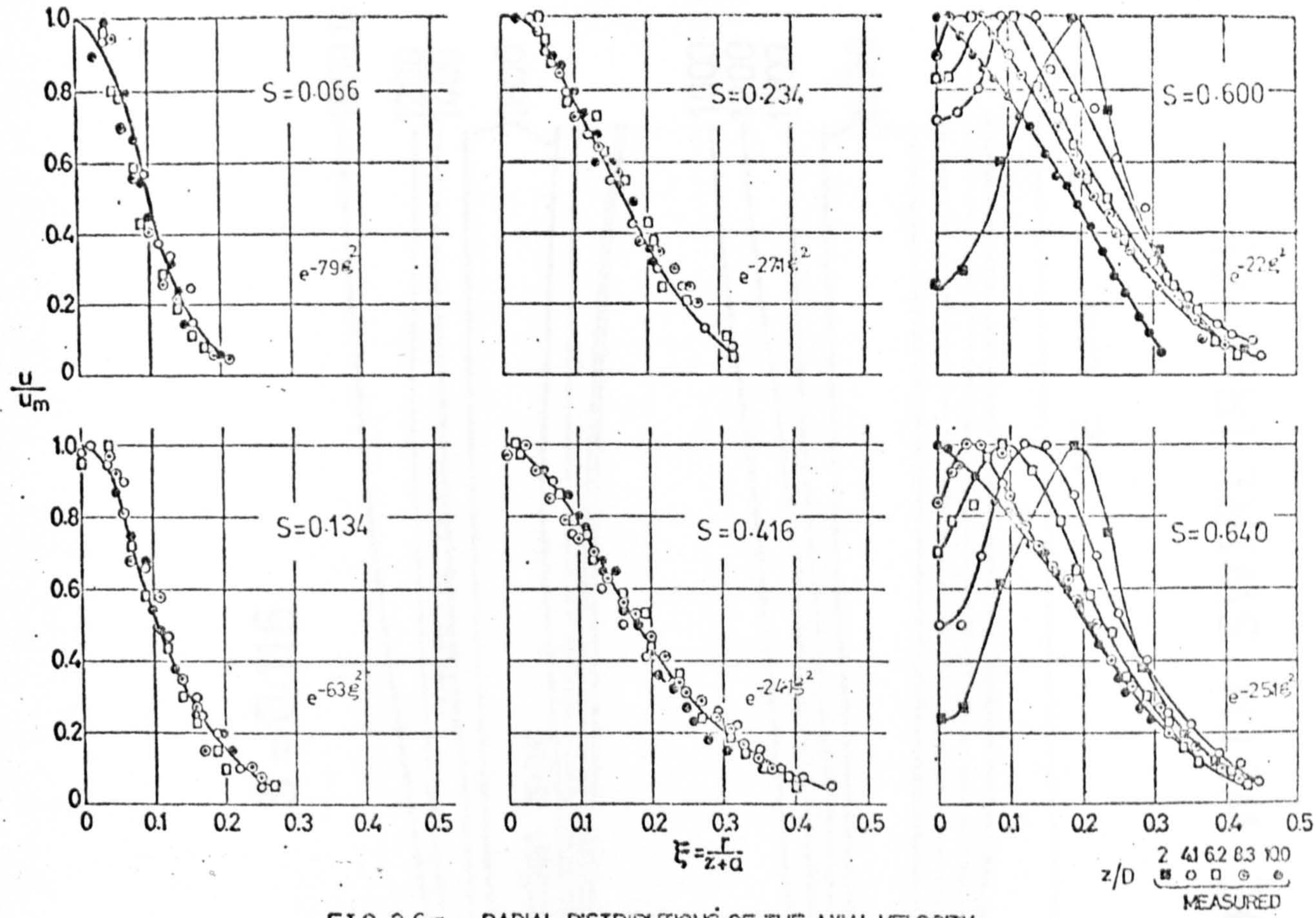

FIG. 3·6 a RADIAL DISTRIBUTIONS OF THE AXIAL VELOCITY

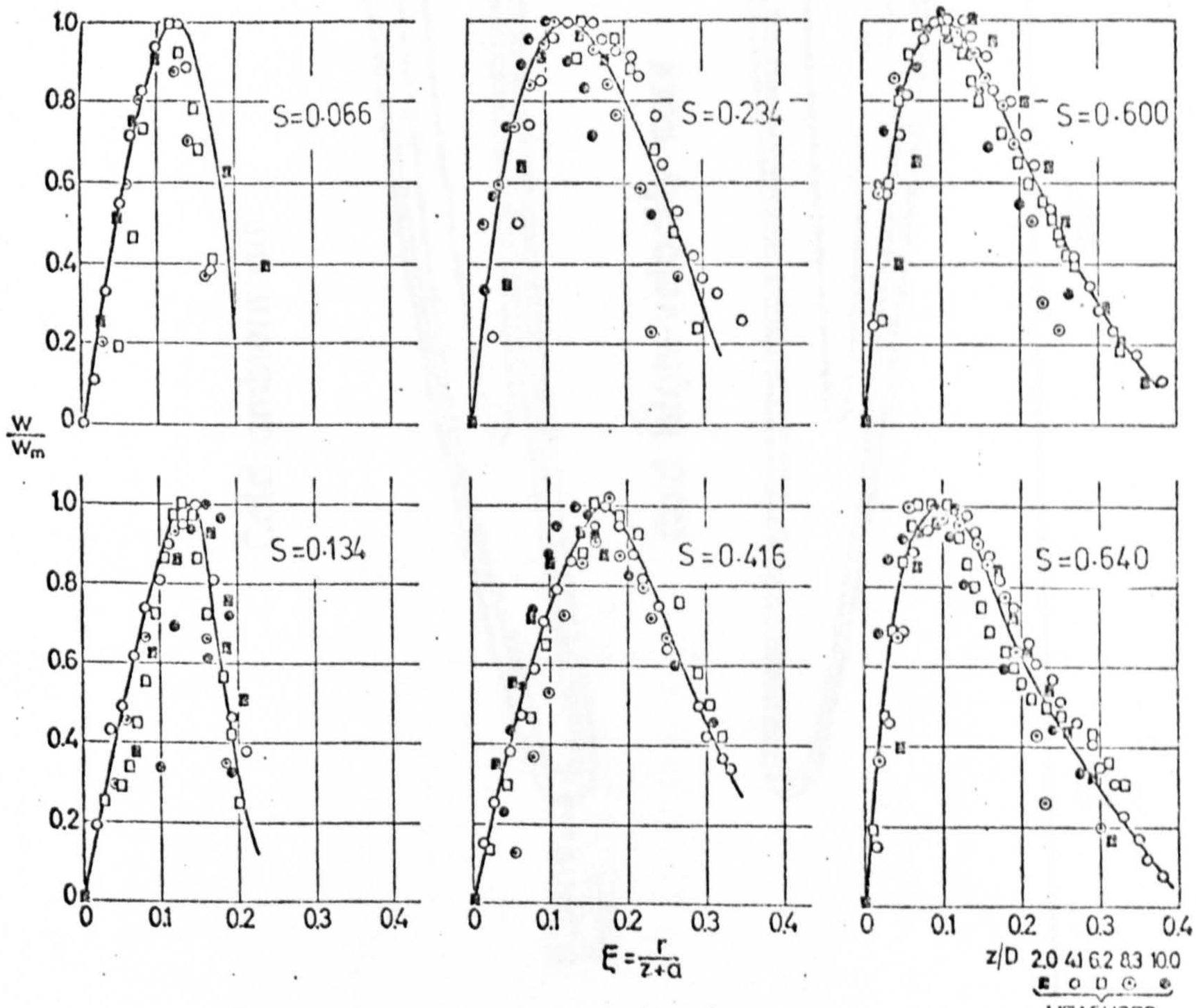

FIG. 3·6 b RADIAL DISTRIBUTIONS OF THE SWIRL VELOCITY

(Reference 58)

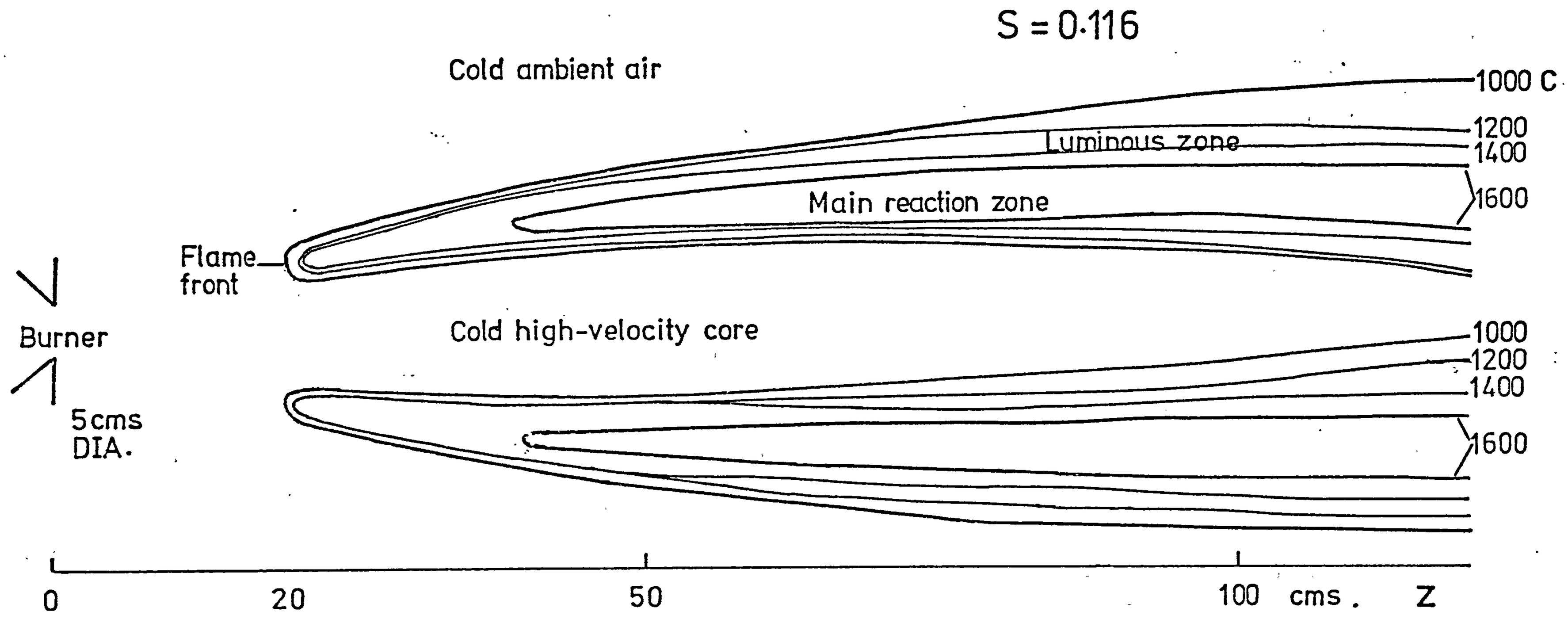

Fig.3·7 TEMPERATURE FIELD IN FLAME WITH SWIRL [Ref·70]

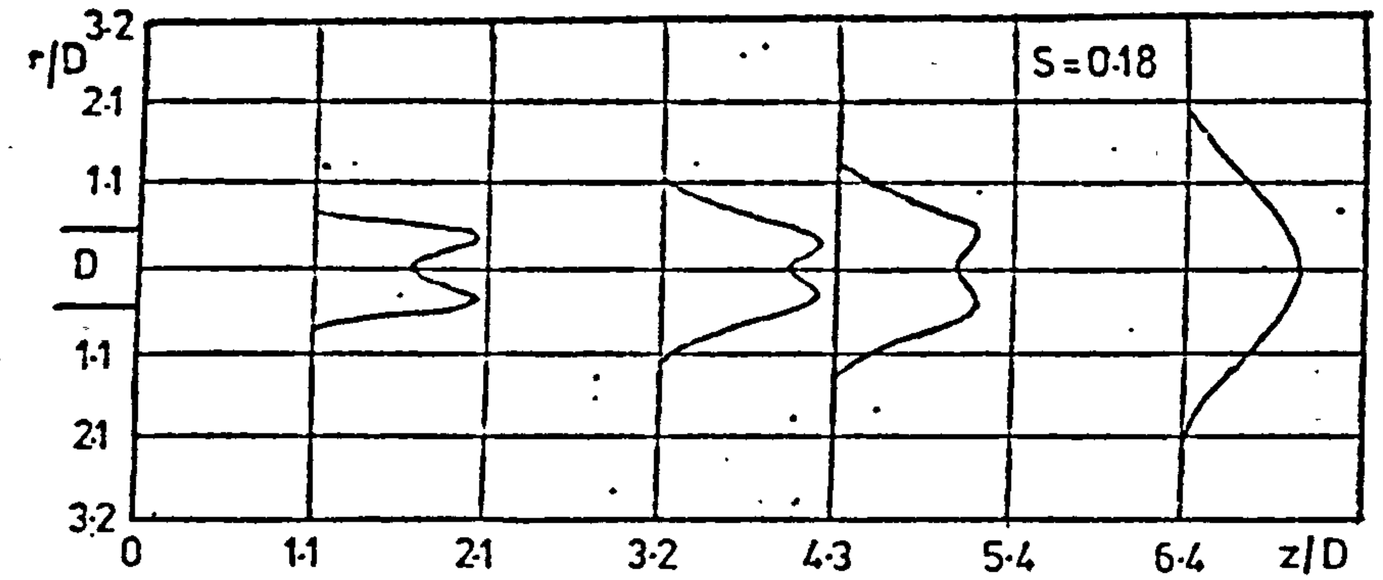

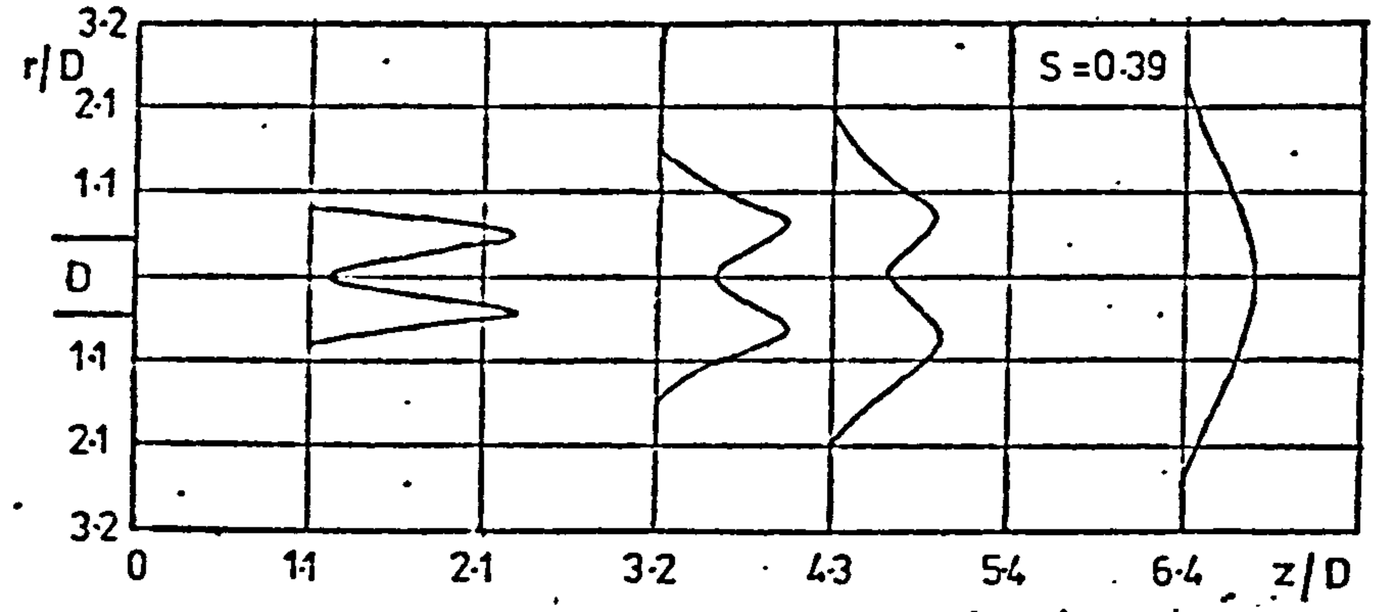

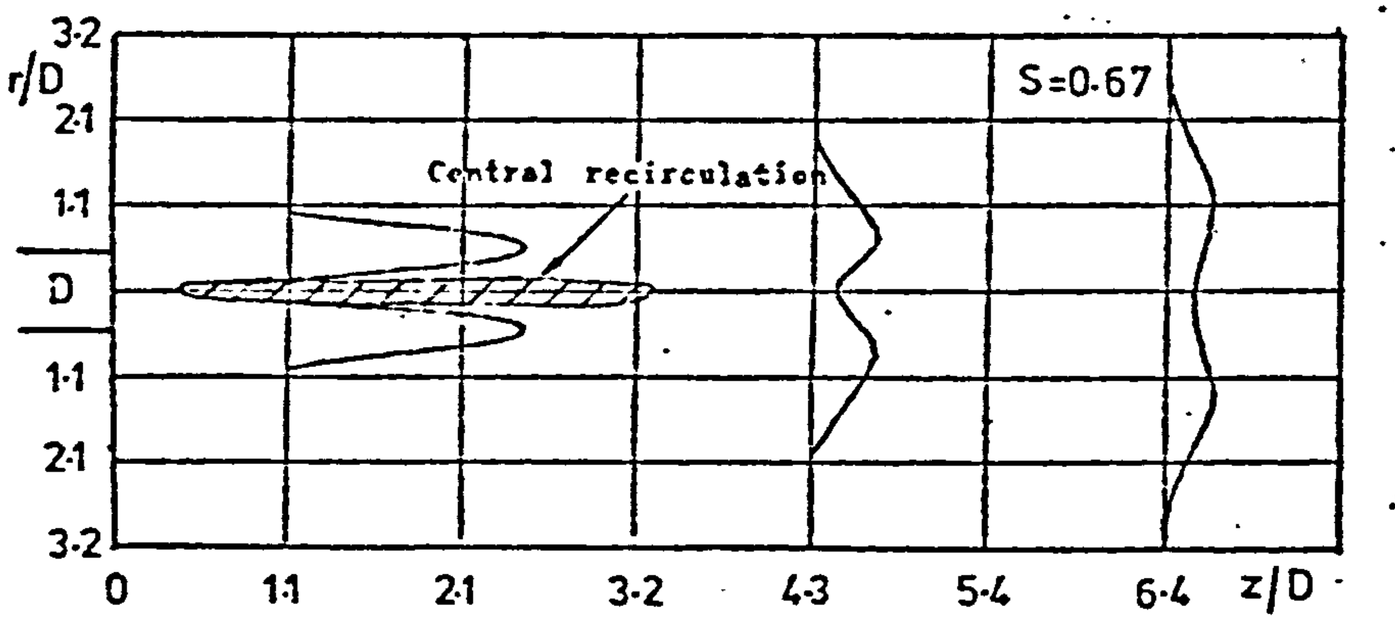

D = 23·7mm
jet velocity = 30·5 m/s

0 10 20
Velocity scale m/s

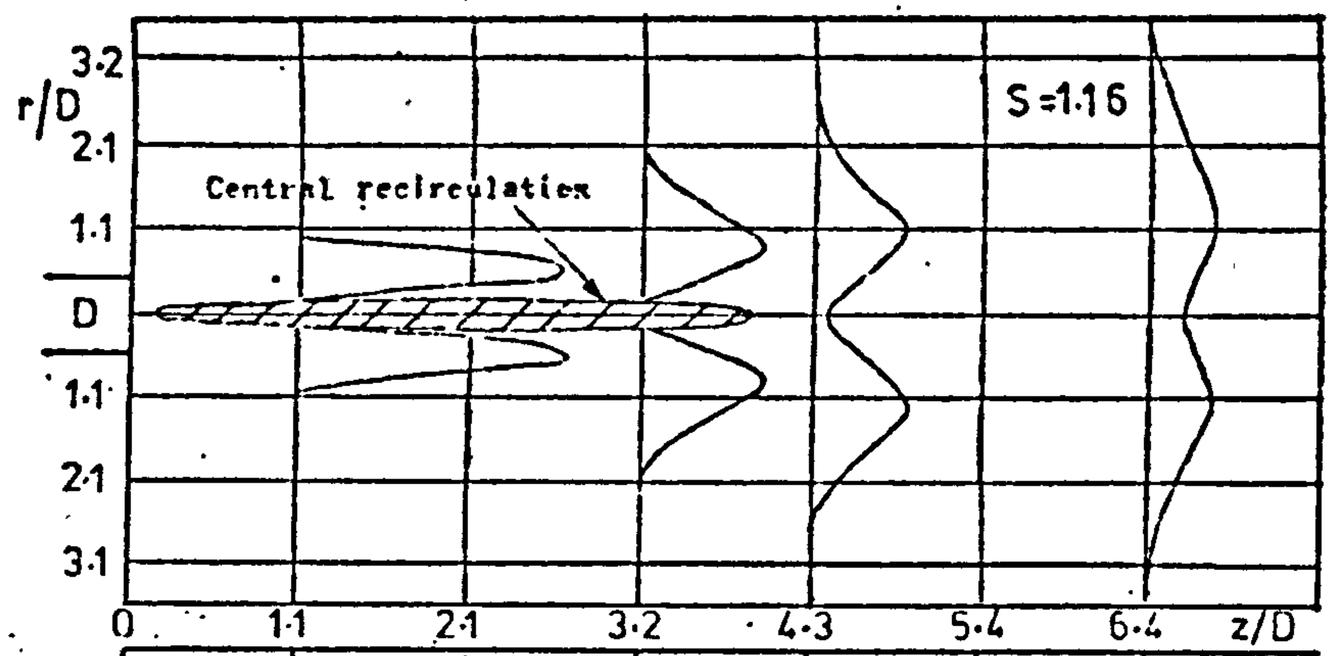

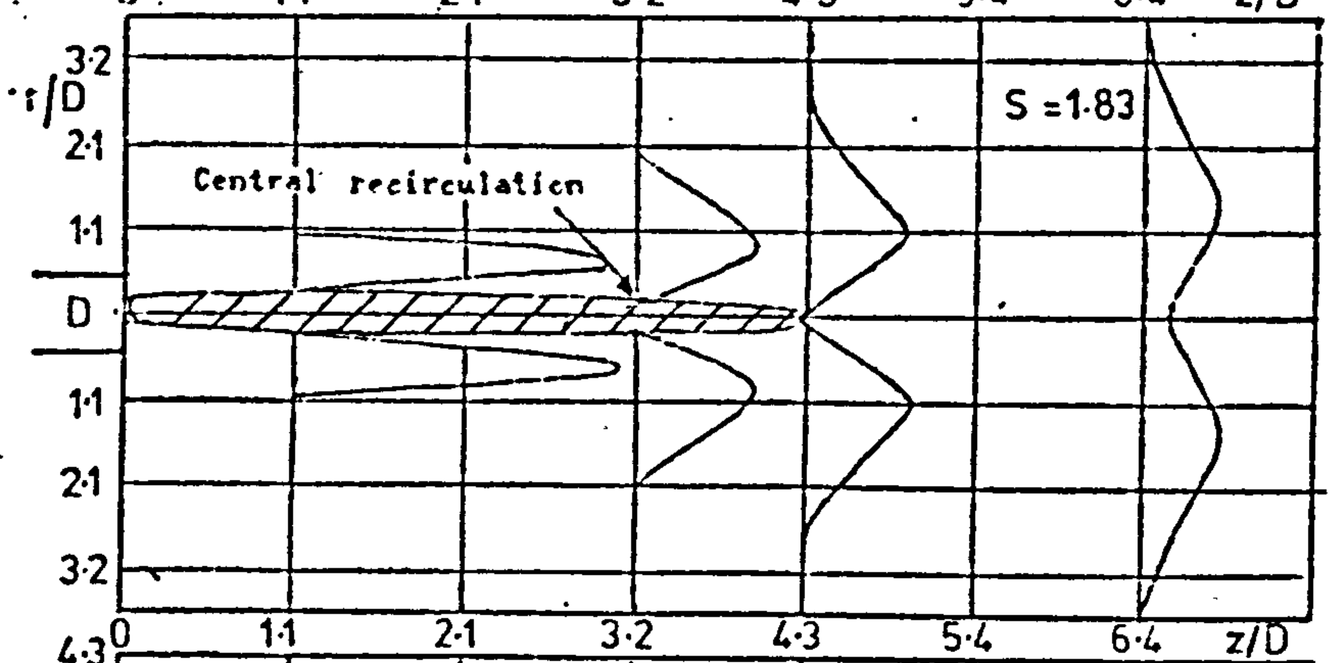

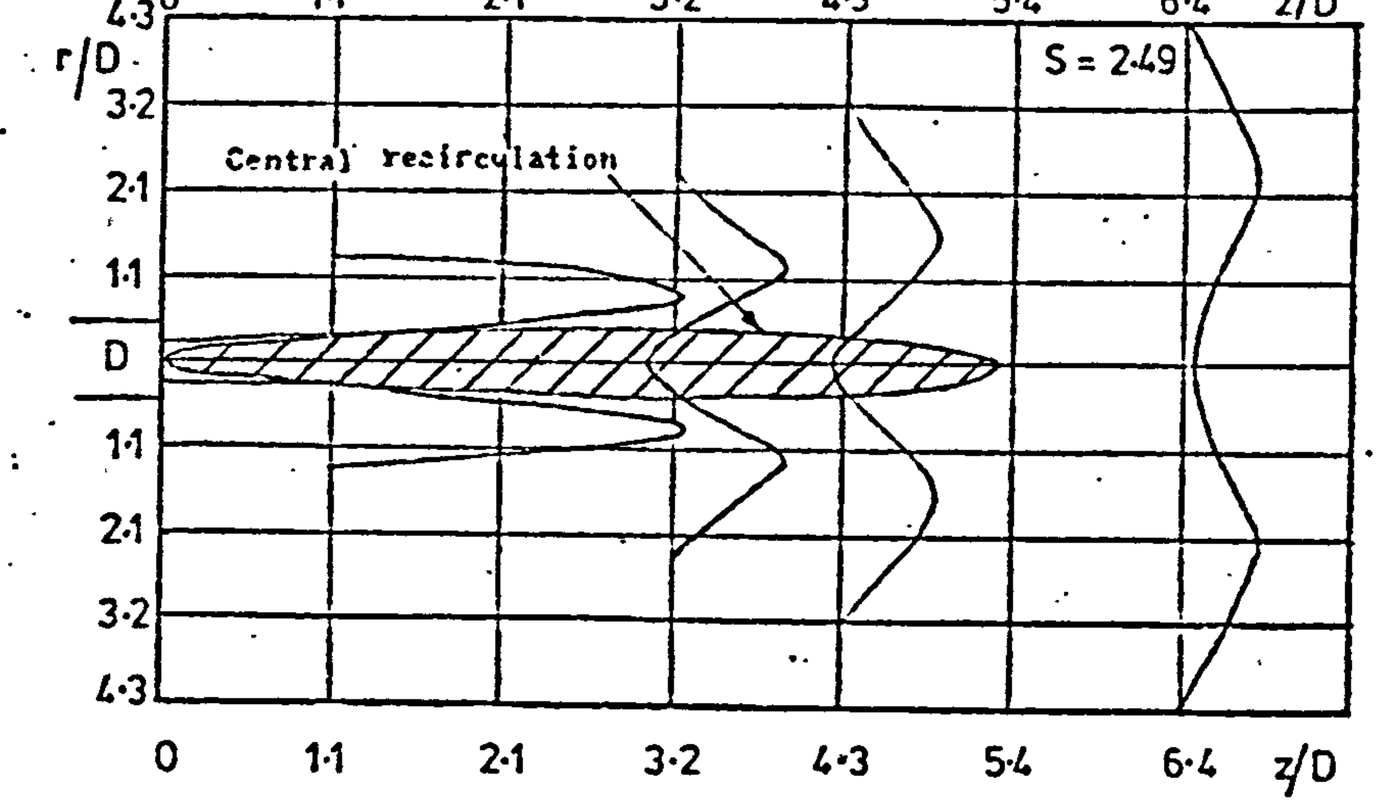

Fig 3·8 a PROFILES OF AXIAL VELOCITY COMPONENT FOR VARIOUS DEGREES OF SWIRL
Ref 55

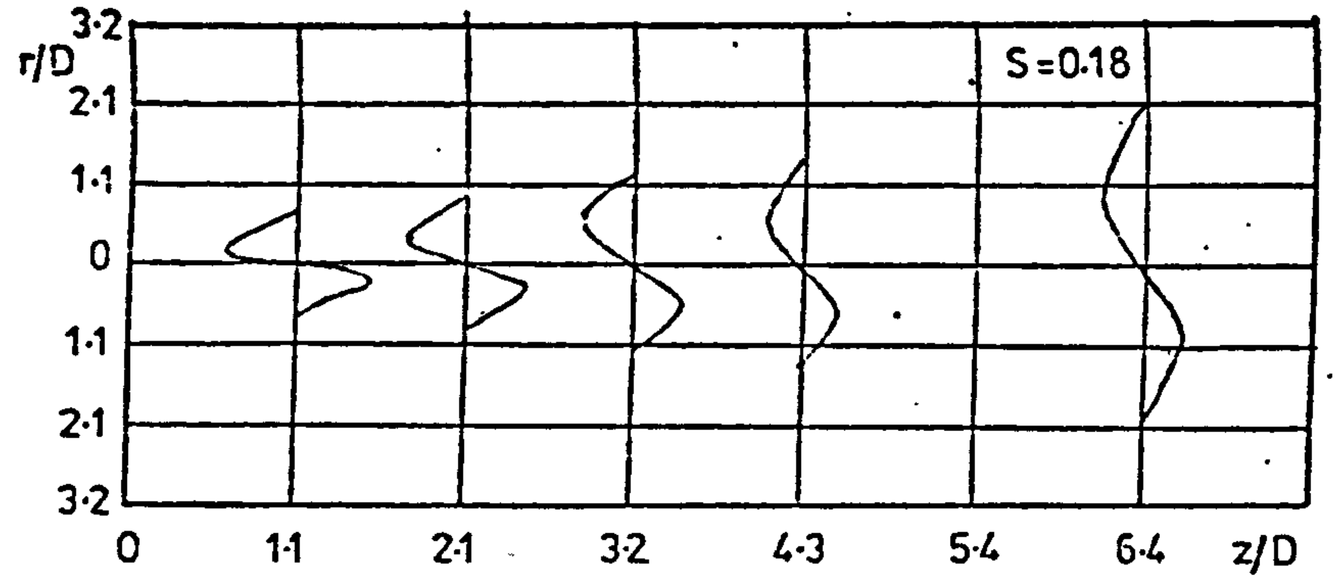

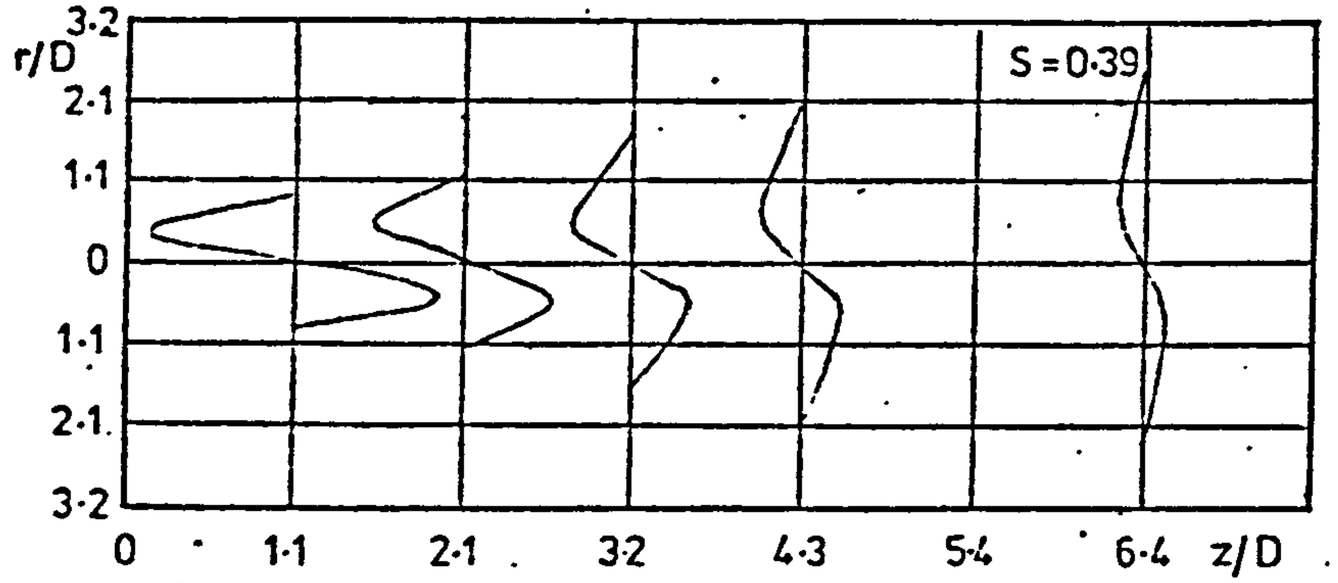

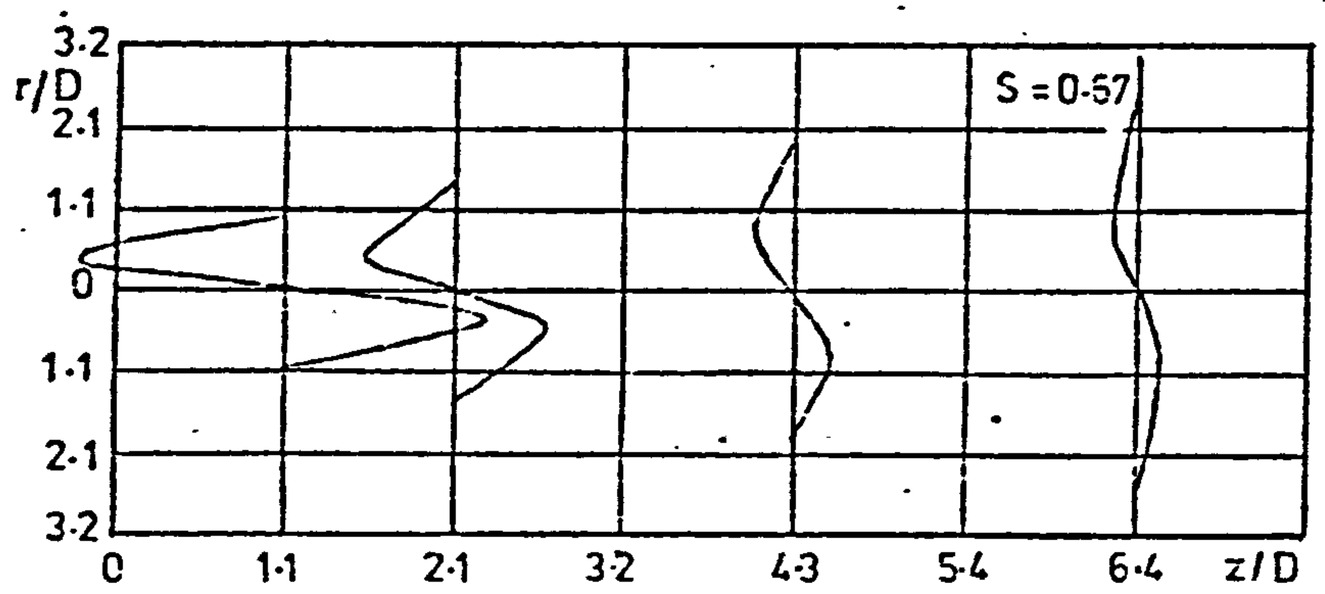

D = 23·7 mm

jet velocity = 30·5 m/s

Velocity scale m/s

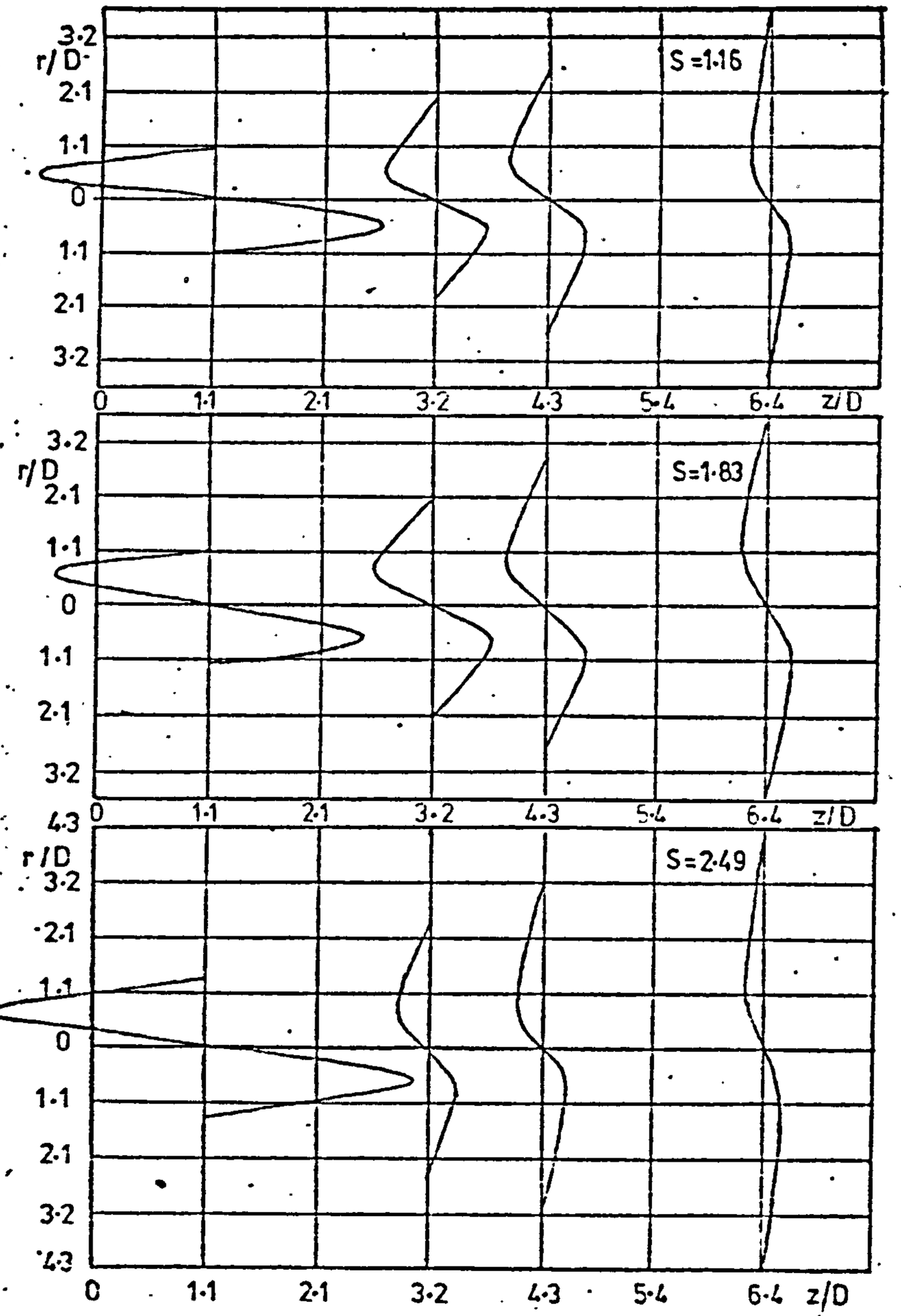

Fig 3-8 b PROFILES OF TANGENTIAL VELOCITY COMPONENT FOR VARIOUS DEGREES OF SWIRL (Ref 55)

CHAPTER 4

SWIRLING JET EXPERIMENTAL RIGS

4.1 INTRODUCTION

Two different air supply systems were used to provide the required flow rates to the single and multiple jet assemblies. The rig employed in the multiple jet studies was initially developed by Dunn (Ref.25) and was used in the present investigation after slight modification.

Of the various available types of swirl generating devices, an axial-tangential entry type of swirler similar to that shown in Figure 3.5 was chosen. This type of swirler was selected primarily because different degrees of swirl can be obtained by varying the ratio between the axial and the tangential mass flow rates. Thus, a range of swirls can be readily produced from a single swirler. Furthermore, these swirlers are relatively easy to manufacture and their characteristics are reproducable. These features were especially important in the construction of the number of swirlers used in multiple jet assemblies. Hubless vane swirlers, which were also considered are, in contrast, often difficult to manufacture and can result in non-symmetric flows (see Refs.55 and 56; Section 3.2). Moreover, since the degree of swirl is dependent on the vane angle, each swirl number would require a separate vane assembly. Thus, the number of swirl nozzles would be greatly increased, particularly for multiple jet studies, unless more complicated variable pitch swirlers are used.

4.2 THE SWIRL GENERATORS.

Figure 4.1 shows a working drawing of the swirl generator used in the single jet studies. Basically, the generator can be split into three components, namely, the inner jet tube, the outer plenum, and the tangential fluid entry tube. The inner pipe was constructed of a 22mm bore plastic tube, and was 292mm long. Four 4.8mm wide parallel slots, 114mm long (equally spaced around the circumference) were machined in the central portion of the wall of this inner tube. The outer plenum, consisting of a plastic cylinder (76mm inside diameter and 1400mm long), was then mounted co-axially around the inner jet tube to enclose these tangential slots. The ends of the plenum were then sealed. The fluid entry tube (of 22mm bore and 76mm long) was glued into the outer plenum such that it had a tangential entry and was slightly inclined to the vertical. The air entering the nozzle tube from the outer plenum thus possesses a high circumferential velocity so that the swirl number can be controlled by variations in the tangential and axial air supplies.

The swirl generators used in the multiple jet studies were

of similar construction and were available from Dunn's original rig (Ref.25). However, they were somewhat smaller in size when compared to the single jet swirler, but were used because of their convenience and the consequent savings in time. The inner jet tube in these designs was of 16mm bore, mild steel tube 165mm long, while the four tangential slots were 2.4mm wide and 38mm long. The other non-critical dimensions are illustrated in Figure 4.2 A photograph of one of these swirlers is also shown in Plate 1.

4.3 SINGLE JET TEST RIG.

The layout of the test rig is shown schematically in Fig. 4.3. Air was delivered from a variable speed centrifugal fan rated at 1.5Kw. This was capable of supplying 0.1 m^3/s at a pressure drop of 1300mm water gauge. The flow was then passed through a water cooler (a cross flow heat exchanger) which was used to control the jet temperature at or near the ambient value. This total flow was measured by an orifice plate mounted in the supply line. The flow was then divided into the axial supply and into a flexible pipe which was connected to the swirler plenum, i.e. the tangential supply. These two separate flows can be individually controlled by gate valves. The tangential flow rate was also measured by an orifice installation. The main or total flow orifice was installed according to BS.1042 (Ref.75). However, non-standard pipe lengths are associated with the tangential flow measuring system so that this orifice plate was calibrated with reference to the standard BS.1042 device.

The whole jet assembly was mounted horizontally on a four-wheeled carriage which was traversed on rails to provide the variation of nozzle-to-target spacing over the required range (i.e. $2 < z/D < 12$). The target plates used in the mass transfer studies were mounted orthogonally to the jet and they are described later in Section 8.3.

4.4 MULTIPLE JET TEST RIG.

The multiple jet test rig is, in many aspects, similar to the single jet rig described in the previous section. Whilst details of this rig are given in Ref.25, a brief description is presented here for the sake of completeness.

.The rig is shown schematically in Fig.4.4. A larger, constant speed, centrifugal fan (rated at 4 Kw) supplying 0.6 m^3/s of air (at 130mm water gauge) was required because of the bigger pressure drop in the multiple nozzle arrangement. The air delivered by the fan was cooled to near ambient, metered, and divided into two streams as in the single jet system. However, these two supplies are then fed to individual rectangular flows. The inlet to each of these plenum chambers consists of a short length

of perforated tube which was fitted with a baffle plate to reduce turbulence and ensure an even supply of air to the plenum. In the axial supply system, the upper portion of the inner jet pipes of the swirl generators were push-fitted into holes drilled in the base of the plenum. The horizontal air flow to the swirlers was supplied through individual flexible plastic tubes connecting the outlet nozzles on the tangential plenum chamber to the tangential entry tubes. The base plate of the axial plenum chamber was drilled such that the swirl generators could be arranged in a 3 x 3 square array with centre-to-centre spacings of 50.8, 76.2 and 101.6mm (giving x/D ratios of 3.2, 4.8 and 6.4). Any holes not required during a particular test were blocked off.

The target plate was mounted orthogonally to the axes of the jets on a frame constructed from 'Dexion' slotted angle. This plate is described in Section 8.3.

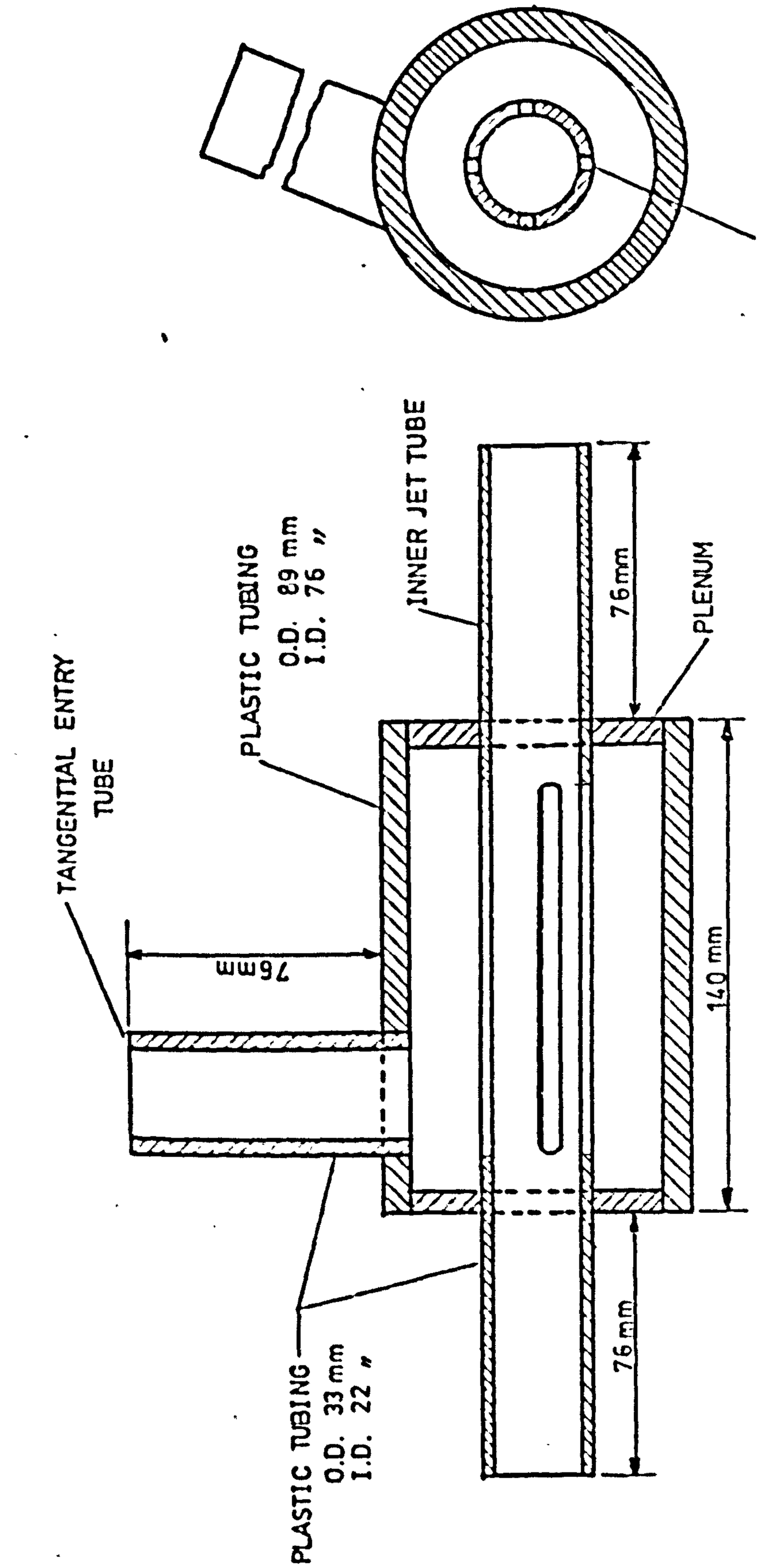

SCALE HALF SIZE

Fig. 4.1 SWIRL GENERATOR — SINGLE JET STUDIES.

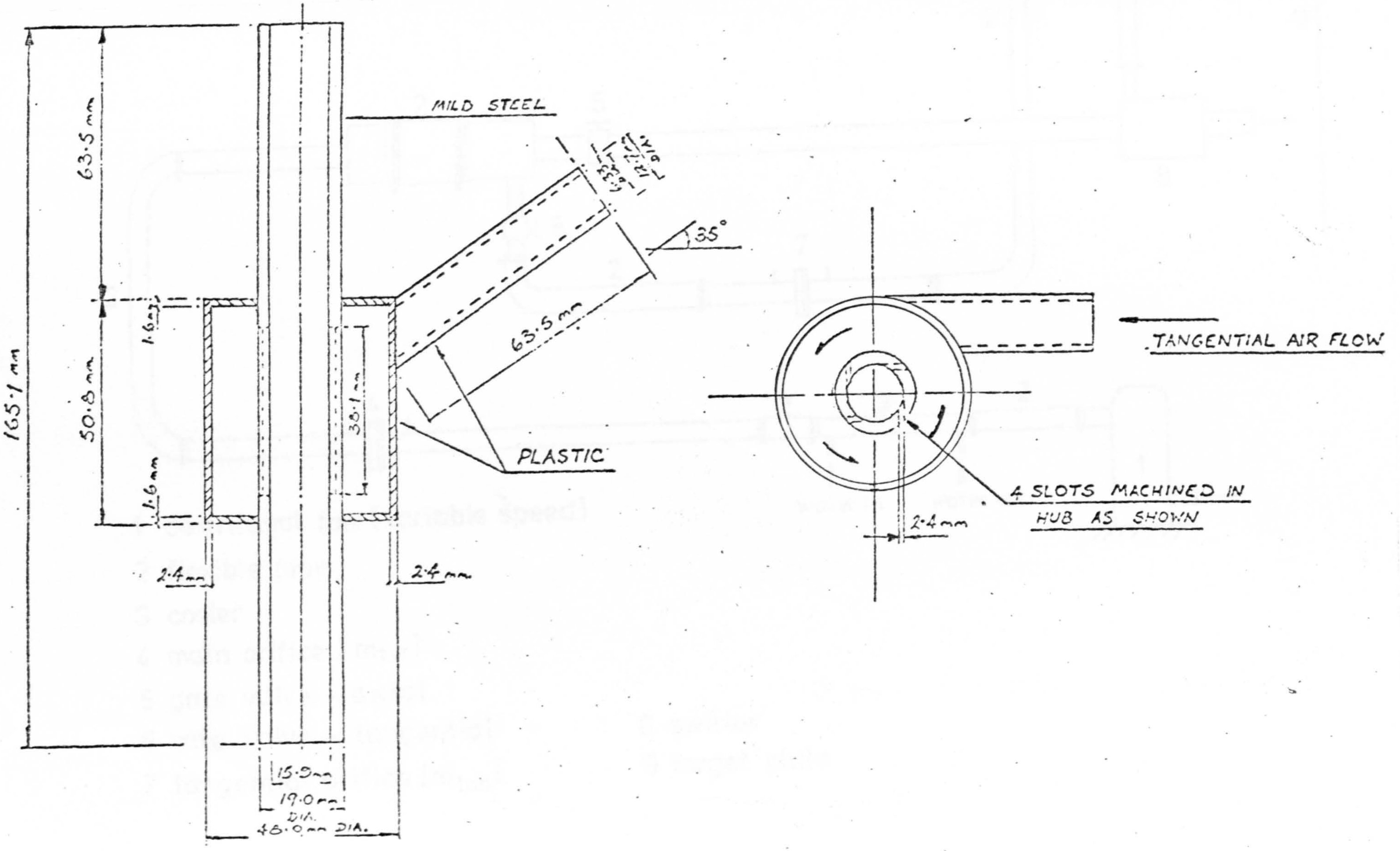

Fig. 42 SWIRL GENERATOR — MULTIPLE JET STUDIES

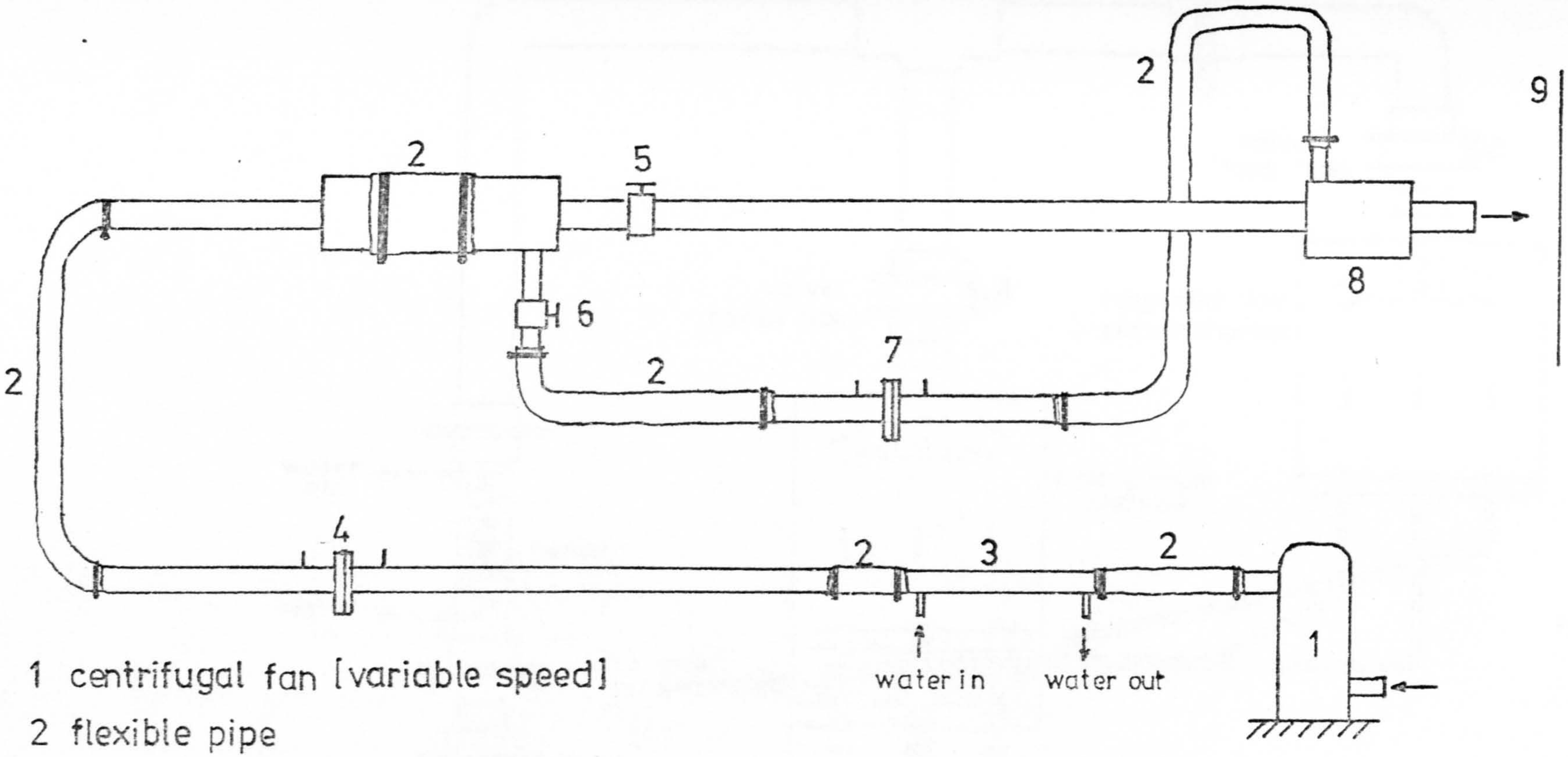

1 centrifugal fan [variable speed]
2 flexible pipe
3 cooler
4 main orifice [m_{tot}]
5 gate valve – axial
6 gate valve – tangential
7 tangential orifice [m_{tan}]
8 swirler
9 target plate

Fig. 4.3 SCHEMATIC REPRESENTATION OF SINGLE JET IMPINGEMENT RIG.

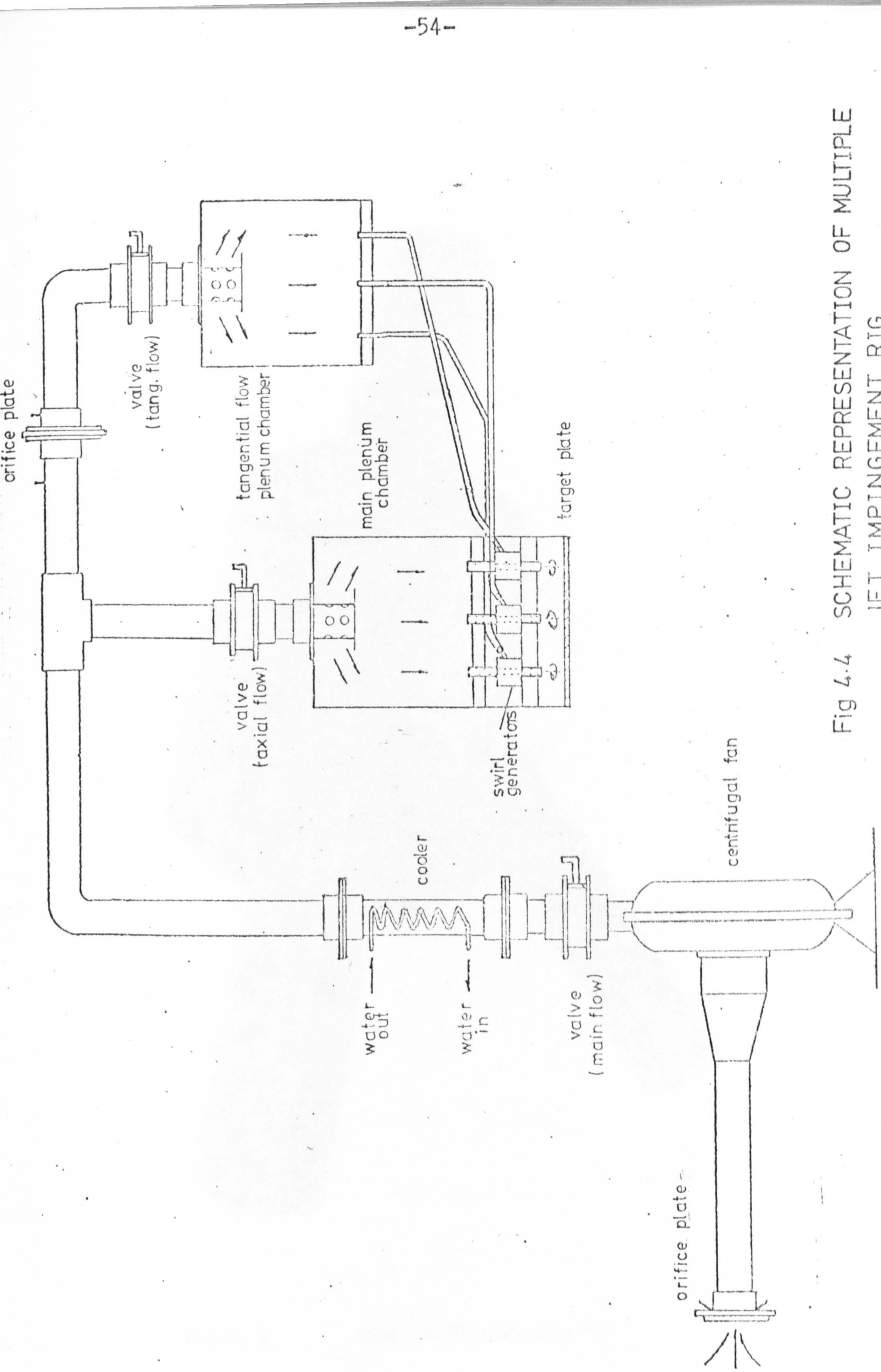

Fig 4.4 SCHEMATIC REPRESENTATION OF MULTIPLE JET IMPINGEMENT RIG

PLATE 1 THE SWIRL GENERATOR

CHAPTER 5

FIVE-HOLE PITOT PROBE MEASUREMENTS - CHARACTERISATION OF SWIRL

5.1 INTRODUCTION

As mentioned in Section 3.3, the swirling jets are characterised in terms of the swirl number ($S = G\Phi/Gx^R$). In the case of vane swirlers, the geometry of the vanes may be used to predict this swirl number. However, for the axial-tangential entry type of swirler, a knowledge of the flow field at any one section perpendicular to the axis of the jet is necessary to evaluate the fluxes of axial and angular momenta. Alternatively, for weak and medium swirl ($S < 0.6$) the maximum values of the axial and tangential velocities at exit from the nozzle can be used to determine the swirl number (Ref.58).

Five-hole spherical pitot probes have often been used to determine the flow fields in swirling jets (Refs.56, 57 and 58). Consequently, a probe of this type of 6mm diameter was employed in the present study. Since the head of this probe was large when compared to the nozzle diameter, accurate local velocity measurement at the nozzle exit plane was not feasible. Therefore, the velocities in the flow field were determined at a section two nozzle-diameters downstream from the exit. The resultant profiles for the axial and the tangential velocities were integrated to evaluate the swirl numbers.

5.2 THE FIVE-HOLE PITOT PROBE

In three dimensional flows (e.g. those with swirl or involving recirculation), it is necessary to measure both the magnitude and the direction of the velocity. The five-hole pitot probe operates by measuring the pressure distribution around a sphere introduced into the flowing stream. Thus, both the magnitude and direction of the resultant velocity can be determined as well as the static pressure.

The restrictions on using a 5-hole pitot probe are its relatively large size, blockage of the holes, and the effects of turbulence in the flow. High turbulence intensities can effect the pressure readings and the error can be estimated from the expression:-

$$p_m = p_s + C\rho\,\overline{u'^2}$$

where 'p_m' and 'p_s' are the measured and true pressure respectively; '$\overline{u'^2}$' is the fluctuating mean velocity component; and the constant 'C' varies between 0 and 0.33.

Similar equations exist for all three velocity components. However, if the turbulence intensities in all three directions exceed 20%, these simple expressions do not hold and the procedure for making corrections for the level of turbulence is involved and tedious.

5.2.1 Probe Description

The spherical probe used in the present tests was supplied by E.Schiltknecht, Gossau, Switzerland, and comprises a 6mm diameter, spherical head with five tappings, each 0.5mm in diameter. The distribution of these sensing holes (denoted as 1,2,3,4 and 5) is such that hole No.2 lies on a pole of the sphere. The remainder of the tappings are equispaced from tapping 2 and are arranged to form two orthogonal meridians and enclose an angle of 45^{o} in their respective planes, see Figure 5.1.

The tappings are connected via capillary tubes to their respective numbered outlet connections. These outlets are fixed on to a solid flange for rigidity, and connections are then brought out to a multi-leg inclined alcohol manometer. The flange incorporates a circular, rotatable dial graduated from 0 to 360^{o} in steps of 2^{o}. A locking device can be employed to fix the scale onto the shaft of the pressure tube. The zero position on the graduated scale can be aligned with the plane containing tappings 1, 2 and 3 by means of a sighting mechanism.

5.2.2 Evaluation of the Flow Velocity and Static Pressure

In order to measure the velocity and static pressure at a particular station, the probe and scale are aligned as described in the previous section. The yaw angle 'ϕ' of the flow is thus related to the plane passing through tappings 1, 2 and 3. Consequently, the reference plane for the pitch angle 'α' is orthogonal to that for the yaw angle. The spherical head is then rotated in the guide (i.e. about the axis perpendicular to the yaw plane) until the pressures at each of the apertures 4 and 5 are equalised. This situation corresponds to the null point in the yaw plane. The pressures indicated by tappings 1, 2 3 and 4 are then recorded and the yaw angle 'ϕ' is read from the dial (see Fig.5.1). These readings are sufficient to obtain all the velocity components and the static pressure at the measurement station.

The pitch angle 'α' for the flow can be related by the following expression:-

$$\alpha = f\left(\frac{H_3 - H_1}{H_2 - H_4}\right)$$

where 'H' is pressure differential measured by the manometer with reference to the ambient pressure. The subscripts correspond to the particular tapping.

This angle 'α' can be determined from the calibration chart for the proble. The flow velocity $\bar{V}$ can be found from:-

$$\bar{V} = \sqrt{\frac{2(H_2 - H_4)}{k_{24}\,\rho}}$$

where k_{24} is a coefficient found from the calibration chart and depends on the pitch angle 'α' determined previously; 'ρ' is the density of the fluid.

The axial (u), radial (v) and tangential (w) velocity components are then found from the equations:-

$$u = \bar{V} \cos\alpha \cos\Phi$$

$$v = \bar{V} \cos\alpha \sin\Phi$$

$$w = \bar{V} \sin\alpha$$

Figure 5.2 presents the relationships between these components and the resultant velocity.

The static pressure 'p' may be found from the relationship:-

$$p = H_2 - \frac{1}{2} k_2 \rho \bar{V}^2$$

where k_2 is again estimated from a calibration chart.

Further details and a sample calculation are given in Appendix A together with the calibration chart for the present probe.

5.3 JET CHARACTERISATION

In general, to characterise the swirling jet it is necessary to obtain radial profiles of velocity and static pressure. However, in the present case, an approximate method using only the axial (u) and tangential (w) components of velocity was used (see Section 3.3). The five-hole probe was mounted on a slide mechanism so that it

could be traversed along an axis parallel to the diameter of the nozzle. This traverse was carried out at a distance of two nozzle diameters from the exit and this station was chosen to avoid any recirculation effects due to the swirl, as recommended by Syred et al (Ref.71). The procedure outlined in the previous section was employed to yield the velocities 'u' and 'w'. Measurements were made at radial steps of 1.6mm and the whole width of the jet (taking into account it's spread) was traversed.

The jet swirl was varied by altering the ratio of the tangential and axial supply flow rates to the jet. At each flow condition, the swirl number was evaluated by using numerical integration to calculate the momenta of axial G_x and tangential flux, G_ϕ. The expressions used to determine G_x and G_ϕ are given in Section 3.3. Measurements were undertaken for mass flow ratios, m_{tan}/m_{tot}, of 0.23, 0.4, 0.53, 0.74, 0.89 and 1 for a total flow rate corresponding to a jet Reynolds number of 60,000 in the 'no swirl' case. A lower Reynolds number of 32,000 was also investigated but, in this case, only the ratios m_{tan}/m_{tot} of 0.33, 0.5, 0.83 and 1 were studied.

5.4 RESULTS AND DISCUSSION

Typical axial and tangential velocity profiles are presented in Figures 5.3 and 5.4 for Re_D= 60,000, and in Figures 5.5 and 5.6 for Re_D= 32,000. The axial velocity profiles were essentially of Gaussian form for the swirl numbers from 0 to 0.36. At higher swirl number (S = 0.48), a central trough appears as the maxima in the jet velocity are displaced from the central axis. The tangential velocity curves show the typical characteristics of a Rankine vortex, i.e. a free vortex in the outer region with a forced vortex at the core.

The present results are similar in trend to those obtained by Dunn (Ref.25) which are illustrated in Figure 5.7. The general characteristics of the present results also show good similarity to the published data of Mathur and Maccallum (Ref.55), see Figure 3.8.

The jet velocity profiles were essentially symmetrical about the longitudinal axis so that numerical integration of the velocity profiles was readily carried out. However, velocities ($\bar{V}$) of less than 3 m/s were difficult to measure with the present manometer. Thus, the velocity curves were extrapolated near the edges of all the jets and also in the central regions (for the 'u' curve) for S = 0.48. The errors introduced by these extrapolations into the integration procedure for G_x and G_ϕ were negligible since the areas under the velocity curve in these regions were relatively small. Complete details of the integration technique together with a sample calculation are presented in Appendix A.

The calculated swirl numbers are plotted against the fractional tangential flow rate (i.e. ratios of the tangential mass flow rate to the total flow rate, $^{m}_{tan}/^{m}_{tot}$) in Figure 5.8 which also presents curves obtained by other investigators (Refs. 23 and 25).

It is apparent from the results that in the present study the swirl number of the flow may be readily controlled by adjustment of the air supply to the axial and tangential ports of the swirler. Furthermore, for the limited range investigated in the present study, the characteristics of the swirlers are independent of the flow Reynolds number. A similar observation was also reported by Beer and Chigier (Ref.23). The differences in the swirl characteristic of the various swirlers are probably due to differances in their geometries. For example, the two swirlers used by Dunn (Ref.25) and the present investigator, though similar in construction, had different types of slots; parallel slots were employed in the present work, whereas tangential entry slots were used by Dunn, see Figures 4.1 and 4.2 The tangential slots would be more efficient in maintaining the swirling flow so that this device would generate higher swirl for the same fractional tangential flow ($^{m}_{tan}/^{m}_{tot}$), see Figure 5.8.

The calibration curve presented by Dunn (Ref.25) is for one of the 16 swirlers constructed for the multiple jet investigation. Since these swirlers have been used in the present multiple jet studies, it was thought desirable to check the reproducibility of the swirl generated by various individual swirlers. The 'u' and 'w' curves for three such swirlers (selected at random) were integrated at a particular $^{m}_{tan}/^{m}_{tot}$, see Figure 5.9. The resultant swirl numbers were 0.54, 0.55 and 0.56. These values demonstrate that for all practical purposes the swirl generators were mutually interchangeable and their characteristics can be represented by a single curve as shown in Figure 5.8.

The effects of turbulence on the velocity measurements are difficult to assess. However, comparison of the profiles obtained by the five-hole pitot probe with those obtained later by hot-wire anemometry show satisfactory agreement (see Figures 6.14 and 6.15). The two other restrictions mentioned in Section 5.2, namely blockage of the holes and the size of the probe head, were not a problem since the air jet was dust-free and measurements were not taken near the nozzle exit. It can, therefore, be concluded that five-hole pitot probe can be used successfully to obtain the flow velocities in swirling jets.

Since the velocities and turbulence intensities in the swirling jets were also measured by hot-wire anemometry, further discussion has been given at the end of the next chapter, see Section 6.7.

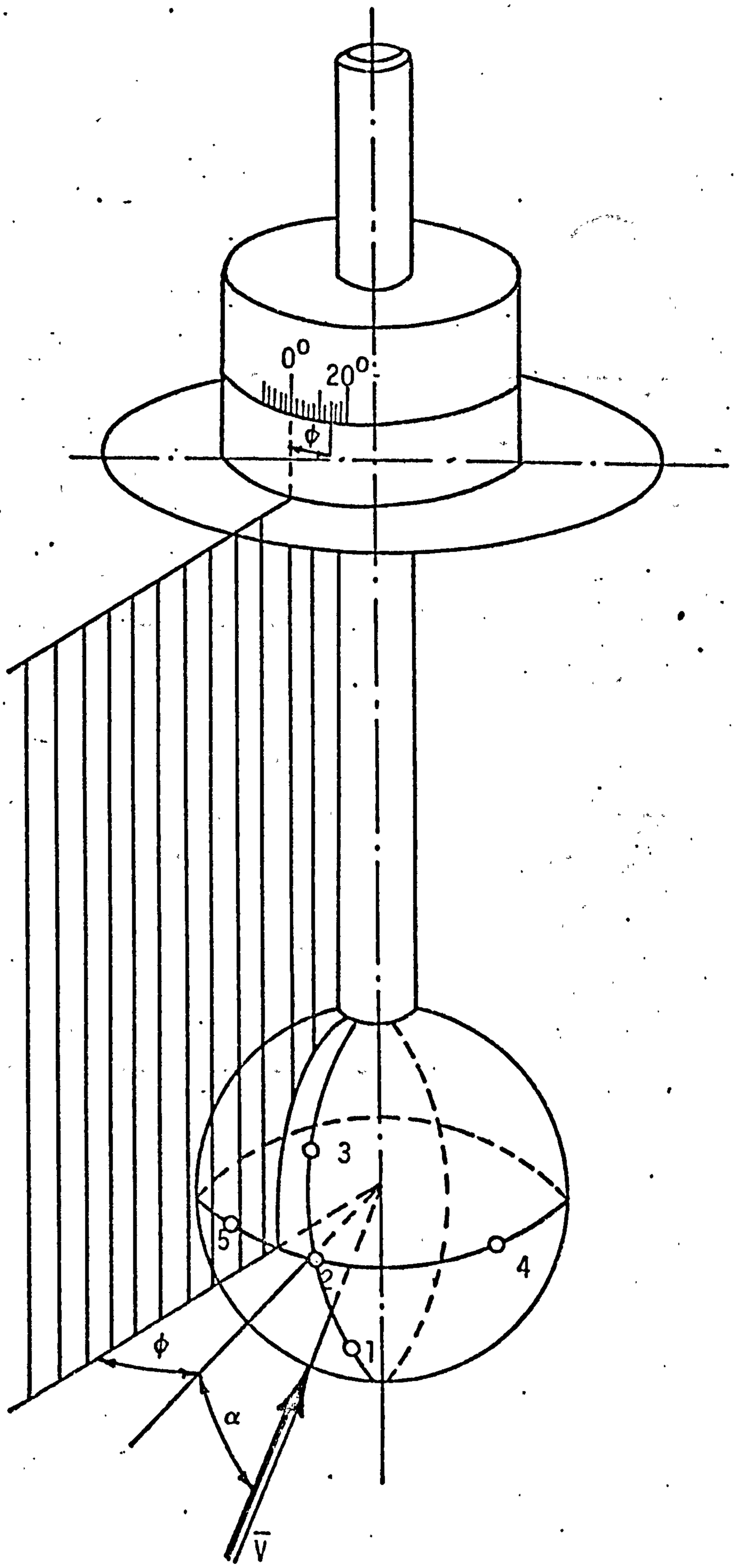

Fig. 5.1 FIVE HOLE SPHERICAL PRESSURE PROBE

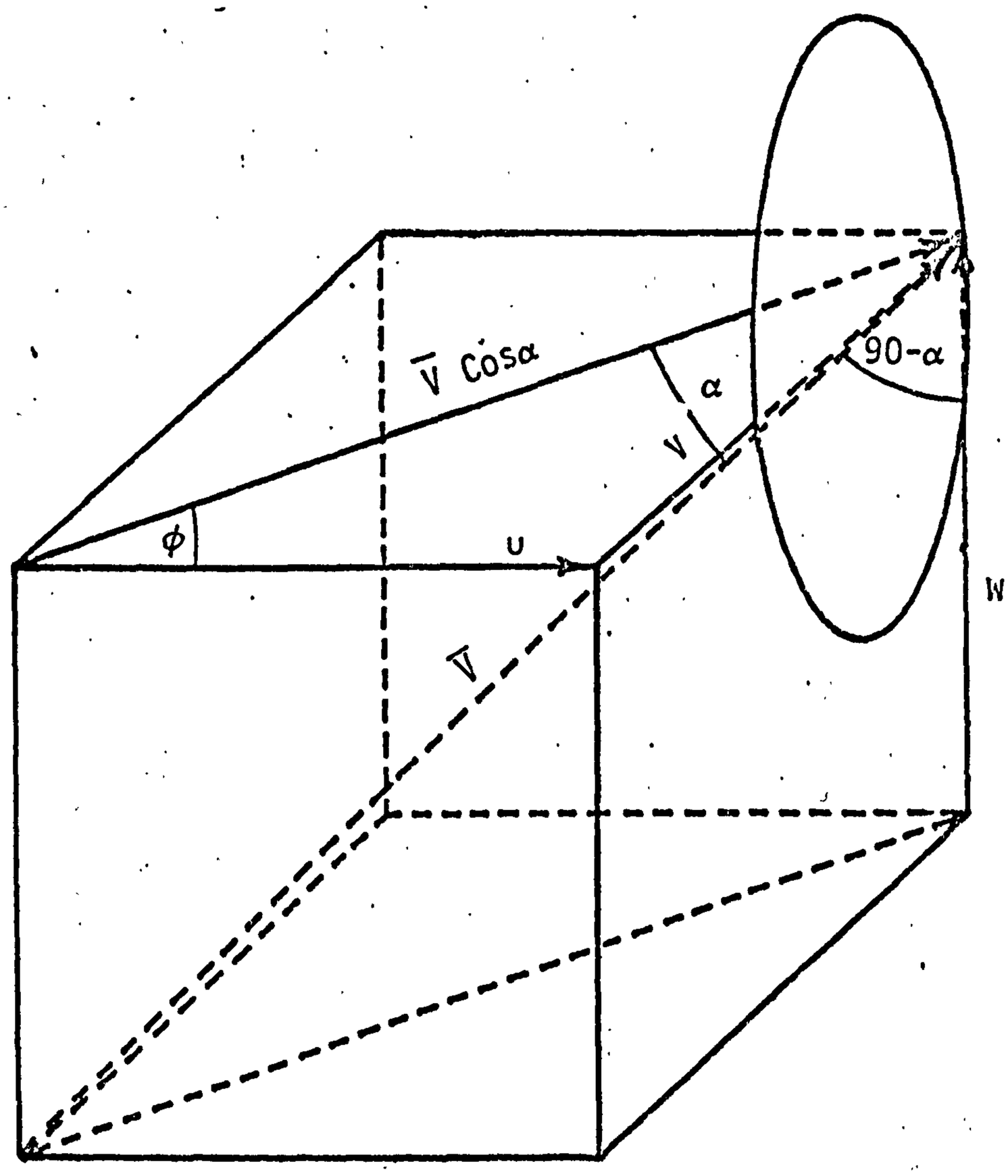

Fig. 5.2 THE RELATIONSHIP OF THE VELOCITY COMPONENTS TO THE RESULTANT

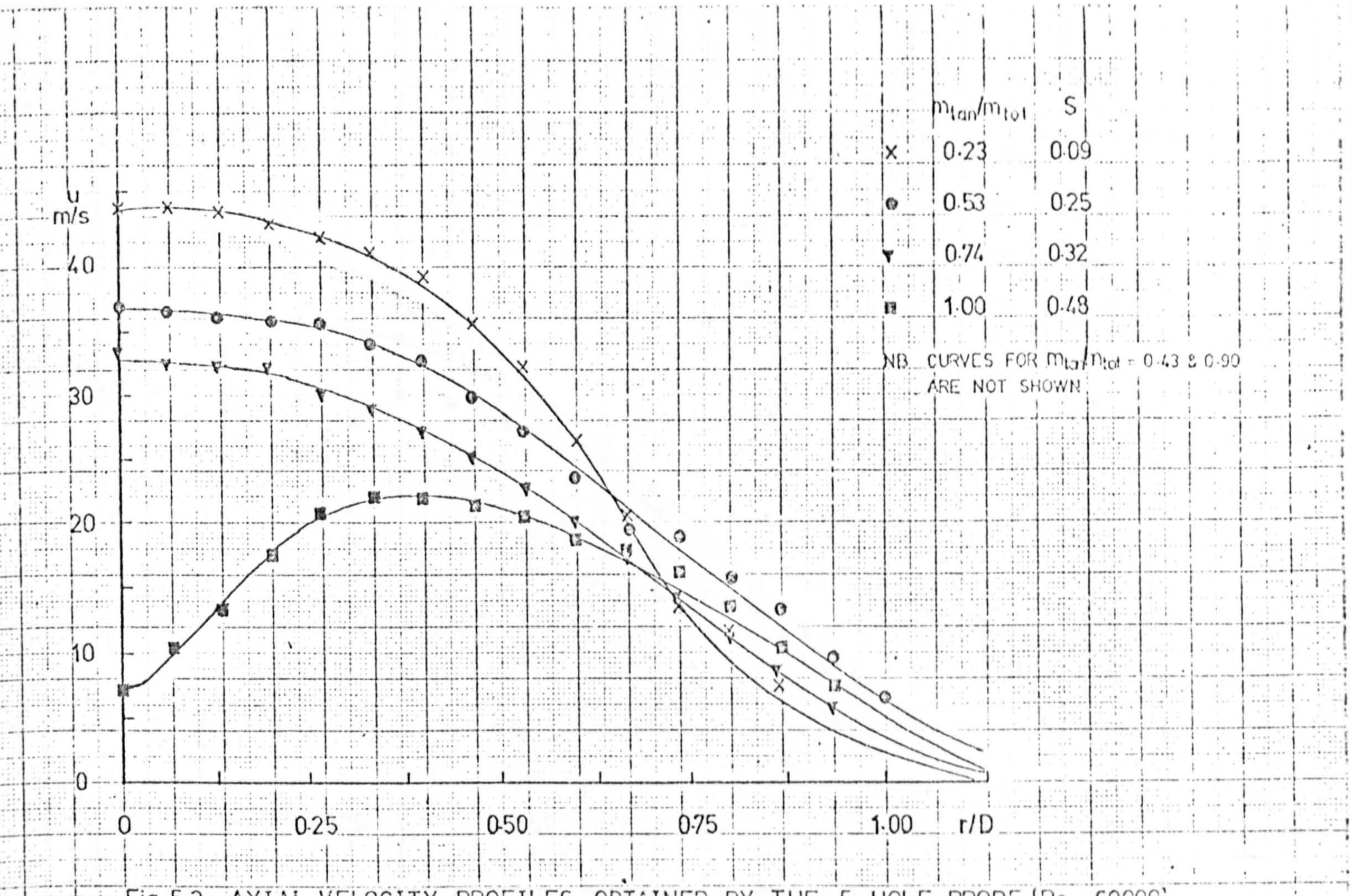

Fig. 5.3 AXIAL VELOCITY PROFILES OBTAINED BY THE 5-HOLE PROBE (Re_D=60000)

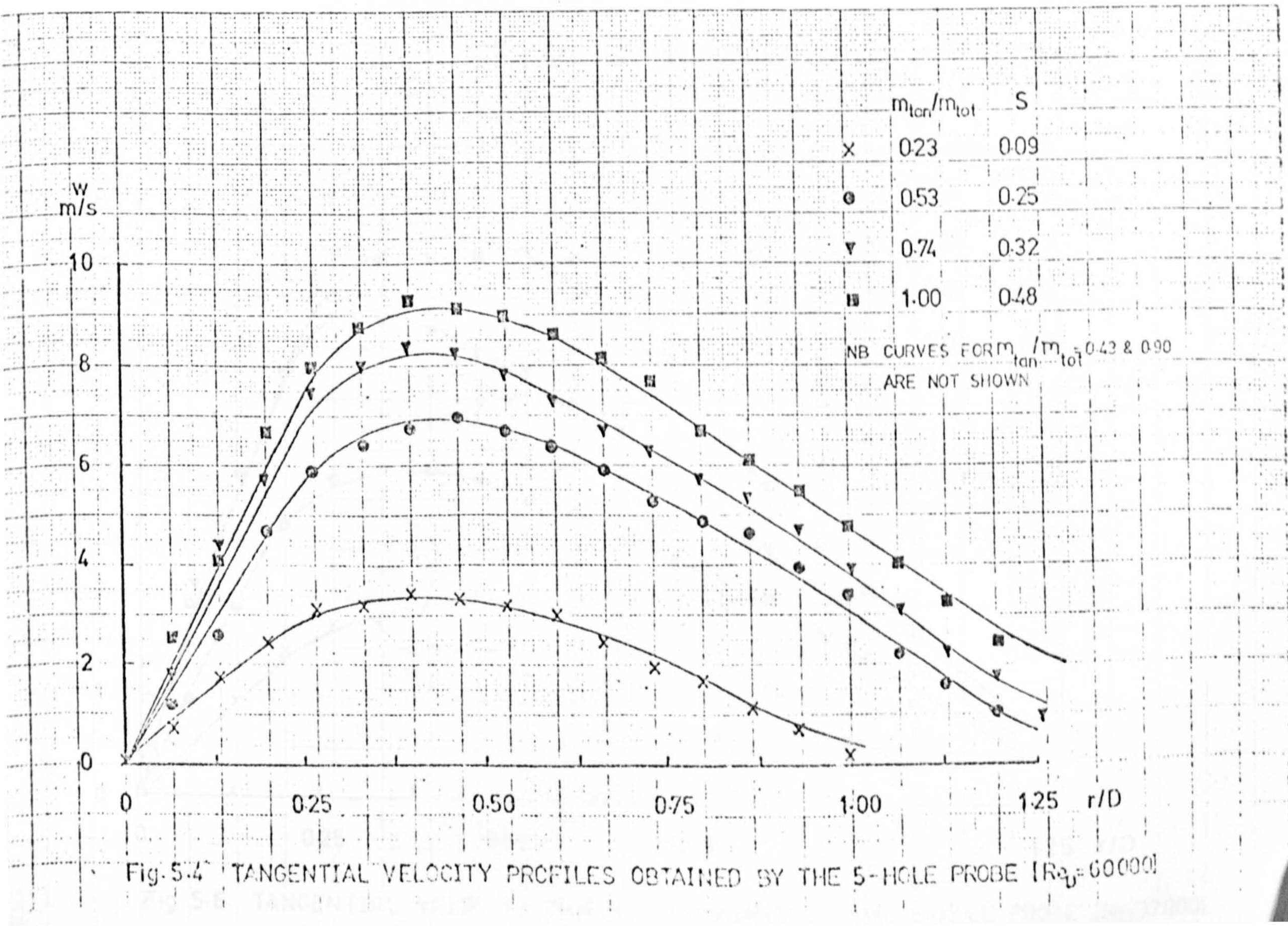

Fig. 5.4 TANGENTIAL VELOCITY PROFILES OBTAINED BY THE 5-HOLE PROBE (Re_D=60000)

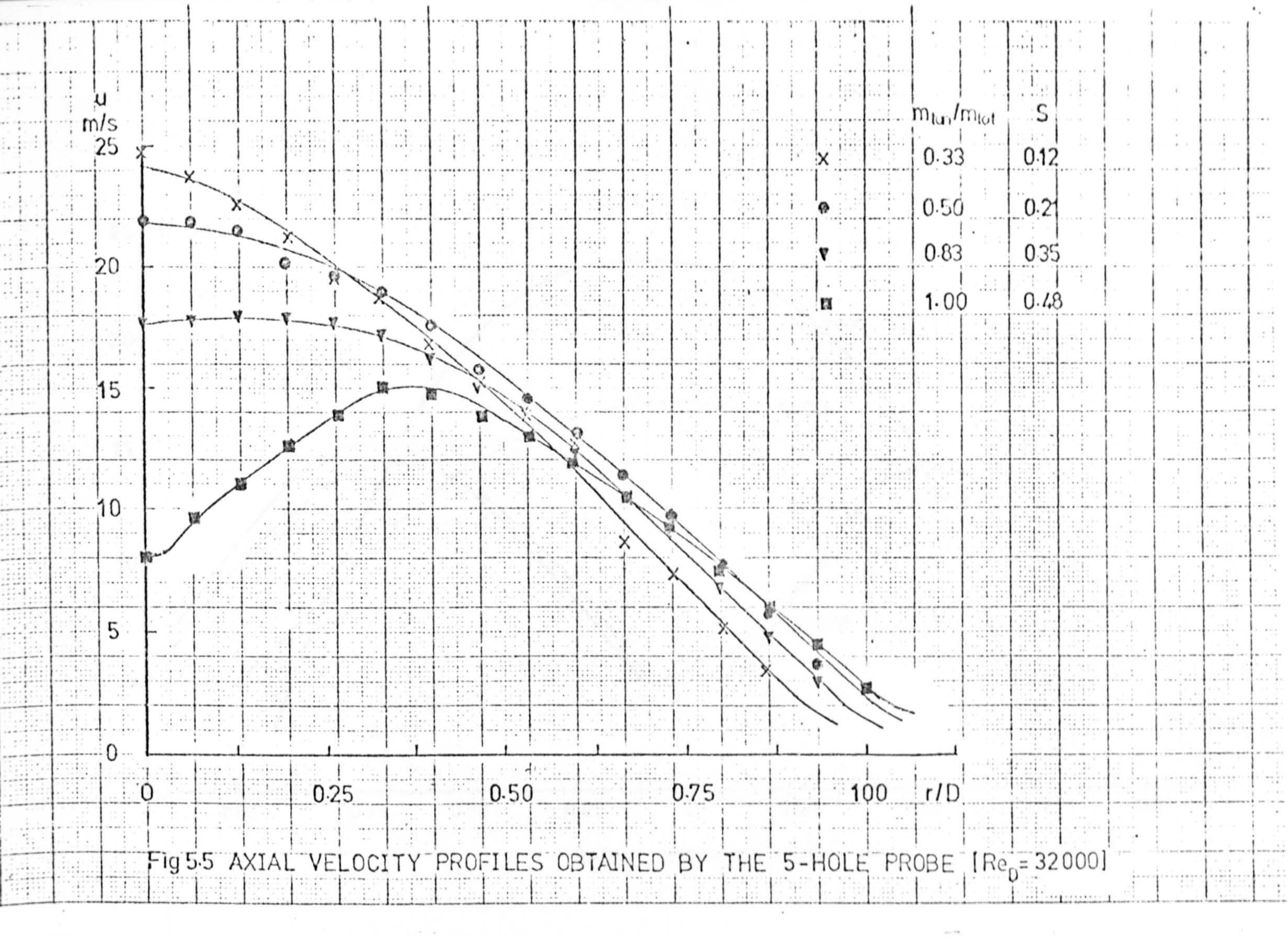

Fig 5.5 AXIAL VELOCITY PROFILES OBTAINED BY THE 5-HOLE PROBE [$Re_D = 32000$]

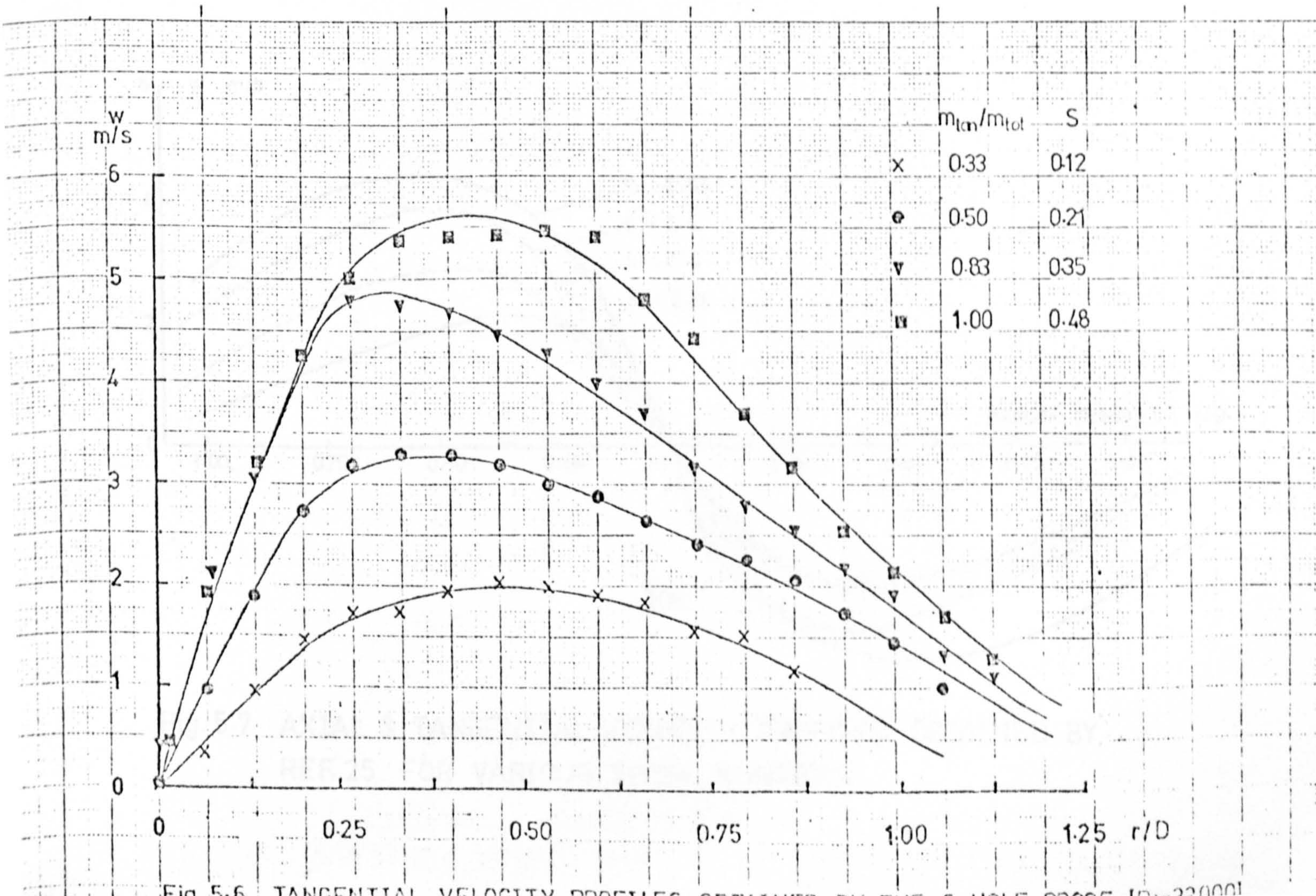

Fig 5.6 TANGENTIAL VELOCITY PROFILES OBTAINED BY THE 5-HOLE PROBE [$Re_D = 32000$]

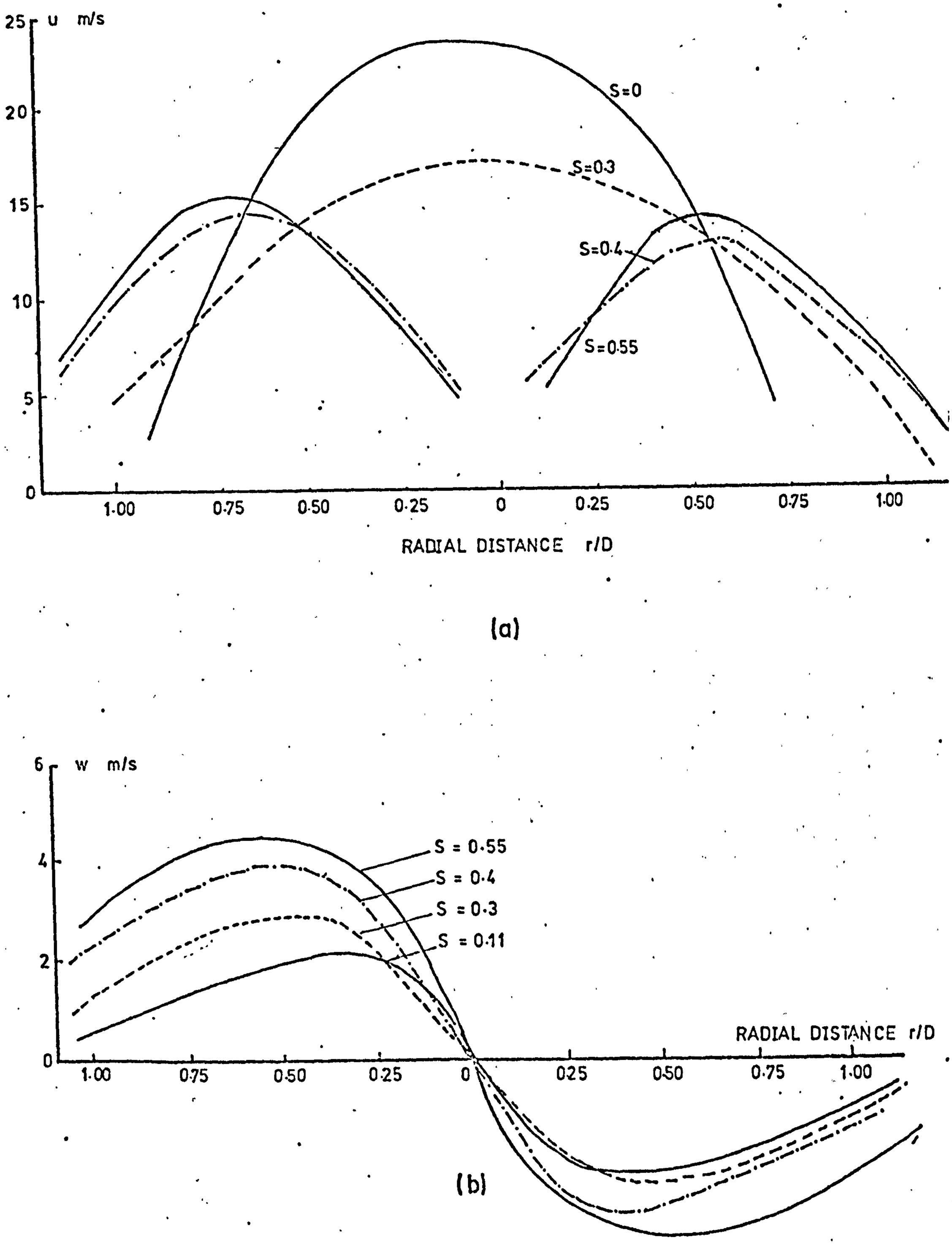

Fig. 5.7 AXIAL & TANGENTIAL VELOCITY PROFILES OBTAINED BY REF. 25 FOR VARIOUS SWIRL NUMBERS.

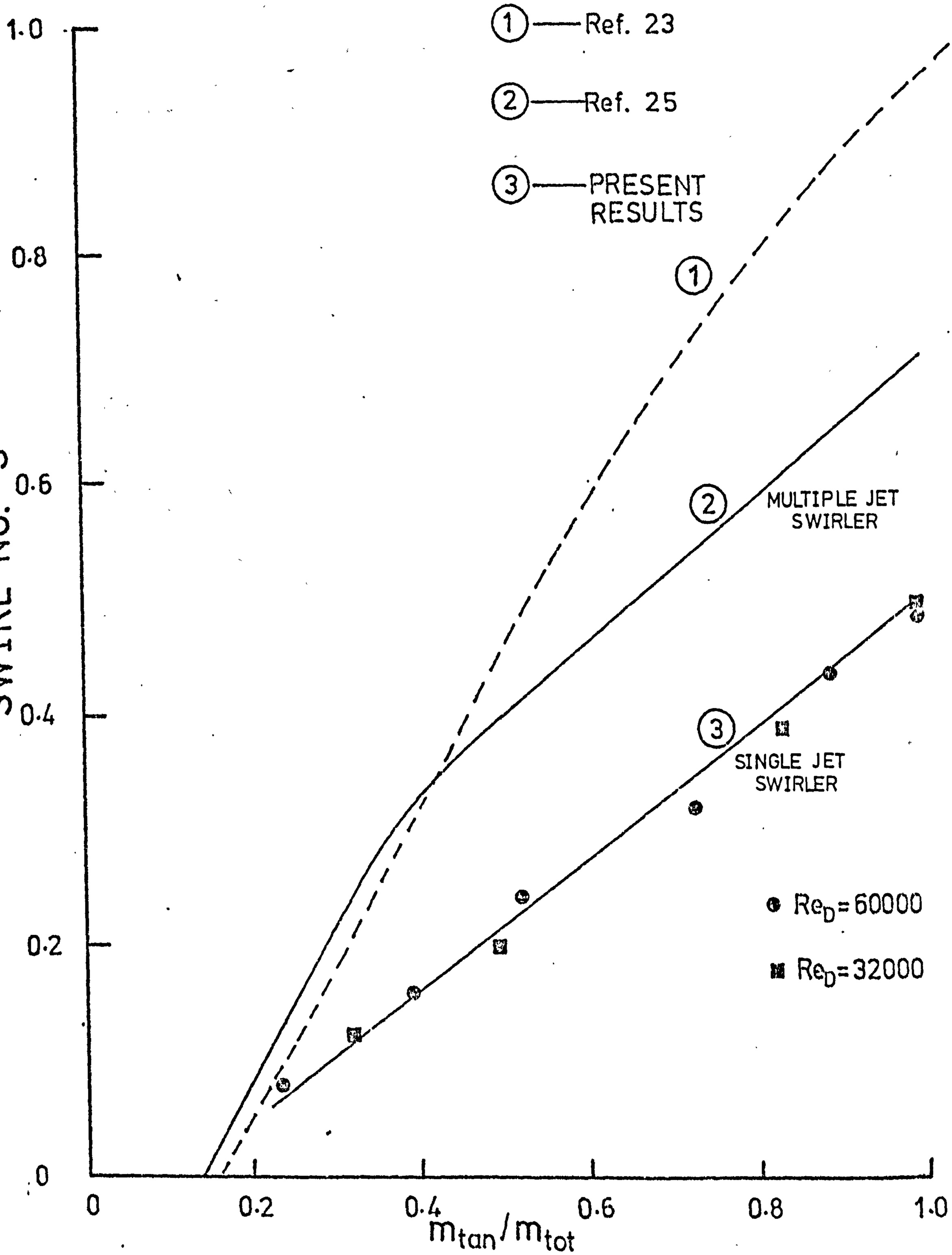

Fig. 5.8 SWIRL NUMBER AS A FUNCTION OF TANGENTIAL & TOTAL MASS FLOW RATES

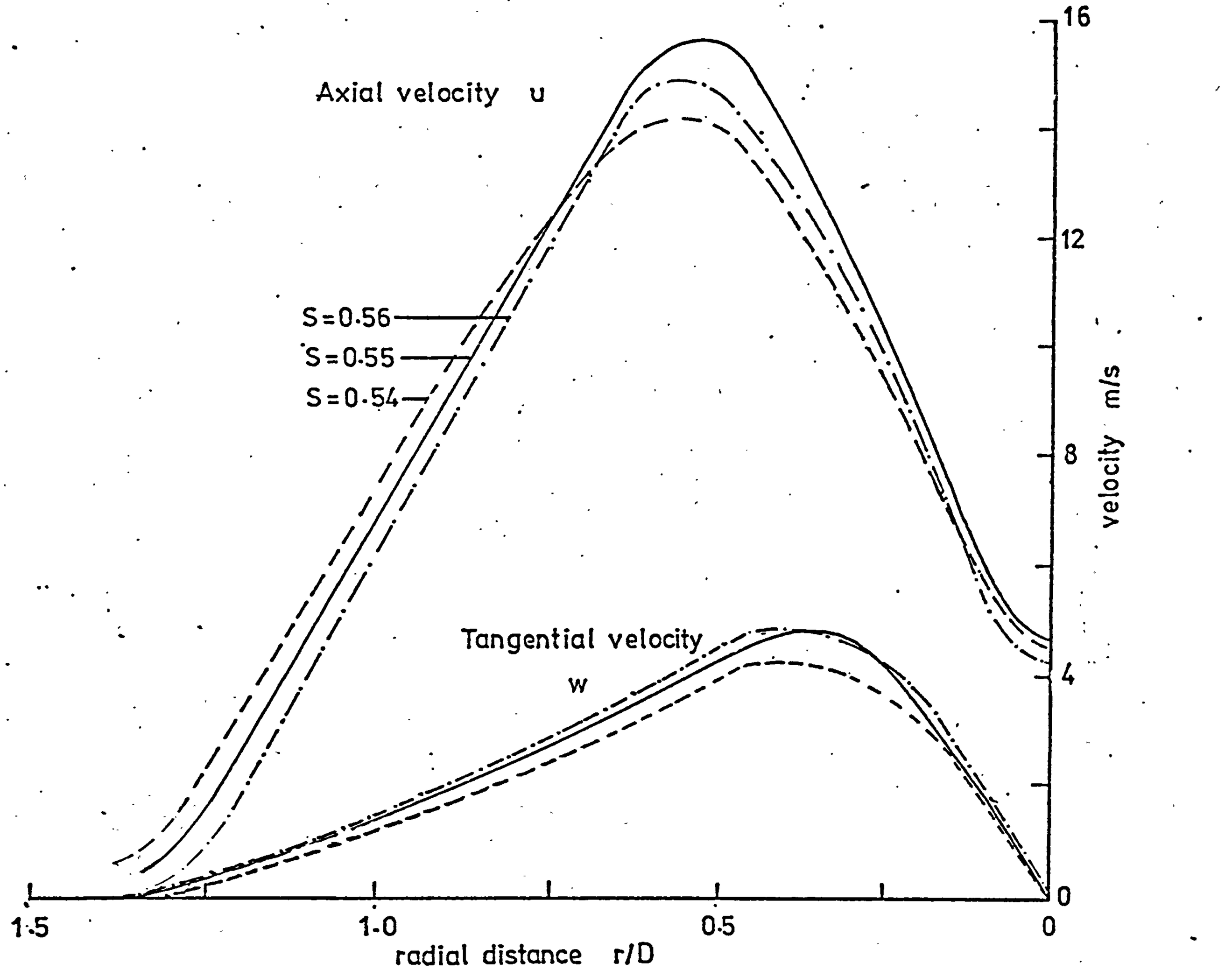

Fig. 5.9 COMPARISON OF VELOCITY PROFILES FOR THREE RANDOMLY PICKED SWIRLERS.

CHAPTER 6

HOT-WIRE ANEMOMETRY

6.1 INTRODUCTION

The rate of heat transfer in the impingement region of a jet is dependent on the turbulence characteristics of the flow. The application of swirl changes these characteristics so that it was considered necessary to measure turbulence levels in the present jets. Detailed measurements of turbulence in three dimensional flows (such as those associated with swirling jets) are complicated and lie beyond the scope of the present work. Therefore, only limited measurements were undertaken for the single jet set-up. The resultant knowledge of the turbulence characteristics has been used as an aid in interpreting the heat transfer results near the stagnation point. These heat transfers, if quoted without any reference to the turbulence levels, can be misleading.

Several techniques have been developed for the investigation of turbulent flow fields including hot-wire, pulsed-wire and Laser-Doppler anemometry and also Glow and Corona discharge methods (Ref.76). Amongst these, the use of hot-wire probes is established and used most extensively, although of late Laser-Doppler techniques are finding increasing applications. A hot-wire anemometer has been used in the present work, mainly because of its availability and relative ease of operation. Refs.(56) and (77) have employed this instrument at Cranfield whilst investigating swirling and recirculating flows. These workers, together with Ref.(76), may thus be consulted for the details of this technique. However, in this chapter the basic principles and method of application of the hot-wire anemometer are discussed briefly for the sake of completeness.

The use of the anemometer to measure the turbulence levels also yields the components of the flow velocity vector. These results thus provided corroboration of the earlier five-hole probe measurements as well as offering additional data concerning the rate of decay of the velocity along the jet axis.

6.2 BASIC PRINCIPLES OF HOT-WIRE ANEMOMETRY.

The hot-wire probe essentially consists of a very thin, electrically heated tungsten wire (approximately 5μm in diameter) supported between two prongs (see Figure 6.1(a). The basic principle of the instrument is that the rate of heat transfer from this wire can be related to the fluid velocity. The mean and the r.m.s. value of the fluctuating rates of heat transfer are then indicated in the form

of two separate voltages. The probe head (i.e. the wire and the supporting prongs) is normally sufficiently small so as not to cause any serious disturbance to the flow. Furthermore, the probe has a short response time and this, together with its sensitivity, renders it suitable to measure 'instantaneous' velocities in turbulent flow fields.

The electrically heated wire is made one of the arms of a Wheatstone Bridge. The system can be operated in either the constant current or the constant temperature (resistance) mode. This latter mode of operation is widely used since the constant current technique results in considerable fluctuations in the wire temperature, thus disturbing the calibration. Moreover, the frequency response in the constant current mode is limited by the thermal inertia of the wire. Details of the constant current mode of operation are presented in Ref.(76).

By operating at a constant wire temperature (resistance), the effect of the thermal inertia of the probe is minimised. Figure 6.2 illustrates the connections for a hot-wire device operated in the constant temperature mode. The probe resistance and, hence, its temperature is kept constant by maintaining the bridge in balance. Any instantaneous out-of-balance in the bridge generated due to the fluctuations in the flow is rapidly corrected by the amplifier circuit. The amplifier is polarised so that a decrease in the probe resistance due to extra cooling results in an increase in the amplifier output current. The square of this current, or its associated voltage drop, is a measure of the rate of power dissipation from the wire. The feedback principle used in the anemometer makes it especially suited for the measurement of high frequency flow fluctuations. Without this feedback, the upper frequency limit is restricted to about 100 Hz by the thermal capacity of the probe. This response is improved to an upper frequency limit of 85 KHz for a 5μm tungsten probe in systems with feedback.

For a particular probe at a constant temperature, the convective heat loss from the wire depends on the surrounding fluid velocity, density and temperature. If the density and temperature are constant, the probe heat loss is a function only of the velocity of the fluid. In principle, this rate of heat loss can be related analytically to the velocity from a knowledge of the momentum and energy equations for a two-dimensional laminar flow around an 'infinitely' long circular wire. However, the actual heat transfer-velocity relationship deviates from this ideal due to the finite l/d (length/diameter) ratio of the wire, the conductive heat leak to the prongs, and also due to natural convection and radiation effects. Furthermore, the probe geometry is subject to slight variation during manufacture so that a universal calibration cannot be applied. Thus, for each individual probe

the relationship between the rate of heat loss and the flow velocity is obtained experimentally.

The earliest type of relationship discussed in the literature is King's law (Ref.78), namely:-

$$Nu = A + B\ u^{0.5} \qquad (6.1)$$

A and B are experimentally determined constants and the Nusselt number, Nu, is a measure of the rate of heat loss.

Since the heat loss in the hot-wire is measured in the form of a voltage, King's law can be re-written as:-

$$E^2 = A' + B'\ u^{0.5} \qquad (6.2)$$

The validity of the dependence of the heat transfer on the square root of the velocity has been the subject of subsequent investigation (Ref.76). An improved expression has been suggested, namely:-

$$E^2 = a + b\ u^n \qquad (6.3)$$

where 'u' is effective cooling velocity normal to the wire, and 'n' is a constant varying between 0.45 to 0.5 over a wide range of Reynolds numbers.

As a further improvement, Siddall and Davies (Ref.79) have proposed the use of a second order equation so that:-

$$E^2 = a' + b'\ u^{\frac{1}{2}} + c'\ u \qquad (6.4)$$

This relationship was found to provide a better fit over a wider velocity range (0 - 160 m/s).

The hot-wire probes are directionally sensitive, i.e. their calibration is dependent on the orientation of the probe. Various emperical relations, e.g. the cosine law, have been proposed to relate the 'effective cooling velocity' to the velocity components in the flow field. For the generalised three dimensional case, the effective cooling velocity can be expressed by the relationship:-

$$U^2 = u^2 + G^2v^2 + K^2w^2 \qquad (6.5)$$

where 'u', 'v' and 'w' are the three velocity components; G and K are probe constants in the 'v' (perpendicular to the wire) and 'w' (along the wire) directions respectivcly.

For the miniature DISA probes, G and K are typically around 1 and 0.25 respectively.

6.3 USE OF HOT-WIRE ANEMOMETRY IN FLOW FIELDS.

The hot-wire probe responds according to the relationship of the form:-

$$E^2 = f(U)$$

where f(U) is the function containing the experimentally determined calibration constants for the probe.

Various types of probes can be used to evaluate the turbulence properties (depending on the flow field and the information required). The simplest is the measurement of turbulence in one-dimensional flow with turbulence intensities less than 20%. In these cases, a single straight wire probe is employed, see Figure 6.1(a). The turbulence intensities and the mean velocity can be found (assuming King's law applies) by the following expressions:-

$$\sqrt{\frac{\overline{u'^2}}{\overline{U}}} = \frac{4(\overline{E'^2})^{\frac{1}{2}}\overline{E}}{\overline{E}^2 - E_0{}^2} \quad \text{and} \quad \overline{U} = \left(\frac{E^2 - A}{B}\right)^2 \qquad (6.6)$$

where $\overline{U}$ is the mean velocity, $\overline{E}$ is the probe mean 'output' voltage, $(\overline{U'^2})^{\frac{1}{2}}$ and $(\overline{E'^2})^{\frac{1}{2}}$ are the r.m.s. values of velocity and voltage, and the subscript '0' refers to the zero velocity condition.

In the case of two dimensional flow situations (e.g. in boundary layers) where $(\overline{u'^2})^{\frac{1}{2}}/\overline{U}$ and $(\overline{v'^2})^{\frac{1}{2}}/\overline{U}$ are required, the so-called 'X' type of probe (Fig.6.1(b)) can be employed. Separate anemometer units are required for each wire of the probe which is orientated so that the velocity 'U' bisects the angle between the wire. The details of the use of this type of probe can be obtained from Klatt (Ref.80). The slanting 45° type probes (Fig.6.1(c)) can also be used to study these flow fields (Ref.81).

In more complicated cases, such as swirling flows, a direct approach using a three dimensional probe (Fig. 6.1(d)) can be used. This probe has three mutually perpendicular wires each connected to a separate anemometer unit. Inaccuracies can arise due to interaction of the thermal wakes unless the mean velocity vector lies within the octant formed by the wires. This method can be unattractive because of its comparatively low spatial sensitivity, the necessity for pre-knowledge of the flow field, and also the need for three anemometer units.

Methods requiring several orientations of the probe at a particular station have also been developed. Two such examples (developed to study highly turbulent flows) using this technique are discussed in Refs. (82) and (83). Two probes are used, a 45° slanting probe together with

a straight probe. The instantaneous velocity vector is calculated from a set of six measurements (six orientations). The disadvantage of these 're-orientation techniques' may be summarised as follows:-

(i) The flow state may alter during the measurement.

(ii) The two probes may not be placed at exactly the same station after re-orientation, and

(iii) The method assumes that all six voltages are regular, are of similar frequency distribution, and are in phase.

Hoffmeister (Ref.84) has discussed a method whereby a single 'slant wire' probe can be employed to determine the three velocity components and all six Reynolds stresses by rotating the probe to successive orientations.

Beer and Chigier (Ref.23) suggested using a single straight wire probe at four different orientations. This method was selected for the present work because of its relative simplicity since it utilizes only a single probe/anemometer unit. This method requires at least a broad knowledge of the flow field so that the probe can be aligned such that the main velocity component is always perpendicular to the hot-wire. In the present work, the five-hole probe measurements provided this initial velocity information.

6.4 THE TECHNIQUE USED IN THE PRESENT STUDY.

As mentioned in the previous Section, a simple straight probe was employed at four different orientations. This method assumes:-

(i) The turbulence is 'stationary', i.e. the state of the flow at a point in the field does not change from one orientation to the other. Additionally, the flow should be homogenous and at a constant temperature.

(ii) The voltage signal at each measurement is assumed to be of similar wave form and frequency. The shape of the wave form (assumed square in the present case) makes little difference.

(iii) The relationship between the voltage drop along the wire and the effective cooling velocity normal to the wire is assumed to obey King's Law.

(iv) The effective cooling velocity is expressed by Equation 6.5 (Section 6.2). The compon-

ent 'u' is the largest component of the velocity vector and the probe is aligned so as to be perpendicular to this component.

The determination of the velocity components and turbulence intensities are described in detail in Ref.(23). However, a brief description of the response Equations and the evaluation of the velocities and turbulence is given in Appendix B.

6.5 EXPERIMENTAL PROCEDURE

6.5.1 Setting-up of the hot-wire probe.

The probe used in the present tests was a DISA 55P11 probe with a single, straight, 5μm diameter tungsten wire as the sensing element. This was used in conjunction with the following DISA equipment:-

a 55 D01 type anemometer.

a 55 D31 DC digital voltmeter.

a type 55 D35 r.m.s. voltmeter.

a 55 H30 shortening probe, and

a 55 D25 auxilliary unit which was applied in the square wave test.

The hot-wire anemometer was operated in the constant temperature mode according to the instructions of DISA operating manual (Ref.85). The probe is operated at a temperature of about 300C. A square wave test was performed initially to check for any oscillations generated by poor bridge balance or by the choice of an unsuitable amplifier bandwidth. The upper frequency of the probe response in the present tests was found to be about 40 KHz.

6.5.2 Probe Calibration

Before carrying out the experimental measurement on the swirling jets, the hot-wire probe was calibrated to determine the constants in the King's Law expression, see Section 6.2. This was achieved by placing the hot-wire probe adjacent to a small pitot probe in the potential core of a low turbulence jet (turbulence intensity about 2%). The rate of flow and, hence, the velocity of the jet was varied and the corresponding voltage noted. Figure 6.3 presents the resultant plot between the square of the voltage and the square root of mean velocity. The values for A' and B' were found by a curve fitting procedure (based on the least squares method) and were 7.58 and 2.64 respectively. The range of velocity over which Equation 6.2 applies satisfactorily varies

from 1 - 50 m/s.

6.5.3 Direction Sensitivity of the Probe.

Tests were also carried out to determine the directional sensitivity of the probe in the yaw and pitch directions. These measurements were also made in the potential core of the jet and the resultant probe voltage drops were plotted against the jet velocity. Values of the constants G and K in Equation (6.5) were determined by comparison of the velocities producing a particular voltage, as shown in Figure 6.4 For the probe used in this investigation, G = 1.023 and K = 0.26, and these are similar to those quoted for DISA miniature probes (see Section 6.2).

6.5.4 Measurements in the Swirling Jets (single jet).

The hot-wire probe was mounted on a slide mechanism and traversed along a radial line across the jet. The probe was held so that the wire was perpendicular to the axis of the jet, i.e. perpendicular to the main velocity component. The mean voltage (D.C) and the fluctuating voltage (r.m.s.) were recorded at each measurement station with probe orientation of 0, 45, 90 and 135 degrees, see Appendix B.

The swirl was varied in steps from 0 (no swirl case) to 0.48 (the maximum swirl) for both the Reynolds numbers employed in this work. Nozzle-to-target spacings (z/D of 0, 2, 4 and 8 were studied for Re_D = 32,000 and 0, 2 and 4 were investigated for Re_D = 60,000. These latter readings were used basically to confirm the trends found at the lower Reynolds number. The traverse at each plane covered the whole radial field of the jet (including the spread).

A 650 step programme was written for a WANG 600 programmable desk calculator to calculate the velocities $\overline{u'}$, $\overline{v'}$ and $\overline{w'}$, and the turbulence components $\overline{u'^2}$, $\overline{v'^2}$ and $\overline{w'^2}$ from the four sets of values for the mean and r.m.s. voltages at each measurement station.

6.6 RESULTS AND DISCUSSION

As mentioned previously, the measurements of velocity and turbulence intensity were of a limited nature and did not allow detailed comparisons with previously published data. The similarity equations quoted in the published literature were also often not applicable since many of the present measurements were undertaken relatively near to the nozzle exit. In this region, the velocity and turbulence intensity profiles are dependent on the type and geometry of the nozzle so that similarity is not yet established.

However, the present results are self-consistent and limited comparisons have been drawn wherever possible.

The present jets were essentially symmetrical so that, in general, results are only presented for one-half of the field.

6.6.1 Velocity Measurements

Radial distributions of both axial and tangential velocities are presented at different axial distances from the nozzle exit for jets of varying swirls in Figures 6.5 to 6.10. These velocities have been normalised by dividing by the centreline nozzle exit velocity (in the non-swirling case). The radial distances from the axis of the jet have also been normalised in terms of the diameter of the jet. Results are presented for both the jet Reynolds numbers examined in this study (i.e. Re_D = 32,000 and 60,000). The velocity profile at the exit section, for a non-swirling jet, is of the form expected for a turbulent jet, see Figure 6.5. Moreover, it is also apparent from this same diagram that, as the swirl number is increased up to about 0.36, the axial component at the nozzle exit of the velocity is relatively unaffected. This has also been observed by Rose for S = 0.23 (see Fig.25, Ref.62). At the maximum swirl presently studied, S = 0.48, the shape of the jet exit velocity is shifted from the axis of the jet, thus resulting in characteristic 'double-peak' profile.

Downstream from the nozzle exit at z/D = 2, the differences between the swirling and non-swirling jets are more apparent even at the lowest value of swirl number, S = 0.12, see Figure 6.6. The velocity profile becomes flatter as the swirl number is increased up to S = 0.36. The 'double-peak' is still present at S = 0.48, although it is somewhat less pronounced. At z/D = 4, see Figure 6.7, these trends are continued and, even for the highest swirl number studied (S = 0.48), a virtually flat velocity profile is observed. The potential core still exists in the non-swirling case so that $u/u_e = 1$. However, this ratio has been reduced to 0.6 for S = 0.12 and to 0.25 at the maximum swirl. At z/D = 8 (Fig.6.8), the flatness of the profiles of axial velocity are even more apparent. Similar characteristics are also displayed in the presentation for Re_D = 60,000, see Figures 6.9 and 6.10.

Apart from the change in the shape of the axial velocity profile, Figures 6.5 to 6.8 also show that, in the non-swirling jet, the potential core ceases between z/D = 4 and 8 (i.e. probably at z/D = 5 approximately). This is in accord with the observations of

earlier researchers (see Gauntner et al, Ref.27). However, with the swirling jets, the more rapid rate of mixing results in an earlier breakdown of the potential core so that, even with swirl number S = 0.12 (i.e. the lowest studied), the value of maximum velocity has decreased to about 0.9 u_e at z/D = 2. This corroborates the observations of Chigier and Chervinsky (Ref.58) who found that the potential core is non-existent at about z/D = 2 even at weak swirls.

Radial variations of the tangential (or swirl) velocity for various swirls at Re_D = 32,000 are presented in Figures 6.11 to 6.13 at z/D = 0, 2 and 4 respectively. The values at the nozzle exit, see Figure 6.11, show considerable scatter. This large scatter is probably in part due to the limitations in the measurement technique which requires alignment of the probe perpendicular to the greatest velocity component. At the exit plane (especially for the higher swirls), the tangential velocity could be of the same order as the axial velocity so that this requirement is difficult to fulfil. Moreover, the radial rate of change of the tangential velocity can be high at the nozzle exit with consequent errors in hot wire response. The expected typical characteristic profile of the swirl velocity 'w', (i.e. the Rankine type of vortex), can be seen in Figures 6.11 to 6.13. Near the axis of the jet, 'w' varies as in a forced vortex ($w \alpha r$), and in the outer regions (r/D > 0.25), it varies as in a free vortex ($w \alpha 1/r$). The swirl component decays rapidly along the jet axis so that at z/D = 8, the velocities are fairly low (1 m/s or less) and it is difficult to distinguish the effects of changes in swirl. Thus, these distributions are not illustrated. The variation in tangential velocity at the higher Reynolds number (60,000) exhibited similar trends to those reported at Re_D = 32,000 and have, therefore, also not been presented in this thesis.

The present hot-wire results and those obtained earlier by the five-hole probe measurements are in good agreement, see Figures 6.14 and 6.15. The comparatively small differences in the profiles can be attributed to experimental error. These differences in the velocity profile, however, would not seriously affect the calculation of the swirl number. This was found to be the case when the slightly different velocity profiles for the three multiple jet swirlers were integrated in the previous chapter, see Figure 5.9.

To determine the 'apparent' origin of the jet, the inverse of the maximum velocity ($1/u_m$) was plotted against z/D for the jets of various swirl numbers,

see Figure 6.16. Extrapolating the non-potential part of these plots indicated that the origin 'a' was 1.8 nozzle diameters upstream of the nozzle exit. The position of this 'origin' of the jet was independent of the degree of swirl as reported previously by Ref.(58). Figure 6.16 also illustrates the differences in the mixing characteristics of the jets due to variation in swirl. The rate of mixing, as discussed earlier in this Section, increases as the degree of swirl is increased, e.g. at z/D = 4, for S = 0, the centreline velocity has not decreased whereas, for S = 0.36, it has already been reduced to 0.41 u_e.

The relative rates of decay of the maximum axial and tangential velocities with axial distance 'z' from the exit of the nozzle are shown in Figures 6.17 and 6.18 respectively. The present results are in good agreement with similar curves replotted from Refs. (23) and (33). The tangential velocities decay much more rapidly, see Figure 6.18. According to several earlier workers, e.g. Refs. (23), (62) and (72), the rate of decay for the axial velocity is proportional to 1/z, while the tangential velocity decays as $1/z^2$.

Chigier and Chervinsky (Ref.58) have shown that for a swirling jet the rapid rate of mixing results in similarity of the axial and tangential velocity profiles even at axial distances as small as two nozzle diameters from the exit (or even less for the tangential component). This has been illustrated in Figure 3.6. Similar plots of the present axial velocity measurements are presented in Figure 6.19. For comparison purposes, the lines obtained using an empirical equation suggested by Ref.(58) are also included, see Equation (3.5), Section 3.4. In the present case, similar radial profiles of axial velocity are achieved except for the lower swirls (i.e. S = 0.12 and 0.24) near the nozzle exit at z/D = 2. Thus, the empirical equation (Equation 3.5) can be used (to a good approximation) to predict the behaviour of the present jet except at z/D=2. This, however, as expected does not apply to the non-Gaussian velocity distributions under high swirl conditions (e.g. S = 0.48 for the present case).

Figure 6.20 presents the results for the tangential velocity profiles for S = 0.36 and 0.48 similar to those for the axial velocity in Figure 6.19. The values of 'w' for all other cases (swirl numbers) were comparatively small, particularly at z/D = 8, so that it was not possible to obtain reasonable plots. The empirical relationship suggested by Chigier and Chervinsky (Ref.58) for tangential velocity were not generally applicable. However, the

present figures, although plotted with fewer points, broadly agree with those shown in Figure 3.6(b) for similar swirl numbers.

6.6.2 Turbulence Characteristics

The turbulence intensities in this Section of the thesis are based on the mean velocity, u_e, at the centreline of the exit of the nozzle for the non-swirling case. The choice of this velocity as a reference is appropriate since it provides a common base so that turbulence intensities can be readily compared at various sections.

For the non-swirling jets, the turbulence intensity along the centreline of the jet increases from the nozzle exit to z/D = 6, and then subsequently decreases. This behaviour is similar in trend to that observed by Corrsin (Ref.32), see Figure 6.21. Any differences in the numerical values arise because of the dissimilar turbulence levels at the exit section and different jet Reynolds number.

Figures 6.22 to 6.26 present the radial variations of the longitudinal turbulence fluctuations $\sqrt{\overline{u'^2}}$ at various axial distances downstream from the nozzle exit for both the non-swirling and swirling jets. The longitudinal turbulence intensity $\sqrt{\overline{u'^2}}/u_e$ was used in this case instead of the usual turbulence intensity

$$Tu = \sqrt{\left(\frac{\overline{u'^2} + \overline{v'^2} + \overline{w'^2}}{3}\right)}/u_e$$

primarily because of the erratic behaviour of the measured $\overline{v'^2}$ and $\overline{w'^2}$ at some of the measurement stations. Most of this scatter occurred near the exit of the nozzle (z/D = 0,2) and can probably be attributed to the steep 'v' and 'w' velocity gradients in this region. It may be recalled that the scatter in the measurements for 'w' at the nozzle exit were discussed earlier.

In the non-swirling case, Figure 6.22, it is again apparent that the centreline longitudinal turbulence intensity increases with z/D, initially followed by a subsequent decrease. As the jet expands, the radial distribution of longitudinal turbulence intensity is fairly uniform. Measured values of the longitudinal turbulence at Re_D = 60,000 are also shown and exhibit similar trends.

As the degree of swirl is increased to S = 0.12, there is a rise in the level of turbulence at all sections except z/D = 8, see Figure 6.23. The centreline values of the longitudinal turbulence increased from 5% to 10% at nozzle exit, whilst at z/D = 2 the level

rose from 10% to 17%. The profiles also tend to be more uniform.

Figures 6.24 to 6.26 present similar curves for the other swirls studied in this investigation, i.e. S = 0.24, 0.36 and 0.48. The profiles for S = 0.24 and S = 0.36 are fairly uniform for all z/Ds. In the case of the highest swirl (see Fig.6.26), the maximum turbulence (at z/D = 2) is offset from the centreline to a radial position which approximately coincides with that of the maximum velocity (see Fig.6.6). However, as with the velocity profiles, the turbulence intensities become more uniform as the distance from the nozzle is increased. Figure 6.27 has been plotted at z/D = 4 to illustrate the effects of varying swirl on the turbulence intensities.

Despite the uncertainties of the values of the radial and circumferential turbulence intensities, it was possible in most instances to evaluate the overall turbulence intensity

$$Tu = \sqrt{\frac{(\overline{u'^2} + \overline{v'^2} + \overline{w'^2})}{3}}/u_e$$

Thus, 'Tu' at the radial position corresponding to the maximum velocity is plotted in Figure 6.28 against the axial distance from the nozzle exit. To obtain these overall intensities, the uncertainties in the values of $\overline{v'^2}$ and $\overline{w'^2}$ were corrected by assuming that the behaviour (radial variation) of these fluctuations is similar to that of the longitudinal intensity. This assumption would appear to be justified since it has been shown for both swirling (Ref.72) and non-swirling jets (see Fig.7, Ref. 33) that, for all three fluctuations, the shape of their radial variations is similar, e.g. see Fig. 6.29). This is also corroborated by most of the present measurements in which radial variations (particularly at z/D = 4 and 8, i.e. stations where the measurements of $\overline{v'^2}$ and $\overline{w'^2}$ were reliable) were found to be of similar shape for all three components. Figure 6.30 has been plotted to show the behaviour of the turbulence fluctuations for two particular cases at S = 0.36. It may be seen that, even at z/D = 2, the values as well as shapes of the fluctuations are quite similar. At the greater downstream distance, the value of $\overline{u'^2}$ is greater than $\overline{v'^2}$ and $\overline{w'^2}$ but the profiles still have similar shapes.

As can be seen from Figure 6.28, the turbulence characteristics of swirling jets are quite difference from those of non-swirling flows. The turbulence intensity even for the smallest swirl studies, i.e. S = 0.12, attain a maxima at approximately z/D = 2

and then decreases whereas the non-swirling jet attains a maxima around z/D = 6. The swirls S = 0.24 and 0.36 behave similarly, being constant up to about z/D = 2 and then decreasing montonically. With the highest swirl S = 0.48, maximum turbulence intensity ensues at the nozzle exit and, subsequently, decays along the axis of the jet.

Rose (see Fig.32, Ref.62) has shown that the decay of $\sqrt{\overline{u'^2}}/u_e$ is proportional to 1/z over most of the z/D range studied, i.e. 0 to 100. Detailed comparisons of the present result with Rose's were difficult because of the limited z/D range (0 to 8) studied. However, in Figure 6.31 the present results for S = 0.24 and 0.36 at Re_D = 32,000 are plotted together with Rose's curve for a swirl number of 0.23 at Re_D = 14,000. The trends of these different measurements are similar although the maxima are displaced. Conditions near the nozzle exit are particularly sensitive to detailed design features so that variations in nozzle geometry and methods of generating swirl may well explain any difference.

6.7 CONCLUSIONS ON THE VELOCITY AND TURBULENCE MEASUREMENTS.

6.7.1 Velocity Measurements.

1. The present results suggest that both five-hole probes and hot-wire anemometry can be employed successfully to study flow patterns associated with the swirling jets and characterise the swirl generators.

2. The limited data obtained indicated that the potential core for non-swirling jets extended up to about five nozzle diameters from the exit whereas, even for weak swirls, the length of this core was approximately two nozzle diameters. This reduction is associated with more rapid mixing of the jet with the surroundings due to the application of swirl.

3. The profiles of axial velocities are flatter and, hence, more uniform when swirl is applied except at the highest swirl, S = 0.48, near the nozzle exit. In this situation, typical 'double maxima' types of profile are observed.

4. The radial profiles of tangential velocity exhibit the characteristics of a Rankine type of vortex.

5. The rate of downstream decay of axial velocity is greater for the swirling jets; moreover, the tangential velocities decay at a higher rate

than the axial velocities. The decay of both axial and tangential velocities increases with the degree of swirl.

6.7.2 Turbulence Characteristics.

1. The present measurements of turbulence intensity along the centreline of the jet in the 'no-swirl' case are in good agreement with previous published data.

2. Increasing the degree of swirl can, in many instances, increase the turbulence intensity although this does not necessarily imply that swirling jets always have higher turbulence intensities at all measurement stations. The jets with the higher turbulence intensity at the exit section can decay at a faster rate so that at z/D = 8, as shown in Figure 6.28, the non-swirling flow (with lowest initial turbulence) exhibits the highest turbulence.

3. The decay of turbulence intensity behaves in a similar fashion to the axial velocity decay, i.e. it varies as 1/z approximately.

6.8 GENERAL CONCLUSION

The present jets behave in a very similar fashion to other jets used by previous investigators. Consequently, any heat transfer measurements will have general applicability and will only differ in detail due to the design of the swirler.

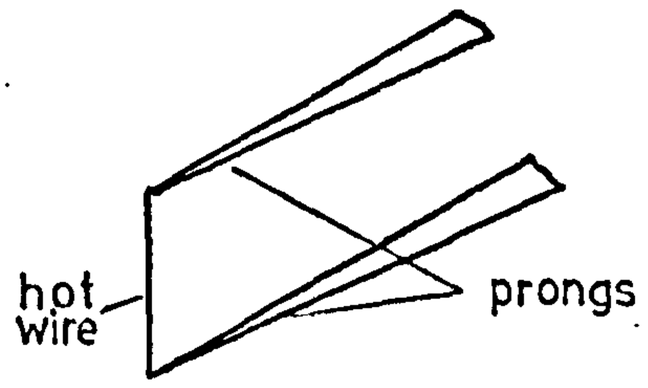

(a) Straight general-purpose type

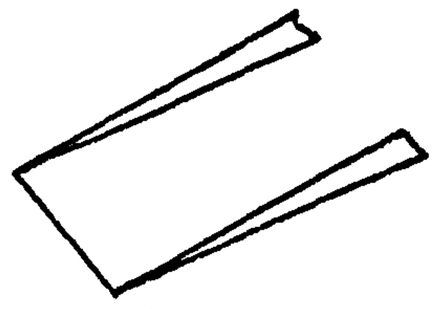

(b) 45° Slanting sensor type

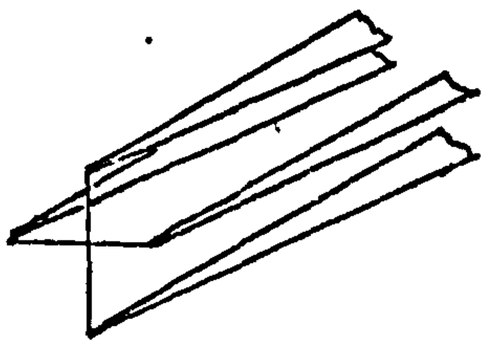

(c) X-array probe

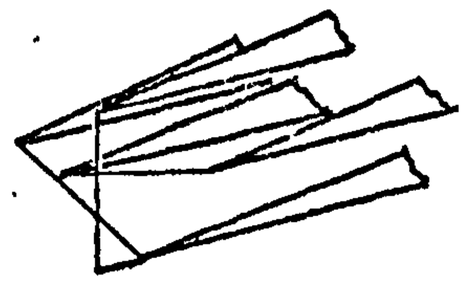

(d) Triple sensor probes

Fig 6.1 VARIOUS CONFIGURATIONS OF HOT-WIRE PROBES.

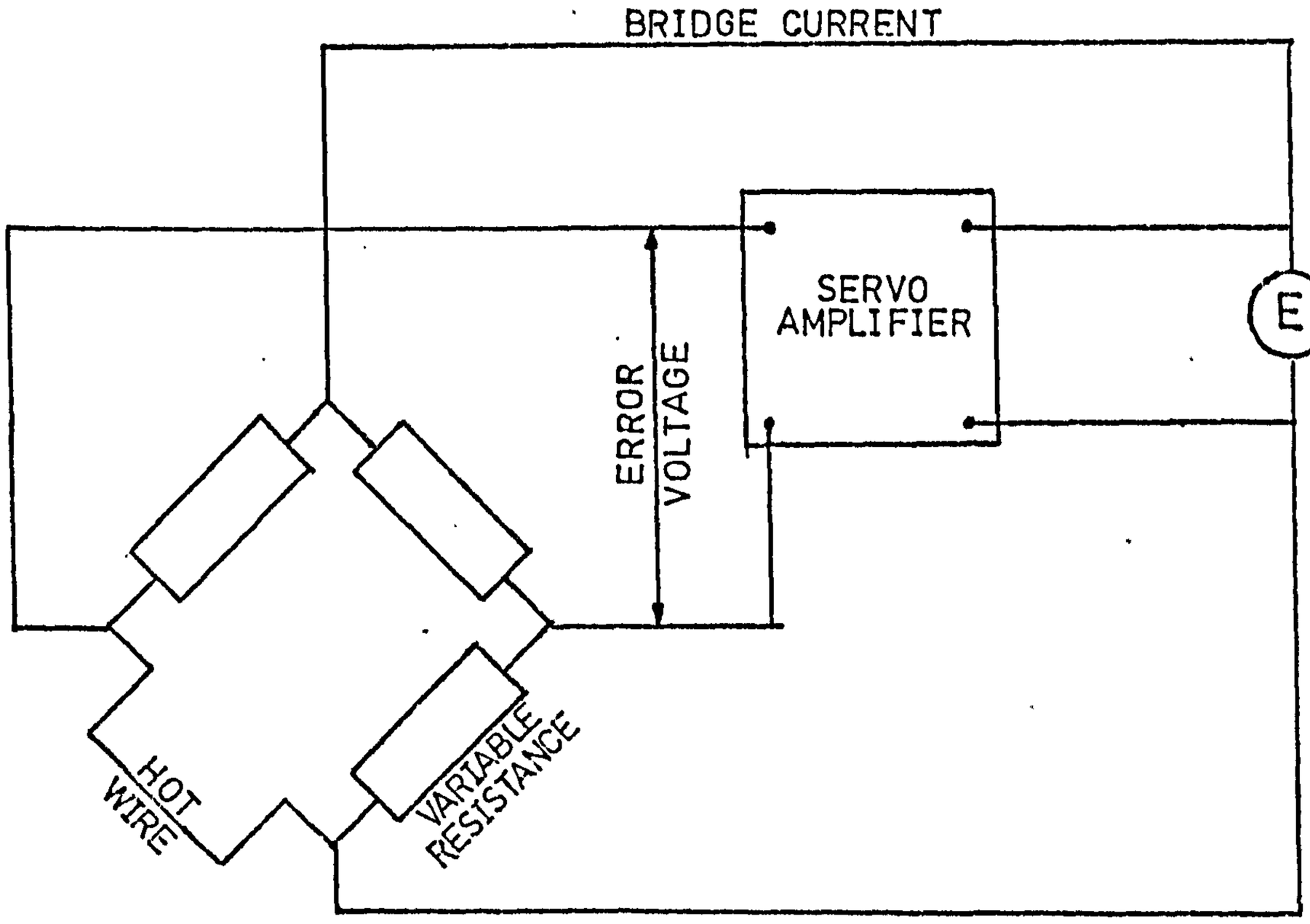

Fig. 6.2 CONSTANT TEMPERATURE CONNECTION FOR THE HOT-WIRE PROBE.

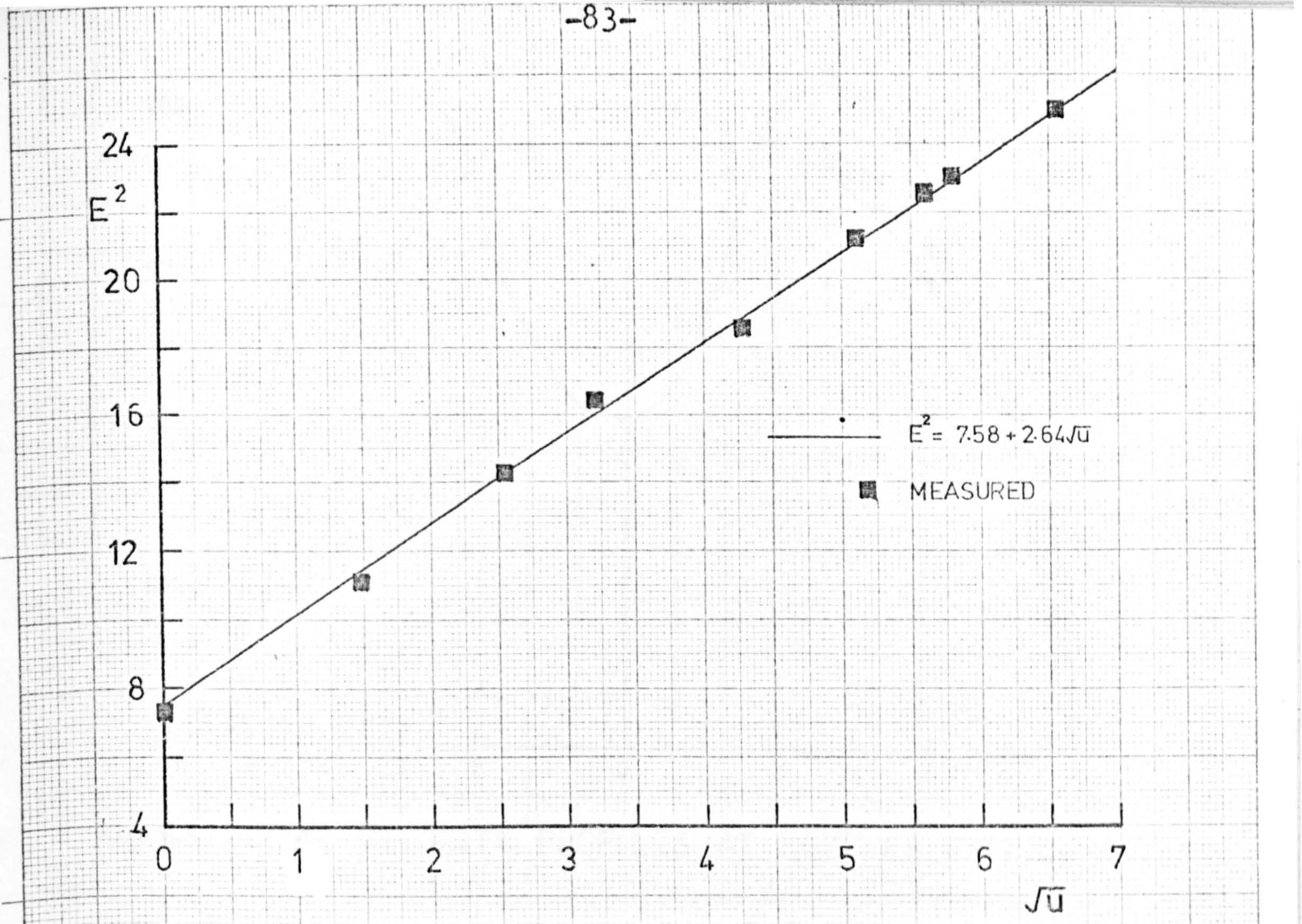

Fig. 6.3 CALIBRATION CURVE FOR THE 'u' DIRECTION

Fig. 6.4 CALIBRATION CURVES FOR THE THREE MUTUALLY PERPENDICULAR DIRECTIONS

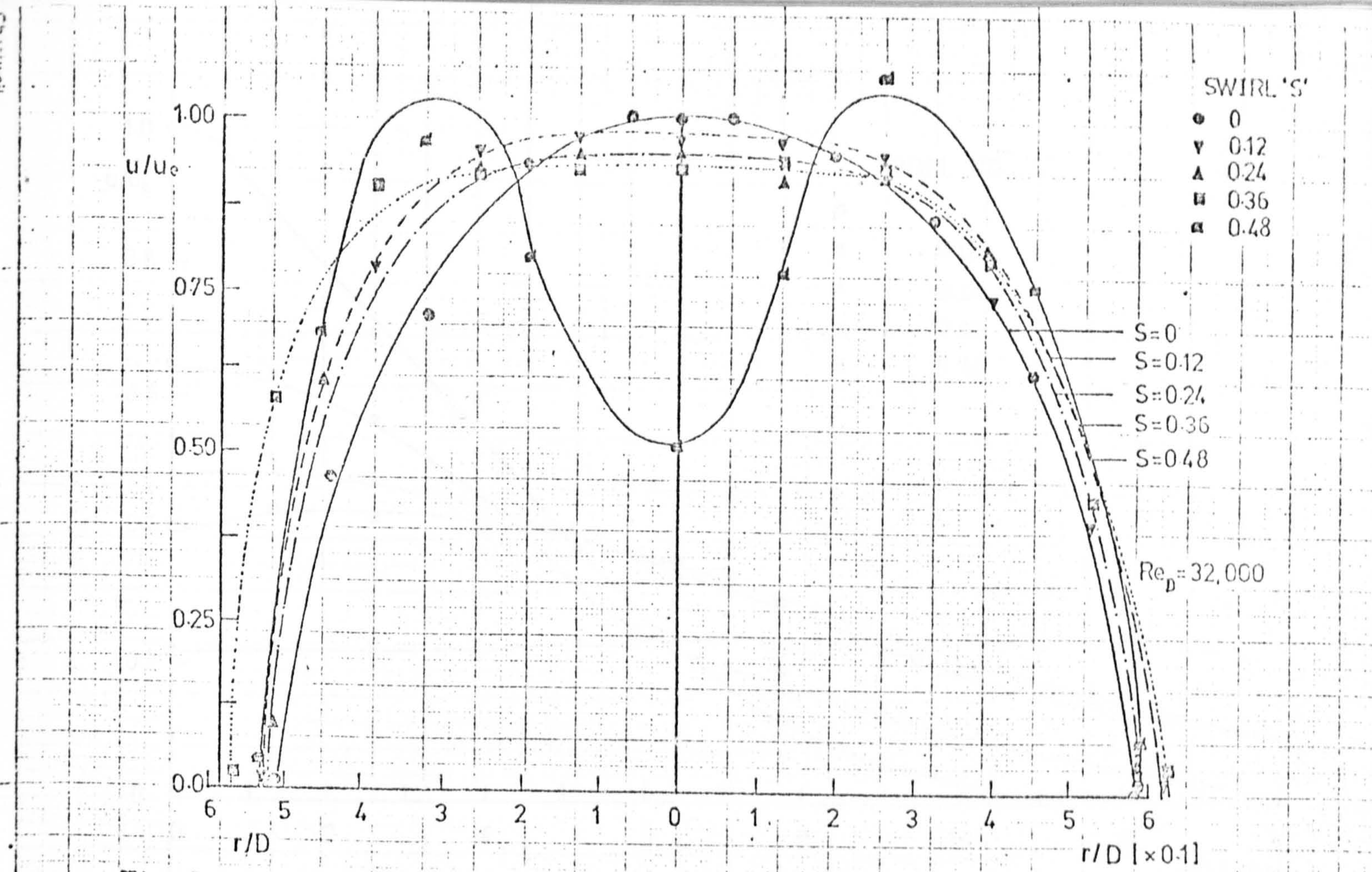

Fig. 6.5 AXIAL VELOCITY PROFILES AT NOZZLES EXIT (i.e. z/D = 0)

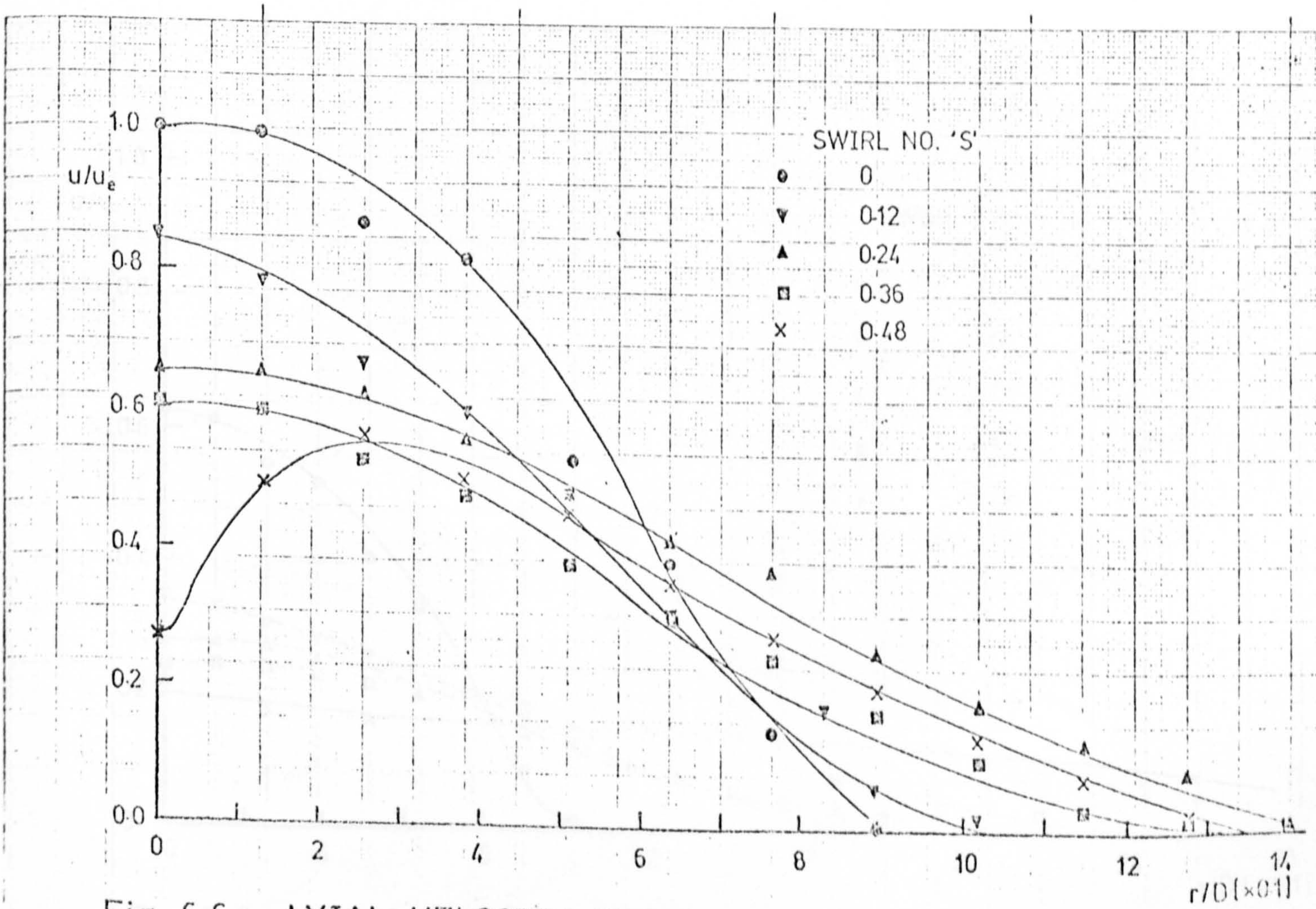

Fig. 6.6 AXIAL VELOCITY PROFILES AT z/D = 2 — Re_D = 32,000

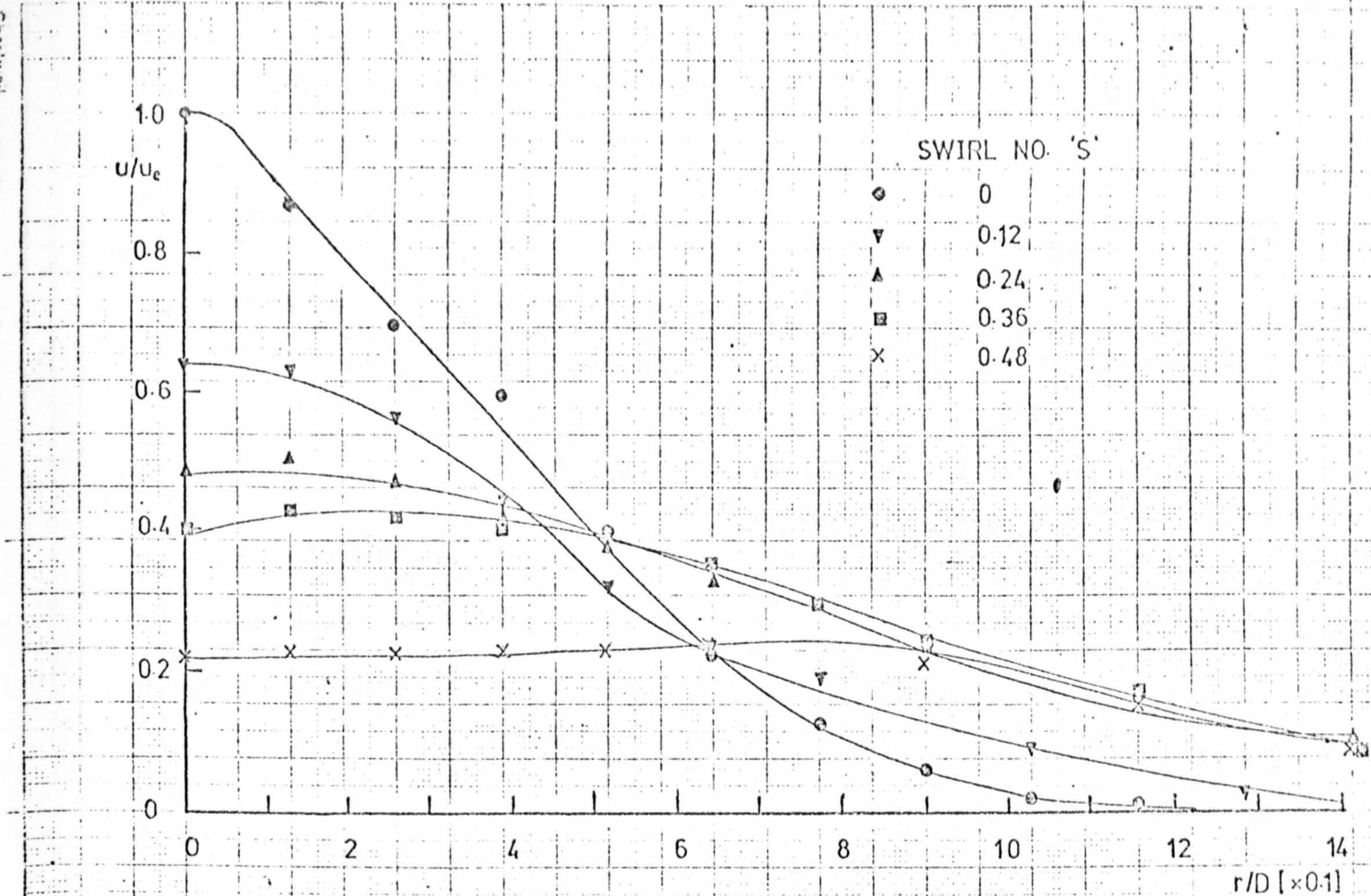

Fig. 6.7 AXIAL VELOCITY PROFILES AT z/D = 4 — Re_D = 32000

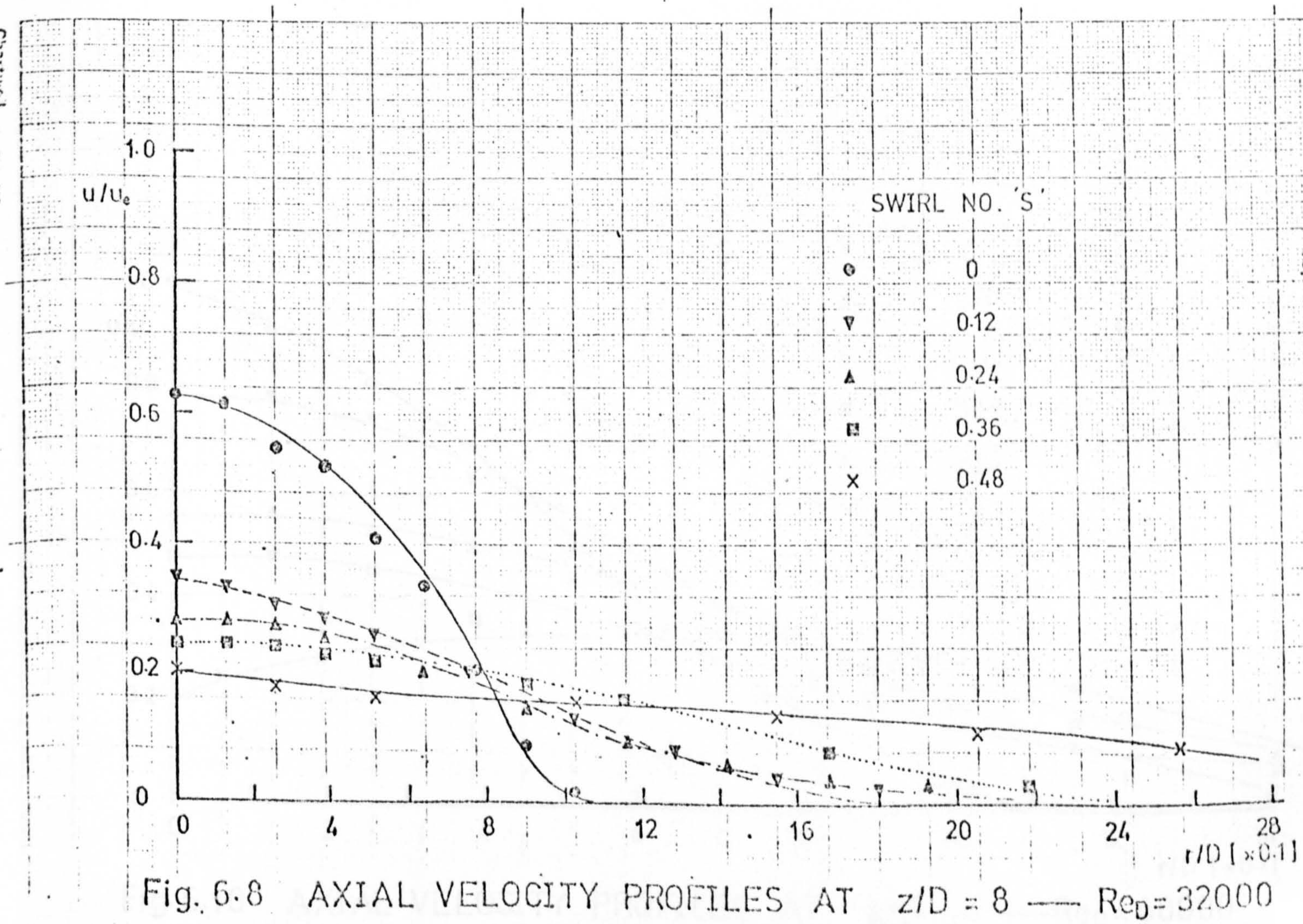

Fig. 6.8 AXIAL VELOCITY PROFILES AT z/D = 8 — Re_D = 32000

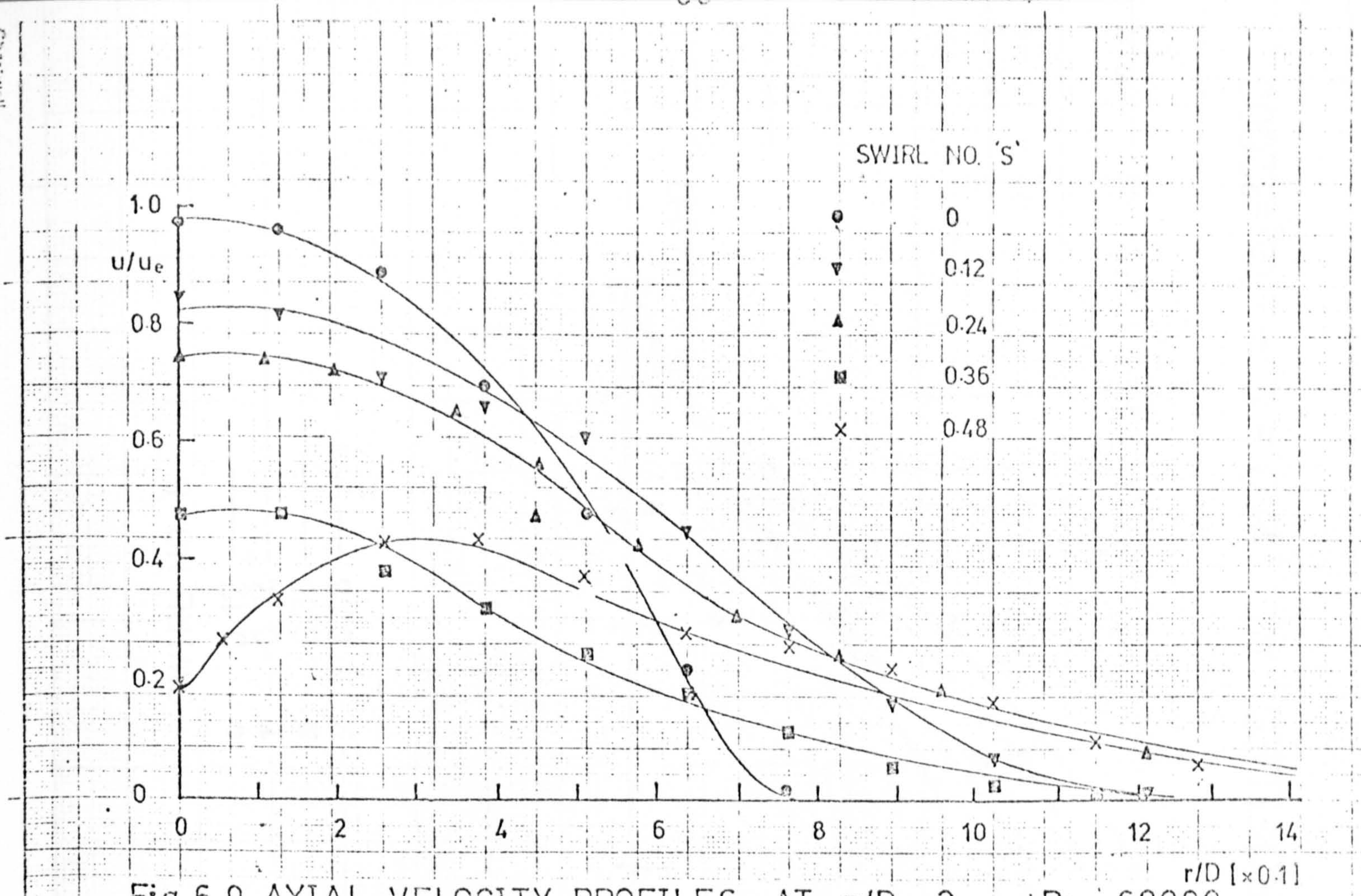

Fig 6.9 AXIAL VELOCITY PROFILES AT z/D = 2 —— Re_D = 60000

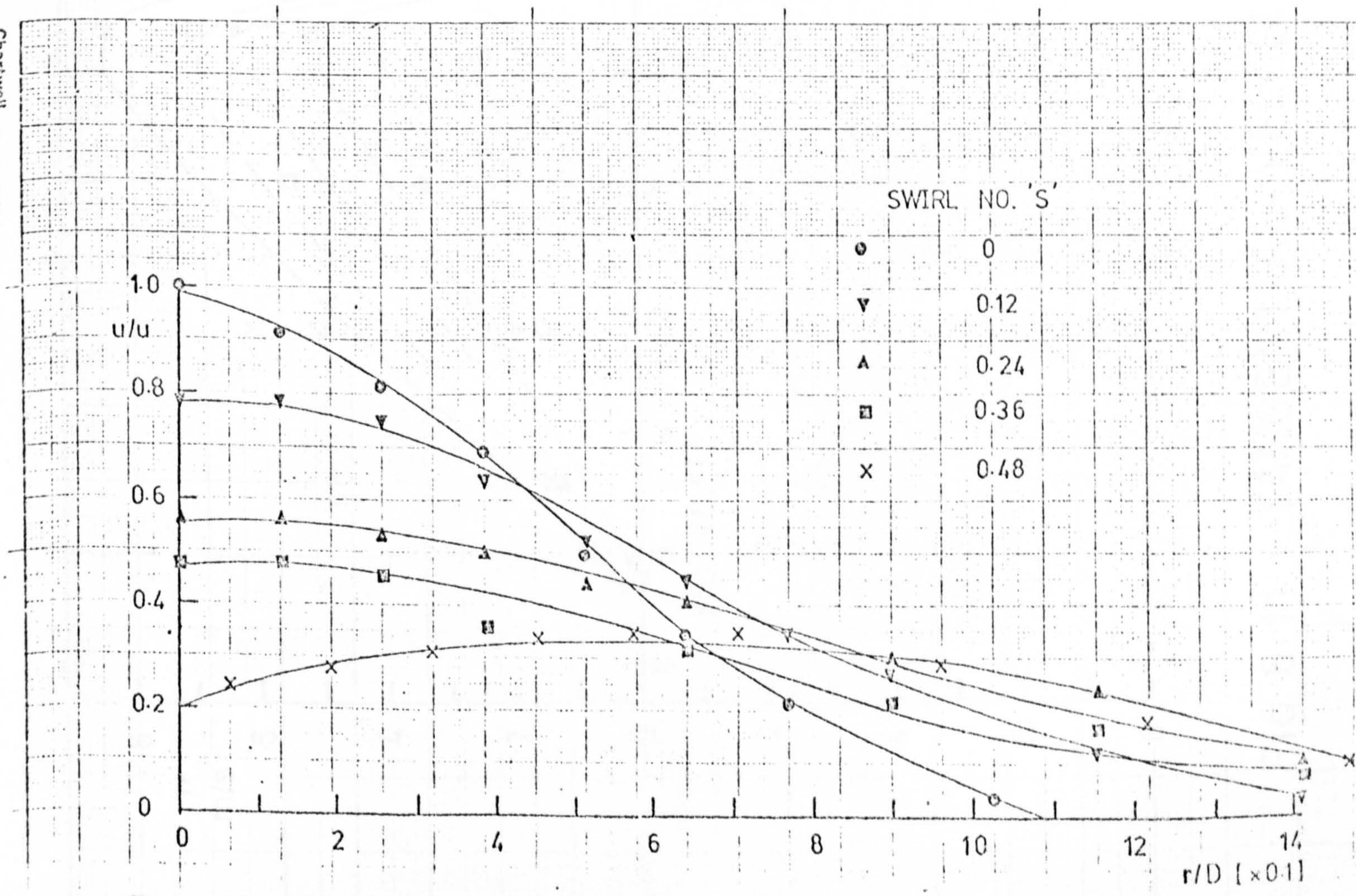

Fig. 6.10 AXIAL VELOCITY PROFILES AT z/D = 4 —— Re_D = 60000

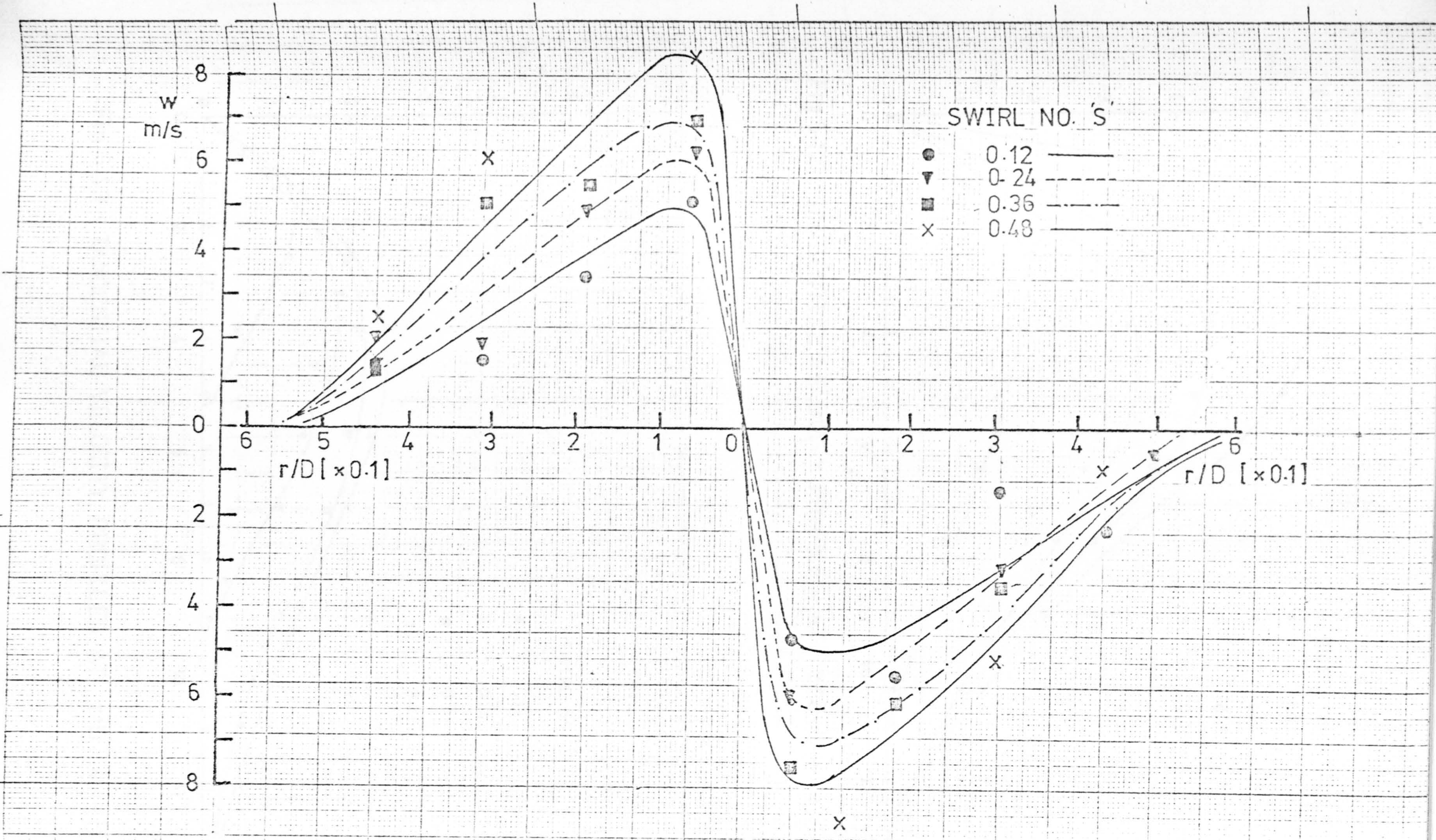

Fig 6.11 TANGENTIAL VELOCITY PROFILES AT z/D = 0 —— Re_D=32000

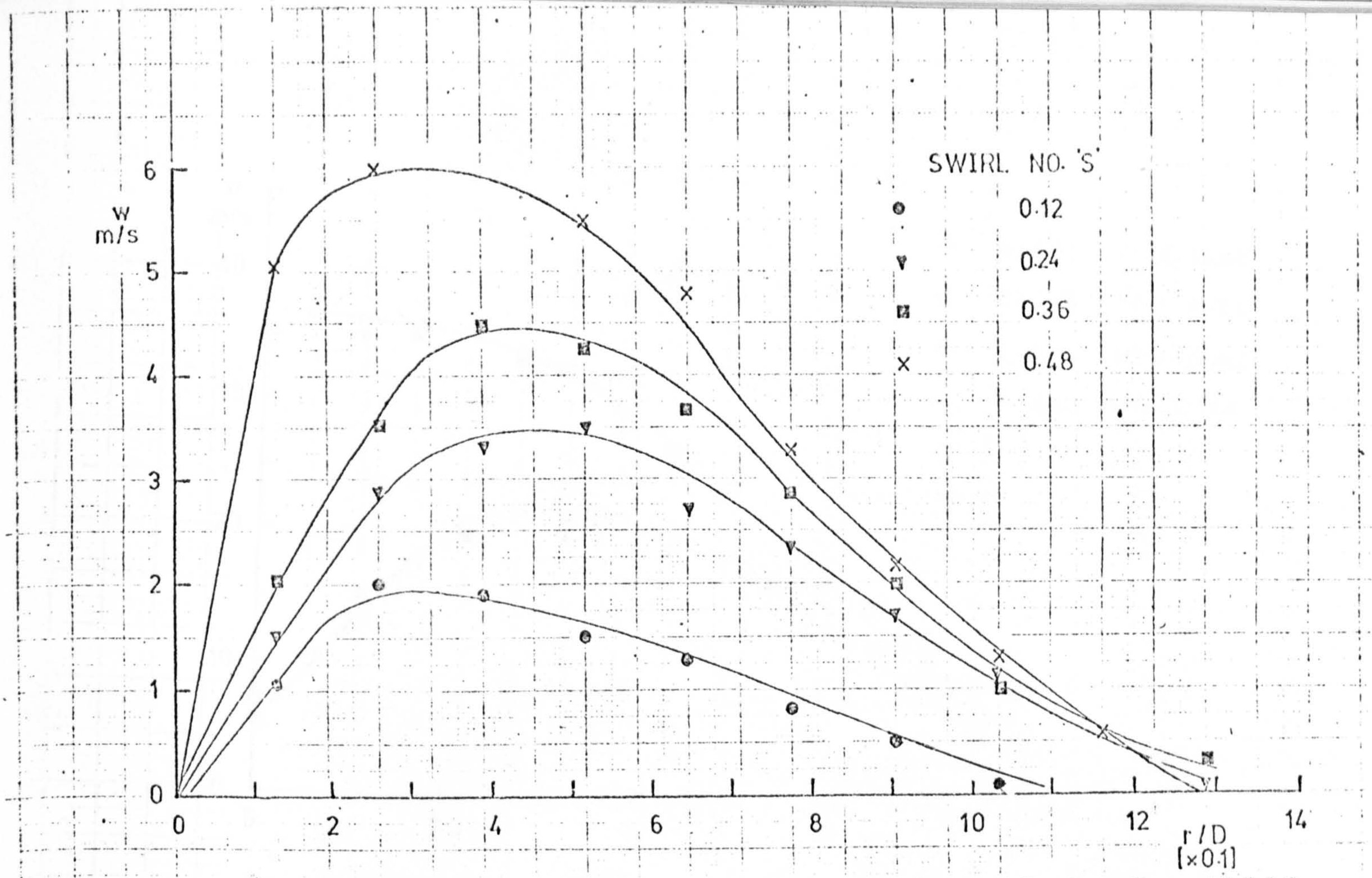

Fig 6.12 TANGENTIAL VELOCITY PROFILES AT z/D=2 —Re_D=32000.

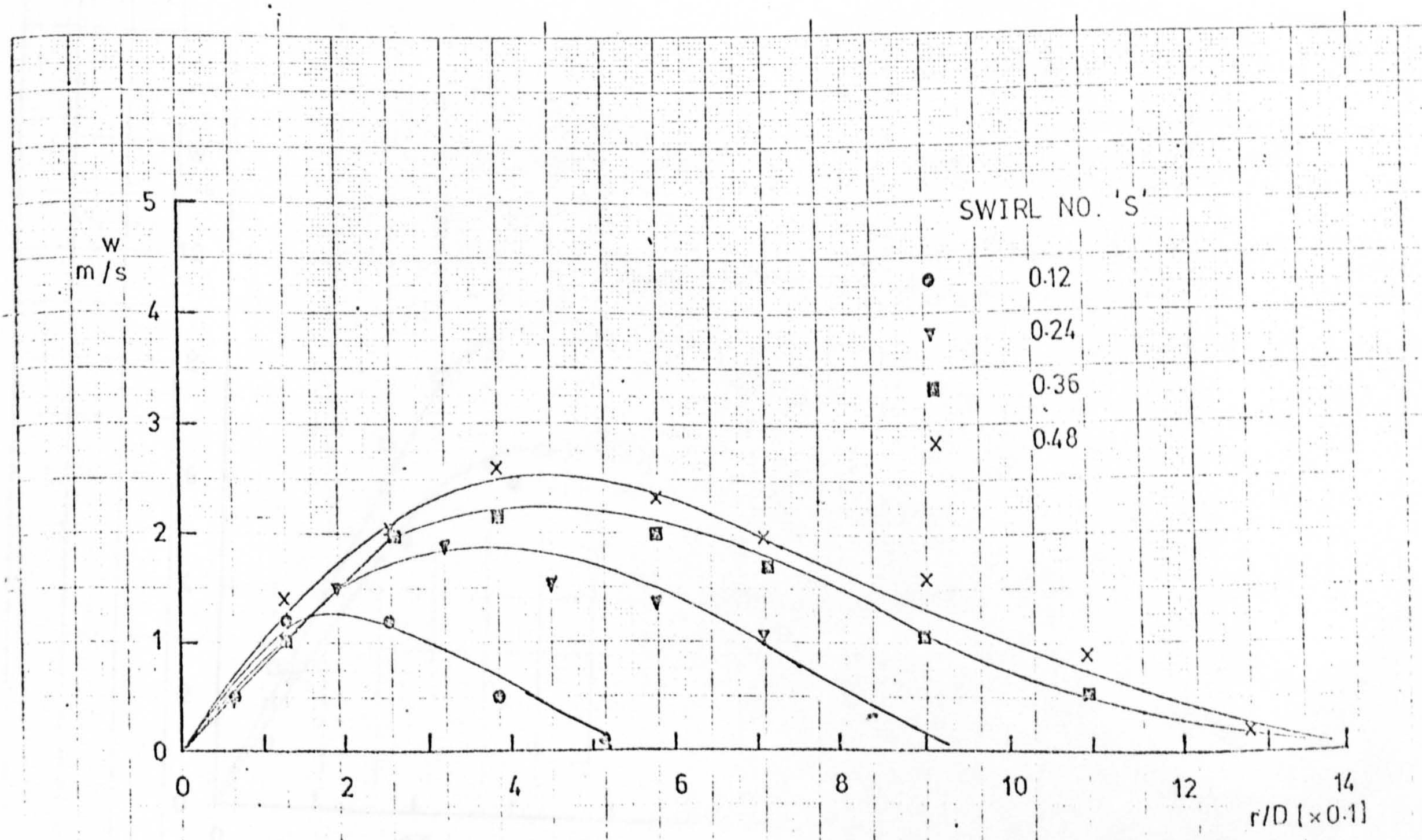

Fig 6.13 TANGENTIAL VELOCITY PROFILES AT z/D = 4 —Re_D=32000

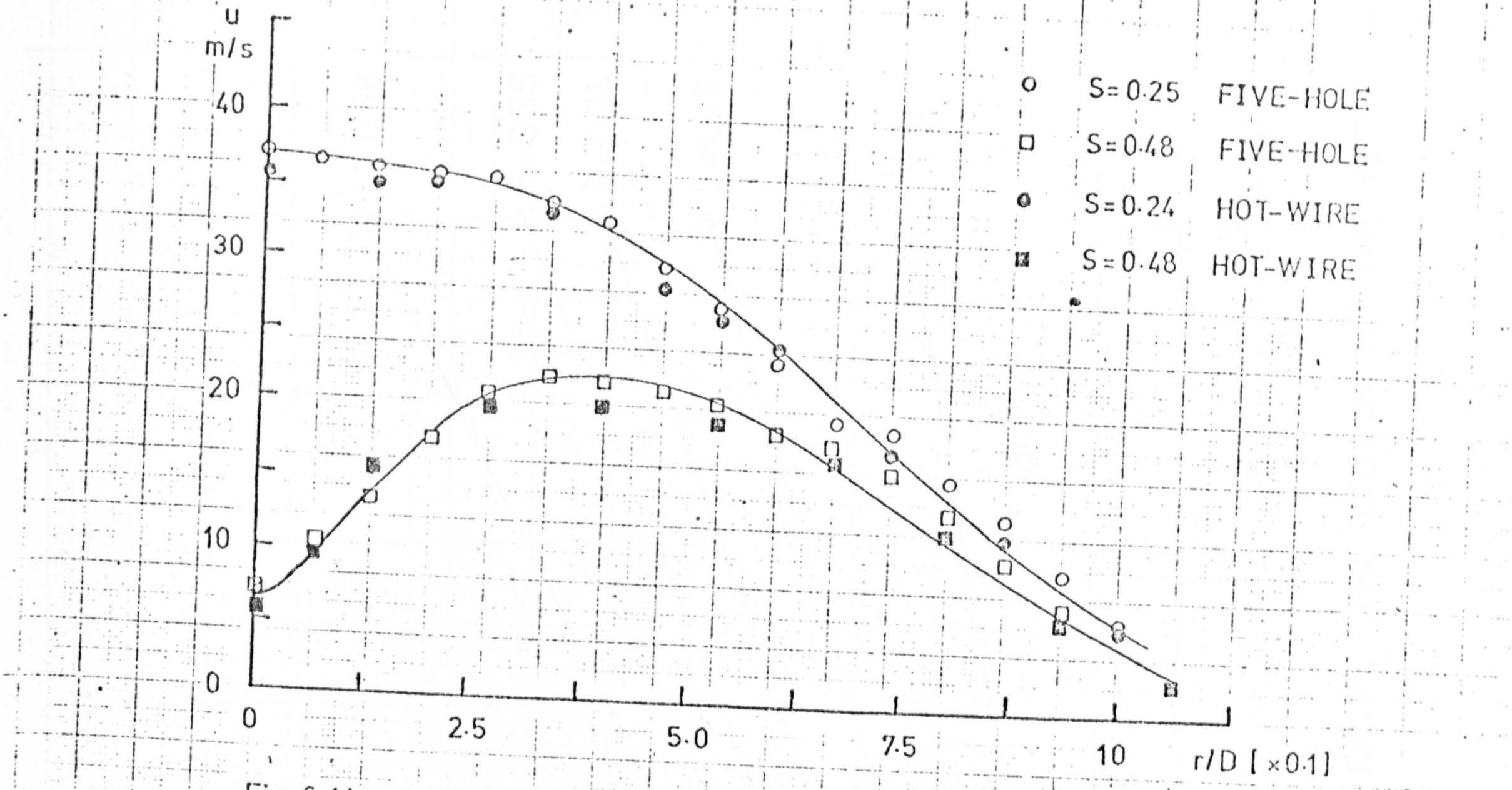

Fig 6.14 COMPARISON OF THE FIVE-HOLE & HOT-WIRE MEASUREMENTS [AXIAL VELOCITY]

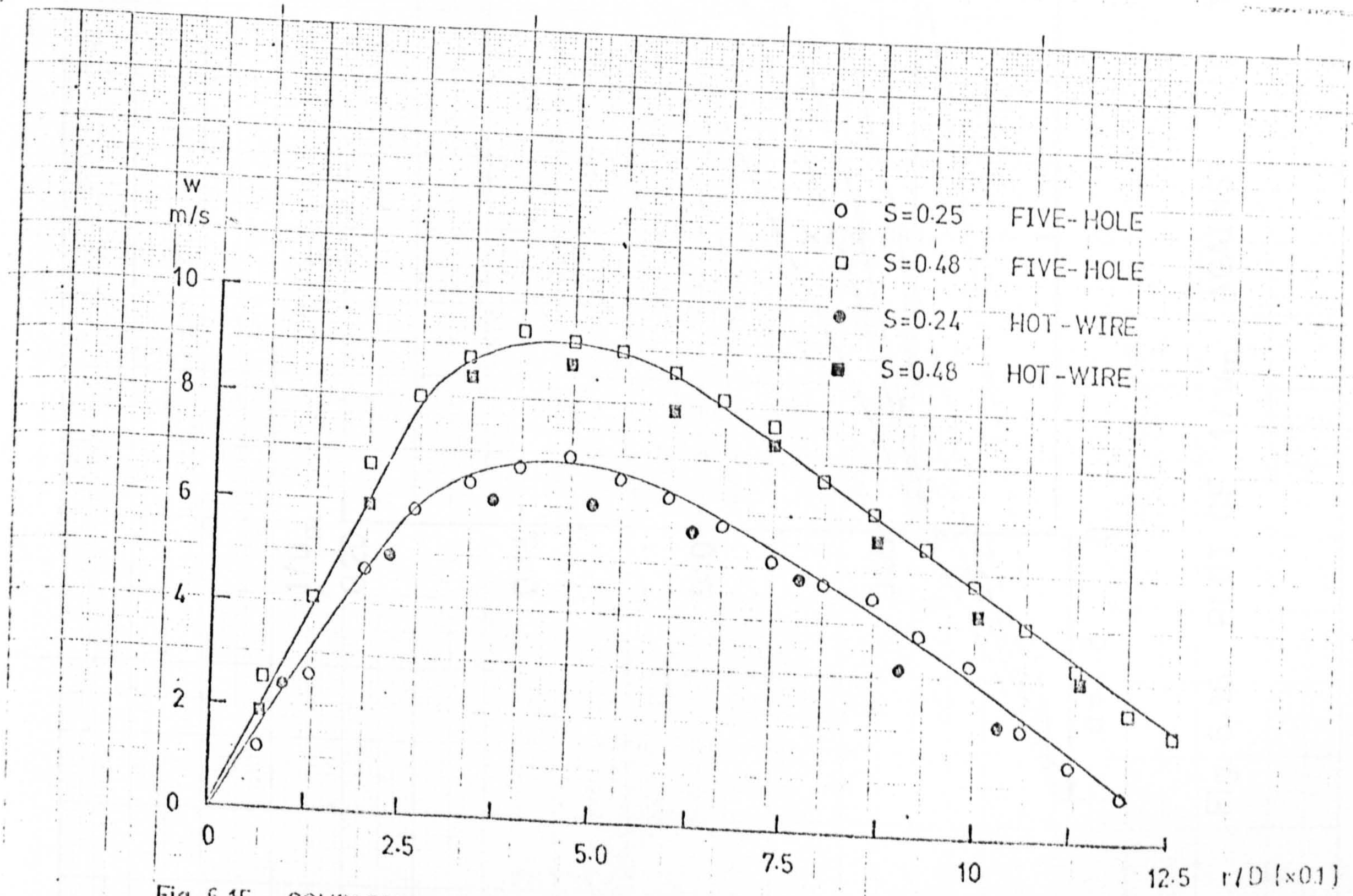

Fig 6.15 COMPARISON OF THE FIVE-HOLE & HOT WIRE MEASUREMENTS [TANGENTIAL VELOCITY].

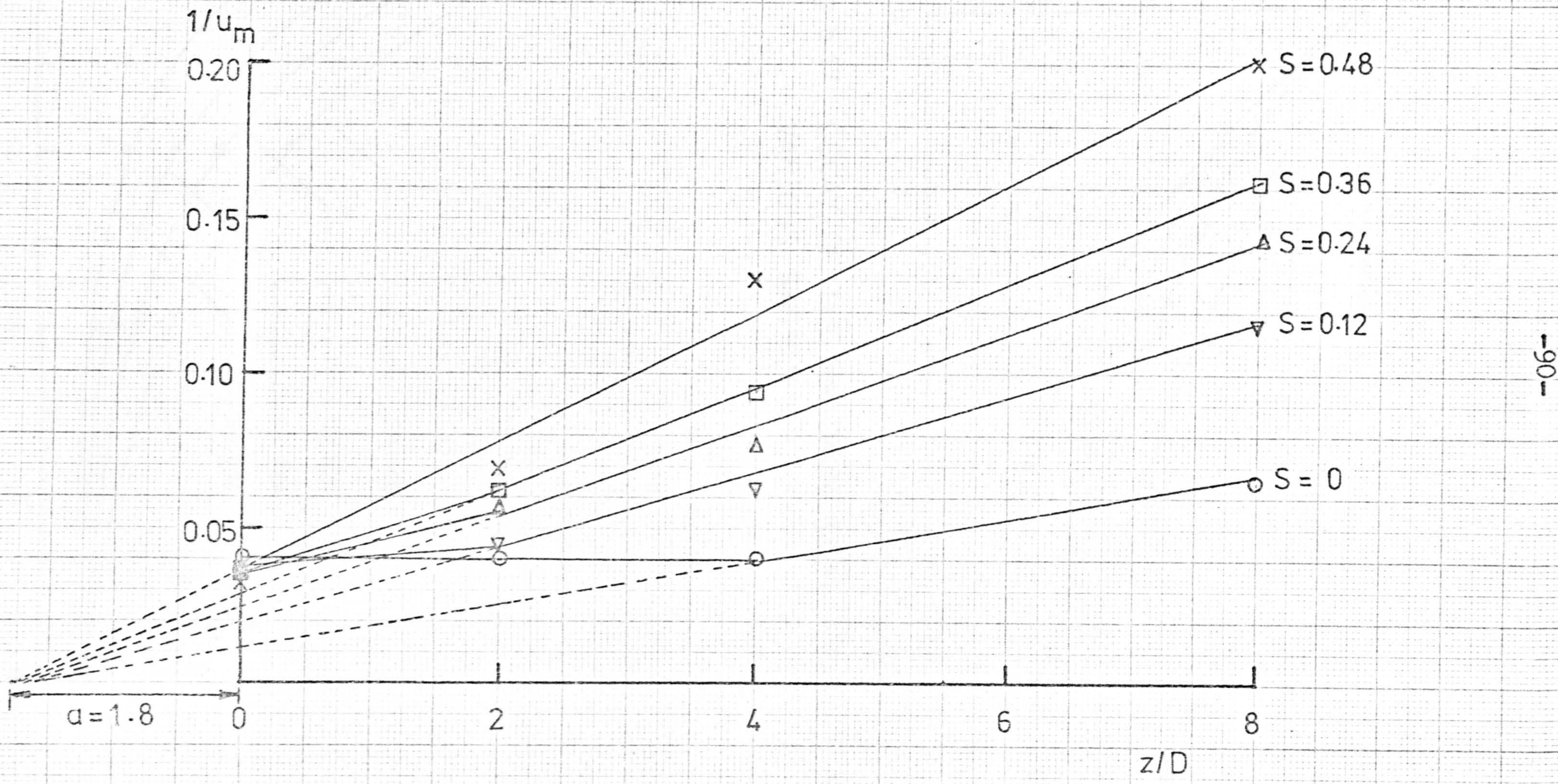

Fig. 6·16 PLOT OF $1/u_m$ AGAINST z/D TO DETERMINE THE ORIGIN OF THE JET

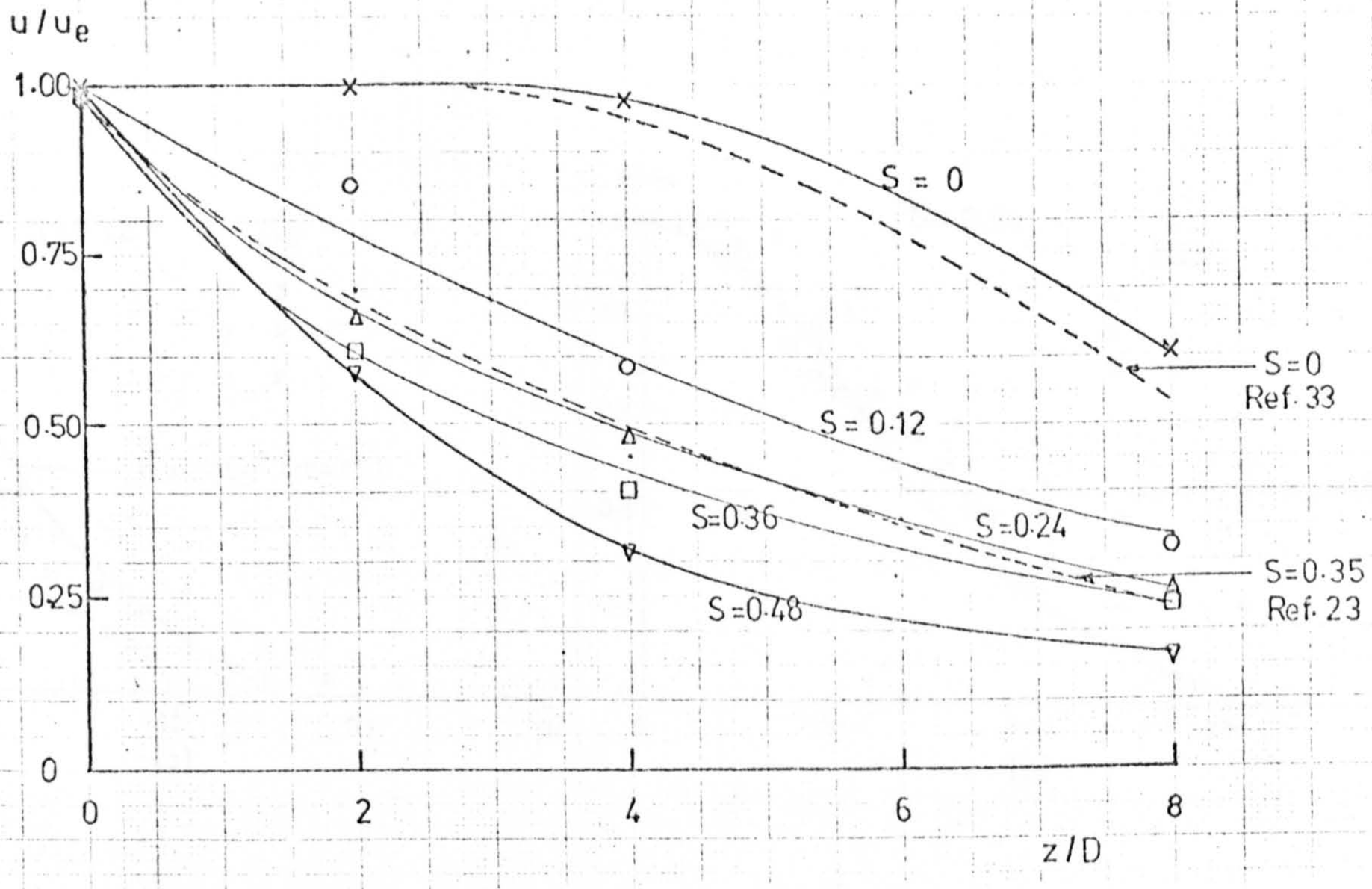

Fig. 6.17 DECAY OF THE MAXIMUM AXIAL VELOCITY AT VARIOUS SWIRLS

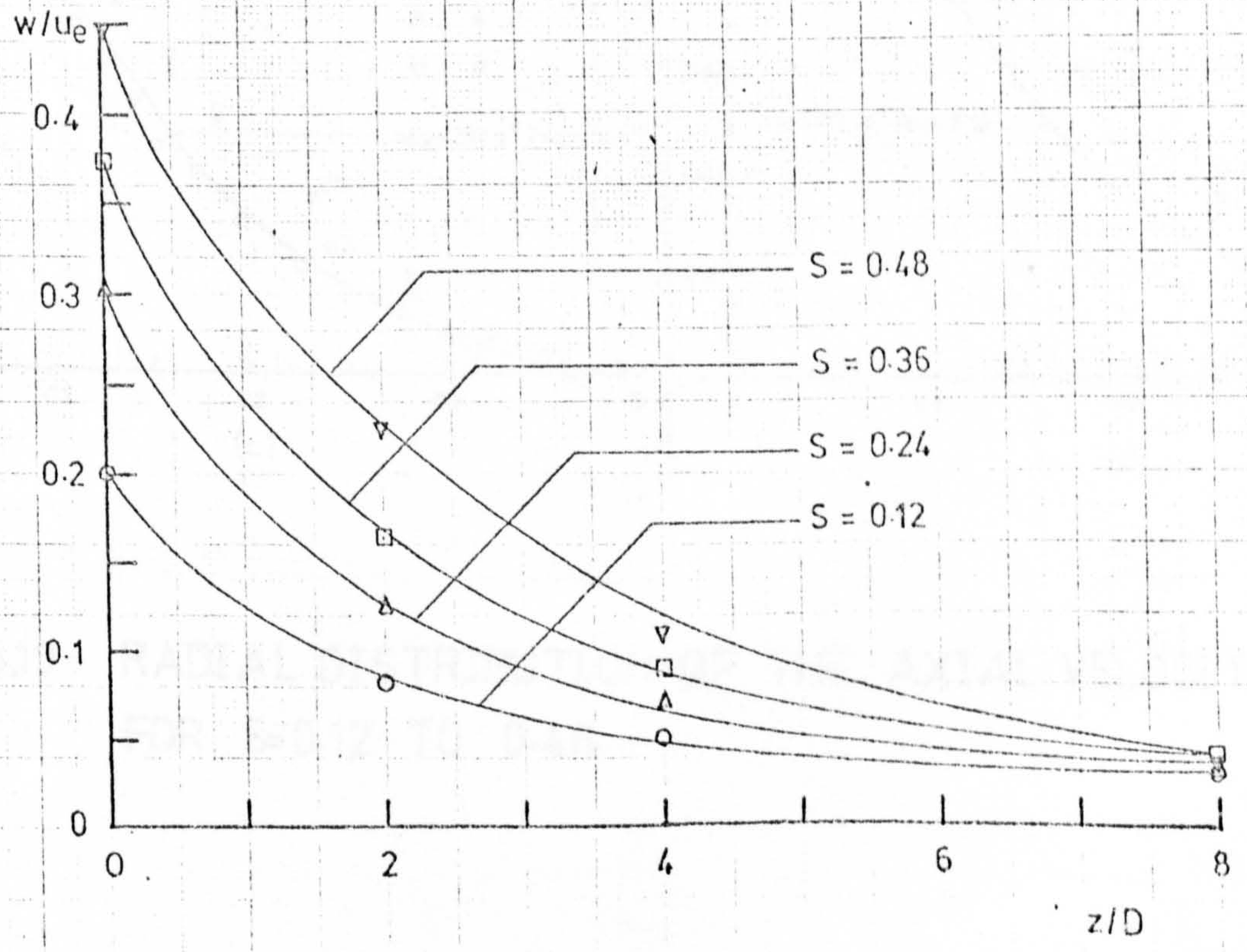

Fig. 6.18 DECAY OF THE MAXIMUM TANGENTIAL VELOCITY AT VARIOUS SWIRLS

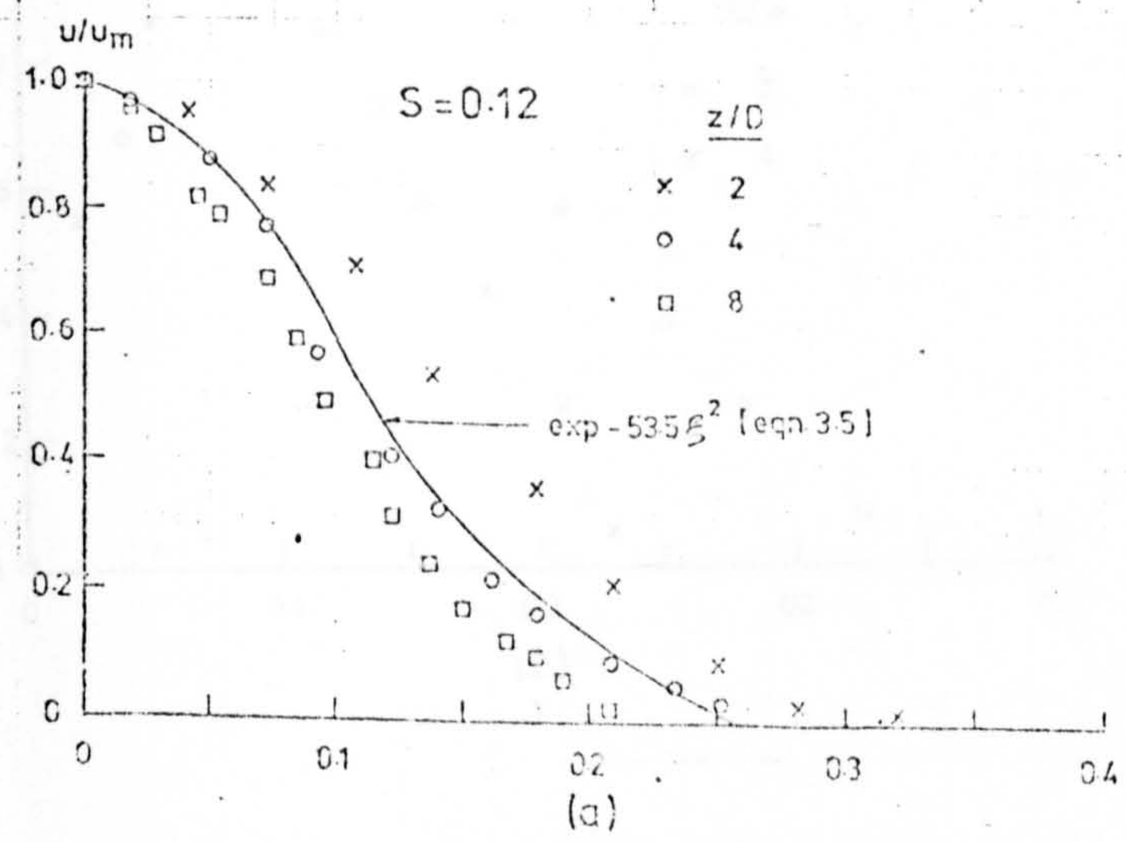

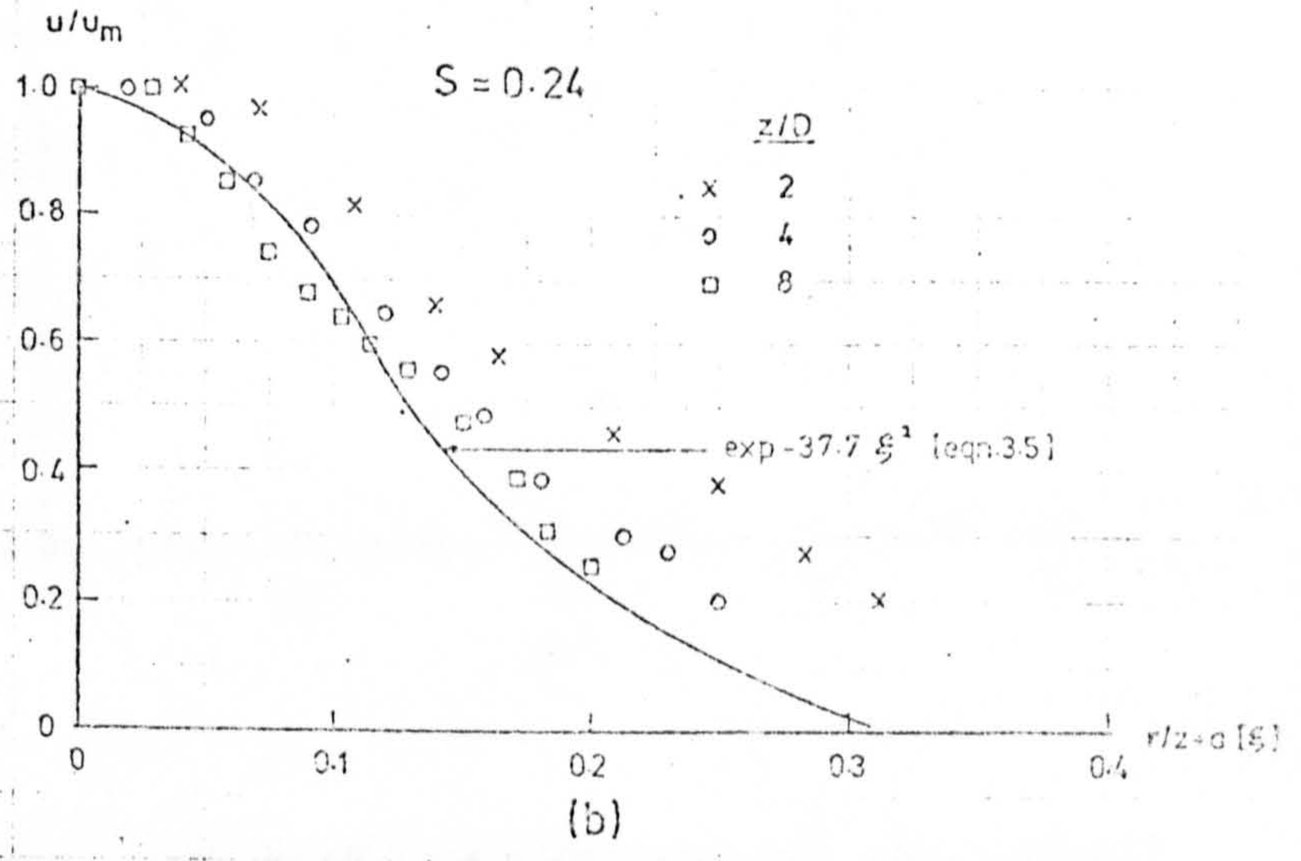

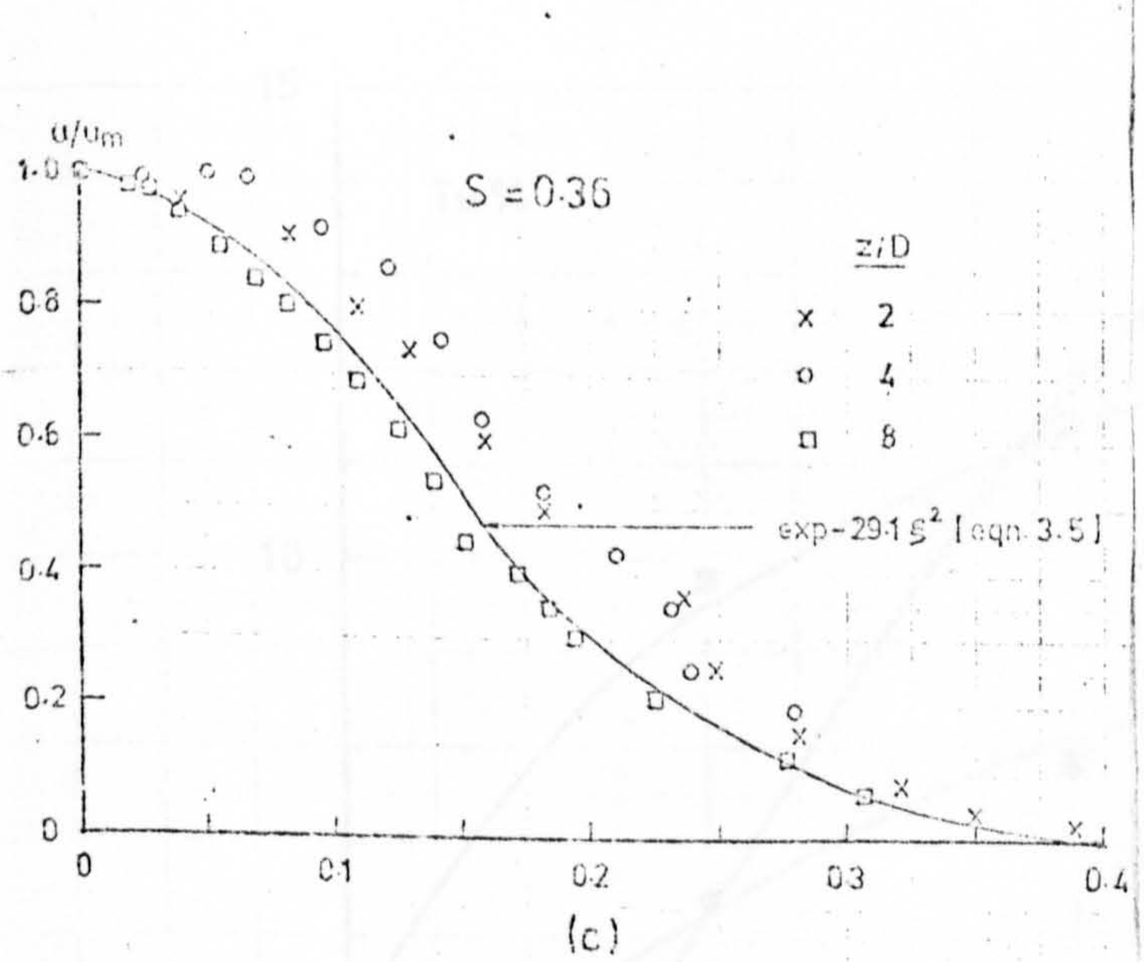

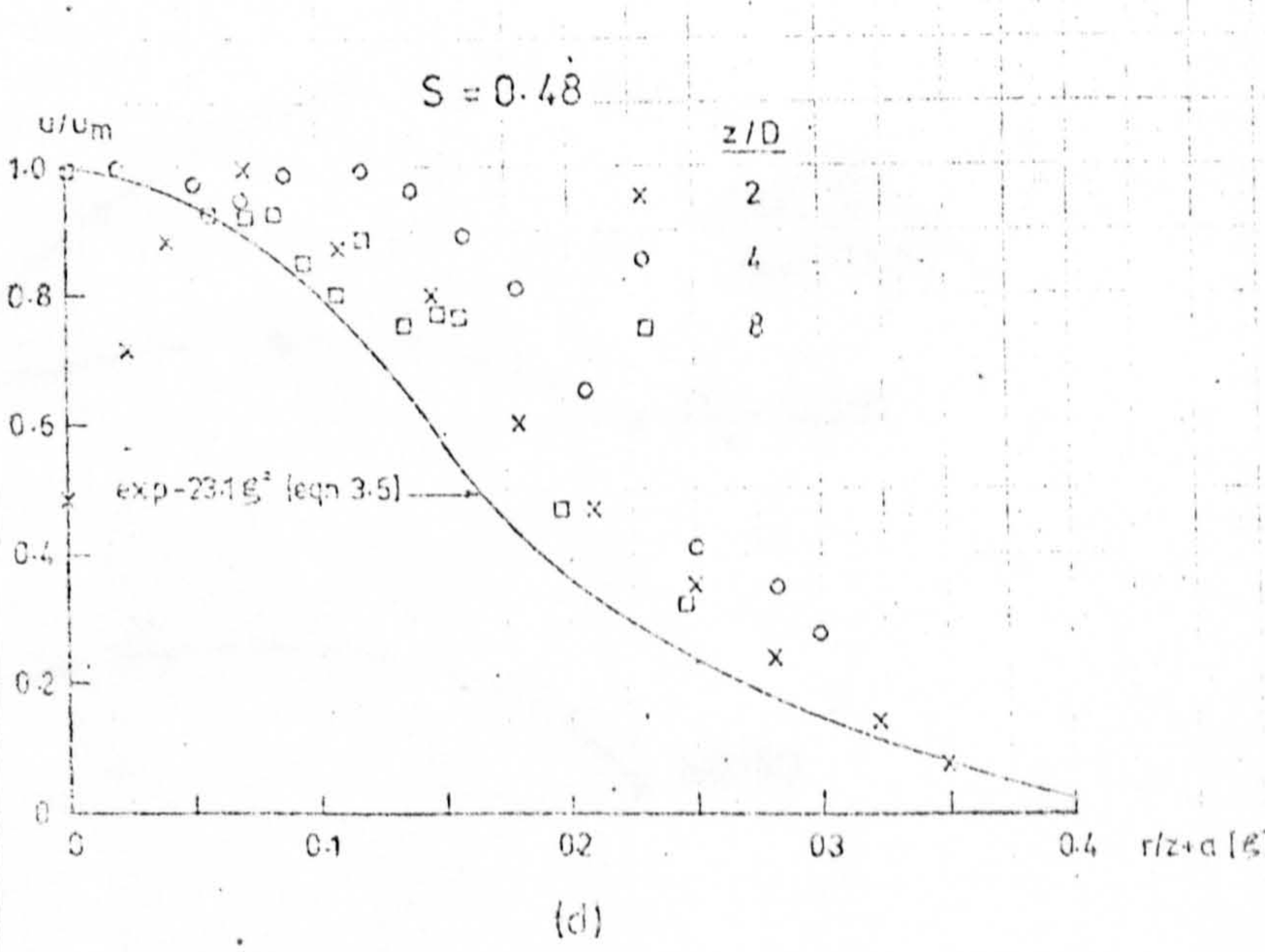

Fig 6.19 RADIAL DISTRIBUTION OF THE AXIAL VELOCITY FOR FOR S=0·12 TO 0·48

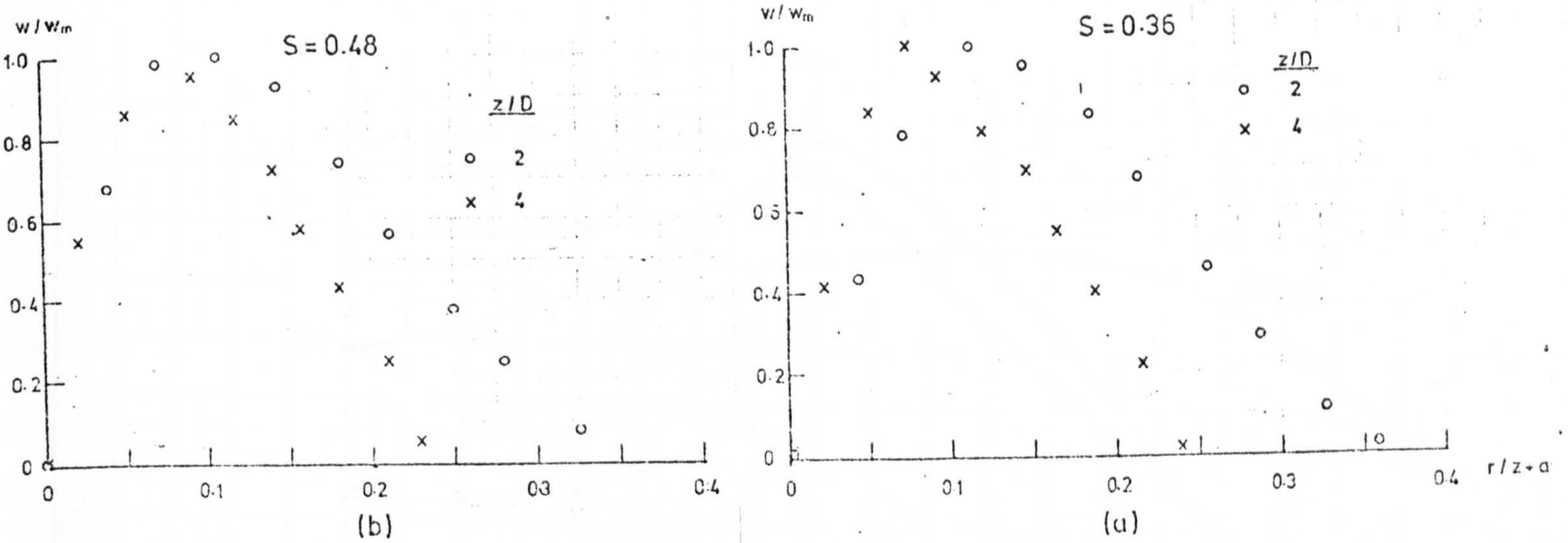

Fig 6·20 RADIAL DISTRBUTION OF THE TANGENTIAL VELOCITY FOR S=0,36 AND S=0,48

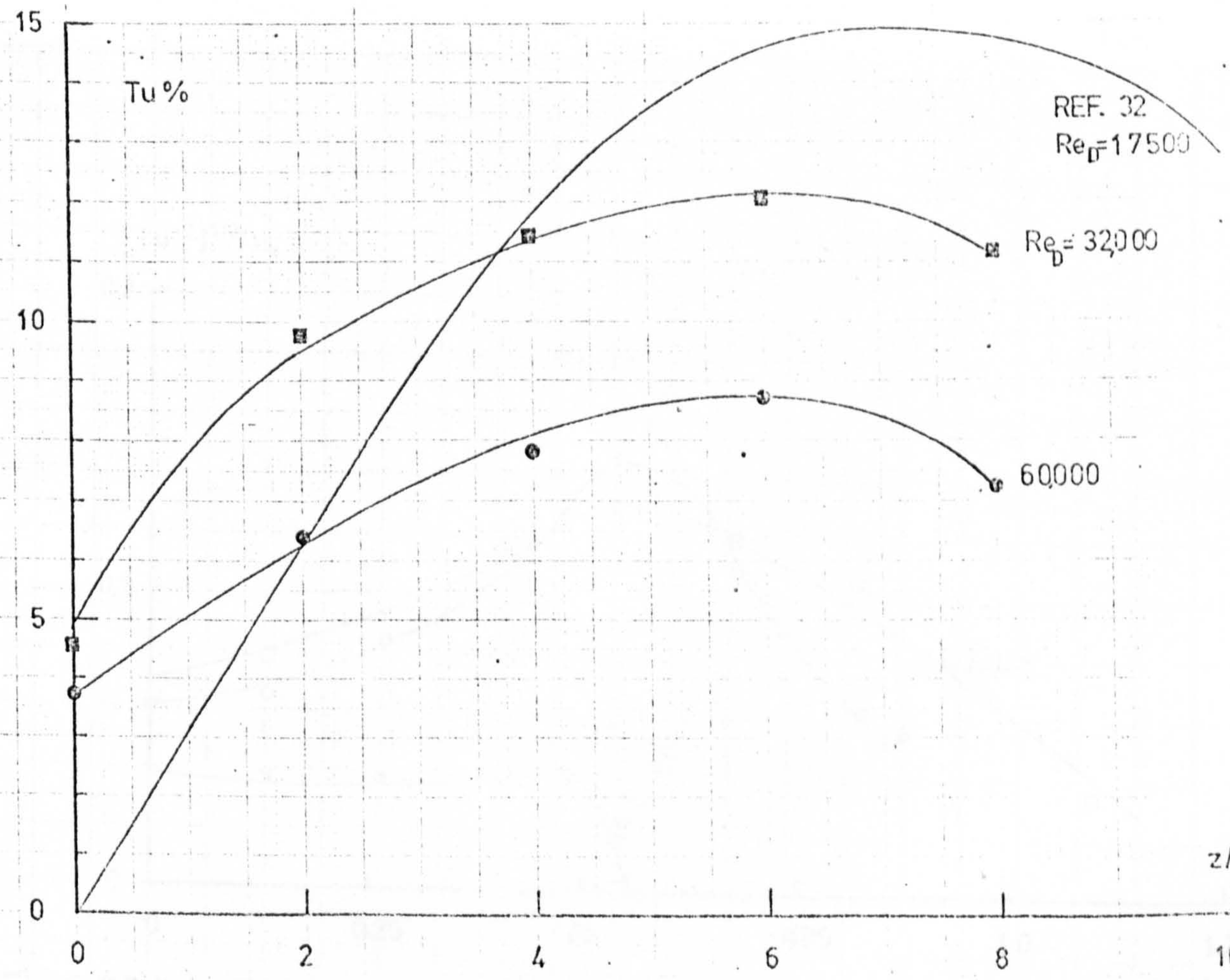

Fig. 6·21 VARIATION OF THE CENTRELINE TURBULENCE FOR THE NON-SWIRLING JET WITH z/D.

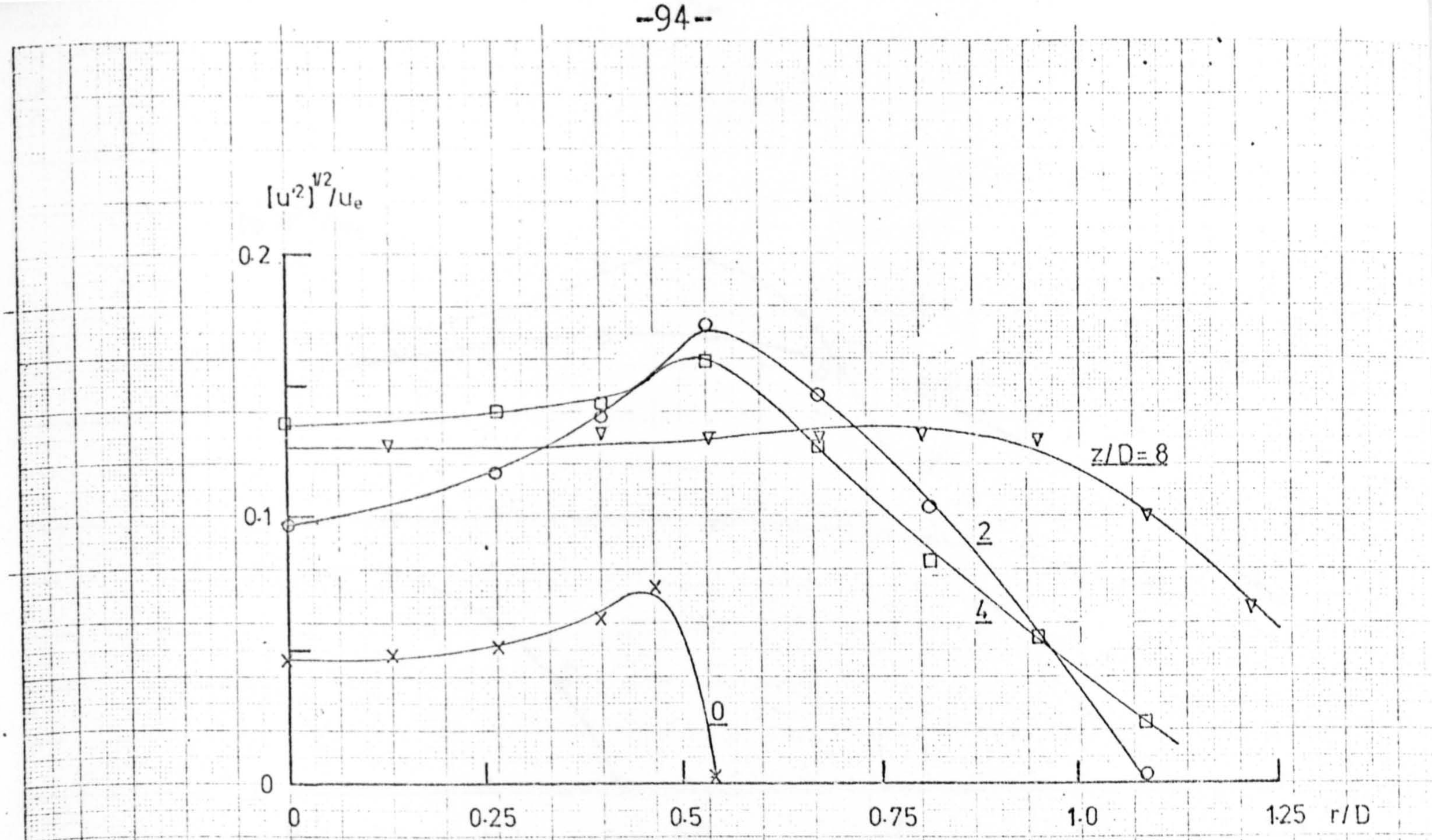

Fig. 6·22 a RADIAL VARIATION OF LONGITUDINAL TURBULENCE INTENSITY WITH z/D [swirl S=0, Re_D=32000]

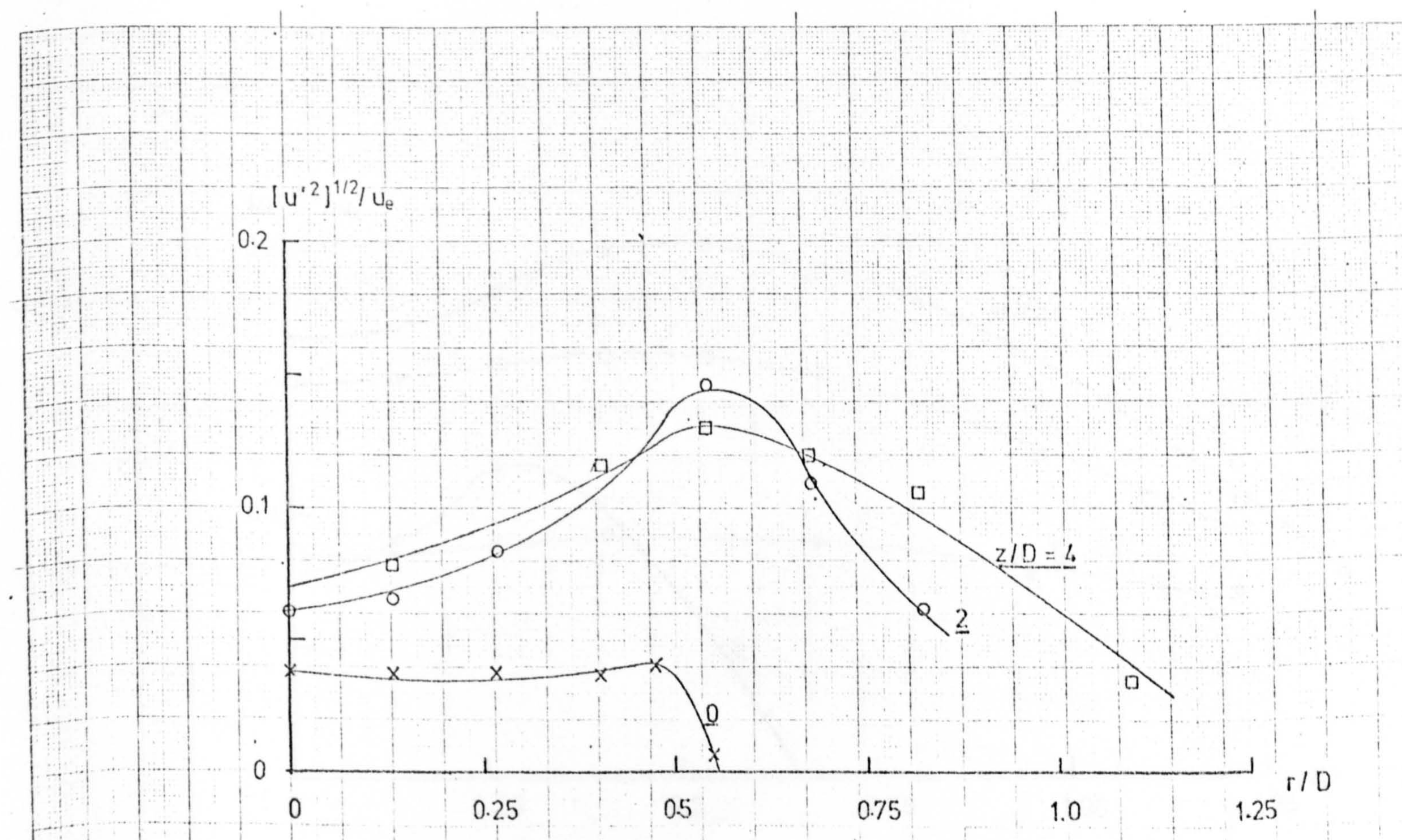

Fig. 6·22 b RADIAL VARIATION OF LONGITUDINAL TURBULENCE INTENSITY WITH z/D [swirl S = 0, Re_D = 60000]

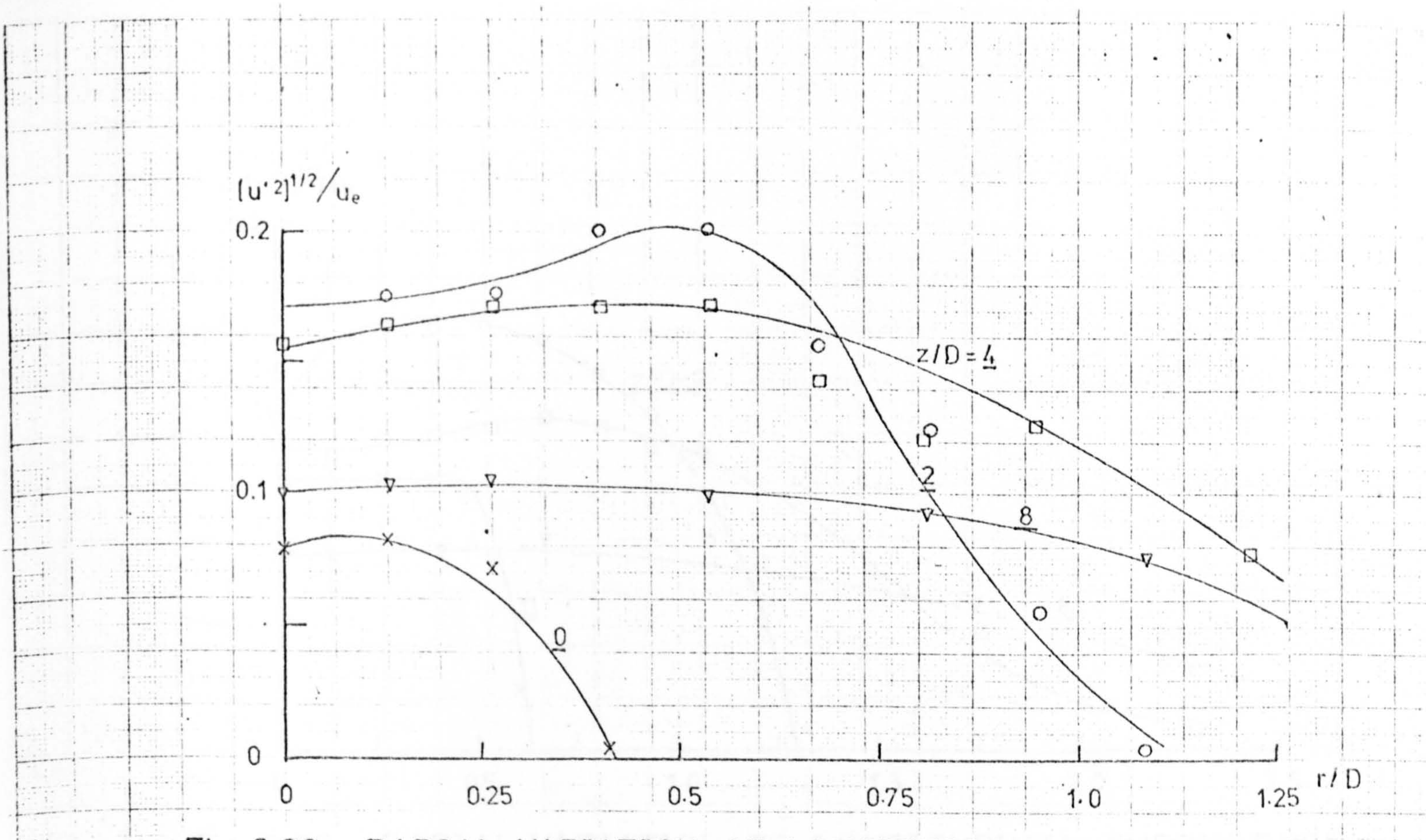

Fig. 6.23 RADIAL VARIATION OF LONGITUDINAL TURBULENCE INTENSITY WITH z/D [swirl S=0.12, Re_D=32000]

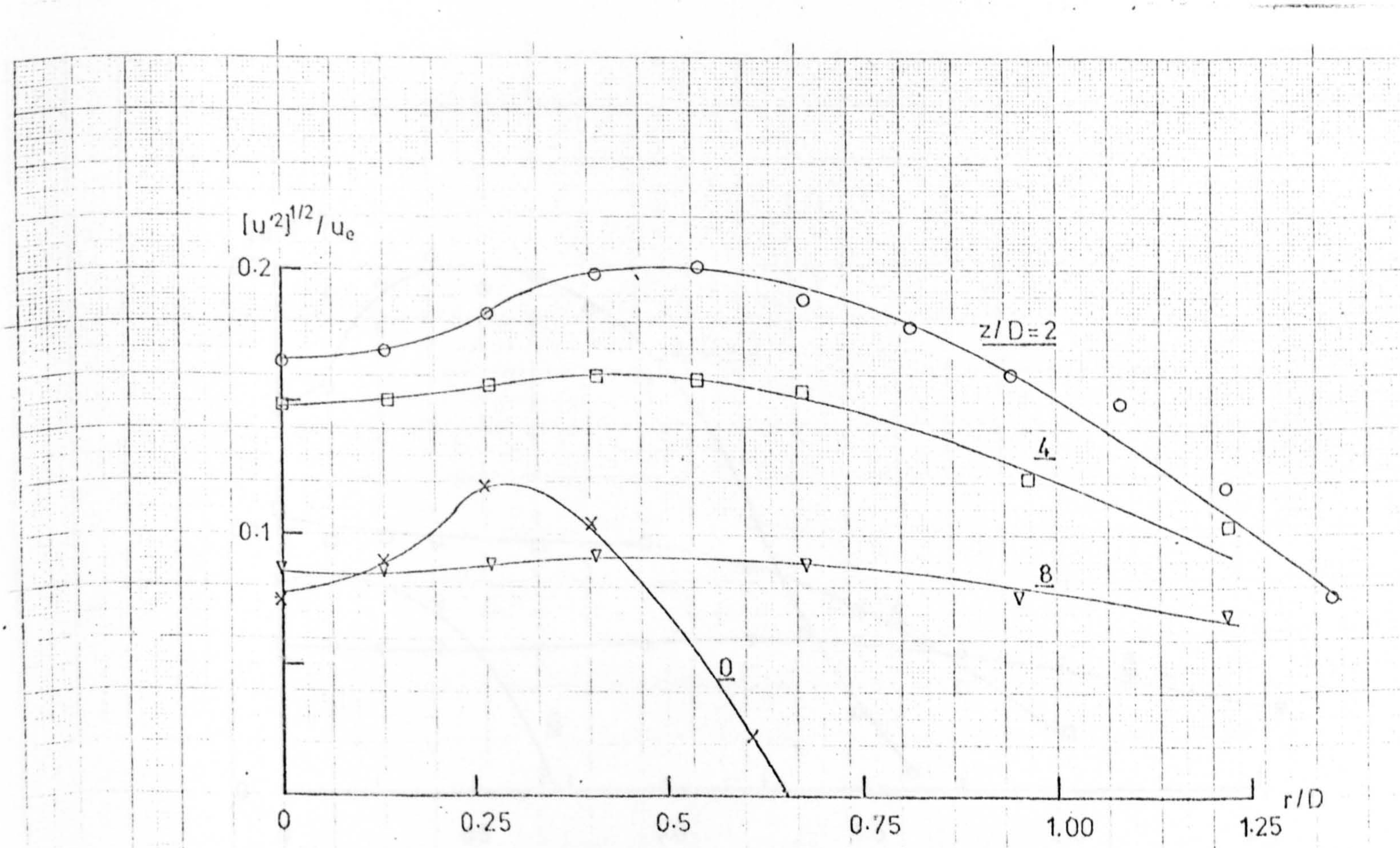

Fig. 6.24 RADIAL VARIATION OF LONGITUDINAL TURBULENCE INTENSITY WITH z/D [swirl S=0.24, Re_D= 32000]

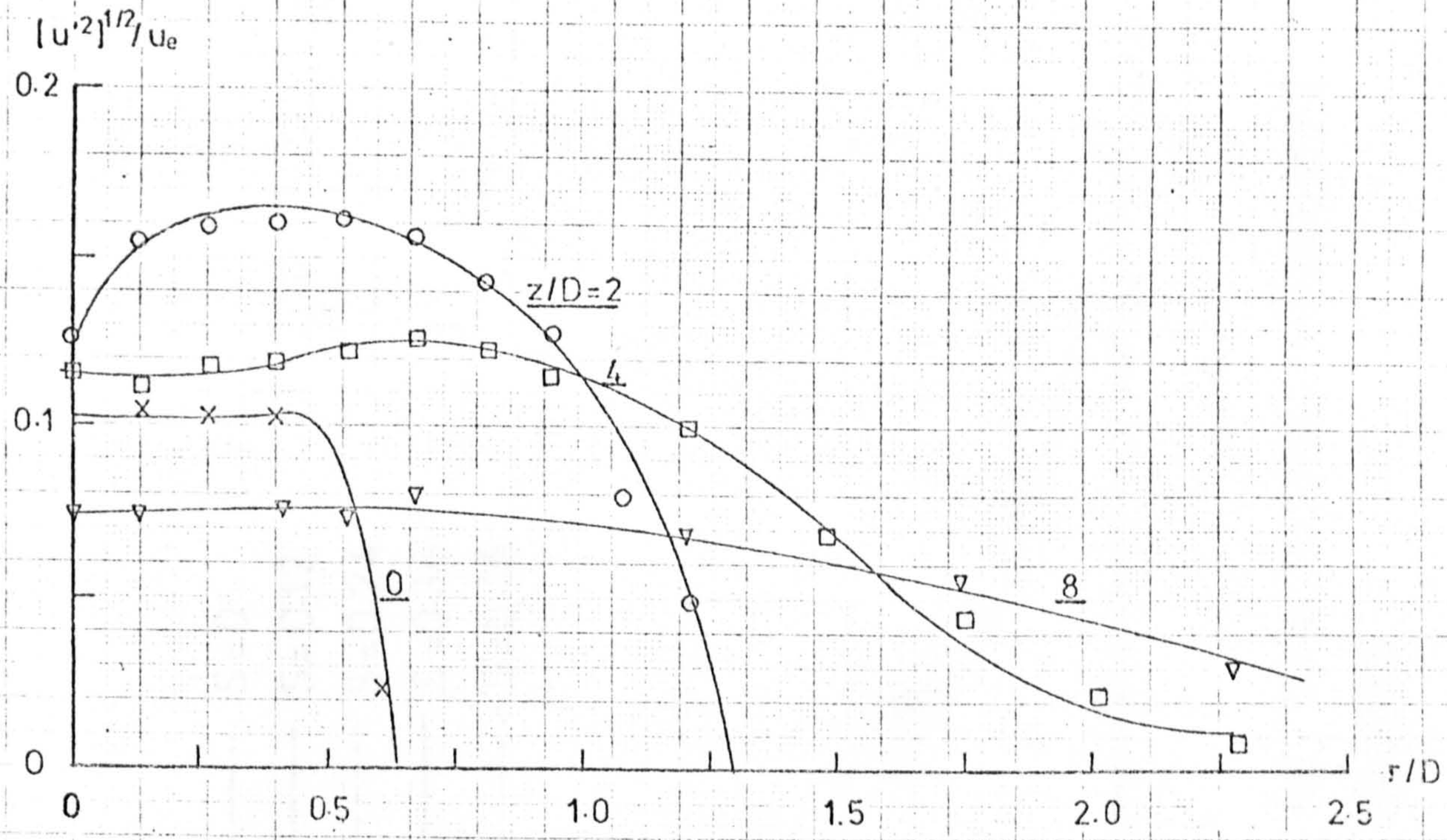

Fig. 6.25 RADIAL VARIATION OF LONGITUDINAL TURBULENCE INTENSITY WITH z/D [swirl S = 0.36, Re_D = 32000]

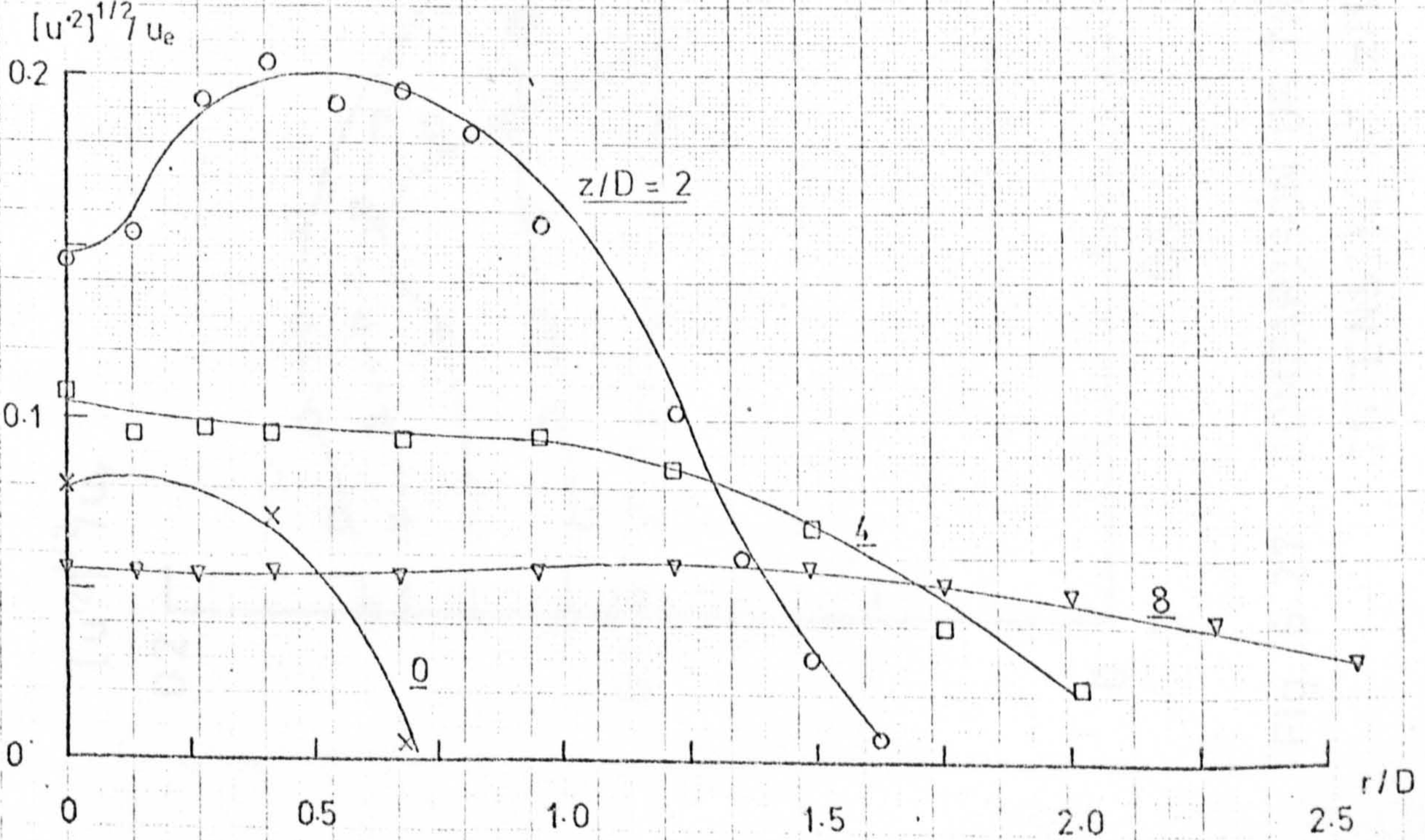

Fig. 6.26 RADIAL VARIATIONS OF LONGITUDINAL TURBULENCE INTENSITY WITH z/D [swirl S = 0.48 Re_D = 32000]

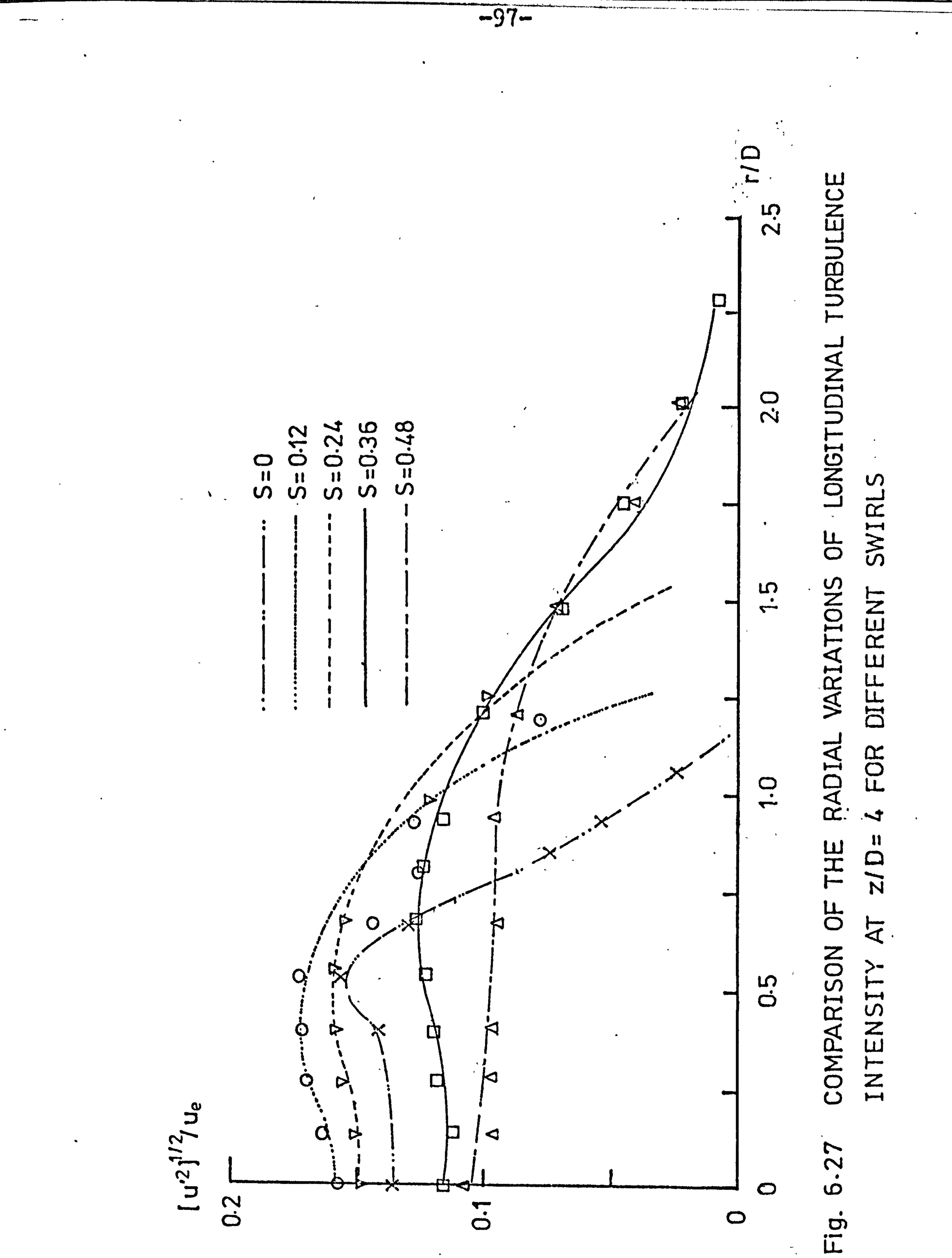
COMPARISON OF THE RADIAL VARIATIONS OF LONGITUDINAL TURBULENCE INTENSITY AT z/D= 4 FOR DIFFERENT SWIRLS
S=0
S=0.12
S=0.24
S=0.36
S=0.48
r/D
2.5
2.0
1.5
1.0
0.5
0
0.2
0.1
0
$[u'^2]^{1/2}/u_e$

Fig. 6.27

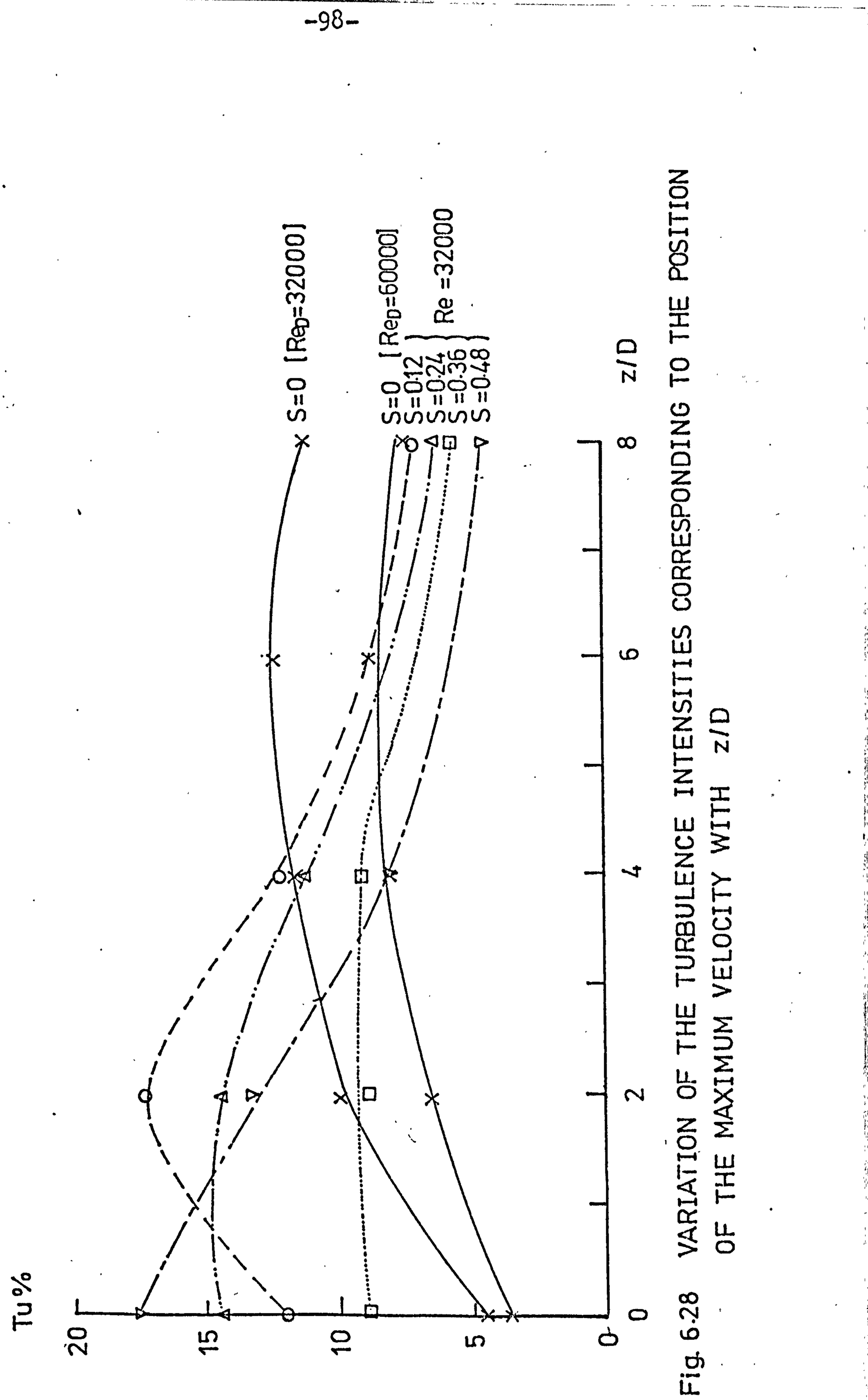
Tu %
20
15
10
5
0
0
2
4
6
8
z/D
S=0 (Rep=32000)
S=0 (Rep=60000)
S=0.12
S=0.24
S=0.36
S=0.48
Re =32000
VARIATION OF THE TURBULENCE INTENSITIES CORRESPONDING TO THE POSITION OF THE MAXIMUM VELOCITY WITH z/D

Fig. 6.28

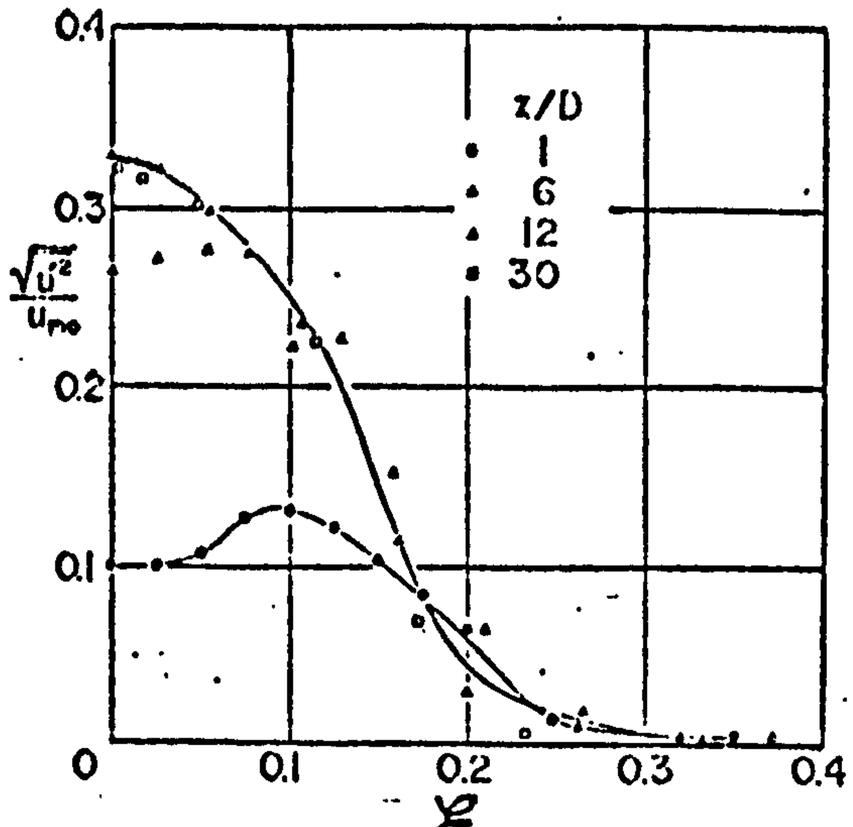

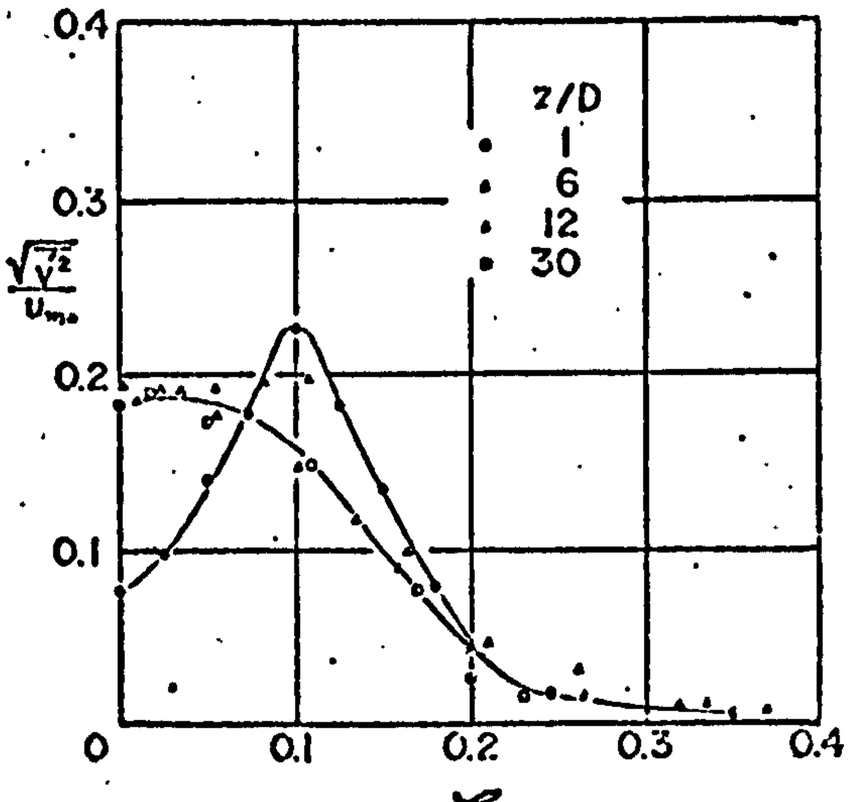

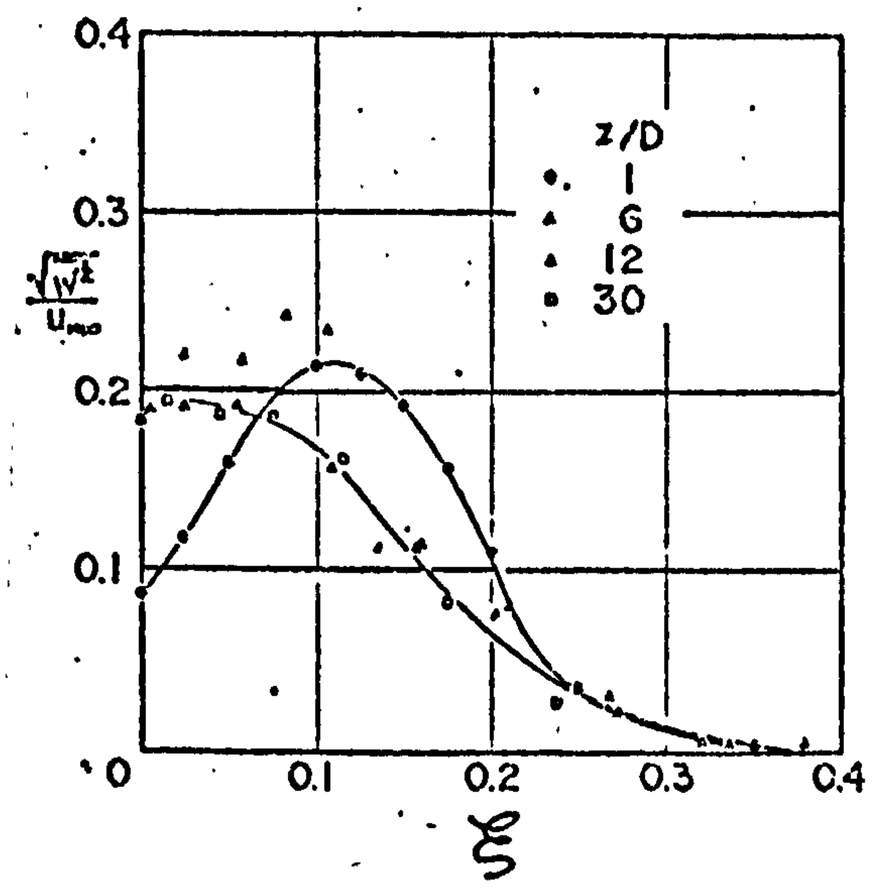

$\xi = r/z+a$

Fig. 6.29 VARIATION OF LONGITUDINAL, RADIAL & TANGENTIAL TURBULENCE INTENSITY FROM REF. 72

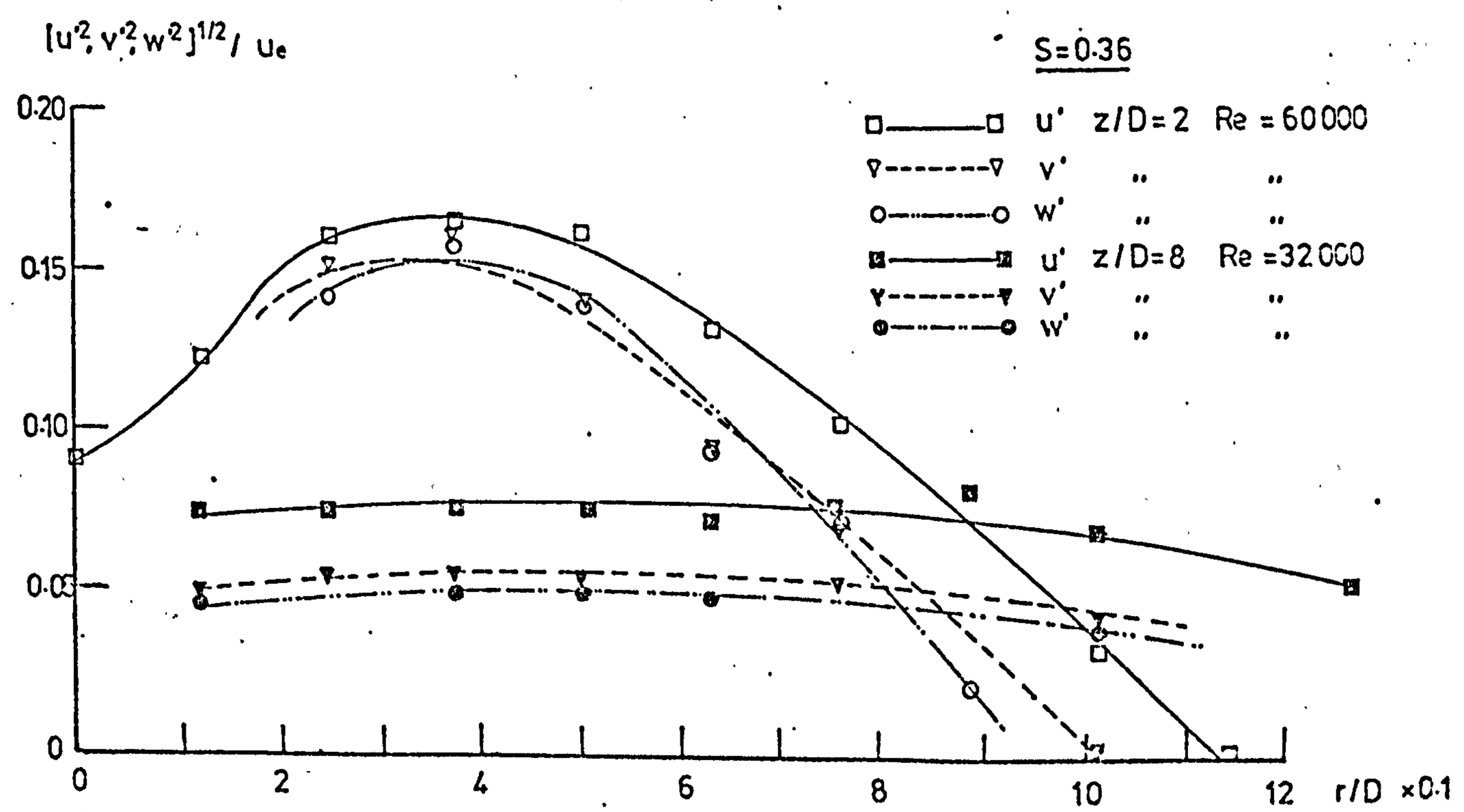

Fig. 6.30 VARIATION OF THE LONGITUDINAL AND LATERAL TURBULENT FLUCTUATIONS FOR TWO SELECTED CASES.

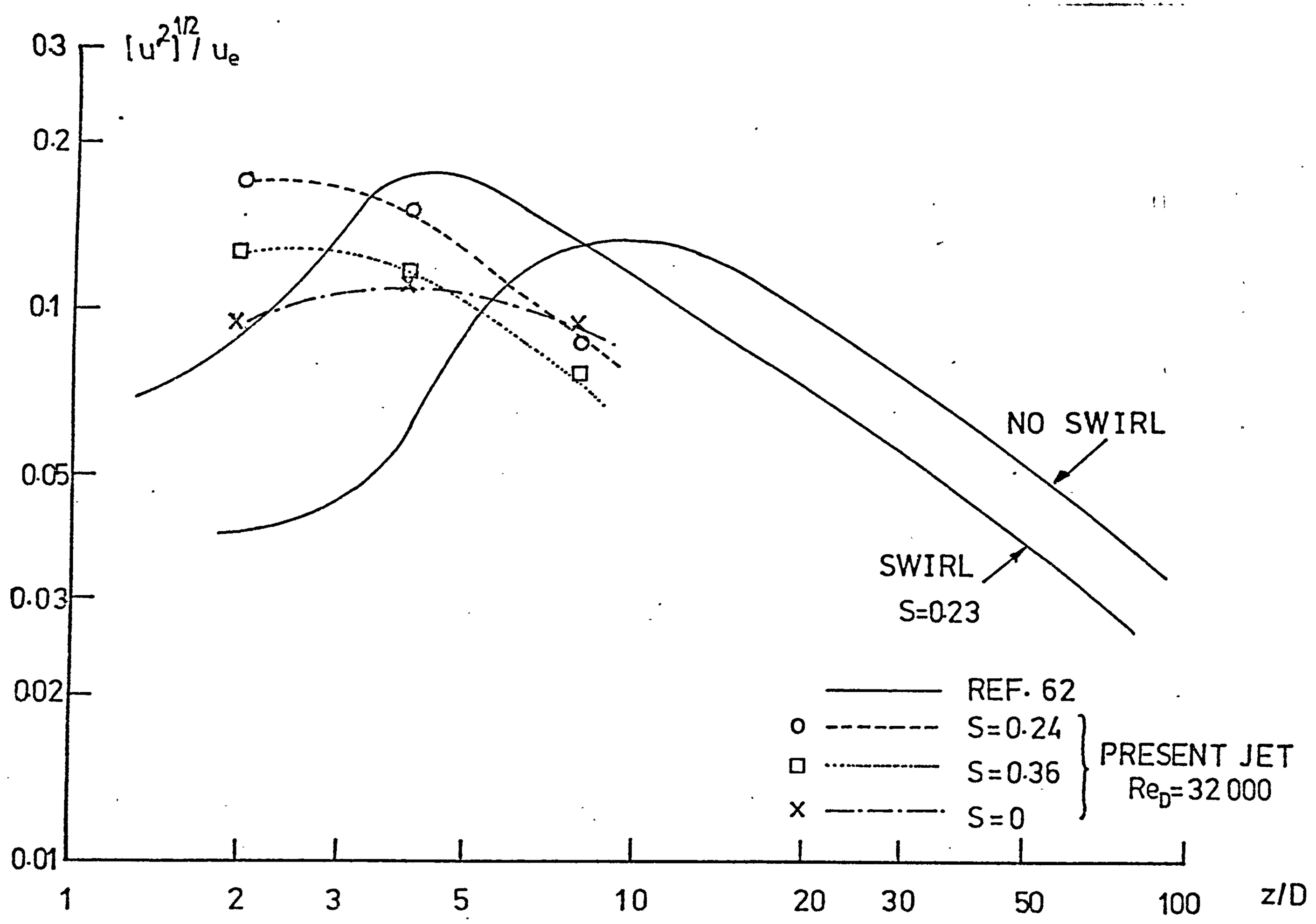

Fig.6.31 DECAY OF THE CENTRELINE LONGITUDINAL TURBULENCE INTENSITY

CHAPTER 7

THE USE OF MASS TRANSFER TECHNIQUES TO ESTIMATE HEAT TRANSFER

7.1 INTRODUCTION

The complicated nature of turbulent flows often precludes the employment of analytical methods to determine heat transfer. This is particularly true for jet impingement systems due to their two or three dimensional geometries and large scale eddies which occur. Thus, one must resort to an experimental technique to obtain heat transfer coefficients. Direct determination involves the measurement of surface temperature and heat flux at each station of interest. Surface temperature measurements often require the insertion of a large number of thermojunctions in the surface and, at high heat fluxes, significant errors can be introduced if measurements are made below the surface due to the problem of location. Conduction within the test surface can also result in errors. Heat flux may be measured either by determining the thermal response of a film or insert thermally insulated from the remainder of the surface. Heat flux may also be estimated by measuring the steady-state dissipation of heat from the test section, e.g. by determining the electrical input to a heated section or by measuring the rate of steam condensation (see Ref.86 for details).

In addition to the problems discussed, direct methods can require elaborate data-logging equipment, and it can become costly to install all the necessary instrumentation. Thus, the use of analogies is finding increasing application in the estimation of heat transfer. The use of these depends upon the similarity of the physical processes underlying the transfer of momentum, heat and mass. These transfer processes can be expressed by similar equations:-

$$\tau = \rho(\nu + \varepsilon)\frac{\partial u}{\partial y} \quad \text{for momentum transfer} \qquad (7.1)$$

(Shear stress = f (velocity gradient))

$$q = \rho C_p(\alpha + \varepsilon_H)\cdot\frac{\partial T}{\partial y} \quad \text{for heat transfer} \qquad (7.2)$$

(Heat transfer = f(temperature gradient))

$$N = (\mathcal{D} + \varepsilon_M)\cdot\frac{\partial c_v}{\partial y} \quad \text{for mass transfer} \qquad (7.3)$$

(Mass transfer = f(concentration gradient))

The practical implication is that, if a correlating equation is known for one of the transport phenomena in a particular situation, then similar functional relationships can be applied to the remaining transport processes by simple insertion of the appropriate dimensionless parameters. Thus, momentum transfer can be applied to determine heat and mass transfer coefficients providing that skin friction data are available for the system of interest. Generally, it is difficult to obtain local friction coefficients (either directly or by velocity profile measurements). However, local mass transfer coefficients are relatively easy to measure so that the analogies between heat and mass transfer are far more commonly employed.

7.2 THE HEAT, MASS AND MOMENTUM TRANSFER ANALOGIES

Osborne Reynolds (Ref.88) was probably the first investigator to point out the similarity between the transfer of momentum and heat in boundary layer flows. This relationship can be expressed as:-

$$St = f/2 \qquad (7.4)$$

where St is the Stanton number, and 'f' is the coefficient of friction.

The relationship, however, is only valid if the molecular heat and momentum diffusivities are equal (Pr = 1). Furthermore, the eddy diffusivities are also assumed to be equal and shear stress and heat flux are supposed to vary in an approximately similar way in the boundary layer.

Prandtl (Ref.89) and, independently, Taylor (Ref.90) both accounted for the behaviour of the laminar layer adjacent to the transfer wall, in addition to the characteristics of the fully turbulent outer core, and modified Reynold's analogy yielding:-

$$St = (f/2)/[1 + u_\ell/u(Pr - 1)] \qquad (7.5)$$

where 'u_ℓ' is the velocity in the laminar-turbulent boundary layer and 'u' is the mean velocity in the turbulent core.

Equation (7.5) holds only for Pr close to unity (0.5 to 2). It also assumes that the eddy diffusivities for both heat and momentum transfer are zero in the laminar layer while in the turbulent layer the molecular diffusivities are negligible compared to the eddy diffusivities.

Von Karman (Ref.91) distinguished a third 'buffer' zone

which separates the laminar flow and the fully turbulent region. He assumed that heat and momentum are transferred by both molecular and turbulent transfer mechanism in the buffer zone. Heat and momentum transfers are thus connected by:-

$$St = (f/2)/\left[1 + 5\sqrt{f/2}\ \{Pr - 1\} + \ell n\{1 + 5/6\ (Pr - 1)\}\right] \quad (7.6)$$

This equation is derived by assuming that the turbulent diffusivities of heat and momentum are equal and, moreover, the molecular and turbulent diffusivities are additive in the buffer region. The equation, however, does not require the previous restrictions on Prandtl number range and results in better predictions, especially at higher Prandtl numbers. For enclosed flows, such as those in pipes, friction factors are often more easily obtainable than heat transfer coefficients, and the analogy is particularly useful. The average heat transfer rates over an area can be inferred from the viscous drag. Care must be taken to avoid the inclusion of any form drag, however, since this is not allowed for in the analogy. This is also true for the Reynolds and Prandtl-Taylor analogies.

The theoretical relationship between heat transfer and skin friction proposed by Reynolds was expressed by Colburn (Ref.92) as:-

$$St\ Pr^{2/3} = f/2 \quad (7.7)$$

The relationship was developed for laminar flow over flat plates but can also be applied to turbulent flow over these plates and, in a modified way, to turbulent flow in pipes. Later, Chilton and Colburn (Ref.93) extended the correlation to include mass transfer by diffusion so that,

$$St\ Pr^{2/3} = St_m Sc^{2/3} = f/2 \quad (7.8)$$

where 'St_m' is the mass Stanton number, and 'Sc' is the Schmidt number.

As already pointed out, the momentum analogy does not allow for the inclusion of any form drag. However, the relation between heat and mass transfer has been confirmed experimentally to be valid for a wide range of geometries and complicated flows. Consequently, heat transfer can often be determined from mass transfer experiments. The relationship can be derived as follows:-

Since, $St\,Pr^{2/3} = (h/\rho_a u\, C_p)\, Pr^{2/3} = j_H$ (7.9)

and, $St_m Sc^{2/3} = (b'/u)\, Sc^{2/3} = j_M$ (7.10)

Equating the j-factors, i.e. equations (7.9) and (7.10), yields:-

$$h = b' C_p \rho_a (Sc/Pr)^{2/3} \quad (7.11)$$

Although this simple relationship has been used frequently and successfully, Lewis (Ref.94) has pointed out its limitations due to the employment of a constant empirical factor $(Sc/Pr)^{2/3}$ to account for the differences in heat and mass diffusivities for all flow velocities. A more accurate form of the heat-mass transfer analogy must take into account the varying contributions of molecular and turbulent diffusivities across the boundary layer.

Jayatillaka (Ref.95) has given an extensive review of previous proposed distributions of turbulent/molecular momentum diffusivities across the boundary layer, and proposed an empirical expression to describe heat transfer in the near-wall region.

$$St = \sqrt{f/2}\,/\,Pr_t\sqrt{2/f} + A\left[(Pr/Pr_t)^{3/4} - 1\right]\left[1 + 0.28\,\exp(-0.007\,Pr/Pr_t)\right] \quad (7.12)$$

where, A = 8.32 and 9.00 for Pr_t = 0.9 and 1 respectively.

The corresponding mass Stanton number is found by substituting Sc and Sc_t for Pr and Pr_t respectively. Consequently, an analogy factor $\gamma = St/St_m$ can be found.

This analogy factor 'γ' can also be derived for the von Karman's expression given in Equation (7.6). The equation which is used to determine the heat transfer Stanton number (St) can be modified to yield the mass transfer Stanton number (St_m) by replacing the Prandtl number 'Pr' with the Schmidt number 'Sc'.

The values of the analogy factor $\gamma = St/St_m$ derived from the expressions given in Equations (7.6) and (7.12), are shown in Fig.7.1 for the situation of fully developed flow in a circular pipe. The Chilton-Colburn constant factor, $(Sc/Pr)^{2/3}$, is also plotted for comparison purposes. The value of the Prandtl number is that for air (Pr = 0.71)

and the Schmidt number is appropriate to the sublimation of naphthalene in air (Sc = 2.44). It can be seen that there are considerable discrepancies between the simple Chilton-Colburn analogy and the more complicated analogies, and that these increase as the Reynolds number increases. However, the use of Jayatillaka or Von Karman's expressions involves knowledge of the friction factor as well as the Schmidt and Prandtl numbers. For many flow situations, this is unavailable (as is the case in the present study), so that the Chilton-Colburn analogy has been preferred. Furthermore, the recent work of Vallis et al (Ref.38) has demonstrated the validity of this analogy in jet impingement systems. Previously, Ward et al (Ref.52), Davies et al (Ref.96) and Kabari (Ref.6) have also successfully employed the Chilton-Colburn analogy for studying jet impingement heat transfers. Thus, it was considered that the use of this analogy would yield useful heat transfer data. Nevertheless, heat and mass transfer experiments are only completely analogous if the following conditions are fulfilled:-

(i) Geometrical similarity exists.

(ii) Equal Reynolds numbers are maintained in the two systems.

(iii) The molecular diffusivities of heat and mass transfer are equal.

(iv) The turbulent diffusivities of heat and mass transfer are equal.

(v) Similar boundary conditions exist.

Conditions (i) and (ii) are, generally, easily satisfied by proper design of the experimental set-up. Condition (iii) is satisfied if the Prandtl and the Schmidt numbers are equal (i.e. the Lewis number is unity). It is difficult to conceive of a mass transfer technique which will satisfy this condition exactly when used to infer the convective heat transfer coefficients due to gas flows. The present study employed measurements of the sublimation rate of a naphthalene surface in an air flow to yield mass transfer data. Since, typically, Sc = 2.44 and Pr = 0.71, this condition is reasonably satisfied when estimating convective heat transfers from 'gas' jets. Alternative methods of measuring the mass transfer rate can more rigourously test the analogy since 'Sc' and 'Pr' can then differ greatly. For example, if an electro-chemical mass transfer technique (Ref.98) is used, the Schmidt number is typically 1,500 or above. Turbulent diffusivities are difficult to measure (see Ref.97) so that there is a paucity of data but investigators seem to agree that the ratio of these diffusivities of heat and mass transfer (i.e. turbulent Lewis Number) is close to unity.

With regard to condition (v), mass transfer techniques usually result in either the vapour concentration (naphthalene tests) or the ion concentration (in electro-chemi-

cal methods) remaining constant over the surface of interest. Thus, the heat transfer data derived from these tests correspond to a boundary condition in which the heat transfer surface is maintained at a constant temperature.

7.3 BRIEF REVIEW OF PREVIOUS MASS TRANSFER INVESTIGATIONS

Various mass transfer techniques have been used by previous investigators to estimate heat transfer coefficients so that only a selection of the large number of publications is discussed in this section to illustrate the progressive improvements made in the experimental techniques. Liquids such as water, benzene, toulene, carbon tetrachloride, chlorobenzene, tetrachloro-ethylene, and solids including ice, naphthalene, camphor, parachlorobenzol have been used as the mass transfer substance.

One of the earliest studies was carried out by Klein (Ref.99) in 1933, when he employed heated air flows to melt cylinders composed of ice. The overall heat transfer rates were proportional to the weight of melted ice. To determine the local mass heat transfers, the deformed cylinders after the test were initially cast in plasticine so that reproductions could then be made in plaster of Paris. The changes in the dimensions of the cylinders were obtained from these models. Errors occurred due to radiative transfer, conduction losses along the cylinders, and also since the humidity of the air was not taken into account. This publication, however, led to the further use of mass transfer techniques, particularly those employing solids with melting points above near-ambient temperatures. Moreover, these solids also have relatively high vapour pressures at ambient temperature so that the mass transfer coefficients can be calculated from the sublimation rates after only a comparatively short duration test.

For example, Winding and Cheney (Ref.100) cast naphthalene tubes using split brass moulds, and employed air as the working fluid. Average and local heat transfer coefficients were determined by the change in the weight of the naphthalene casting, and the variation in the local dimensions. These local variations were found by using 'feeler' gauges to measure gaps between the naphthalene castings and the original moulds. The Chilton-Colburn analogy was used to infer the heat transfers.

Significant improvements to the techniques were introduced by Christian and Kezios (Ref.101) who investigated mass transfer from sharp-edged naphthalene cylinders in axisymmetric flow with laminar boundary layers. They measured the local sublimation rates with a micrometer dial indicator and found that the average mass transfer ob-

tained by integrating these local results agreed to within ± 3% with those determined by the direct weight loss measurements.

Recently, Koopman and Sparrow (Ref.50) also employed profilometric measurements to estimate local mass transfer coefficients from a row of impinging jets. They employed a semi-automatic data acquisition system to simplify the determination of local naphthalene mass losses. Comparisons between overall mass transfers obtained by direct weighing and those from numerical integration of the local mass transfer distributions were within 6%.

Electrochemical techniques can also be employed to determine mass transfers and have been comprehensively reviewed by Mizushina (Ref.98). Of all the many investigations using this technique, the work of Vallis et al (Ref. 38) has the most relevance to the present study since they also examined jet impingement mass transfer.

Previous jet impingement studies at Cranfield have used naphthalene techniques extensively. Surface profilometry was used by Jones (Ref.2), Kabari (Ref.6) and Oladiran (Ref.5). Dunn (Ref.25) measured the average mass transfers due to impingement of swirling jets of air by determining the loss in weight of naphthalene cast in trays. Ward et al (Ref.52) also used these techniques to determine local and average heat transfers in models of rapid heating furnaces.

In the present study, the local mass transfer coefficients from both single and multiple jets were determined by a "thin-film naphthalene technique". Average values were obtained by integrating these local values. Owing to its importance in the present work, this 'thin film technique' has been described in detail in the next section.

7.4 THE 'THIN-FILM' NAPHTHALENE TECHNIQUE.

Wilkie and White (Ref.103) initially used the method to examine the variation of heat transfer coefficients along the ribbed surface of AGR nuclear fuel elements. The element was coated with a 'thin-film' of naphthalene and then mounted in a perspex chamber through which air (the test fluid) was drawn. The time taken for the naphthalene to clear from the surface was inversely proportional to the mass transfer coefficient. Coating was achieved by using a simple spray gun attached to the tool holder of a lathe. This was fed with a solution of naphthalene dissolved in acetone, and it was traversed automatically while the fuel element was simultaneously rotated between the lathe centres. In this fashion, a layer of naphthalene of consistent thickness (approximately 0.025mm) was sprayed in a single traverse. The specific weight per unit area of the coating was not measured so that only

the relative values of the mass transfer coefficients were obtained. Figure 7.2 presents a comparison of their results with heat transfer data obtained directly for similar conditions. It may be concluded from their work that the 'thin-film' spray technique is a quick and inexpensive method of obtaining qualitative mass transfer distributions and it can be especially useful in predicting the position of 'hot spots'.

More recently, however, investigators at the Central Electricity Research Laboratories (C.E.R.L.), Leatherhead, developed a spray rig which produced a thin-film of naphthalene in a controlled manner. The exact weight (per unit area) of the naphthalene coating was determined by weighing a 'dummy' surface which was sprayed under the same conditions. Therefore, absolute values of mass transfer coefficients were found from the evaluation of the 'time for clearance'. The details of their device and technique are presented in publications by Neal et al (Ref.104) and Neal (Ref.105). They dissolved crystalline naphthalene in an organic solvent with the proprietary name of "Inhibisol" (produced by Bestobell Chemicals Ltd., Cramlington), and fed this solution under pressure to the central nozzle of a co-axial jet. The naphthalene solution issuing from this central nozzle is atomised by the air jet exiting from the outer annulus, thus forming a conical spray. The annular jet also prevents build-up of solid naphthalene at the nozzle exit which would otherwise result in rapid blockage. The flow rates of the solution and the atomising air are controlled by needle valves. Cylindrical surfaces were coated in a similar fashion to Wilkie and White (Ref.103), i.e. the automatic traverse of a lathe was employed. However, Neal et al (Ref.104) also developed an automatic linear motion spray table which uniformly coated flat surfaces. A naphthalene thickness of approximately 0.015mm was obtained at a solution flow rate of 60 mm^3/s, and a spray head traverse velocity of 0.8m/s.

Figure 7.3 presents the results obtained by Neal (Ref.105) using this thin film technique for flow in a cylindrical pipe, and comparisons are made with direct heat transfer results. It was concluded that the thin-film technique coupled with a suitable mass transfer analogue yielded forced heat transfer accurately and economically. A further advantage of the method is that it also provides data over the full field of interest. Moreover, the development of the 'clearance pattern' is visual and, therefore, can be used to demonstrate various flow phenomena.

A similar 'thin-film' naphthalene spray technique was chosen for the present work since it offers the following advantages:-

(i) It appears to yield heat transfer data which are just as accurate as those found by other mass transfer methods.

(ii) The test duration is considerably reduced in comparison with the alternative profilometric method for determining local naphthalene sublimation rates.

(iii) It is difficult to determine whole field data in flow fields as complicated as those associated with multiple jets using other techniques.

(iv) Visualisation of the clearance patterns can be especially useful in setting up the experiments with multiple jets.

Thus, a suitable spray rig was developed to coat flat surfaces with a thin film of naphthalene, and this rig is described in Chapter 8.

7.5 DETERMINATION OF MASS TRANSFER COEFFICIENTS FROM MEASUREMENTS OF NAPHTHALENE SUBLIMATION RATES.

Isothermal models which conform to the necessary conditions of dynamic and geometric similarity mentioned in section 7.2 may be used to obtain convective heat transfer data from mass transfer measurements. If a naphthalene sublimation technique is employed, a mean mass transfer coefficient 'b''may be defined as:-

$$m/t = b' A_n (C_n - C_o) \qquad (7.13)$$

where 'm' is the sublimation weight loss during the test duration and A_n is the area over which this loss takes place. C_n and C_o are the concentration of naphthalene vapour at the test surface and in the free stream respectively.

The partial pressure of the naphthalene vapour is negligibly small so that the vapour can be regarded as a perfect gas with temperature 'T_N' at the mass transfer surface. Thus,

$$C_n = p_n/R_n T_n \qquad (7.14)$$

where p_n and T_n are vapour-solid equilibrium values.

Moreover, the vapour concentration of the naphthanlene in the free stream can usually be neglected, i.e. $C_o = 0$. Thus, equation (7.13) can be reduced to:-

$$b' = \frac{m}{A_n t} \cdot \frac{R_n T_n}{p_n} \qquad (7.15)$$

Although sublimation depresses the surface temperature of naphthalene below that of the free stream, this difference is generally negligible (Ref.106). Therefore, the saturation vapour pressure can be evaluated at the mean free stream temperature. Several empirical correlations (Refs.107-109) have been proposed for the variation of vapour pressure with temperature in the literature, see Appendix C. In this study, the relationship of Sherwood and Bryant (Ref.107) has been used since this yields approximately medial values when compared to other correlations, see Figure 7.4. The general properties of naphthalene are also described in Appendix C.

Heat transfer coefficients can be evaluated from a knowledge of mass transfer coefficients by assuming the equality of the respective j-factors (i.e. the Chilton-Colburn analogy) when coupled with equation (7.15). This yields:-

$$h = (m/A_n t) \cdot \rho_a . C_p (R_n T_n / p_n)(Sc/Pr)^{2/3} \qquad (7.16)$$

where 'h' is the heat transfer coefficient, and 'ρ_a' is the density of air.

The values of Schmidt numbers can be found by using the expression:-

$$S_c = 7.00\ (T)^{-0.185}$$

where 'T' is in degrees Kelvin.

This equation is valid for the range 100 to 500 K (Ref.110).

The results obtained in Equation (7.16) may also be applied to determine local values by choosing suitable 'A_n' and estimating a local mass loss.

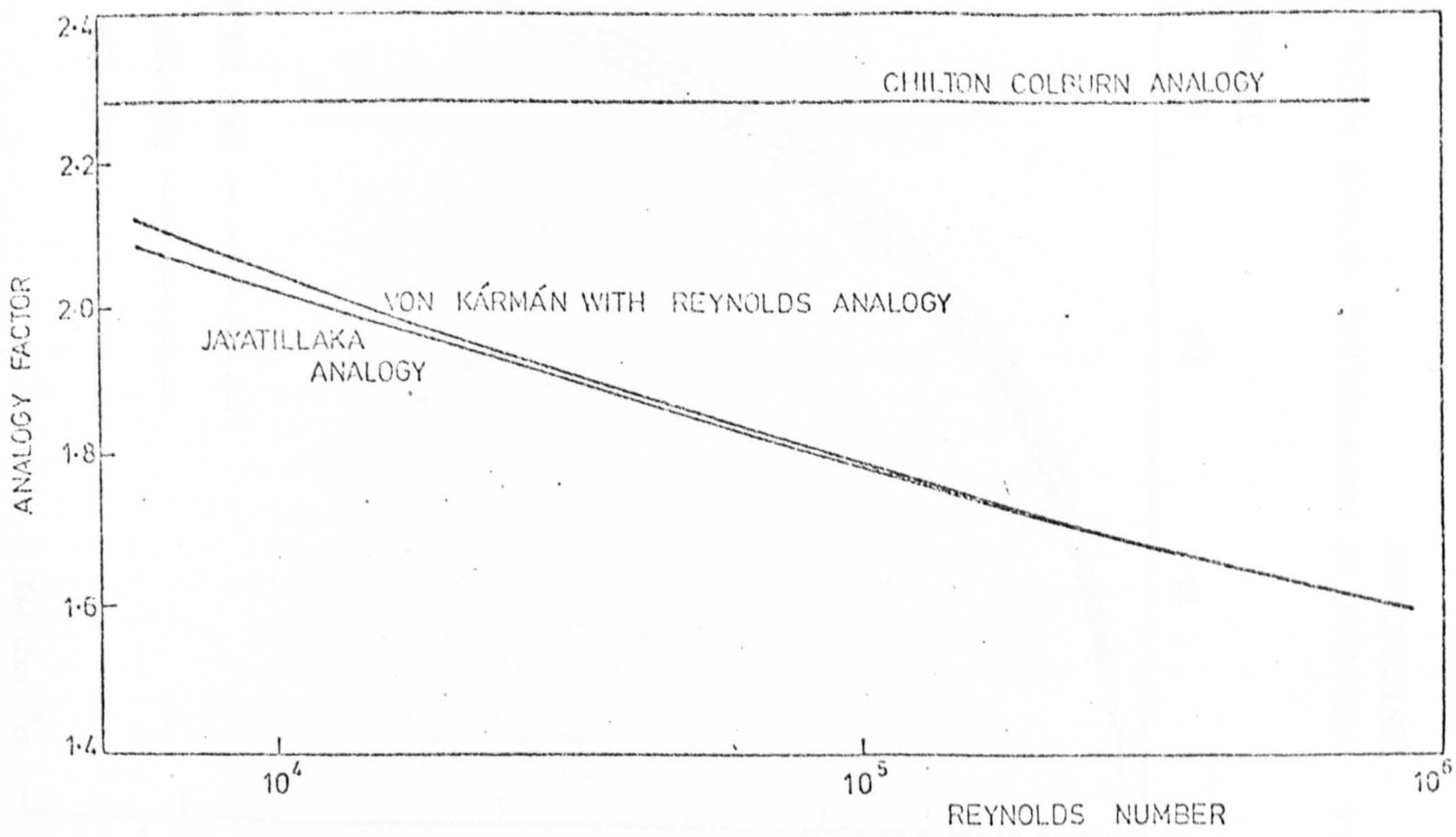

Fig. 7.1 GRAPH SHOWING MASS / HEAT TRANSFER ANALOGY FACTORS vs REYNOLDS NUMBER

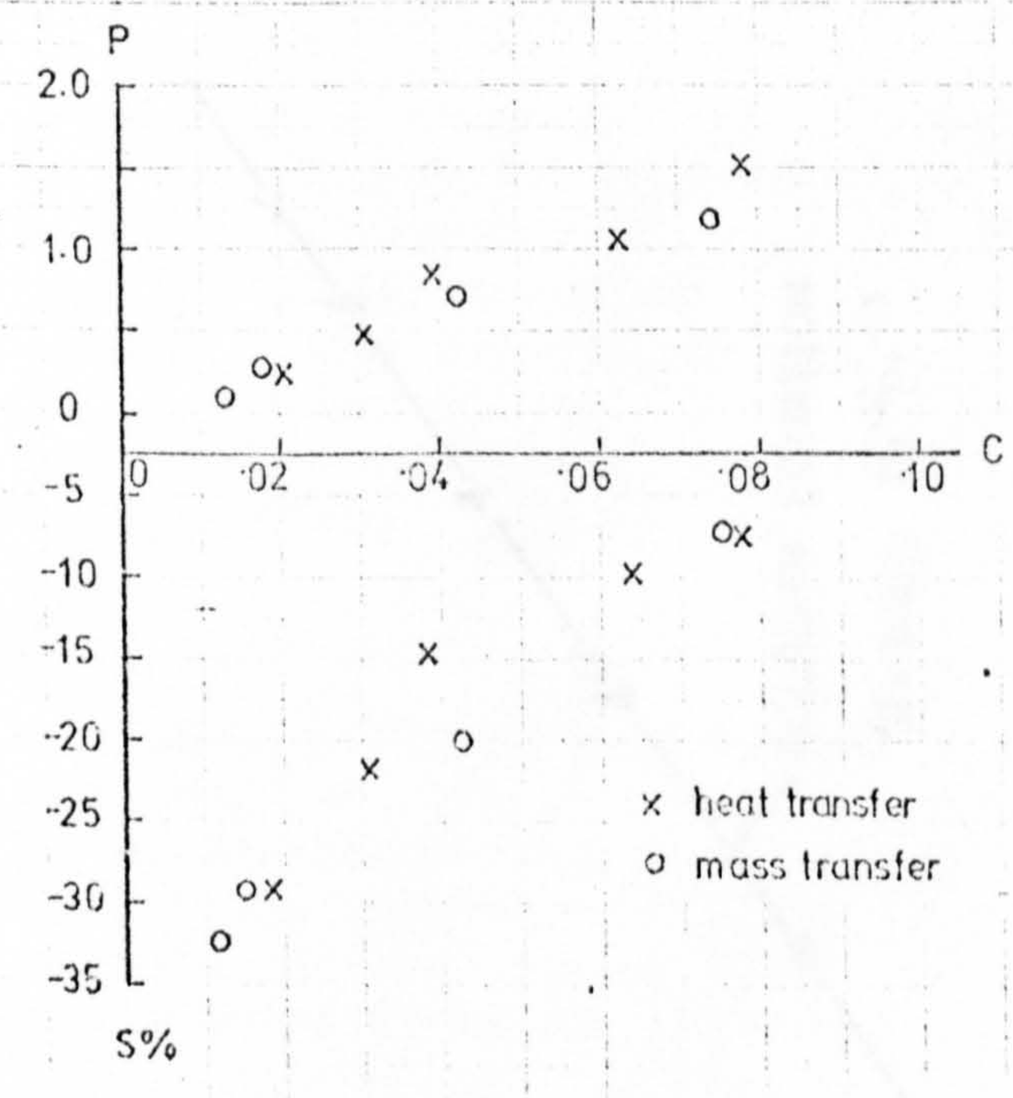

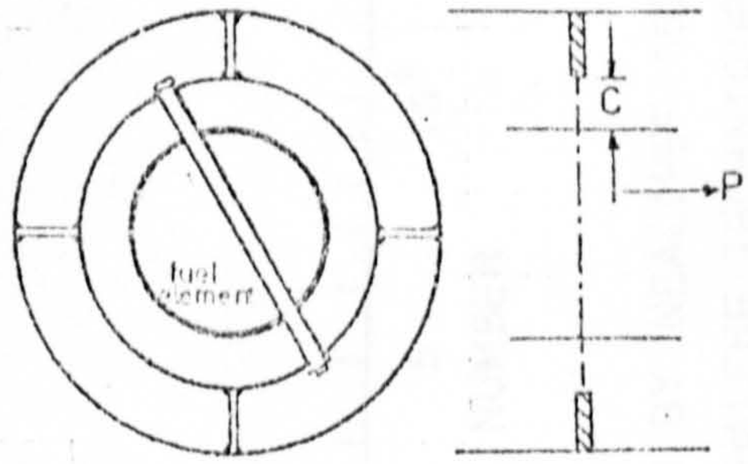

(a) simplified design of brace

S Maximum value of % change in Stanton number from fully developed condition.

P Distance of S from centreline of brace / Equivalent dia.

C Radial clearance between rib tip & bore of brace / Equivalent diameter

Fig. 7.2 COMPARISON OF HEAT AND MASS TRANSFER DATA OBTAINED BY REF. 103.

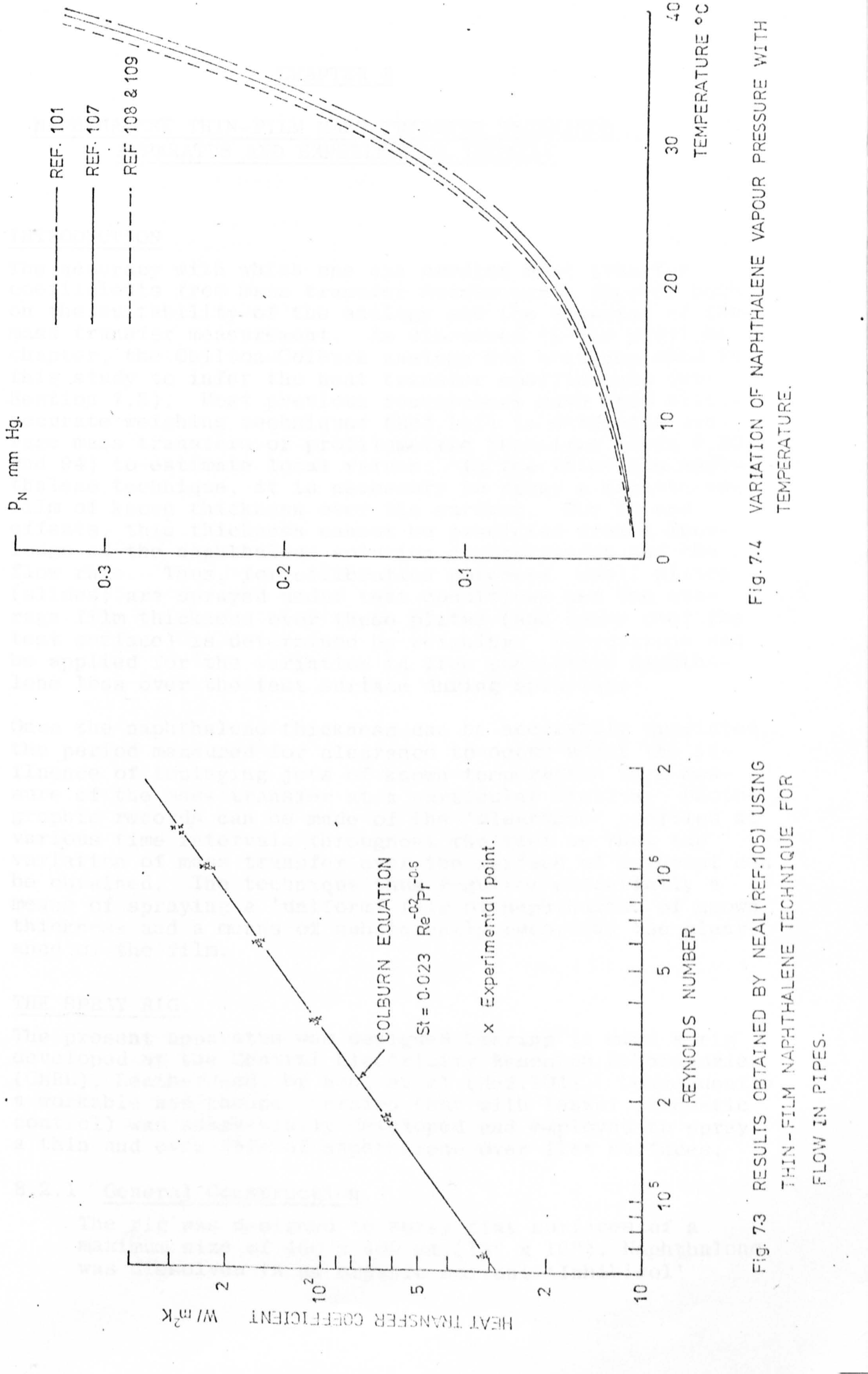

Fig. 7.4 VARIATION OF NAPHTHALENE VAPOUR PRESSURE WITH TEMPERATURE.

Fig. 7.3 RESULTS OBTAINED BY NEAL(REF.105) USING THIN-FILM NAPHTHALENE TECHNIQUE FOR FLOW IN PIPES.

CHAPTER 8

NAPHTHALENE THIN-FILM MASS TRANSFER TECHNIQUE - APPARATUS AND EXPERIMENTAL DETAILS

8.1 INTRODUCTION

The accuracy with which one can predict heat transfer coefficients from mass transfer measurements depends both on the suitability of the analogy and the accuracy of the mass transfer measurement. As discussed in the previous chapter, the Chilton-Colburn analogy has been employed in this study to infer the heat transfer coefficients (see Section 7.2). Most previous researchers have used either accurate weighing techniques (Ref.111) to determine average mass transfers or profilometric technique (Refs.6,50 and 94) to estimate local values. In the thin-film naphthalene technique, it is necessary to spray a naphthalene film of known thickness over the surface. Due to end effects, this thickness cannot be predicted from a knowledge of the naphthalene solution concentration and the flow rate. Thus, for calibration purposes, small plates (slides) are sprayed under test conditions and the average film thickness over these plates (and hence over the test surface) is determined by weighing. Corrections can be applied for the variation in free convective naphthalene loss over the test surface during spraying.

Once the naphthalene thickness can be accurately predicted, the period measured for clearance to occur under the influence of impinging jets of known temperature is a measure of the mass transfer at a particular station. Photographic records can be made of the 'clearance' profiles at various time intervals throughout the test so that the variation of mass transfer over the surface of interest can be obtained. The technique thus requires essentially a means of spraying a 'uniform' film of naphthalene of known thickness and a means of subsequently recording the clearance of the film.

8.2 THE SPRAY RIG.

The present apparatus was designed bearing in mind a rig developed at the Central Electricity Research Laboratories (CERL), Leatherhead, by Neal et al (Ref.104). Consequently, a workable and cheaper version (but with lesser automatic control) was successfully developed and employed to spray a thin and even film of naphthalene over flat surfaces.

8.2.1 General Construction.

The rig was designed to spray flat surfaces of a maximum size of 460 x 400 mm.(18" x 16"). Naphthalene was dissolved in an organic solvent 'Inhibisol'

(supplied by Bestobell Chemicals Ltd., Cramlington) and fed under pressure to the central nozzle of a coaxial jet where it was finely atomised by mixing with high pressure (4-5 atm) air (see Fig.8.1 and Plate 2). The resulting jet was sprayed onto a perspex plate. The solvent then evaporated leaving a fine film of naphthalene.

The mechanical arrangement was maintained as simple as possible so that the movement of the spray nozzle and the plate was controlled by independent mechanisms. The whole operation, i.e. traverse of the spray head and advancement of the plate, was controlled by limit switches and electronic logic circuit designed in the Instrumentation Section at Cranfield.

Plate 3 shows a general view of the spray rig. To facilitate an adequate explanation, the description of the rig has been split into the various functional units.

8.2.2 Mechanical Details

The spray nozzle, shown in Fig.8.1 and Plate 2, was made according to the design specified by Neal (Ref. 105). This spray nozzle was mounted on a carriage block, 50.8mm x 25.4mm x 22.5mm, which was guided by means of two 10mm diameter stainless steel bars, each 610mm long. Two linear roller bearings (Unimatic Engg.) were employed to reduce the sliding friction between the carriage and the guide bars. These bars were held parallel by two support blocks at each end. The carriage was traversed in the horizontal plane by means of a string. The appropriate to and fro motion was achieved by reversing the rotation of the d.c. motor (variable speed, 12V). Appropriate gearing reduced the linear speed of the carriage to give velocities ranging from 0.8 m/s to 1.2 m/s. Two limiting switches were fixed near the end blocks to restrict the length of traverse. A striker plate was mounted on the carriage to actuate these limiting switches. Fig.8.2 shows diagrammatically the assembly of this set-up.

Since it is essential for the sprayed layer to be of constant thickness, the sprayhead should travel at a constant velocity during the spraying operation. Thus, the acceleration period after reversal of the carriage should be short. This motion was checked by observing the displacement of the carriage with time on an oscilloscope trace. Plate 4 shows the displacement trace for various d.c. motor speeds. The variation of the carriage position with time is linear for that part of the travel during which the plate is sprayed, i.e. the sprayhead travels at a constant velocity so that

a uniform coating across the plate is obtained, provided that the flow of the solution is also invariant.

The plate to be sprayed was located on a carrier plate beneath the sprayhead. The carrier plate was mounted on a 910mm long lead-screw (16 tpi). This lead-screw was driven by a stepper motor (ASTROSYN) which controls the feed rate of the plate very accurately. The stepper motor can be controlled to give a maximum of 1000 steps, with each step being as small as 1.8 degrees. Fig.8.3 shows the aspect of the assembly associated with the movement of the plate.

The sequence of the spraying operation, as controlled by the electronic logic circuit, was:-

1. The stepper motor rotated a fixed number of steps (previously selected) to give the required displacement to the spray plate normal to the axis of traverse of the spray head.

2. The d.c. motor was then energised to drive the carriage and sprayhead across the plate so that a strip of the plate was sprayed with naphthalene.

3. The carriage travel was arrested by a limit switch and the d.c. motor rotation reversed such that the carriage returns along the same path in the opposite direction, thus spraying a second layer of naphthalene on top of the first. This motion was stopped by the other limiting switch.

This second limit switch de-energises the d.c. motor and restarts the stepping motor so that the plate is again advanced. The sequence is repeated until such a time as the whole plate has been completely sprayed with a uniform coating of naphthalene. Typically, the mass of naphthalene sprayed varied from 1.4 to 2.8 mg/cm^2.

8.2.3 Control of the Spraying Operation.

The sequence of the spraying was determined by a 'control unit' which generated signals to either the stepper motor or the d.c. motor as required. The logic of the control unit was activated by limit switches. The rotational speeds of the d.c. motor were set on a dial, while the number of 'steps' advanced by the stepper motor was selected on a counter. The sequence of operation has already been described in Section 8.2.2. Figure 8.4 illustrates this sequence and also the layout of the various

controls. It may be noticed from Fig.8.4 that the actual time spent spraying the plate is only a fraction of the total cycle. The delay at each end of the spray head traverse during spraying actually helps to dry out the deposited film of naphthalene. The speed of the traverse of the spray head over the plate is essentially uniform as can be seen from the traces of the displacement of the head obtained on an oscilloscope, see Plate 4.

8.2.4 Flow Control

The flow circuit is diagrammatically shown in Fig. 8.5 The naphthalene dissolved in the 'Inhibisol' was contained in a steel bottle (5 litre capacity). This vessel was tested to a pressure of 15 atmospheres. In the preliminary tests, a concentration of 200 grams of naphthalene per litre of solvent was used but this often resulted in clogging of the spray nozzle by naphthalene particles. The concentration, therefore, was reduced to 100 grams per litre to avoid this problem.

Compressed air (at 4 atmospheres) and the naphthalene solution were fed to the sprayhead through nylon tubes. The solution was supplied to the fine diameter central nozzle tube, shown in Fig.8.1., whilst the air was supplied to the outer annulus tube. The result was a finely atomised conical spray. It was important that the nozzle produced a spray layer which was considerably wider than the pitch between the adjacent passes. Thus, the spray nozzle was mounted at least 25mm above the plate and also inclined 30-45 degrees to the vertical.

The flow of the naphthalene solution was monitored by a rotameter (Fisher Porter FP 1/8 20-G-5/81). Except in some of the preliminary tests, the flow rate was maintained about 0.2 ml/s. The flow rate of the solution and the compressed air were comparatively small, so that two needle values (Edwards High Vacuum) were necessary for final adjustment and control. It was not found necessary to measure the air flow.

8.3 TEST SURFACES

To study the heat transfer due to jet impingement, three different sizes of test target Perspex plates were used. The first plate was 460mm x 410mm x 6mm, used initially for single jet studies, covering a field of 8 nozzle diameters (r/D = 8) measured from the stagnation point. It was then considered that with higher swirl jets the 'r/D' field should be increased to accommodate the greater spread. Thus, a second plate of 420mm x 420mm

x 3mm was fitted flush with a larger plywood plate so that the Perspex formed one quarter of the area of the whole plate (see Fig.8.6). This extended the 'r/D' field to 16. Since the multiple jets studies were carried on a separate rig, a third plate of dimensions 370mm x 370mm x 3mm was used to cover the array of 3 x 3 square jets.

To assist in the interpretation of the photographic records, all these plates were inscribed with a series of grid lines forming 1.25mm squares. The plate used for the multiple jet studies had a further finer 0.625mm square grid. The grooves of the grid lines were filled with black ink, which provided a suitable contrast with the background of naphthalene.

These test plates are mounted in the impingement test rigs as described in Chapter 4.

8.4 EXPERIMENTAL DETAILS (SPRAYING)

8.4.1 Control of Naphthalene Film Thickness.

For successful application of the thin-film naphthalene mass transfer technique, it is essential that the film is of uniform thickness over the plate. It is also important to ensure that the naphthalene surface finish is smooth, otherwise some particles may be eroded away during the test. Furthermore, the resultant surface roughness could effect and increase the mass transfer rate. These requirements can be fulfilled if only small amounts of naphthalene are sprayed during each traverse and also if the sprayed solution does not flow freely over the surface, i.e. the solvent must evaporate almost immediately after spraying.

One of the advantages of the naphthalene spray technique is that the thickness of the film can be controlled so that the suitable test duration can be obtained. The factors which effect the quality and thickness of the deposited film include:-

(i) The concentration of the solution. The higher the concentration of naphthalene in the solution, the thicker the layer of naphthalene sprayed during each pass. As previously mentioned, a concentration of 200 g/l resulted in clogging of the spray nozzle and a concentration of 100 g/l was then used.

(ii) The solution flow rate. The main consideration in dictating the flow rate is that the amount of solution sprayed must not result in the solution flowing freely over the surface of the plate.

(iii) Air pressure. Airline pressure effects the atomisation of the solution and, to some extent, the clogging of the nozzle.

(iv) Surface and nozzle geometry. The distance of the nozzle from the plate and it's inclination were as recommended by Neal (Ref.105) and were found to be acceptable. However, these factors did not affect the spray to a great extent.

(v) Stepper motor feed rate. The spread of the jet was fairly wide so that low stepping rates resulted in a thick (fine) spray since each station on the plate was subjected to numerous spray passes. However, this also resulted in long spray duration to cover the plate. A stepping rate of 200 steps (i.e. a linear displacement of 1.6mm) was chosen so that a length of about 40 cms. could be sprayed in an hour.

(vi) Traverse speed. The effect of various d.c. motor speeds on the velocity of the sprayhead have already been illustrated in Plate 4. The traverse speed selected for most of the tests was 0.9 m/s. Higher speeds involved long acceleration periods whilst lower speeds could result in the deposition of excessive solution on the plate.

It should, however, be pointed out that all the above-mentioned factors are interacting. Trial tests were carried out to achieve a suitable combination to give the required qualities in the naphthalene surface. The various settings used were as follows:-

(a) Solution concentration : 100 g/l.

(b) Solution flow rate : 0.2 ml/s.

(c) Air pressure : 4 atmospheres.

(d) Nozzle position : 22mm above the spray surface at an angle of 45°.

(e) Plate feed rate : 200 steps; linear feed 40 cms/hr.

(f) Sprayhead traverse : 0.9 m/s.

8.4.2 Measurement of Naphthalene Film Thickness.

To determine the average naphthalene mass concentration on the test surface, six thin glass slides of $75 \times 25mm^2$ surface area were mounted at various positions on the surface. The weight gained during spraying them yielded the film mass concentration. A balance with a resolution of 10^{-4} grams was used for weighing the slides. The scatter between various calibration slides in the same test was about 3-5%. In later tests, thin plastic slides were used and this reduced the scatter (see also Section 9.2).

Figure 8.7 illustrates the various positionings used for the slides. If the slides were not mounted in line, their weights varied due to the free convection loss. This could, however, be allowed for to give an average weight per unit surface area.

The average film mass data must be corrected to allow for the rate of naphthalene loss by natural convection before the actual jet impingement mass transfer test. Two loss components can be identified. The first applies to the whole plate and represents the loss during the period between the end of the spraying operation and the beginning of the actual mass transfer test. The other component occurs during the spraying and varies linearly over the plate. For a 410mm long plate, spraying can take as long as 3500s; the resultant film density (naphthalene mass per unit area) variation can be 5-7% between the first and the last deposited layer. The necessary corrections can be determined from a knowledge of the spray period and the period from the end of spray to commencement of test.

8.4.3 Recording of Clearance Patterns.

To evaluate the mass transfer from the jet impingement tests, it is necessary to make a record of the clearance of naphthalene as the test proceeds. Photographs taken at suitable intervals can be used for this purpose and curves of the radial variation (r/D) of mass transfer coefficient can be obtained from successive photographs. Average mass transfer can then be found, if required, by integrating these local variations. The whole procedure involved in determining the mass/heat transfer coefficients from a typical pattern is given in Appendix D.

The camera used in the tests was a Practicka LTL.3 with a wide angle Flektagon 35mm lens. Clearance patterns were recorded using a black and white 125 ASA film. The aperture settings were adjusted manually to f 5.6 with an exposure time of 1/30 seconds. This, however, was dependent on the lighting arrangement.

DRAWING NO. PD 12291

SCL	MODIFICATION
A1	—

ALL DIMENSIONS IN ~~MILLIMETRES~~ INCHES UNLESS OTHERWISE STATED.

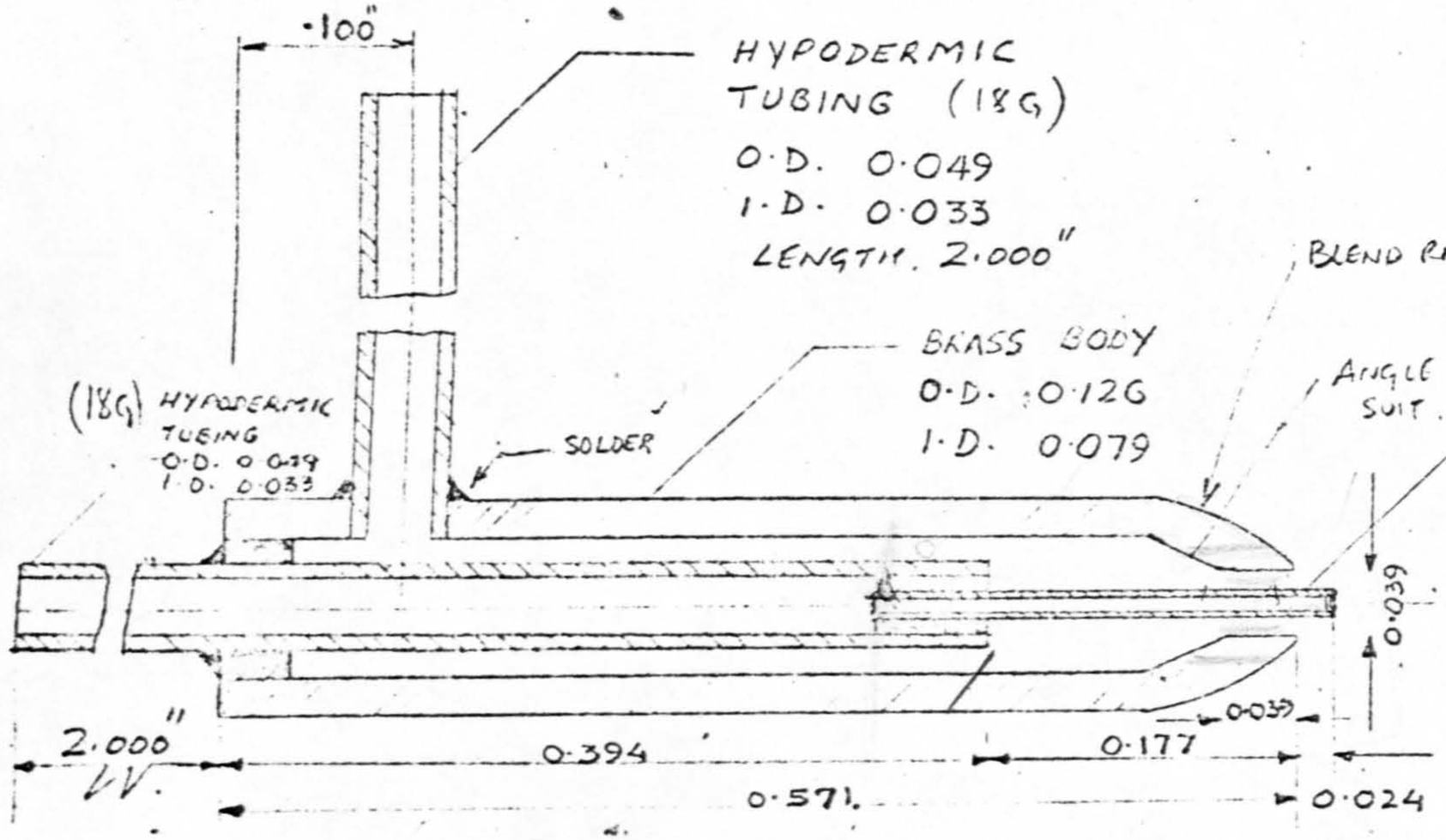

Fig. 8.1 THE SPRAY NOZZLE

1	PD12291	SPRAYING NOZZLE	2	EX SME					
ITEM	PART No.	DESCRIPTION	No. OFF	MAT'L	SPEC.	REMARKS			

THIRD ANGLE PROJECTION

GENERAL TOLERANCE ON DIMENSIONS
MACHINED ±·005
CASTINGS
SHEET METAL WORK AS STATED
EDGE MARKS SHOWN THUS ⌐¬
FINISH OF SURFACE SHOWN THUS √

JOB No.	No. OF SETS REQ'D
	1
USED ON DRG.	

SHEET SIZE A 3
SCALE 10/1
FINISH SELF

DRAWN	CHK'D	APP'D	ISSUED
M PRICHARD			
17-12-76			

ISSUED BY SME.

CRANFIELD INSTITUTE OF TECHNOLOGY
CRANFIELD.

TITLE:- SPRAYING NOZZLE

DRAWING No. PD 12291

SHT. 1 OF 1 SHEETS

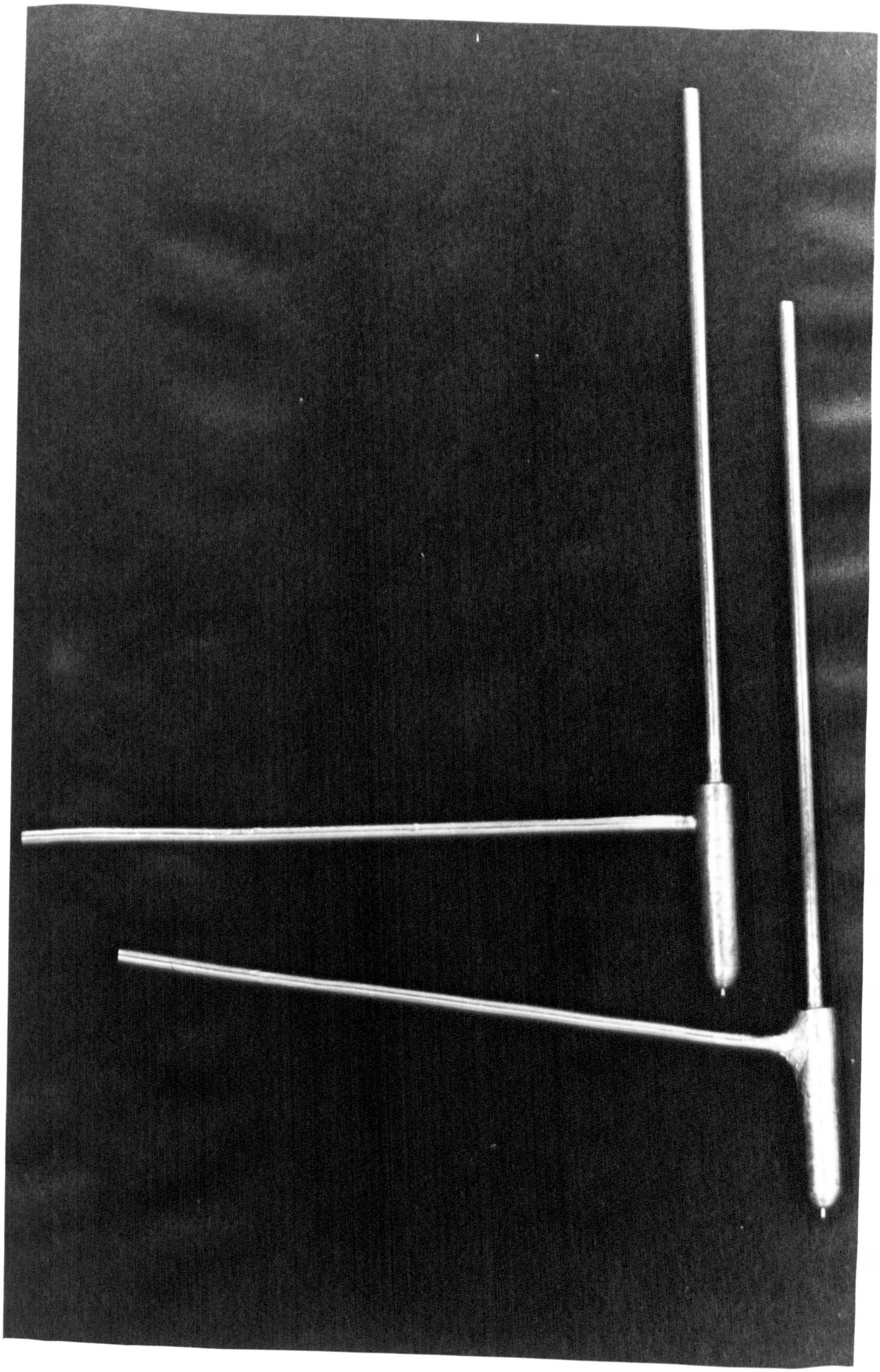

PLATE 2 THE SPRAY NOZZLE

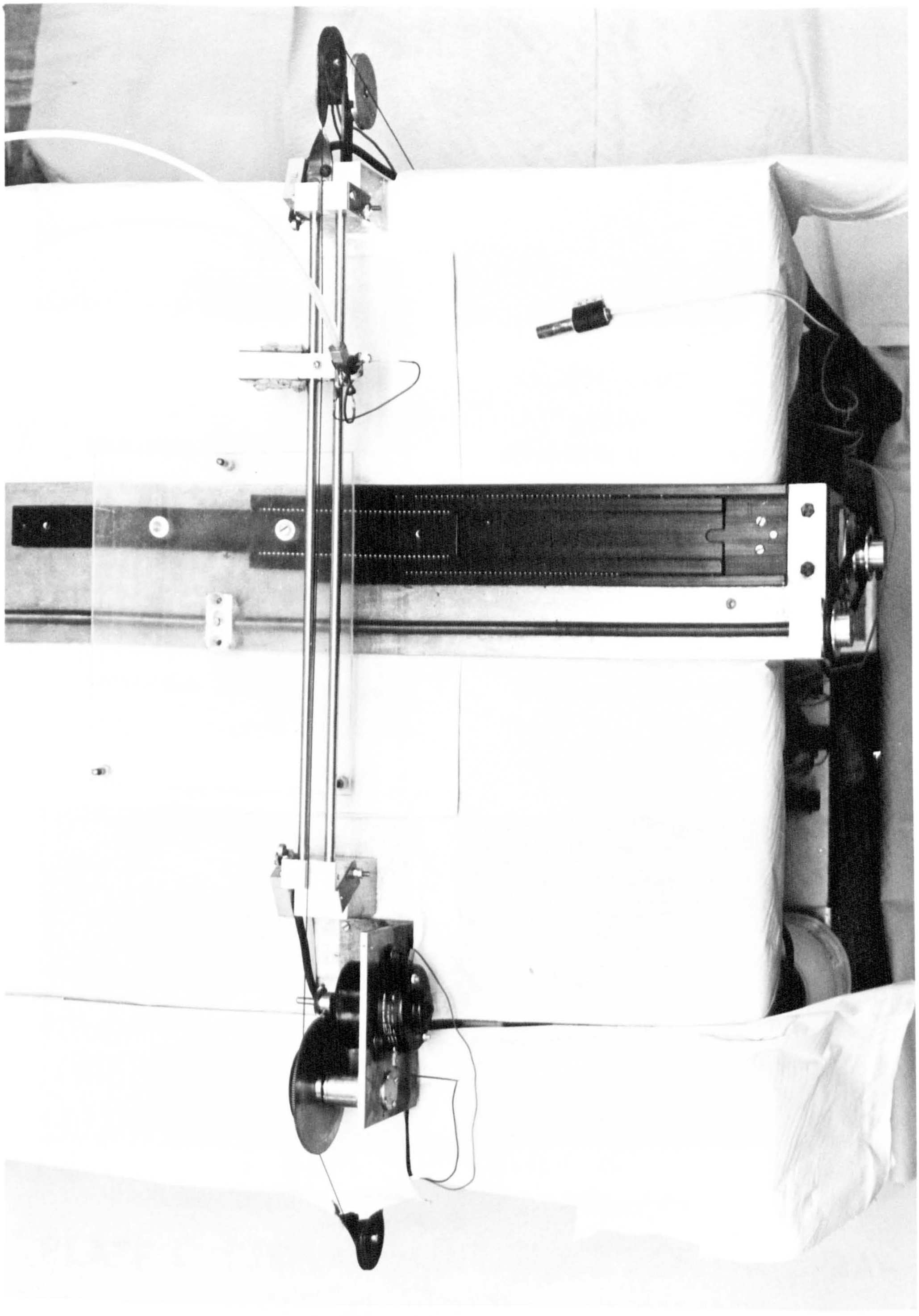

PLATE 3 GENERAL VIEW OF THE SPRAY RIG

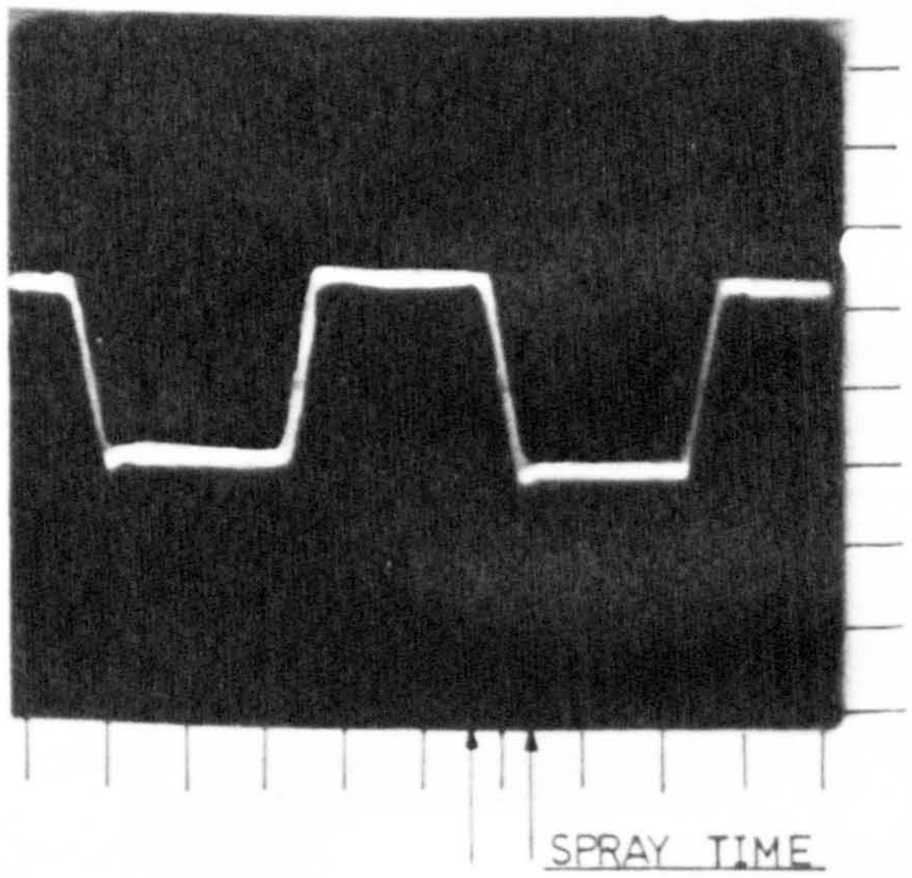

1·0 s / div

SPRAY-HEAD VELOCITY = 0·9 m / s

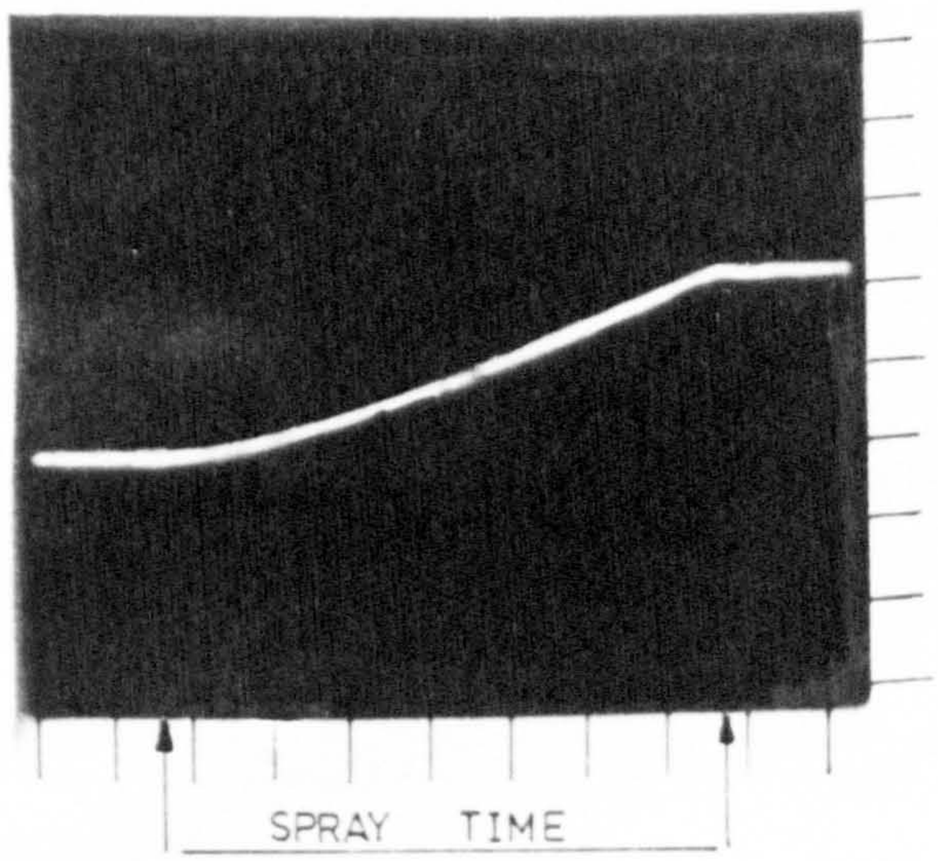

0·1 s / div

SPRAY-HEAD VELOCITY = 0·9 m / s

[NOTE LINEAR TRACE DURING SPRAY]

SPRAY-HEAD VELOCITY OF 0·9 m/s USED FOR ALL TESTS

0·1 s/div

SPRAY-HEAD VELOCITY = 1·2 m / s

[NOTE NON-LINEARITY DURING SPRAY]

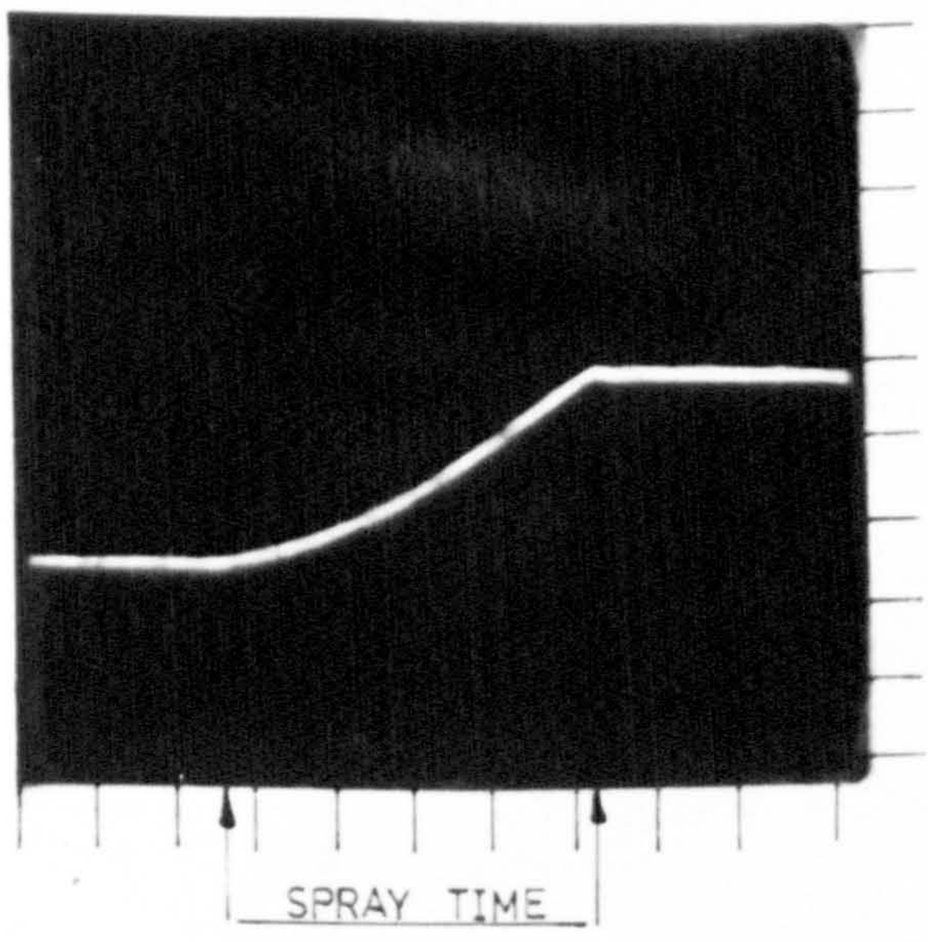

0·1 s/div

SPRAY-HEAD VELOCITY = 0·8 m/s

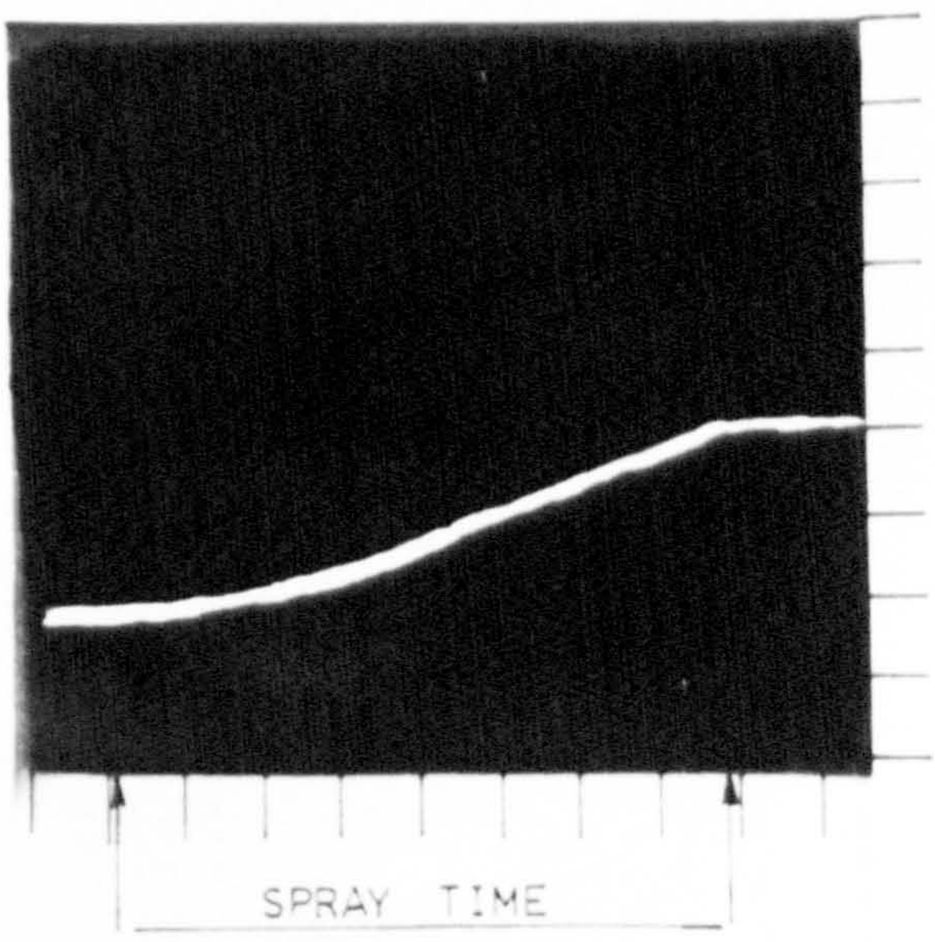

PLATE 4 DISPLACEMENT TRACES OF THE SPRAY-HEAD AT VARIOUS VELOCITIES

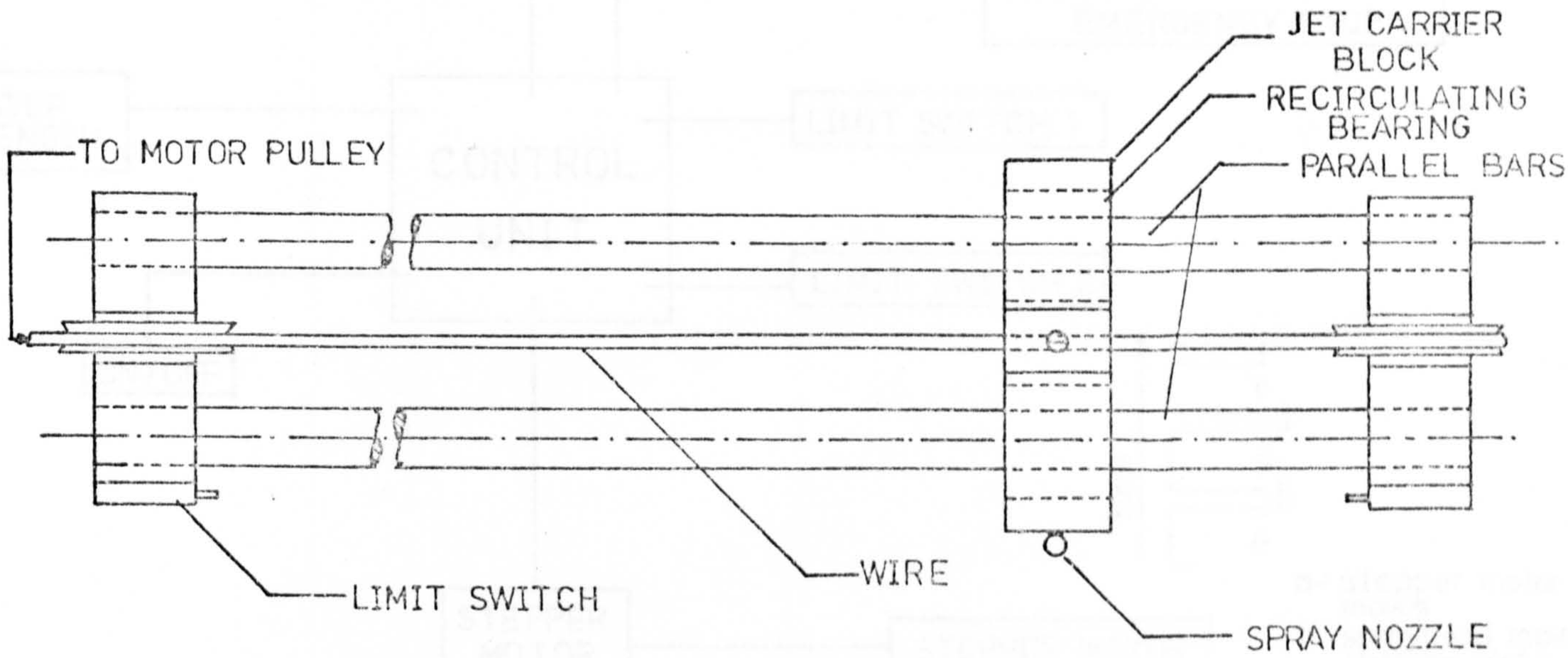

Fig. 8.2 SCHEMATIC VIEW OF THE SPRAY NOZZLE MOVEMENT

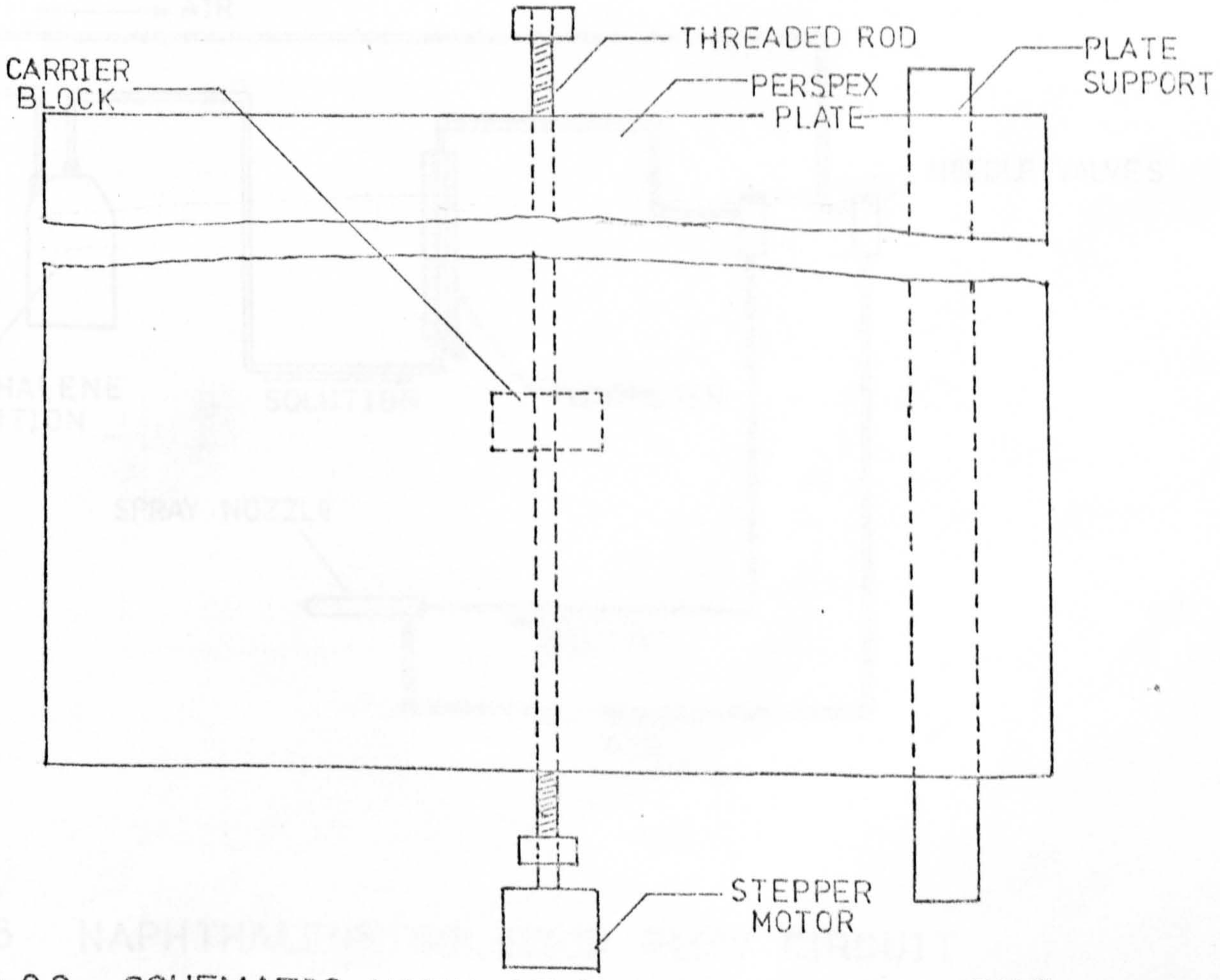

Fig. 8.3 SCHEMATIC VIEW OF THE PLATE MOVEMENT

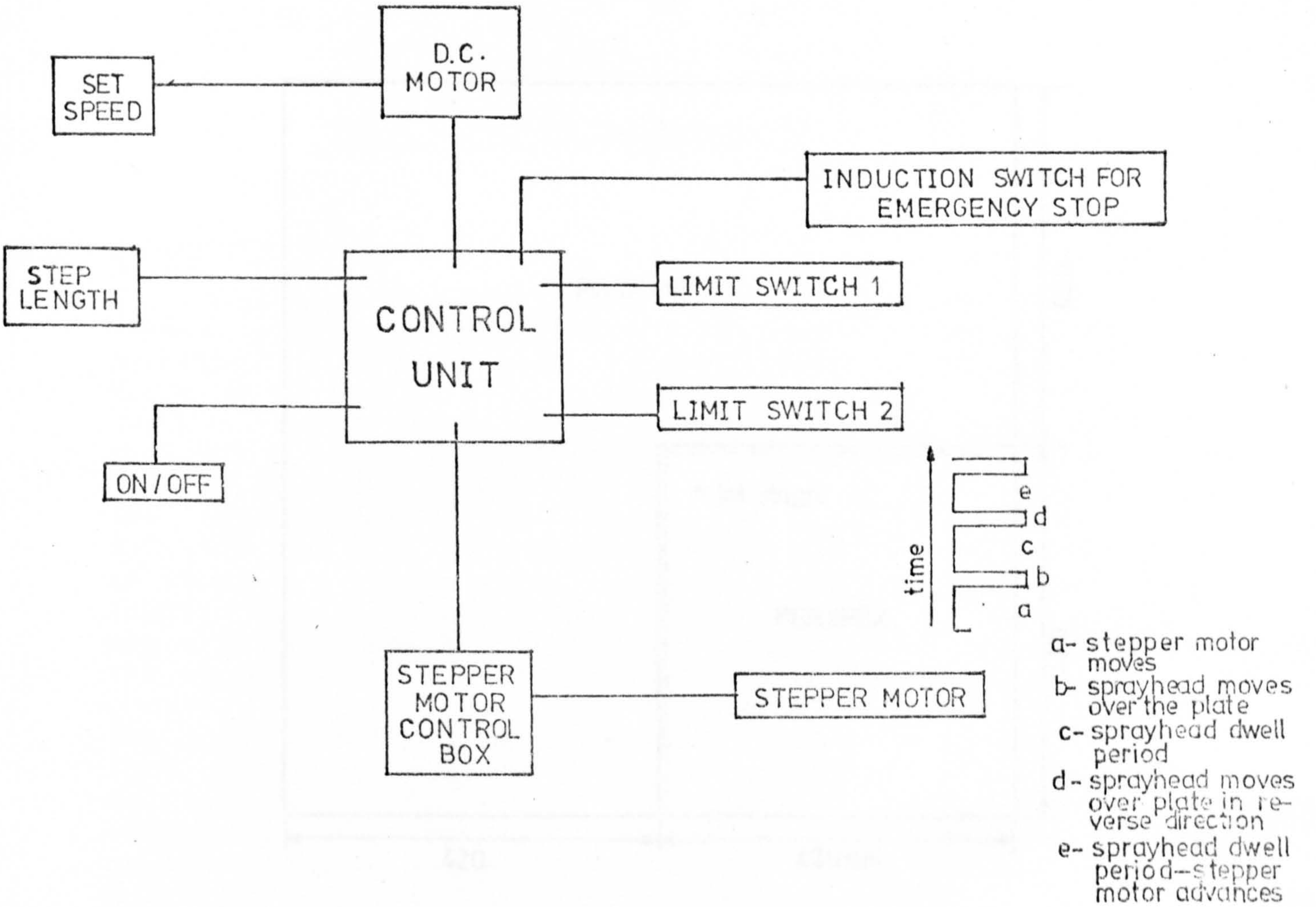

Fig. 8.4 LAYOUT OF THE VARIOUS CONTROLS [Electronic]

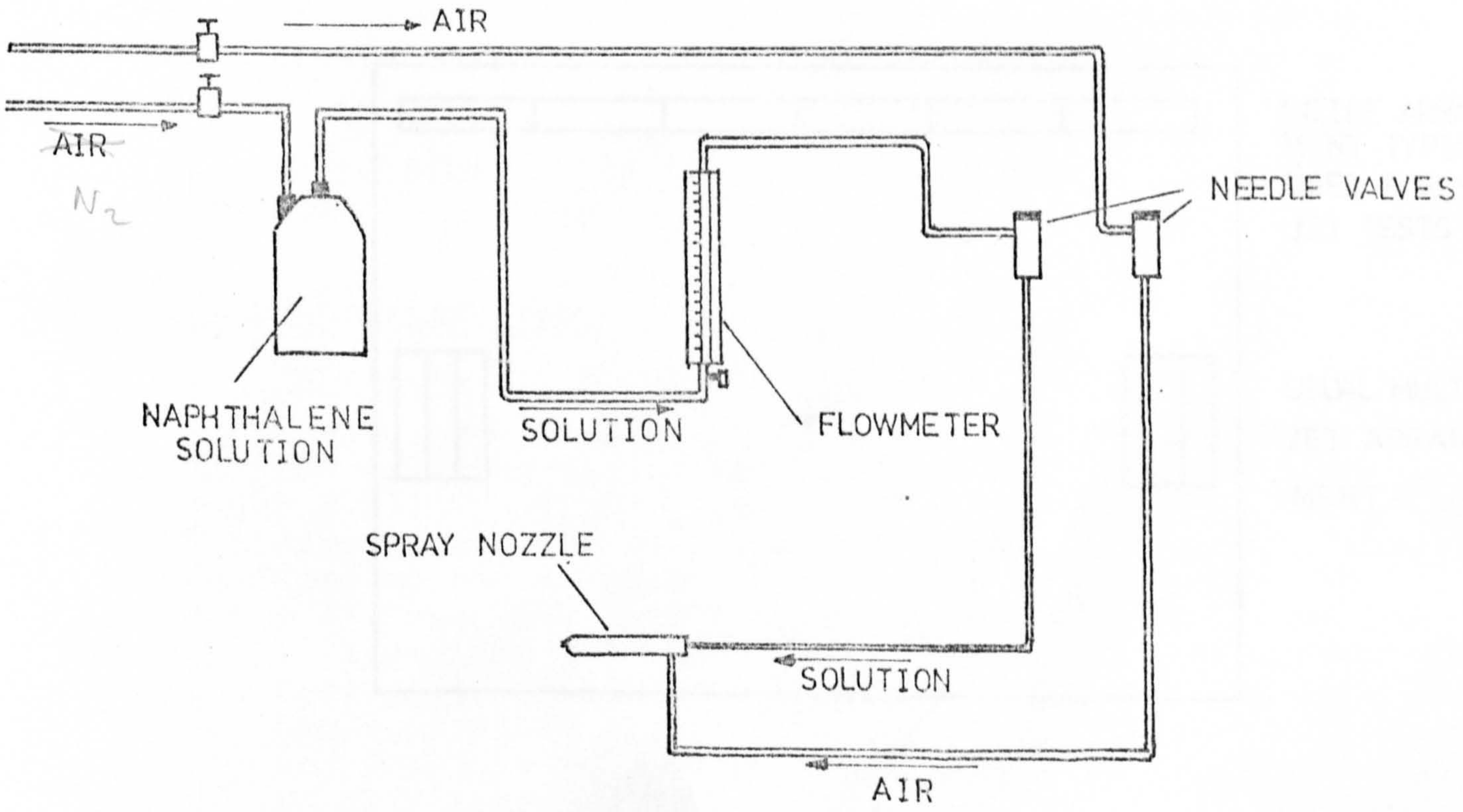

Fig. 8.5 NAPHTHALENE SOLUTION FLOW CIRCUIT

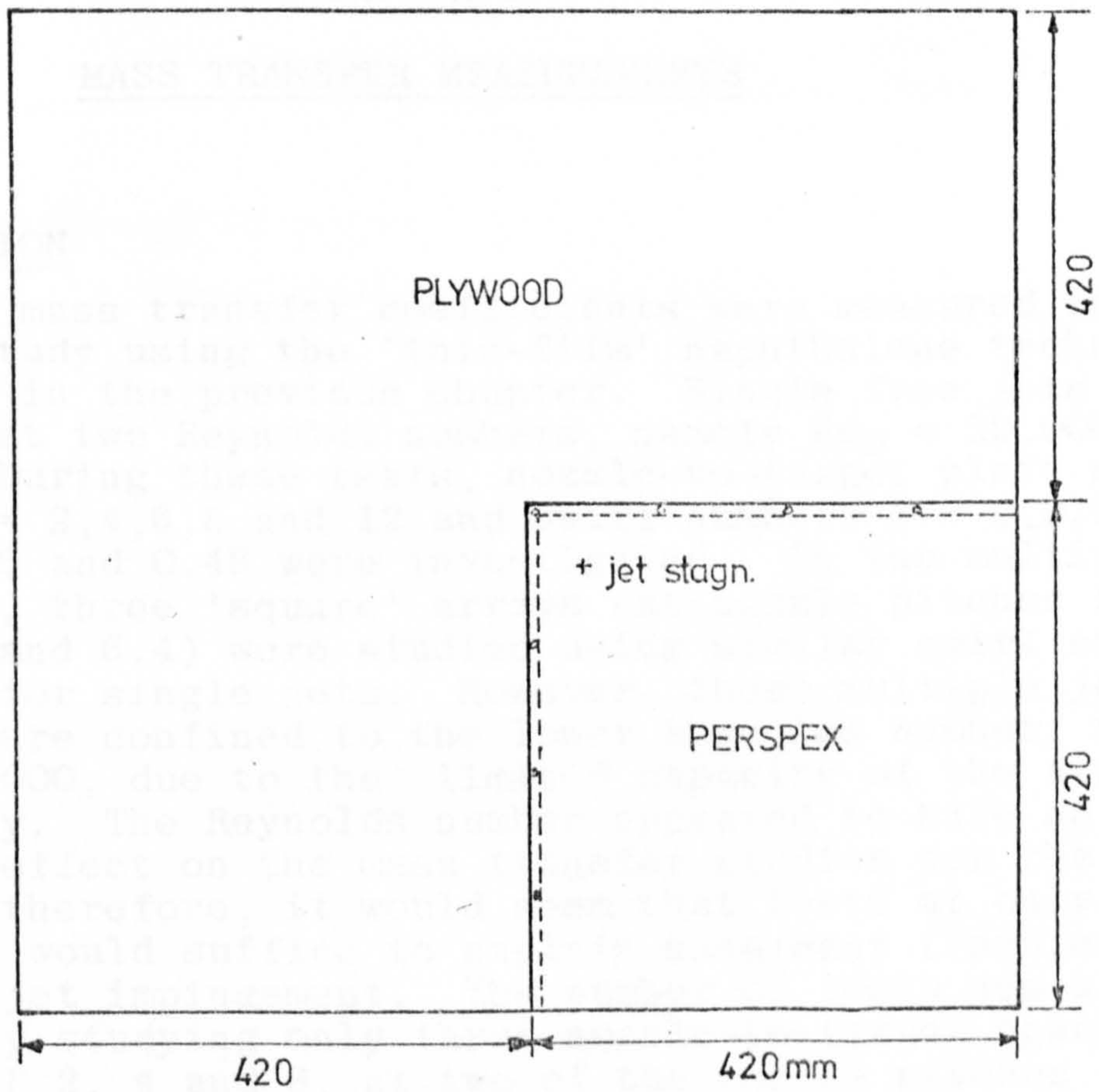

Fig. 8.6 TARGET PLATE USED TO EXTEND r/D RANGE.

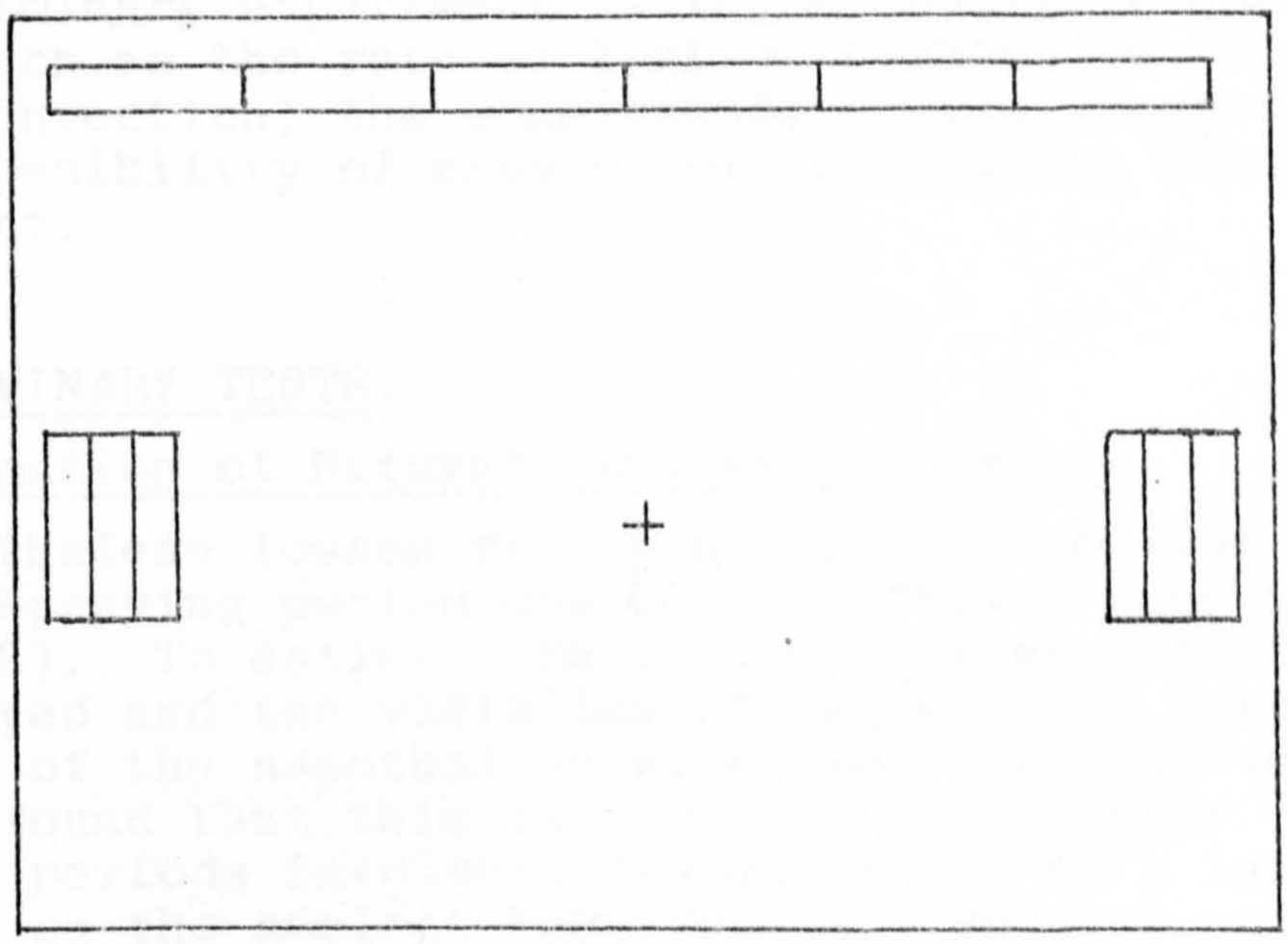

Fig. 8.7 VARIOUS POSITIONINGS OF THE CALIBRATION SLIDES.

CHAPTER 9

MASS TRANSFER MEASUREMENTS

9.1 INTRODUCTION

The local mass transfer coefficients were measured in the present study using the 'thin-film' naphthalene technique described in the previous chapter. Single free jets were examined at two Reynolds numbers, namely Re_D = 32,000 and 60,000. During these tests, nozzle-to-target plate spacings z/D = 2,4,6,8 and 12 and swirl numbers S = 0,0.12, 0.24, 0.36 and 0.48 were investigated. In the multiple jet tests, three 'square' arrays (at nozzle pitches x/D = 3.2, 4.8 and 6.4) were studied using similar swirl numbers as those for single jets. However, these multiple jet studies were confined to the lower Reynolds number, i.e. Re_D = 32,000, due to the limited capacity of the available air supply. The Reynolds number appeared to have no peculiar effect on the mass transfer studies for the single jet and, therefore, it would seem that tests at only one flow rate would suffice to explain mass/heat transfer for multiple jet impingement. The number of tests was also reduced by studying only three nozzle-to-target spacings, namely z/D 2, 4 and 8, at two of the nozzle pitches - x/D = 3.2 and 6.4. Despite the reduced number of tests, sufficient information was obtained to determine the effects of swirl on jet-impingement heat transfers.

Prior to commencement of the actual heat transfer tests, some preliminary experiments were necessary to examine effects such as the rate of loss of naphthalene due to natural convection, the consistency of the sprayed film and the possibility of erosion of naphthalene during jet impingement.

9.2 THE PRELIMINARY TESTS.

(a) Estimation of Natural Sublimation Losses.

Naphthalene losses due to natural convection during the spraying period can be significant (see section 8.4.2). To estimate this effect, test slides were sprayed and the variation of the natural weight (mass) loss of the naphthalene with time was observed. It was found that this rate of loss was linear (over the test periods involved) and dependent to a large extent on the ambient temperature. However, due to other variable disturbances in the laboratory, it was not possible to predict the losses solely on the basis of this temperature (see Fig.9.1). Thus, it was decided that the slides which were sprayed together with the surface to measure the coating density would also be used to estimate the rate of weight loss due to natural convection (see section 8.1). Consequently,

the slides were weighed on two separate occasions, initially to establish the coating 'mass density' and secondly, to evaluate the natural rate of weight loss.

(b) Consistency of Spray.

In the present tests, no attempt was made to measure the thickness of the sprayed coating since this information is not required in the calculation of the mass transfer. The uniformity of the film was observed, however, by examining the mass deposition on several slides. The mean weight of these slides was compared, and the coefficient of variation (standard deviation/mean) was found to be 0.006. The details of this analysis are given in Appendix E.

A further check on the spray uniformity was obtained during one of the tests when two rows of four slides each were fixed 410mm apart on the test surface, see Fig.9.2, and, subsequently, coated with naphthalene during the normal spraying process. As expected, the 'apparent' deposition on set B was greater due to natural sublimation effects during the spray period. A second weighing of set A was employed to determine this effect, and the corrected coating mass densities were then in good agreement, see Table 9.1.

TABLE 9.1

COMPARISON OF THE NAPHTHALENE COATING DENSITY

	Apparent Coating Density	Corrected Coating Density	Time Between Spraying and Weighing
Set A.	3.309 mg/cms^2	3.653 mg/cms^2	4000s.
Set B.	3,635 " "	3,721 " "	1000s.

Loss Rate: 8.59×10^{-5} mg/cms^2/s.

Distance Between 'A' and 'B' = 410mm.

Since the supply of the naphthalene/solvent solution was maintained at a constant rate over the whole test surface, the closeness of comparison between these two rows corroborates the assumption of the coating uniformity.

A final qualitative, but nevertheless valuable, con-

firmation of spray uniformity was also the symmetrical appearance of the clearance pattern obtained from the single jet tests. These patterns were slightly ovalish in shape but, when 'corrected' for natural naphthalene losses, were in good agreement with the expected circular patterns associated with an axisymmetric jet, see Figure 9.3(a). Any sharp perturbations in coating thickness (e.g. due to temporary spray nozzle blockage) were reflected in the visual appearance of the clearance pattern, see Figure 9.3(b).

(c) Erosion of the Naphthalene Coating.

A test was conducted to establish whether erosion as well as sublimation was involved in removal of the naphthalene coating. A thin circular perspex sheet of 155mm diameter was sprayed in the usual fashion and subjected to a jet impingement test. The weight loss from this surface was determined at frequent intervals. The decrease in weight was observed to be linear throughout the test, as shown in Figure 9.4. The test was discontinued before any clearance was apparent so that any erosion of the surface would cause the curve shown in Figure 9.4 to depart from linearity, and this indicates that, with the present technique, naphthalene erosion does not occur.

9.3 EXPERIMENTAL PROCEDURE

The experimental procedure is described in detail in this section, mainly with the aim of assisting future users of the present rig. The steps followed during a test were:-

1. The test surfaces were cleaned and de-greased with a suitable solvent (acetone). The calibration slides were then weighed and fixed at the appropriate positions on the test surface by means of double-sided adhesive tape.

2. The spray mechanism was checked for any malfunction and, in particular, the head of the spray nozzle was cleared of any blockages.

3. The test plate was mounted on its carrier, as shown in Figure 8.3, and aligned so that it was horizontal and its axis of traverse was perpendicular to the motion of the sprayhead.

4. The plate was then sprayed, as discussed earlier in Chapter 8. It is important that the digital clock is started upon commencement of coating and that the duration of the spray period is recorded.

5. The 'calibration' slides were carefully removed from the test surface and weighed to determine the

initial coating density.

6. During the spraying period, the air supply to the main test rig was switched on and adjusted to the appropriate test conditions. This allowed the temperature of the jet to settle to a steady value prior to the mass transfer measurement. The period required for the attainment of this steady state was about 30 minutes.

7. The sprayed test surface was mounted in the mass transfer rig and aligned orthogonally to the jet(s). During this operation, the naphthalene was shielded from the jet.

8. The shield was removed and the mass transfer test was commenced. The time (i.e. the zero) for the clearance profile was recorded.

9. The photographic equipment was arranged so that the camera was mounted at the rear of the test surface with the source of illumination shining through the test surface.

10. Whenever a photographic record was made, the corresponding period from the commencement of the test was noted. No predetermined 'time-steps' were followed. The need for a photograph was based on visual observation of the clearance pattern. In general, shorter intervals were maintained between photographs during the early clearance stages since these provided information in regions of high mass transfer. The 'clearance' time corresponding to the 'stagnation point' was recorded from visual observation. The measurement of clearances within small radial distances ($r/D \leqslant 0.3$) from stagnation presented special problems and these are discussed later in section 9.4.

    Approximately 8 to 12 photographs were taken during each test. These were sufficient to obtain the distributions of the mass (heat) transfer coefficient.

11. The surface and free stream temperatures were measured at various stations during the test. Accuracy of temperature measurement is important with this mass transfer technique and is discussed further in section 9.5.

12. Finally, the calibration slides were re-weighed after a period of at least 2,000 seconds had elapsed since the original weighing. The difference between the two weights gave the rate of sublimation loss of naphthalene by natural convection.

13. The calculation procedure to obtain heat transfer coefficients from the data generated in the test are presented in

Appendix D.

9.4 STAGNATION POINT MEASUREMENTS.

As mentioned in the previous section, the 'near-stagnation point' clearance was difficult to determine, particularly in the tests at high swirls or large z/D's (generally z/D > 6). One is attempting to estimate clearance at a 'point' and this can be rather 'inexact'. Therefore, two readings were taken, one corresponding to the earlier estimate and the other when a definite clearance was established. The mean of these values was then used. Alternatively, in some tests photographs were obtained at frequent intervals as the regions cleared and these mass transfer results were extrapolated to the stagnation point value (also see Appendix E).

A possible development is to use transmission of a laser beam through the plate at the stagnation region (Ref.112). A laser light source is arranged so that the beam passes through the stagnation point if the plate is clear and falls onto a photocell. The output from the cell is fed to a chart recorder. The uncertainty involved in the analysis of the chart recorder traces is, however, similar to that for visual estimations. Nevertheless, the laser method excludes subjective 'human error'. In the present tests, unfortunately, the use of this method is hindered since the initial clearance, i.e. the maximum mass transfer, can often not occur on the jet central axis due to the swirl effects.

9.5 NAPHTHALENE TEMPERATURE MEASUREMENT.

The driving force for the sublimation of naphthalene is the difference in vapour pressure between the surface and the free stream, see section 7.5. The vapour pressure of naphthalene can be estimated accurately if the surface temperature is known. However, this is often difficult to measure and it is more convenient to determine the temperature of the free-stream fluid. The error due to this is small unless the test duration is short, since the effects of surface temperature depression due to sublimation are small. At temperatures above ambient, i.e. 25C, the change of vapour pressure with temperature is high so that extremely accurate estimates of temperatures are required. Even at temperatures around 15C, vapour pressure can vary with temperature by approximately 10% per degree C.

In the case where the temperature of the jet is equal to that of the surroundings, mixing of the jet does not alter the temperature of the flow. The determination of the temperature at the naphthalene surface becomes relatively easy. Unfortunately, this ideal could only be achieved for the single jet tests at the lower Reynolds number. For some of the tests at Re_D = 60,000, the initial difference between the jet and the surroundings was about

2C. This difference was even more marked in the multiple jet studies where, in some cases, the difference was as high as 5C. In both these cases, the use of a single station measurement for the jet temperature was obviously inaccurate. Therefore, the temperature of the air stream flowing over the surface was measured using a digital thermocouple (Kane and May Instrumentation) with a resolution of 0.1C. This probe had a 0.8mm diameter cylindrical tip which, in fact, was the junction of the thermocouple.

In the case of the multiple jet assemblies, measurements were made at the surface of a 'dummy plate' which replaced the usual test surface. Small holes were drilled in this plate and the temperature probe was inserted through the rear of the plate approximately flush with the surface, see Figure 9.5. Temperatures were recorded when the jet achieved steady-state, and it is estimated that the individual temperatures measured to within 0.3C of each other. Since the multiple jet tests were of comparatively shorter duration, the ambient temperature remained constant during this period. Thus, the temperatures measured at the 'dummy' plate were used for the test surface.

9.6 EFFECT OF THE VARYING BOUNDARY CONDITIONS

Wilkie and White (Ref.103) were first to point out that the mass transfer boundary condition, equivalent to one of constant temperature, is modified by the appearance of bare patches during the thin-film sublimation process. The effect of these bare patches is to cause increased mass transfer immediately downstream. Neal (Ref.105) found this effect to be negligible and pointed out that the 'bare patch' effect is transient in nature and influences a particular position for a relatively short time. Furthermore, it may also be emphasized that the mass transfer process is only affected immediately before the naphthalene clears from the plate surface. Thus, in the present work, the effect of the varying boundary conditions was considered to be negligible. The possible error introduced by this assumption may be the prediction of slightly higher heat transfer coefficients. Further details on the 'bare patch' effect may be seen in Ref.105.

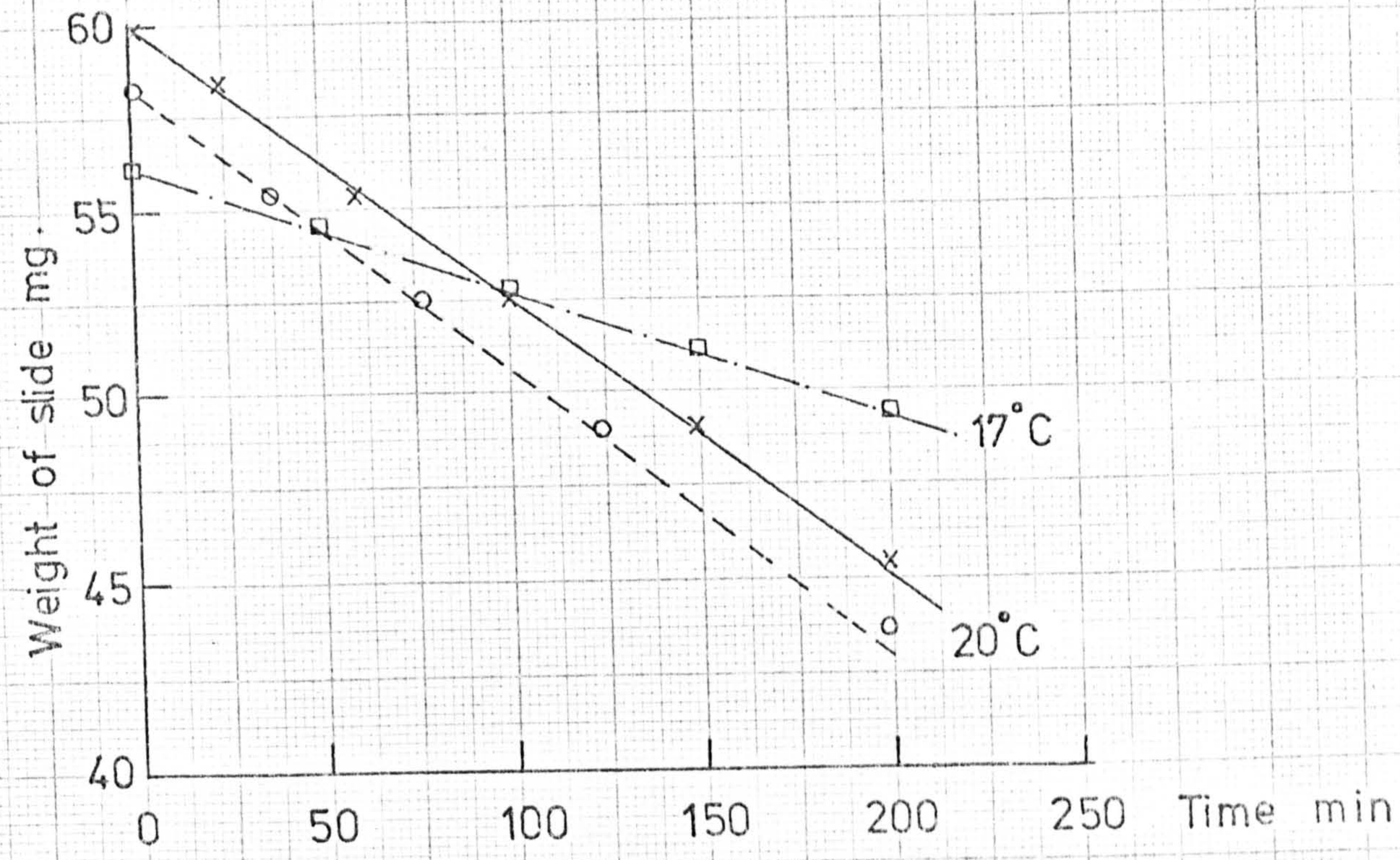

Fig. 9.1 LOSS OF NAPHTHALENE FROM THE SLIDES DUE TO NATURAL CONVECTION

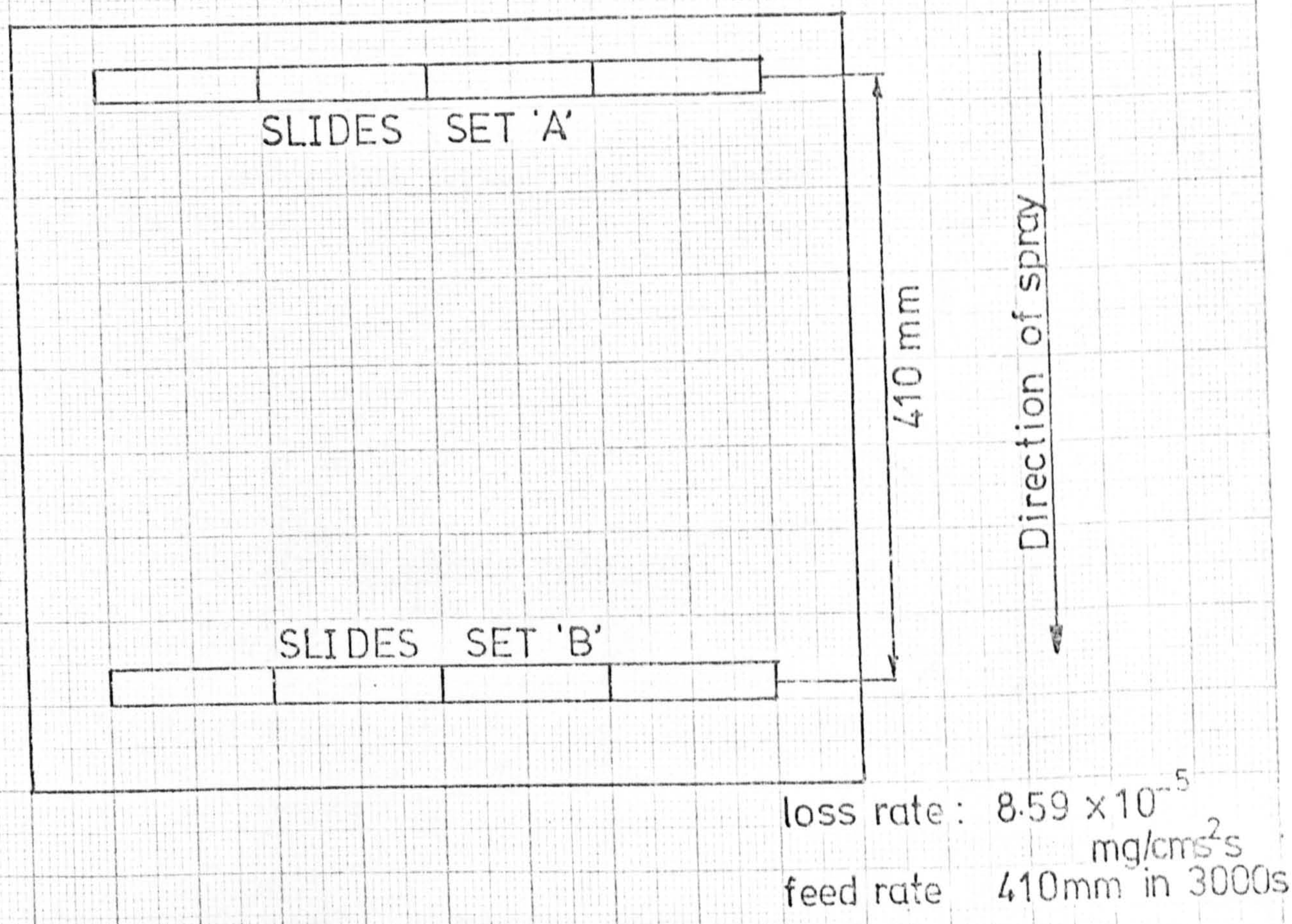

Fig. 9.2 ARRANGEMENT OF SLIDES TO CHECK THE CONSISTENCY OF SPRAYING.

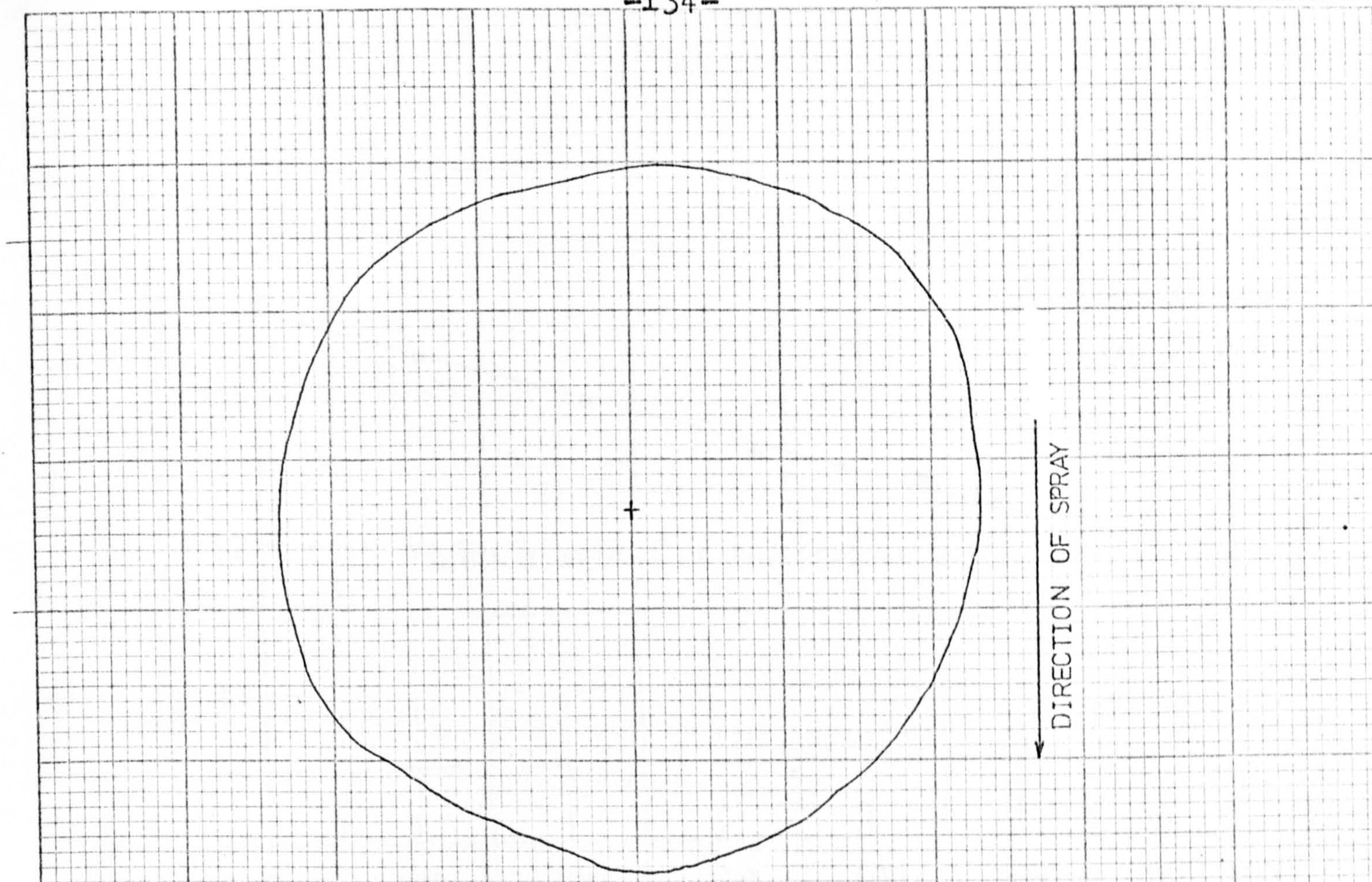

Fig. 9.3a CLEARANCE PATTERN OBSERVED FOR A TYPICAL CASE.

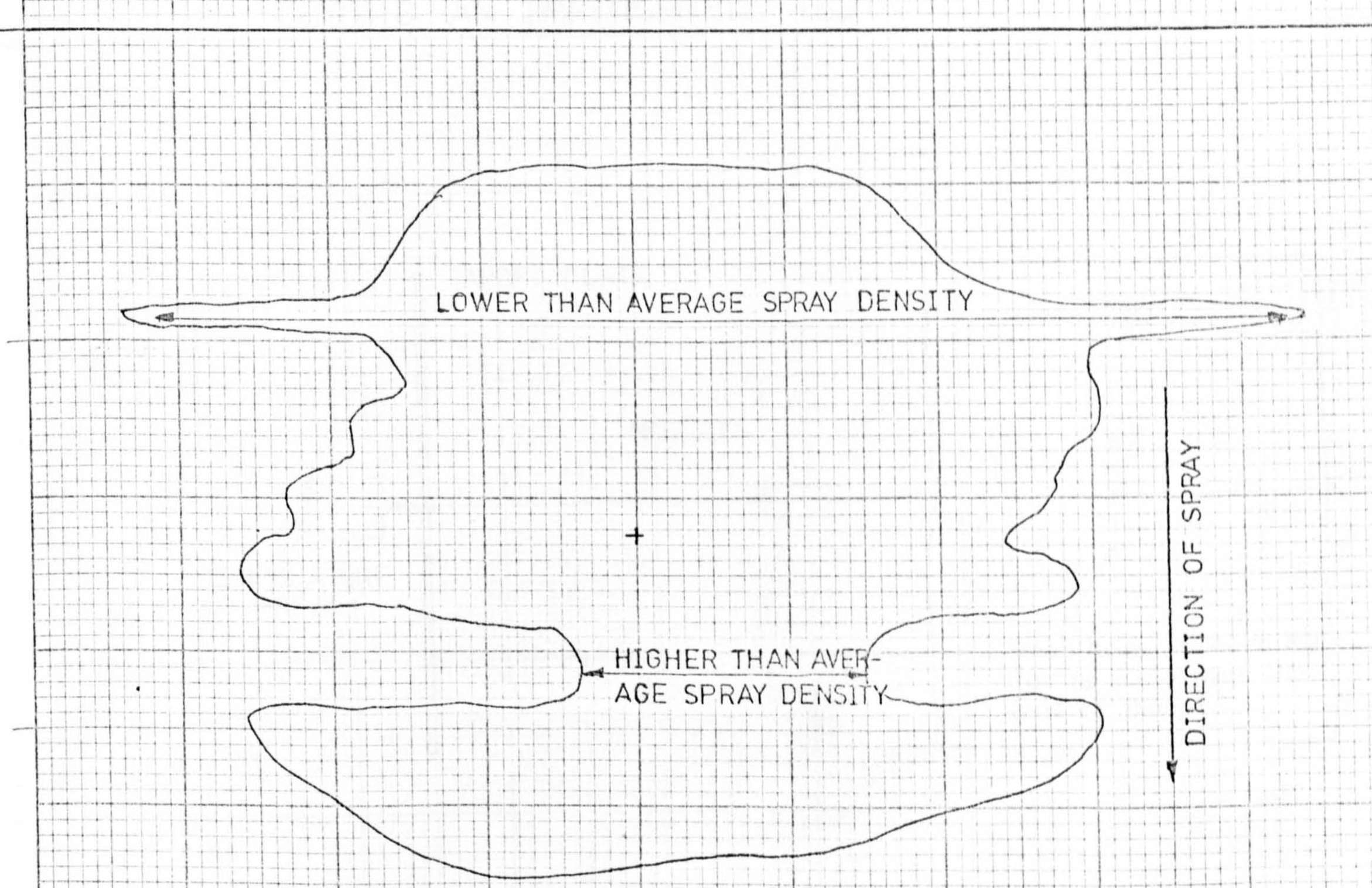

Fig. 9.3b CLEARANCE PATTERN OBSERVED FOR AN UNEVEN SPRAY.

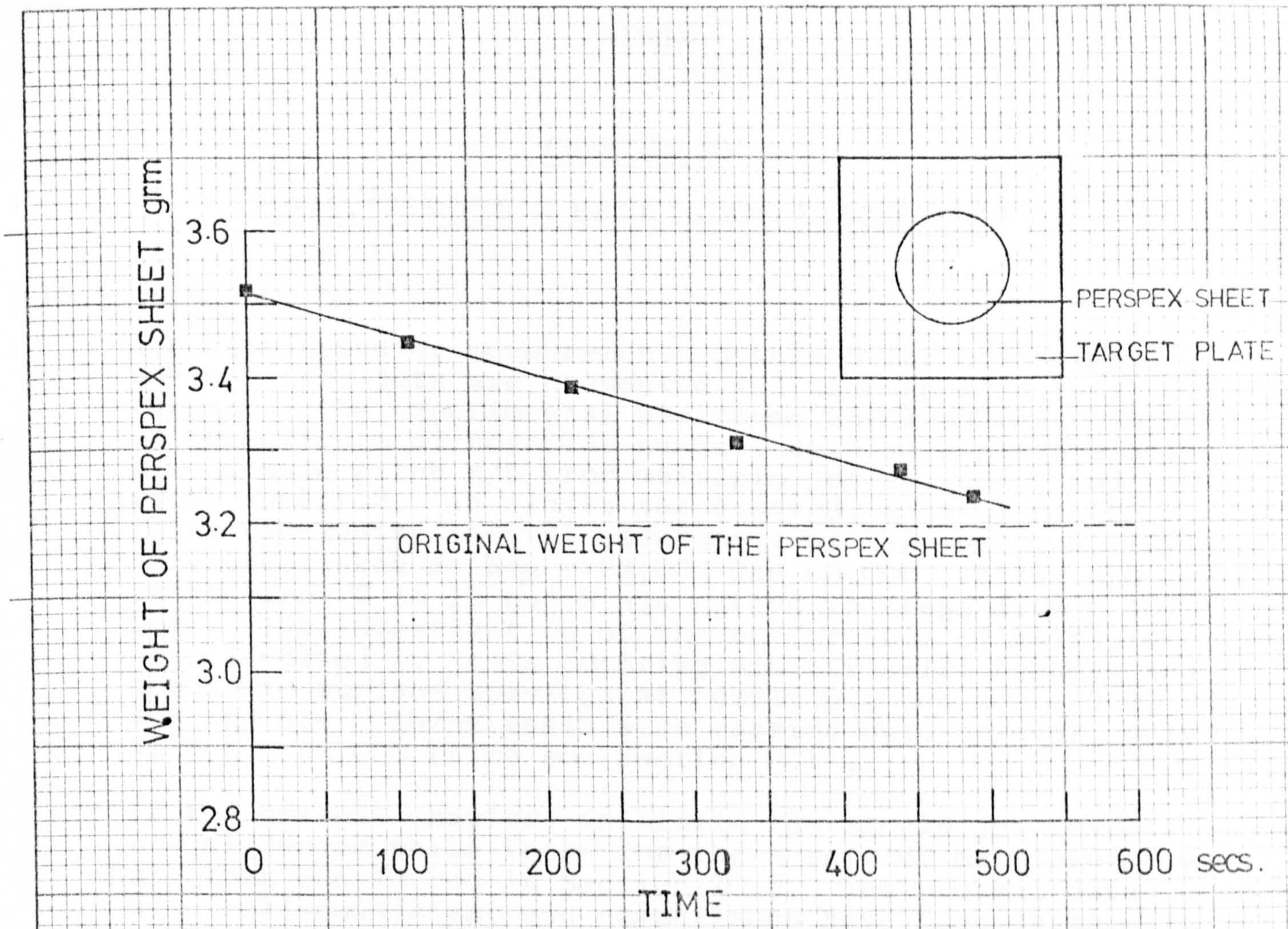

Fig. 9.4 VARIATION OF THE WEIGHT OF A SPRAYED SHEET DURING AN IMPINGEMENT TEST.

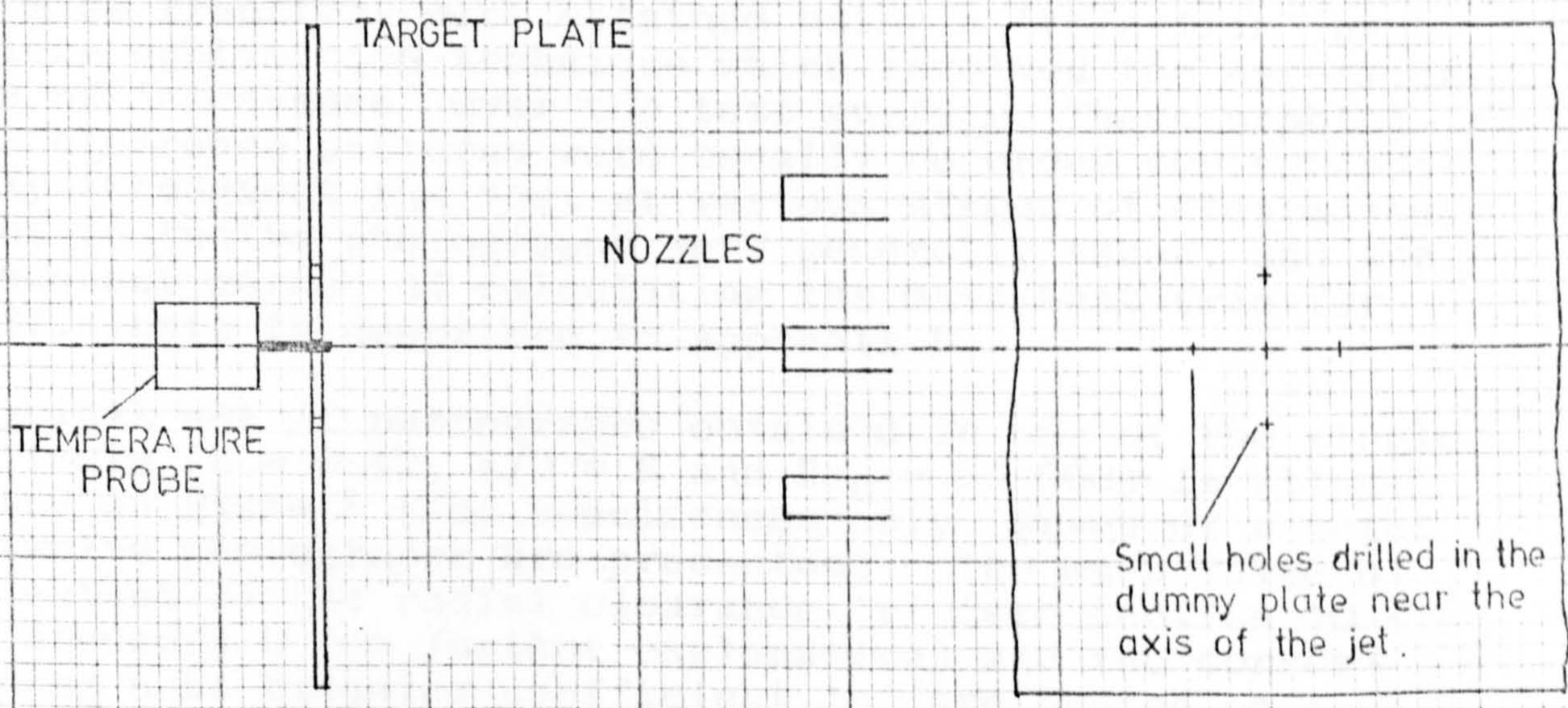

Fig. 9.5 TEMPERATURE MEASUREMENT FOR MULTIPLE JET SET-UP.

CHAPTER 10

HEAT TRANSFER - RESULTS AND DISCUSSION

10.1 INTRODUCTION

The heat transfer measurements obtained for both single and multiple jets are presented and discussed in this chapter. The experimental programme involved measurements of the effects of Reynolds number, nozzle-to-plate spacing z/D, nozzle pitch x/D (for multiple jet systems), and swirl number S. In single jet studies, a total of 52 tests (including initial assessment of the repeatability) were undertaken at Re_D = 32,000 and 60,000, whilst z/D ranged from 2 to 12 and S was varied in steps from 0 to 0.48. The investigation of the performance of multiple jets involved 55 tests covering similar swirl numbers and nozzle-to-surface spacings at nozzle pitches x/D = 3.2, 4.8 and 6.4. These tests were carried out, however, only at Re_D = 32,000 (also see Section 9.1).

In the present chapter, initially the single jet results are discussed while those for the arrays of multiple jets are then considered in Section 10.5. The present data were self-consistent and comparisons have been drawn with published results of previous studies wherever possible. In general, these results are only available for non-swirling jets but the average measurements of Dunn (Ref. 25) for arrays of multiple, impinging swirling jets are also examined and compared. Tests were also carried out to examine the repeatability and validity of the present experimental technique.

10.2 CLEARANCE PATTERNS

The mass transfers were obtained using a 'thin-film' naphthalene sublimation technique which involved the determination of 'clearance' over the test surface. These naphthalene clearance patterns were usually recorded photographically throughout the test at various stages of clearances. Eight to twelve photographs were generally taken, and the subsequent method of calculating the mass/heat transfer coefficients is described in Appendix D.

A typical set of photographs obtained in one of the single jet tests (S = 0.12, z/D = 6 and Re_D = 60,000) is illustrated in Plate 5 (for conciseness only, seven of a total of twelve photographs are presented). The mean value of the extent of the radial clearance 'r' (see Section 10.4.3 and Appendix D for further explanation) and the corresponding heat transfer coefficient 'h' are quoted on each photograph. The radial variation of 'h' in this test is also shown and the data points appropriate to the photographs are marked. Plate 5 also illustrates that a symmetrical pattern is obtained for the initial clearances. However, as the clearance extends, the pattern tends to become more oval due to the initial variation in the thick-

ness of the naphthalene on the test plate. The difficulties discussed in Section 9.4, namely the problem of determining stagnation point mass transfer and also of accurately estimating clearance radii of less than 6mm, are also apparent from this series of photographs.

10.3 INITIAL REPEATABILITY TESTS

Three independent single jet tests were undertaken with the following conditions maintained constant, swirl S = 0.12, Re_D = 60,000 and z/D = 4. The resultant radial variations of the heat transfer coefficient are plotted in Figure 10.1. The three distributions are in good agreement except for near stagnation values where differences of about 10% are apparent. However, as discussed in Section 9.4, it is difficult to estimate the 'exact' time for clearance at the stagnation point. Moreover, extrapolation of the separate variation curves to r/D = 0 produced more consistent results in this case.

Thus, the present experimental technique appears to be reasonably repeatable. Sources of error in the determination of the heat transfer coefficients are discussed in Appendix E.

10.4 SINGLE JET STUDIES

10.4.1 Stagnation Point Heat Transfer

The variation of the heat transfer coefficient at the stagnation point (h_o) with the nozzle-to-plate spacing at a particular swirl is similar at both the Reynolds number of Re_D = 32,000 and 60,000, and is illustrated in Figure 10.2. In the subsequent discussion, the swirling and non-swirling jets are treated separately.

(a) Non-swirling jets.

For the non-swirling jets (i.e. S = 0), h_o increases up to z/D = 5.0 (approximately) and then subsequently decreases. Such maxima were also observed by previous researchers, e.g. Gardon and Cobonpue (Ref.35) and Koopman and Sparrow (Ref.50). They attributed this behaviour to an initial increase in turbulence along the jet axis due to mixing with the quiescent surroundings. This increase in turbulence can even outweigh the effects of velocity decay, as discussed earlier in Section 2.3. Gardon and Cobonpue found that the axial position of this maximum heat transfer was dependent on the nozzle diameter (which affected the turbulence characteristics) and varied from 5.5D to 8D. Moreover, as in the present study, the Reynolds number was found to have little effect on this position. In Koopman and Sparrow's study, the maxima occurred at z/D = 4 (approximately). However, it should be noted that this value was approximate and was selected subjectively because of the paucity of data between z/D = 4 to 7. The present estimated

value of 5.0 is, thus, broadly in accordance with the findings of these early studies and, moreover, approximately coincides with the end of the 'potential core' of the present jet.

Vallis et al (Ref.38) proposed that the stagnation point heat transfers can be correlated as

$$Nu_o = 1.93\ Re_D^{0.58}\ Pr^{0.33}\ (z/D)^{-0.74} \qquad (2.5)$$

quoted earlier in Section 2.3.1. This equation is strictly valid only for $3,880 \leqslant Re_D \leqslant 23,000$ and $10 \leqslant z/D \leqslant 20$ so that the direct comparisons cannot be made with the present arrangement. However, once the jet is fully developed, the above formula can be extended to higher Re_D (unless compressibility becomes significant). Thus, it is probably reasonable to compare the present measurements at $z/D = 8$ and 12 with Vallis' predictions, see Table 10.1. Table 10.1 also quotes values from Refs.6 and 35 at approximately similar Reynolds numbers.

TABLE 10.1

COMPARISON OF MEASURED 'Nu_o' WITH THOSE OBTAINED BY PREVIOUS WORKERS

Re_D	z/D	Stagnation Point Heat Transfer Nu_o			
		Present Measurement	Vallis et al	Gardon & Cobonpue	Kabari
32,000	8	183.6	152.3	123.6*	160.0
	12	103.4	112.8	105.8	-
60,000	8	265.1	219.3	172.2**	178.0***
	12	184.2	162.4	153.0	-

* Re_D = 28,000

** Re_D = 56,000

*** Re_D = 55,000

The present values of Nu_o are in reasonably good agreement with other tabulated values since the difference between some researchers has been found to be as high as 70% (Ref.38). These wider differences can generally be explained by differences in the detailed jet geometry and turbulence characteristics.

(b) Swirling Jets

Figure 10.2 also presents the stagnation point heat transfers for various degrees of swirl. In all the

cases except S = 0.48, the stagnation point coincides with the intersection of the jet axis on the plate. For S = 0.48, the maximum value is displaced from the jet axis and is quoted as the stagnation value in this discussion.

In all the swirling jet cases, the maximum value of Nu_o occurs at z/D = 2, i.e. at the closest nozzle-to-surface spacing examined in the present tests. The heat transfer coefficient thereafter decreases continuously as the spacing increases. At z/D = 2, the initial application of swirl brings about an increase in the stagnation heat transfer (compare h_o at S = 0 and S = 0.12). This increase is obviously due to the higher turbulence intensities observed in the swirling jets, see Figure 6.28. At Re_D = 32,000, the stagnation heat transfer at S = 0.24 is also greater than that measured in the non-swirling case. In general, it is interesting to note that the turbulence intensity variations presented in Figure 6.28 and the heat transfers 'h_o' in Figure 10.2 exhibit similar trends (e.g. compare the variations for S = 0 and S = 0.12 in Figures 10.2 and 6.28).

The dependence of the stagnation point heat transfer coefficients on the jet velocity at the impingement in addition to the turbulence intensity can also be illustrated by comparing the values for h_o at S = 0 and S = 0.36 for z/D = 2 and Re_D = 32,000. The turbulence intensities in both cases are roughly equal (9 and 9.8 percent for S = 0.36 and S = 0 respectively). However, h_o = 215 W/m^{2}s for S = 0 and h_o = 183.3 W/m^{2}s for S = 0.36, and this may be explained since the corresponding arrival velocity at the higher swirl is only 15.8 m/s as compared to 22.5 m/s for the non-swirling jet.

10.4.2 Heat Transfers in the Impingement Region of the Non-Swirling Jets.

Due to the strong dependence of the stagnation point heat transfer on detailed jet geometry and turbulence characteristics, it is often difficult to make comparisons between various studies. This may be overcome to some extent by determining the heat transfers over an impingement region surrounding the stagnation point. This region, as discussed in Section 2.4, is characterised by the presence of a strong negative pressure gradient at the impingement surface. The extent of this region was defined earlier in Equation 2.1 (Ref.30) as:-

$$r_p = 0.284\, z$$

where, r_p = radius of the impingement region.

Equation 2.1 is valid for z/D > 12. In the present

tests, the possible comparison with other researchers such as Vallis et al (Ref.38) and Gardon and Akfirat (Ref.36) can only be made for the heat transfer variations obtained at $z/D = 12$, see Figure 10.3. Both the Nusselt and Reynolds numbers are based on the diameter of the target (i.e. the impingement region). The present results are about 5% higher than the previous published results.

10.4.3 Radial Variation of Heat Transfer Coefficient.

The radial variations of the heat transfer coefficients over the impingement surface were essentially symmetrical about the central axis of the jet, so that the plots are centered about this axis in all the figures from Fig.10.4 to 10.23. The radial distance corresponding to a particular coefficient represents an 'average' radius of the clearance pattern. The method of obtaining the average 'r' is discussed in detail in Appendix D. Figures 10.4 to 10.8 present the heat transfer at the Reynolds number $Re_D = 32,000$ at various nozzle to target spacings ($z/D = 2$ to 12). Each of the plots corresponds to one of the swirls ($S = 0$, 0.12, 0.24, 0.36 and 0.48) in this investigation. Similar presentations for $Re_D = 60,000$ are shown in Figures 10.9 to 10.13. The heat transfer data are also replotted in a different form, i.e. the variation of 'h' with r/D for varying swirls at each value of z/D. Figures 10.14 to 10.18 are such plots at $Re_D = 32,000$ and Figures 10.19 to 10.23 present the results at $Re_D = 60,000$. The radial fields for these results are $0 \leqslant r/D \leqslant 8.5$ at the lower Reynolds number and $0 < r/D \leqslant 10.5$ at $Re_D = 60,000$.

Observations of these plots, Figures 10.4 to 10.23, indicate that the heat transfer generally behaves in a similar fashion at both the Reynolds numbers. Therefore, in the ensuing discussion, reference is only made to the results at $Re_D = 32,000$. Minor differences in the behaviour at $Re_D = 60,000$ are discussed later in the text.

(a) Non-swirling jets.

As illustrated in Figure 10.4, the heat transfers at $z/D = 2$ and 4 for the non-swirling flow exhibit secondary peaks at $r/D = 2$ (approximatcly). These peaks are associated with the laminar to turbulent transition in the wall jet flowing over the surface of the plate. This phenomenon has been observed by several other authors, e.g. Refs.35 and 36, and has been fully discussed in Section 2.4. The flow transition is less apparent at $z/D = 6$ but is, nevertheless, reflected by a sharp variation in the slope of the plot at $r/D = 2$. The distribution at the higher nozzle-to-target separations (i.e. $z/D = 8$ and 12) display no such perturbation, thus probably implying a completely turbulent flow over the impingement surface. At z/D's from 2 to 8, 'h' decreases

sharply with an increase of 'r/D', whilst radial decay in heat transfer at z/D = 12 is more gradual (e.g. at z/D = 8, in Figure 10.4, the value 'h/h_o' at r/D = 3 is 0.41 whilst at z/D = 12, this ratio is 0.60 signifying more uniformity).

In Figure 10.24, the present radial heat transfer distributions at Re_D = 32,000 for the non-swirling flows are compared with data published by Gardon and Cobonpue (Ref.35) for Re_D = 28,000. The curves are presented in a form similar to that suggested by Wolfshtein (Ref.113), i.e. $St.Re_D^{1/3} Pr^{2/3}$ plotted against r/D for various z/Ds. This form has the advantage of taking into account the variations of Reynolds and Prandtl numbers under different test conditions. For the sake of clarity, comparisons are only made between curves corresponding to z/D = 4, 6 and 12 in the present tests and the plots for z/D = 4, 6 and 16 obtained by Ref.35. At each of the similar nozzle-to-target spacings, the results from the two studies are in good agreement and corroborate the observation that the heat transfers become more uniform with increasing z/D. Furthermore, it may generally be concluded that the present data exhibit similar qualitative and quantitative trends to those of other investigators, thus once again confirming the validity of the experimental technique.

(b) Swirling Jets

The presence of the swirl in the flow considerably affects the heat transfer profiles depending on the swirl number (i.e. the intensity of the swirl). The effects of swirl can be seen by comparing the plots obtained at various swirls with those of the non-swirling jet. For the lowest swirl studied, S = 0.12, the effects of varying the nozzle-to-impingement surface spacing (z/D) can be seen in Figure 10.5. At z/D = 2, the distribution exhibits similar trends to those for S = 0. The secondary peak in the heat transfer due to the laminar to turbulent transition is almost indistinguishable from that for S = 0. This is more clearly apparent in Figure 10.14 which shows plots at various swirls at constant z/D. The values of 'h' are higher at the stagnation point for S = 0.12 when compared to S = 0 due to the increased turbulence in the swirling jet (see Figure 10.2). For radial distances r/D > 2.5, however, the plots associated with S = 0.12 exhibit slightly lower values. At z/D = 4, the secondary peak, although present in the non-swirling case, is absent for S = 0.12, see Figure 10.5. This can possibly be explained in terms of a lower impingement velocity which ensures the presence of a fully turbulent wall jet. It may be recalled that decrease in velocity even for S = 0.12 is considerable. At z/D = 4, the

velocity at the centreline of the jet was found to be 0.7 u_e compared to 1.0 u_e for S = 0, see Figure 6.7 Similarly at z/D = 6, the distribution is smoothly continuous, unlike the variation at S = 0 which exhibited a discontinuity at r/D = 2 (i.e. compare the plots for S = 0 and S = 0.12 in Figure 10.16). At the next highest nozzle-to-plate spacing studied, i.e. z/D = 8, the distribution at S = 0.12 is more uniform than that for the non-swirling jet (e.g. h/h_o at r/D is 0.27 for S = 0.12 and 0.23 for S = 0). At z/D = 12, the shape of the distribution is similar to that for the non-swirling jet, although heat transfers are slightly lower (compare plots for S = 0 and S = 0.12 in Figure 10.18).

Figure 10.6 illustrates plots of the radial variations of 'h' for S = 0.24 for different z/Ds. It is apparent upon comparing Figures 10.5 and 10.6 that heat transfer characteristics at S = 0.24 follow similar trends to those at S = 0.12. Once again a secondary peak is present only at z/D = 2 although the magnitude of the peak in this case is lower than those at S = 0 and 0.12 (see also Figure 10.14). This reduction is in line with the decrease in the axial velocities at the higher swirls, e.g. compare velocity distributions for S = 0.12 and 0.24 in Figure 6.6. At all other z/Ds (i.e. 4 to 12), heat transfer distributions are very similar to those for S = 0.12 though in most cases the values are slightly lower in magnitude.

However, at S = 0.36 the heat transfer characteristics are significantly altered. The secondary peak is now absent at all z/Ds, see Figure 10.7. The heat transfer coefficient for the region r/D = 0 - 6 are considerably lower than those for the non-swirling jet (e.g. compare the plots for S = 0 to S = 0.36 in Figures 10.14 to 10.18). The variation in 'h' is more uniform, e.g. at z/D = 6, h/h_o at r/D = 3 is 0.41 for S = 0 and 0.61 for S = 0.36.

At the highest swirl studied in this investigation, namely S = 0.48, the maximum heat transfer is displaced from the central axis at all z/Ds to a station r/D = 1.25 (approximately), see Figure 10.8. The peaks are extremely prominent at the lower spacings, i.e. z/D = 2 and 4, but become less pronounced at higher z/Ds. Comparatively low heat transfers thus ensue in the central region of the impingement surface corresponding to the central core of the jet. The presence of this low heat transfer region may be expected at low nozzle-to-target spacings because of the double peak profiles observed in the velocity measurements at z/D = 2, see Figures 6.6 to 6.8. However, these peak velocities were found to be at r/D = 0.3. This, coupled with the persistence of the low heat transfer core at spacings up to z/D = 12 suggests that this behav-

iour cannot be explained simply in terms of the velocity distributions. It should be pointed out, however, that the velocity profiles were obtained in a free jet in the absence of the target plate. It would, therefore, seem likely that the heat transfer characteristics are associated with recirculation in the central region.

As mentioned earlier, the heat transfer behaviour at $Re_D = 60,000$ is generally similar in trend to that at $Re_D = 32,000$. However, since the values of 'h' at $Re_D = 60,000$ are higher than those at the lower flow, they do not tend to become asymptotic at $r/D = 8.5$ and the plots have thus been extended to $r/D = 10.5$.

To summarise this discussion, the general effect of swirl is to produce a lower value of 'h', except at or near the stagnation point. The heat transfer profiles also tend to become more uniform, especially at $S = 0.36$. The laminar to turbulent transition of the deflected flow is also affected by the swirl since the impingement velocity decreases considerably with the swirl.

10.4.4 Average Heat Transfer - Single Jet Tests

(a) Non-swirling Jets.

The radial heat transfer variations in Figures 10.4 to 10.13 were integrated to yield average heat transfers ($\bar{h}$ or $\overline{Nu}$). The resultant average value depends largely on the area over which the integration is carried out. Typical effects on $\overline{Nu}$ of altering the area of integration are shown in Figure 10.25 where the average heat transfers are plotted for different nozzle-to-target spacing z/D in the non-swirling case (for both $Re_D = 32,000$ and 60,000). The numerical values of $\overline{Nu}$ obviously decrease as the heat transfers are averaged over a large area, since the local heat transfer coefficients generally decrease with increasing distance from the stagnation point. The plots at $z/D = 2$ and 4, however, exhibit a slight increase in $\overline{Nu}$ between $1.5 \leqslant r/D \leqslant 2.5$ because of the presence of secondary peaks in the lateral variation of 'h' at these separations. The $\overline{Nu}$ - z/D variation is also affected by the integration area or 'target area', see Figure 10.26 which presents $\overline{Nu}$ for two target areas defined by $0 \leqslant r/D \leqslant 4.25$ and $0 \leqslant r/D \leqslant 8.5$. The average Nusselt number based on the smaller integration area decreases sharply as z/D increases from 4 to 6, whereas $\overline{Nu}$ associated with the larger area varies more gradually. Several previous investigators, e.g. Gardon and Cobonpue (Ref.35), Huang (Ref.39) and Sitharammaya and Raju (Ref.40),

have commented that the average heat transfer remain fairly constant for $0 \leqslant z/D \leqslant 8$. However, the average value quoted in these studies corresponds to 'large integration areas' (e.g. Huang averaged between 0 - 20 nozzle diameters). Figure 10.27 reproduced from Ref.35 illustrates the effect of the 'target area' on the variation of $\bar{h}$ with nozzle-to-target spacing. In particular, the relatively slight decrease at the largest integration area (r/D) should be noted. This diagram is in general accord with the present data since the average values corresponding to the larger target area (r = 0 to 8.5D) show only a slight decrease with an increase of z/D, see Figure 26.

The 'average' heat transfers obtained for the present non-swirling jets were compared with the following empirical correlation quoted by Martin (Ref. 34).

$$\overline{Nu}/Pr^{0.42} = D/r \cdot \frac{1 - 1.1(D/r)}{1 + 0.1(z/D - 6)(D/r)} \cdot F(Re) \qquad (10.1)$$

where,

$$F(Re) = 2\ Re_D^{0.5}\ (1 + \frac{Re_D^{0.55}}{200})^{0.5}$$

This equation is valid for $2{,}000 \leqslant Re_D \leqslant 400{,}000$, $2.5 \leqslant r/D \leqslant 7.5$, $2 \leqslant z/D \leqslant 12$, and has been found to provide a reasonable fit to previously published data including those of Gardon and Cobonpue (Ref. 35) and Smirnov et al (Ref.49). As shown in Figure 10.28, the present results lie close to this general curve so that it may be concluded that present tests are in reasonable agreement with previous published results for impingement of a non-swirling jet.

(b) Swirling Jets

The average heat transfers obtained over a target area specified by $0 \leqslant r/D \leqslant 8.5$ are plotted against the degree of swirl for various z/Ds in Figure 10.29. The Nusselt number decreases as the swirl is increased for virtually all the nozzle-to-target spacings. For $z/Ds \leqslant 8$, the rates of decay are similar for all spacings, whilst the decay in heat transfer is less pronounced at z/D = 12. Figure 10.30 is a representation of the data and illustrates the variation of $\overline{Nu}$ with z/D at various swirls. It is clearly apparent from this figure that, for nozzle-to-surface separations up to z/D = 5 and for swirl numbers $S \leqslant 0.24$, the variations in heat transfers are relatively slight. At the

higher swirls, however, the reduction in heat transfers over this z/D are more marked.

The effect of the area of integration on the $\overline{Nu}$ for swirling jets is illustrated in Figure 10.31. The plots refer to only two of the swirls, i.e. S = 0.24 and 0.48 at $Re_D = 60,000$, but these are sufficient to illustrate significant trends. The effects at S = 0.24 are similar to those for the non-swirling jet, as shown in Figure 10.25. The variation at z/D = 2 is consistent with the presence of a secondary peak in the lateral variations of 'h'. The variations for S = 0.48, however, show that the heat transfer increases as the integration area is increased upto r/D = 2 (approximately). This behaviour is obviously due to the presence of the low heat transfer 'inner core' at this high swirl. Nevertheless, for r/D > 3, the heat transfers decrease in a similar fashion to the previously considered variations for S = 0 and S = 0.24, compare Figures 10.25 and 10.31. The effect of the integration area on the heat transfers is such that the conclusions that have been previously drawn are unaffected, i.e.

(i) application of swirl reduced the average heat transfer associated with an impinging jet, and

(ii) the average heat transfer due to an impinging jet (at all swirls $S \leq 0.48$) decrease as the nozzle-to-surface spacing is increased.

An attempt was made to produce a quantitative assessment of the effect of swirl on impingement heat transfer. It appeared reasonable to apply a correlation of the form:-

$$\overline{Nu} = a(Re_D)^b \ (Pr)^c \ (z/D)^d \ (S)^e \qquad (10.2)$$

The indices for the Prandtl number (Pr) and the nozzle-to-target spacing (z/D) were chosen as 0.33 and -0.2 respectively. This first index is most commonly employed to express the effect of changes in Pr in the jet impingement systems whilst the use of an index of -0.2 on z/D has been suggested by Hilgeroth (Ref.51) and Wolfshtein (Ref.113).

Thus, the expression,

$$Nu = C \ Re_D^{0.8} \ Pr^{0.33} \ (z/D)^{-0.2} \ (S)^{-0.2} \qquad (10.3)$$

where C depends on the area of integration and is equal to 0.022, 0.018 and 0.014 for target areas $0 \leq r/D \leq 4.25$, $0 \leq r/D \leq 6.5$, and $0 \leq r/D \leq 8.5$ respectively.

This equation was found to provide 'best fit' for the data and is valid for : S = 0.12 to 0.48, Re_D = 32,000 - 60,000, z/D = 2 to 12, and r/D = 4.25 to 8.5. The scatter associated with this correlation is illustrated in Figure 10.32 where the experimental measurements are compared with the predictions. Percentage scatter bands are also presented, and it appears that 95% of the data fits the correlation within ± 10%.

A further attempt to provide an overall assessment of the effect of swirl on average heat transfer was undertaken. The present data was plotted as the ratio of the average Nusselt number (r/D = 0 - 8.5) in the swirling case to that for the non-swirling flow, i.e. ($\overline{Nu}_S/\overline{Nu}_{ns}$) against the swirl number, see Figure 10.33. The effect is dependent on the nozzle-to-target spacing so that the scatter is considerable, especially at the higher swirls S = 0.36 and S = 0.48. However, a mean line can be plotted and this can be used to provide an approximate estimate of the average heat transfer associated with the swirling jet.

10.5 MULTIPLE JET STUDIES

10.5.1 Local Heat Transfers

The local heat transfers obtained in the multiple jet tests (see Section 10.1 for details of the experimental parameters) are presented as contours of heat transfer coefficient 'h' over the impingement surface. A plot of this form provides information over the whole field and was, thus, selected as being more useful than graphical distributions of 'h' (or Nu) along a particular radial direction, particularly since the axial symmetry does not exist with an array of impinging jets. Furthermore, the contour lines also illustrate the heat transfer distribution over the surface more readily, e.g. lesser lines for a plot mean a more uniform variation of 'h'.

The contours are plotted for the central jet which was completely surrounded by the other 8 jets in the array, see Figure 10.34. Furthermore, only a quadrant of the square area associated with this central jet is considered since the remaining quadrants are symmetrical. A value of 25 w/m^2K was chosen as the increment in 'h' between successive contours. Appendix D outlines the method of obtaining the contours. Tests were only undertaken at Re_D = 32,000.

Figure 10.35 illustrates the effect of the jet nozzle pitch (x/D) and the degree of swirl (S) at a nozzle-to-plate spacing z/D = 2. Each horizontal group of diagrams presents the variation with changes in swirl number, i.e. diagrams are given for S = 0, 0.12, 0.24, 0.36 and

0.48, at a constant nozzle pitch. Figures 10.36 and 10.37 contain similar plots for $z/D = 4$ and 8. In all these plots, stagnation point and integrated average heat transfer coefficient are also quoted. For $S = 0.48$, the maximum heat transfer does not occur on the central axis of the jet for some cases so that a broken line indicates the position of these maxima. It is difficult to determine the effect of nozzle-to-impingement surface separation from Figures 10.35 to 10.37 so a further group of contours are plotted at a constant $x/D = 4.8$, see Figure 10.38. This Figure illustrates the effect of changes in z/D from 2 to 12.

The contours plotted in Figures 10.35 to 10.38 appear to be self-consistent and vary in a regular fashion which can be explained by considering the geometrical parameters (x/D, z/D) and the flow conditions (i.e. degree of swirl). Strong interactions which yielded secondary peaks can be observed and these may be attributed to the meeting of the wall jets from the adjacent nozzles. Laminar to turbulent transitions in the jets flowing over the target surface and the effects of the low pressure, i.e. high swirl 'inner core', are also apparent.

The detailed behaviour of the heat transfer distributions can be studied by initially considering the contour at $z/D = 2$. Changes due to variations in z/D may then be examined later. The diagrams corresponding to $z/D = 2$ and $x/D = 3.2$, (i.e. the top horizontal group in the Figure 10.35) exhibit interactions between the adjacent jets for all the swirls, except for $S = 0.48$. These interactions occur midway along the lateral line joining the axis of the jets, and are particularly strong for $S = 0$ and $S = 0.12$. In these cases, the values of 'h' at $x_i/x = 1$ (i.e. the mid-point between adjacent jets) is, in fact, higher than at the central stagnation point ($x_i/x = 0$). Moreover, it is apparent that the heat transfers are influenced and distributed over a region extending from $x_i/x = 0.75$ to 1.0. These effects become weaker as the degree of swirl is increased, e.g. for $S = 0.36$ the region over which the interactions are apparent extends only from 0.84 to 1.0. The values of 'h' at $x/x_i = 1$ are now less than those on the central axis of the jet. At the maximum swirl studied, $S = 0.48$, these secondary perturbations are no longer observed and this probably signifies that the adjacent jets mix before impingement. The prior mixing results in a relatively more uniform heat distribution when compared to those for the other swirls. This particular plot (i.e. for $S = 0.48$) also exhibits the presence of the 'inner core' region similar to that observed for single free jets, see Figures 10.8 and 10.13. It is also apparent from all these contour plots that the lower heat transfer is observed at $x_j/x = 1$ (i.e. midway along the diagonal pitch). This is because of a relatively stagnant flow in this region.

One of the main differences at an increased nozzle pitch of x/D = 4.8 (i.e. the second row in Figure 10.35) is the presence of a laminar to turbulent transition in the deflected wall jet region for S = 0 and 0.12. Because of this transition and the strong interaction between adjacent jets, a complicated heat transfer distribution ensues over the surface. As the swirl is increased to S = 0.36, the interaction between jets again decreases as was observed for the closer pitch x/D = 3.2. The 'low heat transfer core' for S = 0.48 is still present. However, unlike the situation at x/D = 3.2, some interaction between the adjacent high swirl jets is apparent. Physically, this can probably be interpreted in terms of jets being unable to mix prior to impingement due to the larger initial separations.

At x/D = 6.4, the heat transfer characteristics of the jets are similar to those at x/D = 4.8. A laminar to turbulent transition is still present in the 'boundary layer' type flow at S = 0 and 0.12. The interactions between the adjacent jets at these swirls are also still observable but appear weaker than those at the previous closer pitches, x/D = 3.2 and 4.8. This may be due to the lower velocities in the wall jets as the 'boundary layer' builds up over the target surface. The contours are also found to have a generally 'squarish' shape. At S = 0.48, the low heat transfer inner core region has disappeared. At this comparatively large jet spacing for S = 0.36 and 0.48, the interference phenomena between adjacent jets are stronger. This supports the previous arguments that an increase in the nozzle pitch prevents mixing of the high swirl jets before impingements.

The effects of increasing the initial jet separation at constant swirl is particularly apparent if Figure 10.35 is re-examined in terms of each vertical group of contours. For $S \leqslant 0.24$, generally a more uniform distribution ensues and the contours become 'squarish'. However, at S = 0.36 and 0.48, the secondary interactions become more prominent as impingement of individual jets is possible.

It is also of interest that the transition from laminar to turbulent flow in the deflected wall jet was observed for $S \leqslant 0.24$ in the single jet tests but for multiple jets it only ensues at $S \leqslant 0.12$ at x/D = 4.8 and 6.4

Figure 10.36 presents contour plots at z/D = 4. At the closest nozzle pitch x/D = 3.2 interactions between the adjacent jets occurs only at S = 0 and 0.12, unlike at z/D = 2 (Figure 10.35) where similar phenomena also occurs at S = 0.24 and 0.36. Thus, an increase in the nozzle-to-target spacing results in more uniform heat transfer distributions for the higher swirls $0.24 \leqslant S \leqslant 0.48$. This is not unexpected because the increased effective diameter due to entrainment would tend to

cause mixing prior to impingement for all but low swirls (and no swirl) situations, i.e. S = 0.12. The extent of the region affected by the jet interference is also smaller than those observed in Figure 10.35, e.g. the region extends from $x_i/x = 0.81$ to 1.0 compared to 0.75 to 1.0 at S = 0 and x/D = 3.2. At the intermediate jet pitch x/D = 4.8, the transition from laminar to turbulent flow is absent, thus signifying a turbulent wall jet over the surface virtually from the onset of impingement. Moreover, at this greater jet spacing, interaction between adjacent jets at $x_i/x = 1$ reappears for all swirls. At x/D = 6.4, all the previous trends become more clearly demonstrated, e.g. the 'interference' phenomena are more marked at the high swirls S = 0.36 and 0.48 than at the closer pitches. Furthermore, as at z/D = 2, for the swirls S = 0 and 0.12 there is a weakening in the extent and magnitude of these perturbations because of a decrease in the velocity of the inter-mixing wall jets. The profiles at the largest spacing x/D = 6.4 are again more squarish than those for the other two pitches. Finally, the low heat transfer 'inner core' is absent for all the cases at z/D = 4, unlike the behaviour observed with a single free jet.

Increasing the nozzle-to-plate spacing to 8 diameters, see Figure 10.37, results in generally more uniform distributions, probably due to the more widespread mixing of adjacent jets to impingement. Evidence of jet interaction producing secondary heat transfer peaks is almost absent for all cases except S = 0 and S = 0.12 at x/D = 6.4 and S = 0 at x/D = 4.8. The heat transfer profiles are, thus, more uniform at the higher swirls although the absolute values of 'h' are fairly low due to the high rate of decay of the axial velocities with distance from the nozzle under these flow conditions.

The effect of nozzle-to-plate separation is illustrated directly in Figure 10.38 which presents contour plots at x/D = 4.8 for z/D ranging from 2 to 12. The effect at a particular swirl can be studied by observing a horizontal set of contour plots. Secondary heat transfer peaks near the middle of the lateral pitch are apparent at S = 0 for all z/Ds. The magnitude of the disturbance, however, grows weaker especially at z/D = 8 and 12. As the swirl is increased to S = 0.12, these interaction phenomena are restricted to z/D = 2-6, probably signifying that the jets interact prior to impingement for z/D = 8 and 12. At the higher swirls, the disturbances are confined to z/D = 2 and 4 and, moreover, are only just evident for S = 0.36 and 0.48 at z/D = 4. Thus, the heat transfers are relatively uniform at z/D = 12 for all swirls, and application of swirl also tends to make the contour fairly uniform at lower z/Ds, e.g. compare the plots corresponding to S = 0 and S = 0.24 at z/D = 6 or S = 0 and S = 0.48 at z/D = 4.

10.5.2 Average Heat Transfers - Jet Arrays.

The average heat transfer coefficients were determined by integrating the local heat transfer distributions over the field associated with the central jet in the array; the details of this integration are presented in Appendix D. the average heat transfer coefficients for the non-swirling jets (S = 0) are compared with the results of previous studies in Figure 10.39. In general, most of the present data fall between the correlations proposed by Dunn (Ref.25) and Gardon and Cobonpue (Ref.35). The present tests were carried out on a rig designed and used by Dunn which incorporated relatively long nozzles similar to those employed by Gardon and Cobonpue. Thus, it may be concluded that the present results are in good agreement with appropriate previously published data so that the validity of the experimental technique is verified.

The average heat transfer coefficients associated with the swirling jets are presented in Figure 10.40 which illustrates the variation of $\bar{h}$ with the degree of swirl for particular nozzle-to-plate separations. At all the separations, a decrease in the pitch of the nozzles results in an increase in heat transfer at all swirls. The 'nominal jet Reynolds number' has been maintained constant in these tests. The increase in heat transfer can be associated with the reduction in the area corresponding to each jet as the nozzle spacing is reduced. This is in broad agreement with the results in the single jet tests where (except initially for S = 0.48) the average Nusselt number decreased as the integration area was increased. Thus, for a particular fixed overall heat transfer area, the higher heat transfers associated with the closely spaced geometrics would only be achieved at the expense of additional nozzles and higher total fluid flow rates. It is apparent from Figure 10.40 that the magnitude of the average heat transfers also decreases as the nozzle-to-target spacings z/D are increased. This is due to the decay of axial velocity downstream from the nozzle exit. These phenomena have been reported previously for non-swirling jets by several workers (e.g. Ward et al (Ref.52) and Gardon and Cobonpue (Ref.35)), and are generally applicable for the swirling jet. The rate of decay of the average heat-transfers associated with the swirling jet arrays, however, exhibit somewhat different trends to those for the non-swirling jet as will be discussed later.

The application of swirl to the jet produces effects which are dependent on the nozzle-to-target spacing and the nozzle pitch. At z/D = 2 and 4 (see Figures 10.40(a) and 10.40(b)), an initial increase in the degree of swirl produces a considerable increase in the average heat transfer. The maximum heat transfer ensues at S = 0.24 approximately. This increase is especially prominent at the close nozzle pitches and z/D

= 2, see Figure 41. As the swirl number is increased beyond S = 0.24, the heat transfer subsequently decreases until eventually it falls below the no-swirl value. At z/D = 8, see Figure 10.40c, $\bar{h}$ is virtually constant for swirls up to S = 0.24, and then a reduction occurs as the swirl number is further increased. These heat transfer characteristics are in contrast to those of single swirling jets since, for the latter flows (except for very small integration areas), the average heat transfer coefficients decreased continuously as the degree of swirl was increased, i.e. the maximum coefficients occurred with the non-swirling jets.

The decay in $\bar{h}$ with an increase in nozzle-to-target separation z/D for both swirling and non-swirling jets can be seen in Figure 10.42. It is apparent from this Figure that the rate of decay for the swirling jets is greater than for the non-swirling cases, particularly at the smaller nozzle pitches (x/D). There is also some evidence that the higher swirls are associated with the more rapid rates of decay as illustrated by the plots for S = 0.48 in Figure 10.42.

The presented results exhibit similar trends to those observed by Dunn (Ref.25) whose data are plotted for comparison in Figure 10.43. As pointed out in Section 1.1, Dunn's tests were carried out in conjunction with the present work and covered a larger range of swirls (S = 0 to 0.71). His average heat transfer coefficients were obtained by determining the rate of mass loss from naphthalene test surfaces by direct weighing. This technique avoided any errors in the integration procedure and, from this point of view, probably provided more accurate results. However, Dunn's method of temperature control and measurement was probably less exact than in the present study. He also observed that the average heat transfer coefficient generally increased for swirls up to S = 0.25 at the lower z/Ds. Slight differences can be attributed to the fact that the average integrated values in the present tests were associated with the confined central jet in the array whereas, in the case of Ref.25, the measurement of naphthalene loss over the target surface was associated with the whole 3 x 3 array. Thus, the less restricted jets on the boundaries of the array were also included. Due to the similarity in the two sets of measurements, Ref.25 also observed similar trends with regard to the rate of decay of $\bar{h}$ with nozzle-to-target spacing.

The minimum degree of swirl which brings about an overall reduction in average heat transfers (when compared to the non-swirling jet value) depends on the geometry of the jet system, see Figure 10.44. This 'transition' swirl number decreases in somewhat linear fashion as the nozzle pitch is increased at both z/D = 2 and 4. Moreover, at each nozzle pitch, the overall reduction in $\bar{h}$ ensues at a lower swirl number as the nozzle-to-target spacing is increased. It was not possible to

draw similar conclusions at higher z/Ds since only slight increases in $\bar{h}$ were observed. These plots can be used to readily determine whether the application of a particular swirl brings about an increase or decrease in average heat transfer.

10.6 COMPARISON OF THE HEAT TRANSFERS FOR BOTH SINGLE AND MULTIPLE JET SYSTEMS.

The average heat transfers for these two cases are compared on the basis of $\overline{Nu}_S/\overline{Nu}_{ns}$ in Figure 10.45. The Reynolds number in both these cases is $Re_D = 32,000$ and these plots were obtained in a similar manner to those of Figure 10.33 except that only a mean line is shown for the sake of clarity. However, Figures 10.40 and 10.44 demonstrate that the average heat transfers are relatively insensitive to the changes in x/D so that, for the multiple jets, the mean lines presented are for various z/Ds. For the single jet, the Nusselt number is obtained by averaging over a target area defined by $0 \leqslant r/D \leqslant 4.25$. This is comparable to the area associated with each individual jet in an array with the nozzle pitch of x/D = 6.4 (r/D varies from 3.2 to 4.5 in the lateral and diagonal directions respectively). It is apparent from Figure 10.45 and previous discussion that the variation in average heat transfer due to the application of swirl is different for a single jet than for an array of jets. The increase of heat transfers for the multiple jets up to S = 0.24 is clearly reflected in these plots and this increase is more pronounced for the closer nozzle-to-target separations. Local increases in heat transfers due to the jet interaction have been observed in multiple jet systems, see Figures 10.35 to 10.37. It is possible that these interactions may account for the increases in heat transfer upon initial application of swirl in jet arrays.

However, in order to explore this behaviour further, it is necessary to compare directly the local variations in 'h' for both the single jet and an individual jet in an array. It should be pointed out, initially, that, unlike the 'single jet' contours which were essentially circular, those associated with the multiple jets depend on the radial direction under consideration. Examination of the contour plots illustrate that the variations along the lateral and diagonal pitches represent the two extremes, and the changes in other directions are intermediate cases, see Figure 10.46. It is apparent from this Figure that the variations in all the directions are similar up to about r/D = 2.5 and thereafter depend upon the direction considered.

The differing behaviour of the single and 'multiple' jets can be more effectively compared by considering Figures 10.47 to 10.49. Figure 10.47 illustrates the plots obtained for the single and multiple jets at z/D = 2. Similar plots for z/D = 4 and 8 have been presented in Figures

10.48 and 10.49 respectively. At each z/D, variations are plotted for S = 0, 0.12 and 0.24. Higher swirls have been omitted for the sake of clarity and, moreover, the maximum difference in behaviour between single and multiple jets occurs at S = 0.24. The heat transfer coefficients have again been normalised by dividing by 'h_o' and, in the case of the single jet, the distribution has been restricted to a field defined by r/D = 0 to 4.5. Furthermore, in the case of multiple jets, a nozzle pitch of x/D = 3.2 has been chosen since this situation exhibits the maximum increase of '$\bar{h}$' with initial application of increasing swirl, see Figure 10.40 and, finally, only the variations in the lateral directions are considered for the multiple jets.

At z/D = 2, the plots associated with S = 0.24 for the single jet (see Figure 10.47) lie below those for the non-swirling jet and S = 0.12 in general. The stagnation point values are virtually the same so that the reduction in heat transfer at S = 0.24 is due to the local distributions. However, the plots for the multiple jets at S = 0.12 and 0.24 give higher values than those at S = 0. Again, the maximum (stagnation) values are relatively insensitive to swirl in this region so that the changed distribution of the local heat transfers results in an overall increase in heat transfers for S = 0.12 and S = 0.24.

The plots for z/D = 4, see Figure 10.48, show similar trends although the distribution for the S = 0 in the single jet shows a secondary peak. There is also some evidence that the stagnation value decreases with the increased swirl for the single jet with the reverse occurring in the case of the array. This would tend to exacerbate any difference in the two cases.

At z/D = 8, the plots are similar for the single and multiple jets in that the normalised distribution for the swirling jets lies above those for S = 0. The difference in the average heat transfer characteristics is, thus, now primarily due to the more rapid decrease in h_o (stagnation point heat transfer) with application of swirl in the single free jet situation and not due to the differences in the shape of the local distributions. Thus, while the average heat transfer in the single jet decreases with the increase of swirl despite a more uniform distribution for the swirling jets, in the case of multiple jets the heat transfers for the swirling jets are slightly higher than S = 0.

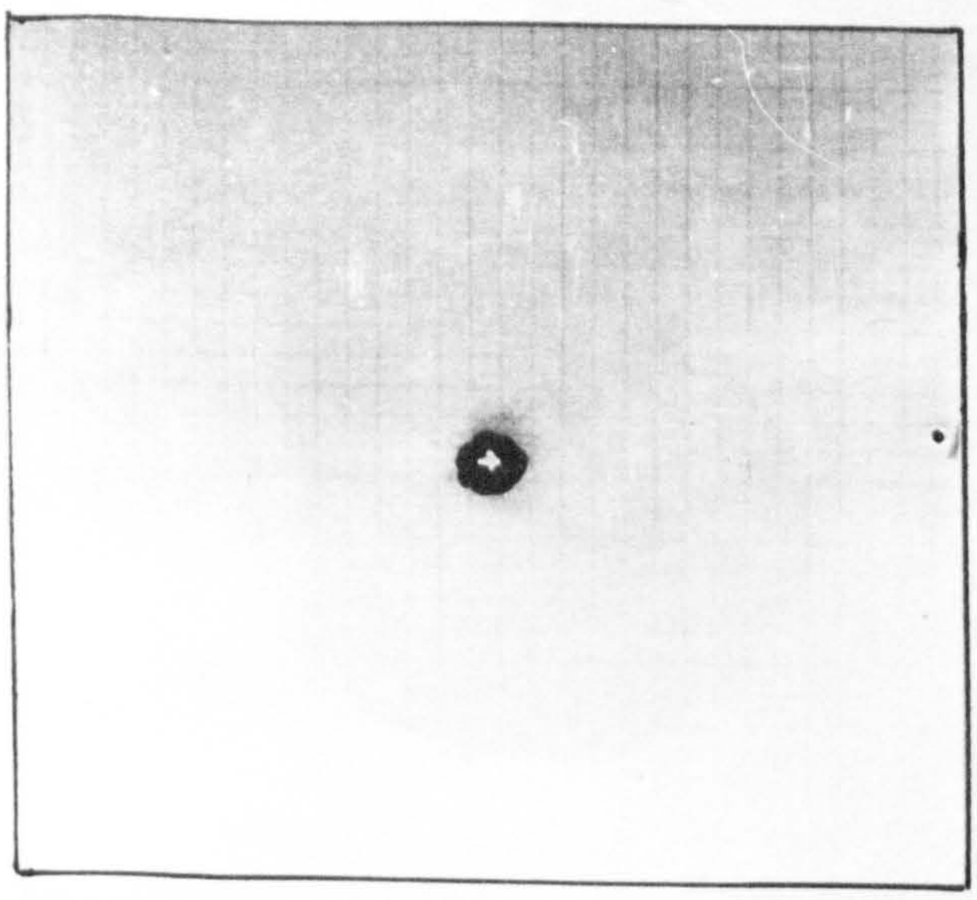

Time t = 650 s
h = 251.9 W/m²K
r̄ = 1.7 cms

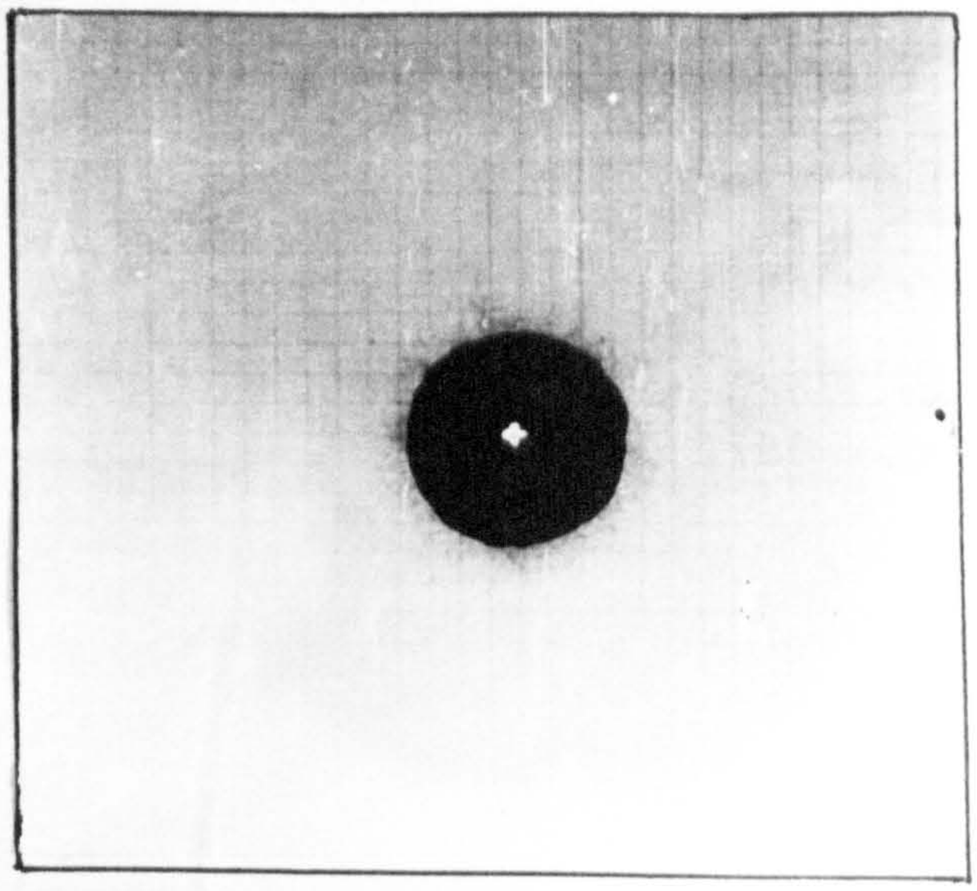

Time t = 920 s
h = 183.9 W/m²K
r̄ = 4.6 cms

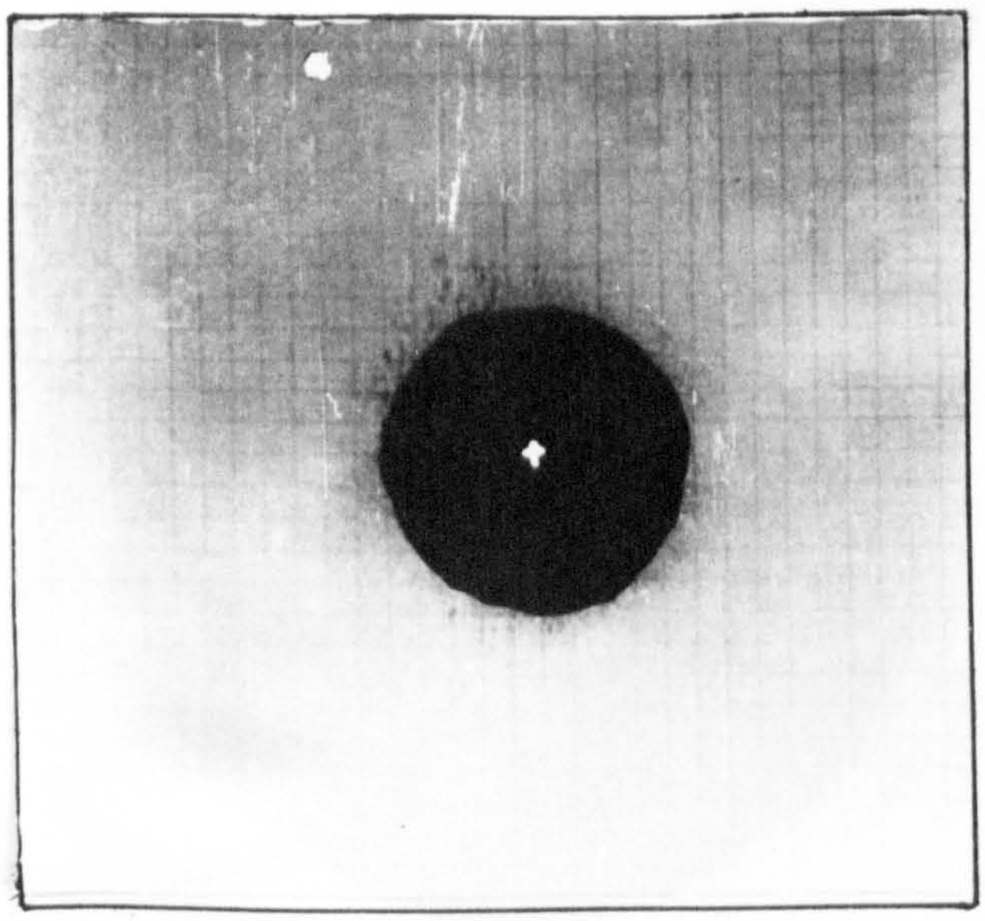

Time t = 1045 s
h = 162.0 W/m²K
r̄ = 5.9 cms

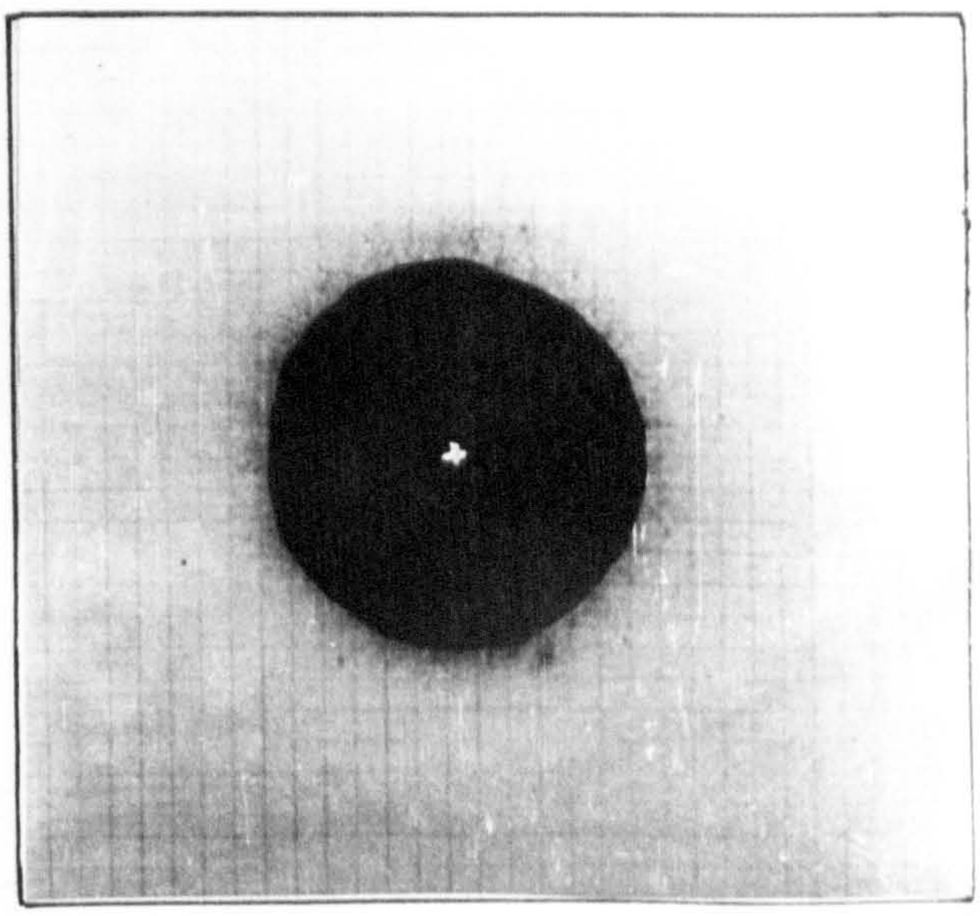

Time t = 1182 s
h = 143.3 W/m²K
r̄ = 7.9 cms

S = 0.12 z/D = 6 Re_D = 60,000 + Stagnation point

PLATE 5 (1) TYPICAL CLEARANCE PATTERNS OBTAINED FOR A SINGLE JET TEST

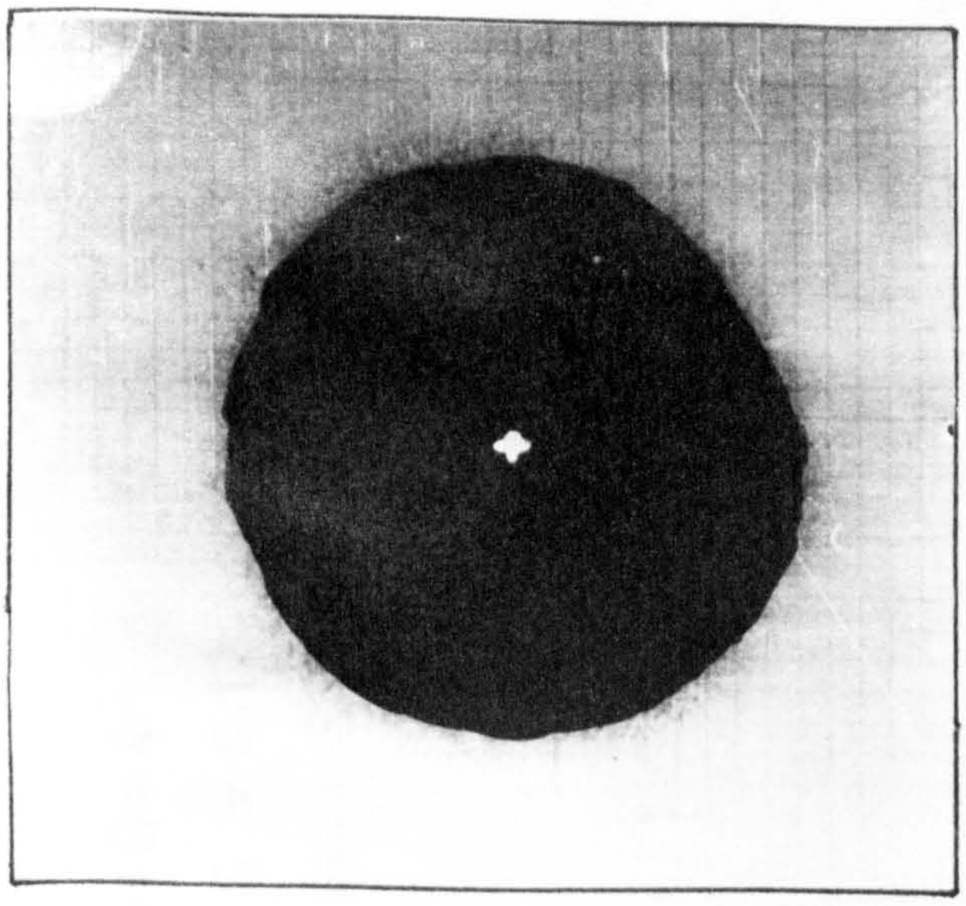

Time t = 1620 s
h = 108.4 W/m²K
r̄ = 11.7 cms

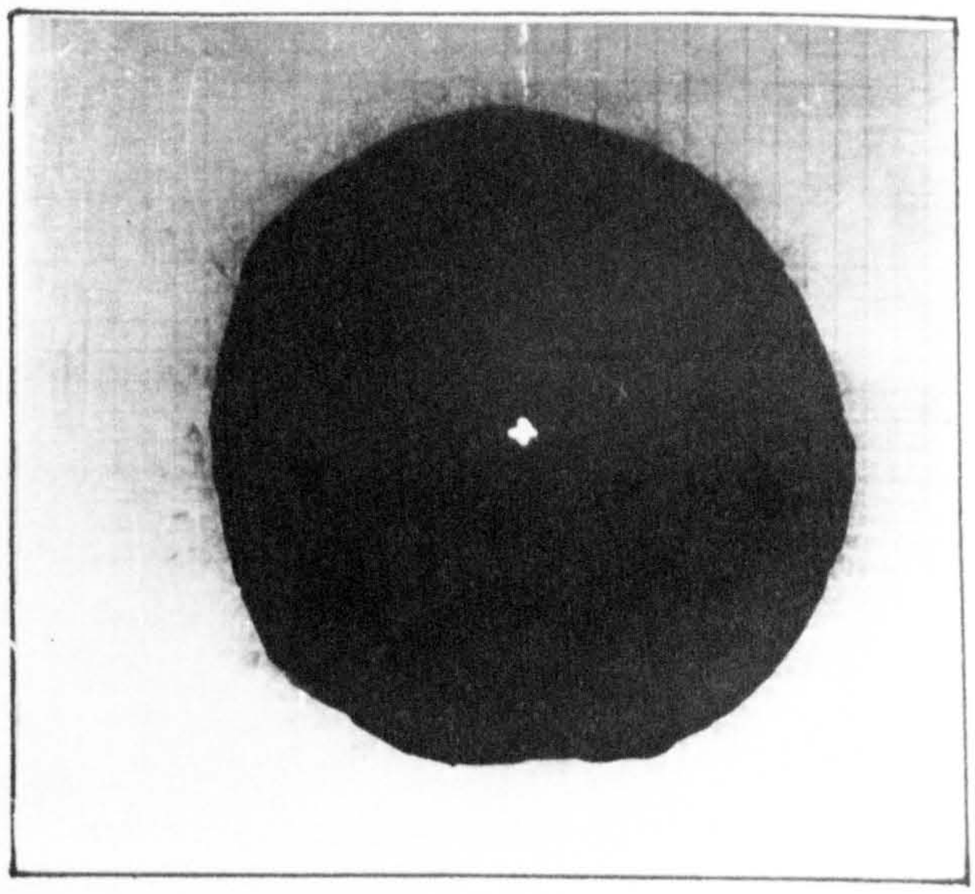

Time = 1840 s
h = 89.92 W/m²K
r̄ = 13.5 cms

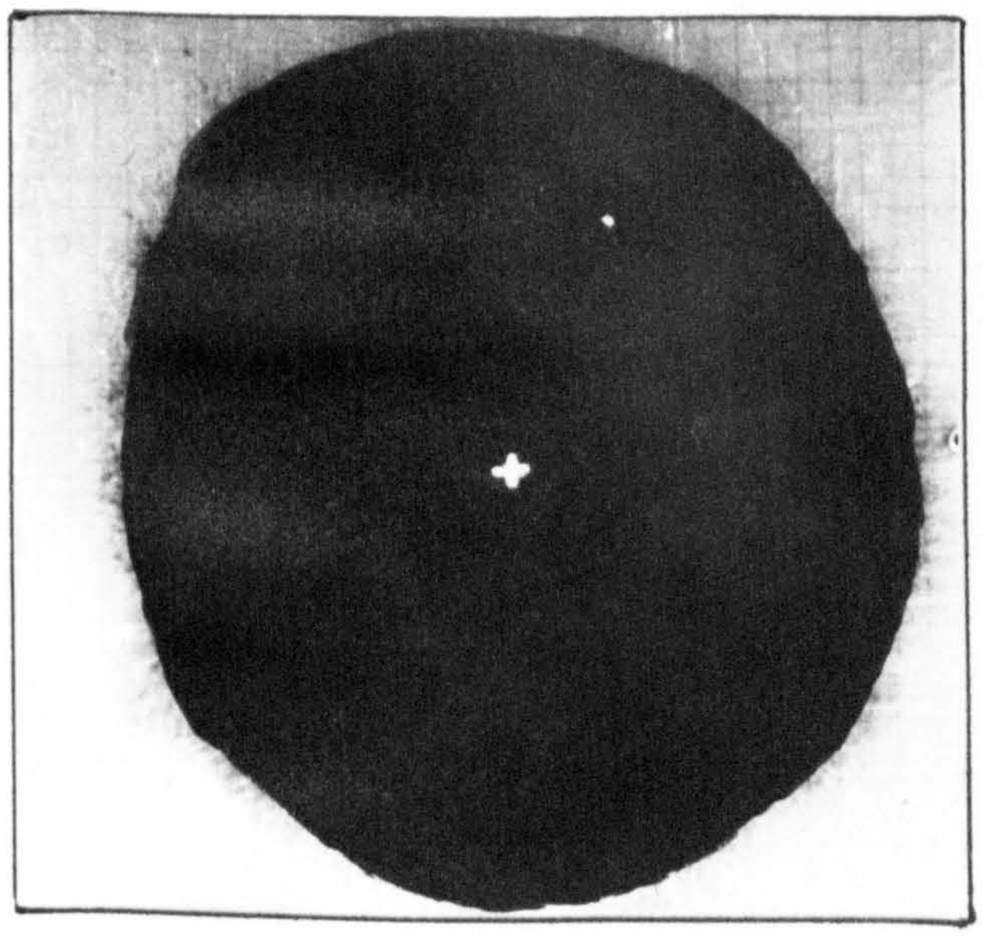

Time t = 2370 s
h = 71.6 W/m²K
r̄ = 16.8 cms

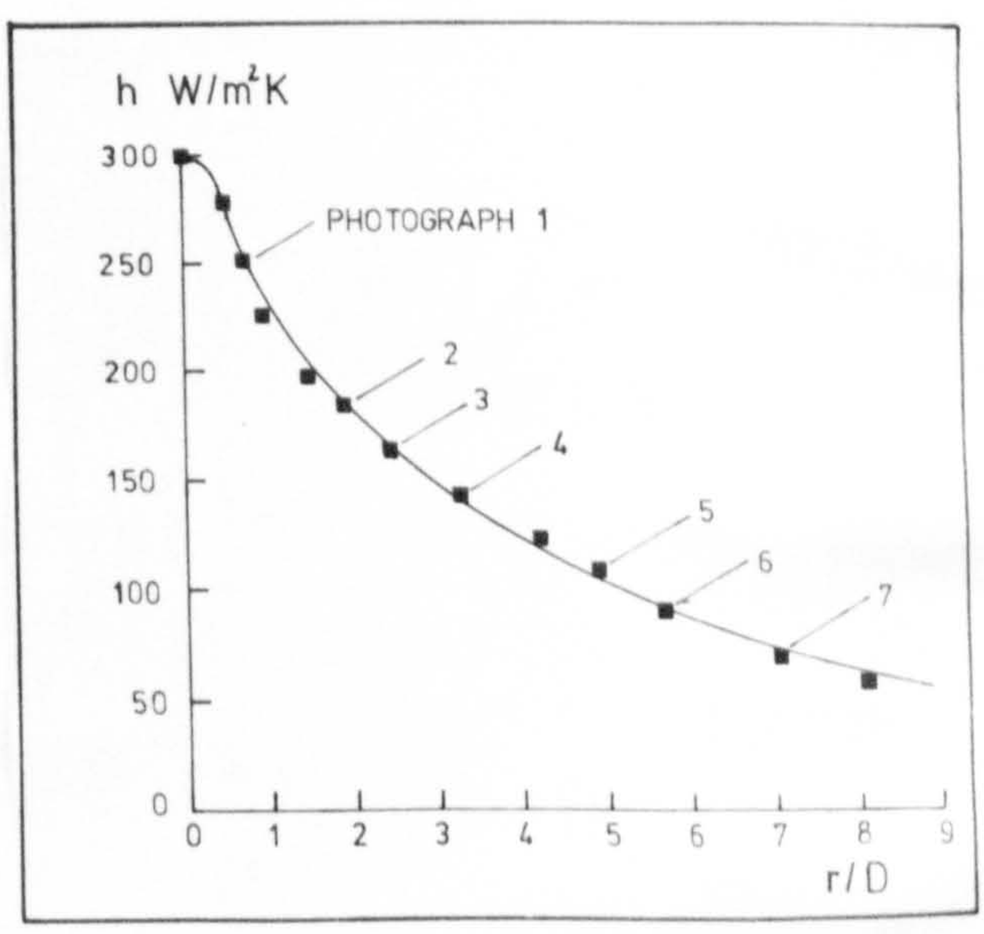

Radial variation of the heat transfer coefficient.

S = 0.12 z/D = 6 Re_D = 60,000 + Stagnation point

PLATE 5 (2) TYPICAL CLEARANCE PATTERNS OBTAINED FOR A SINGLE JET TEST.

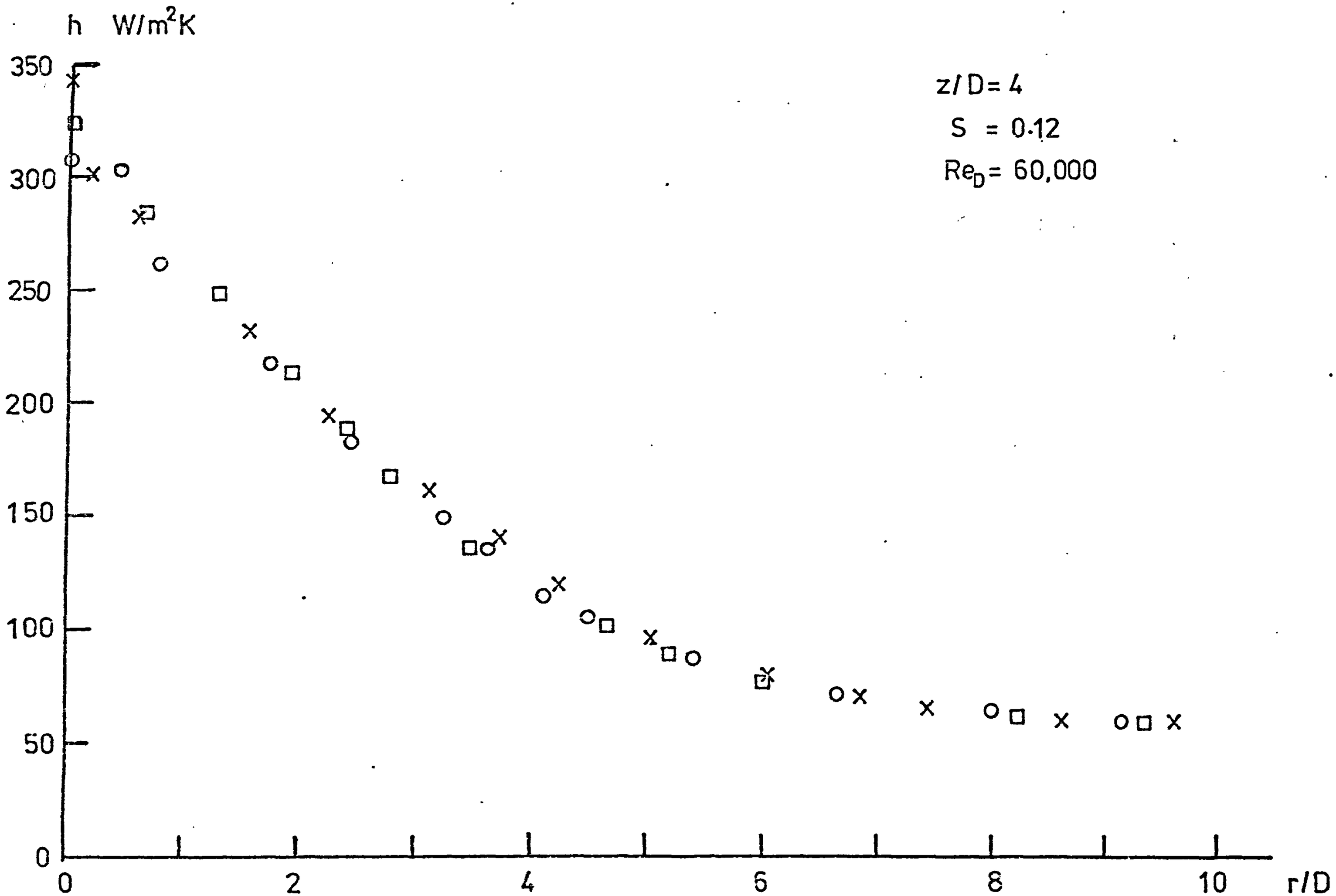

Fig. 10.1 REPEATABILITY OF AN INDIVIDUAL HEAT TRANSER TEST

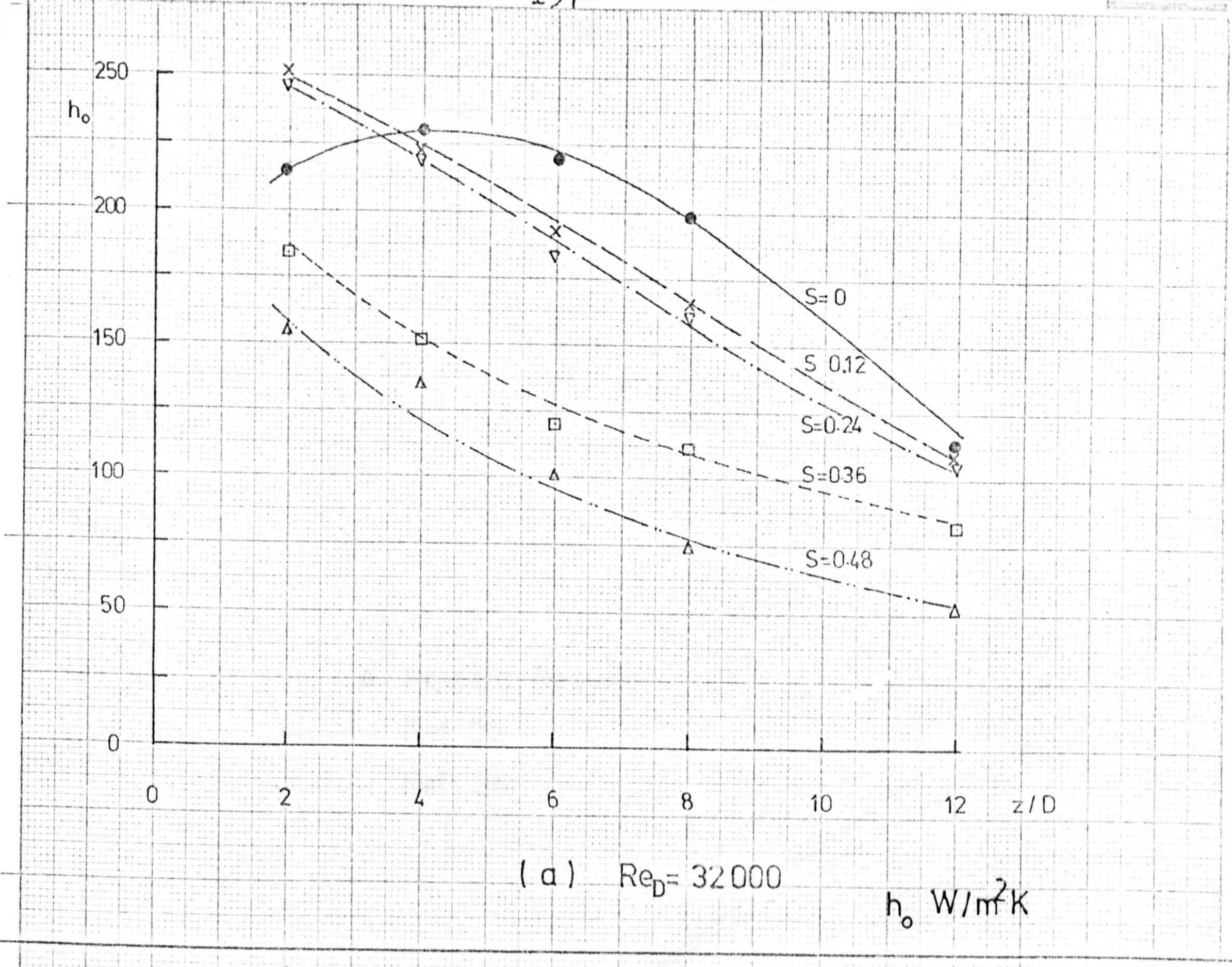

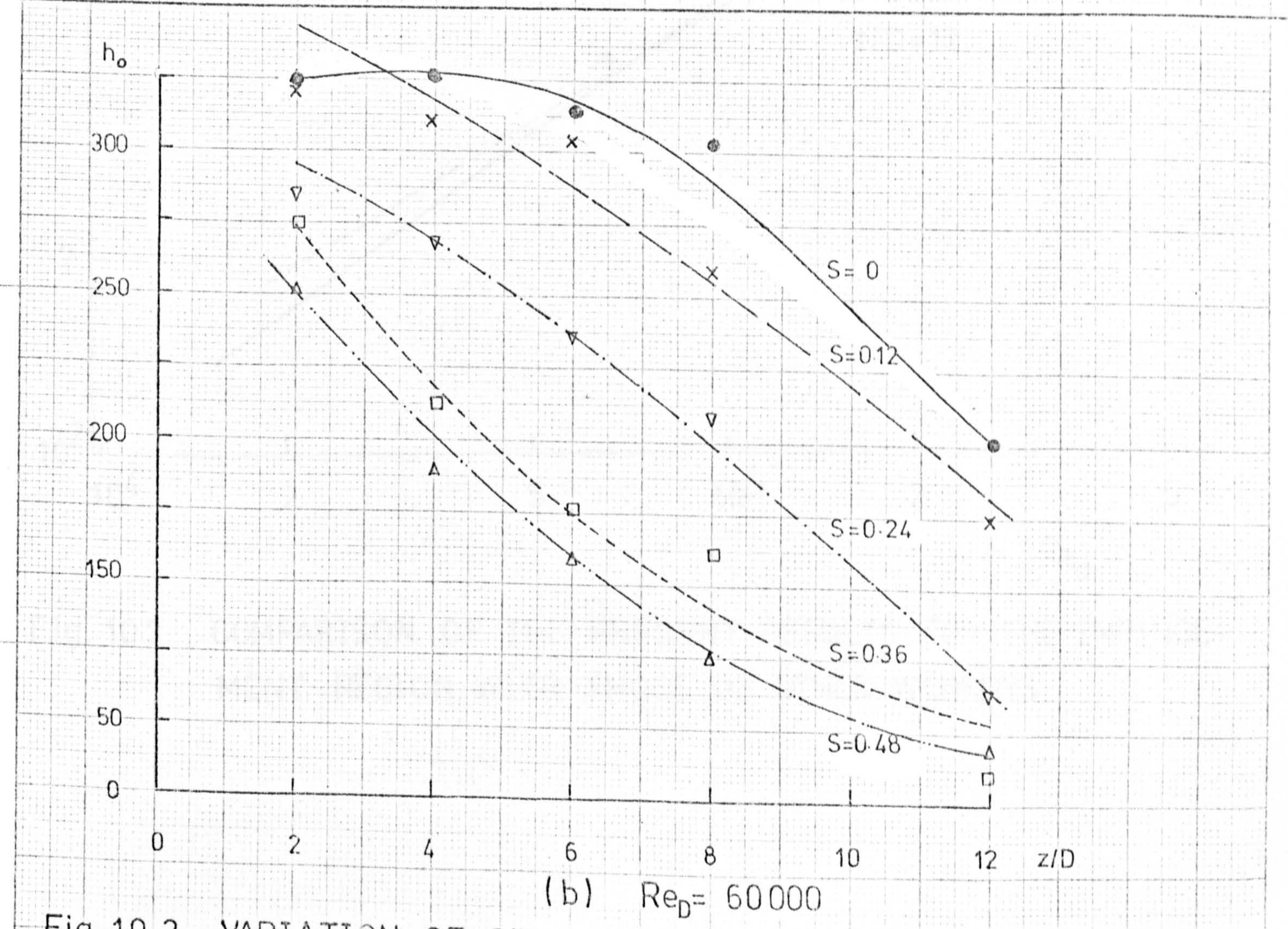

Fig. 10.2 VARIATION OF STAGNATION POINT HEAT TRANSFER WITH NOZZLE-TO-PLATE SPACING AT VARIOUS SWIRLS

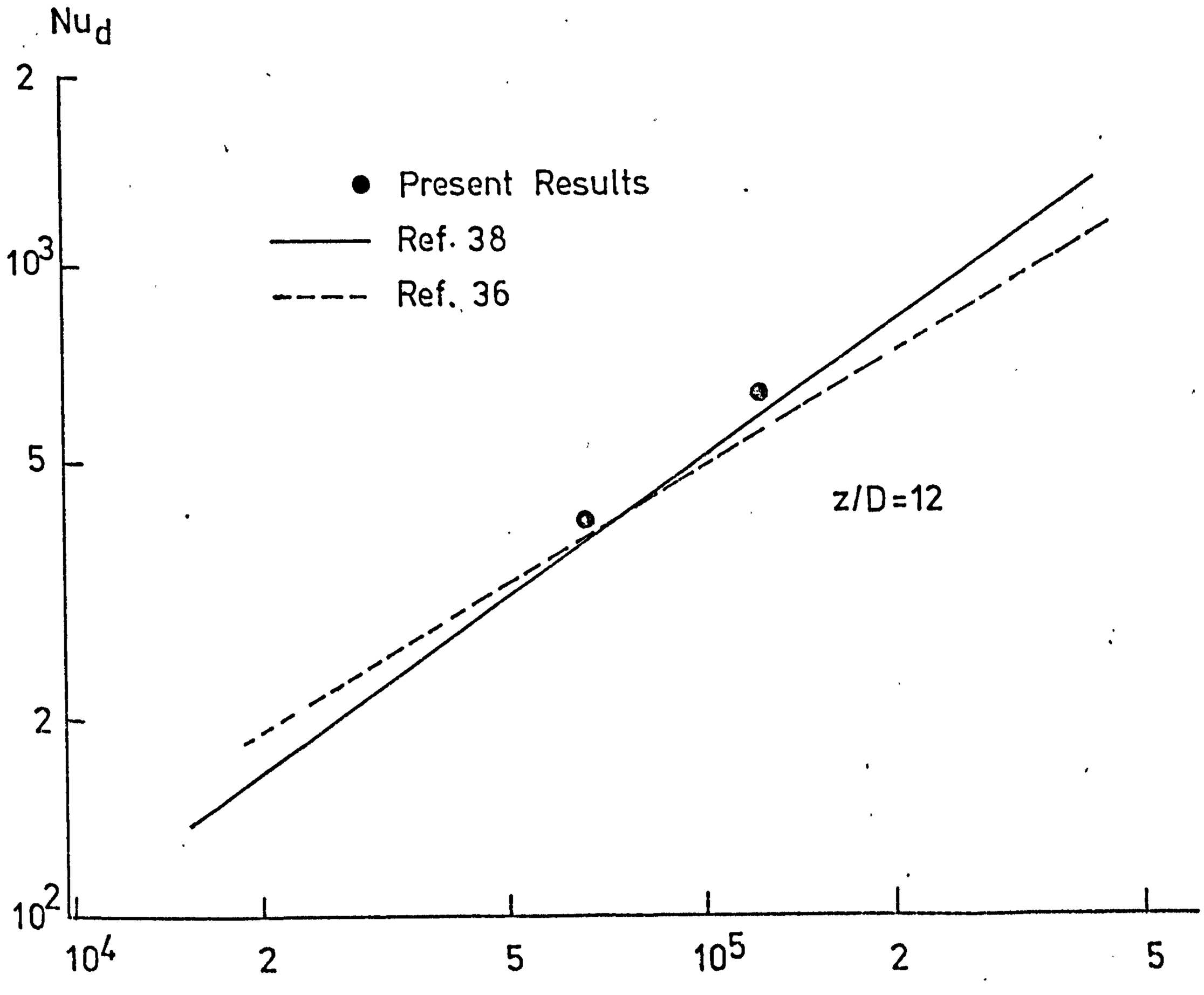

Fig. 10.3 COMPARISON OF THE PRESENT RESULTS FOR THE IMPINGEMENT REGION WITH THOSE OF OTHER WORKERS.

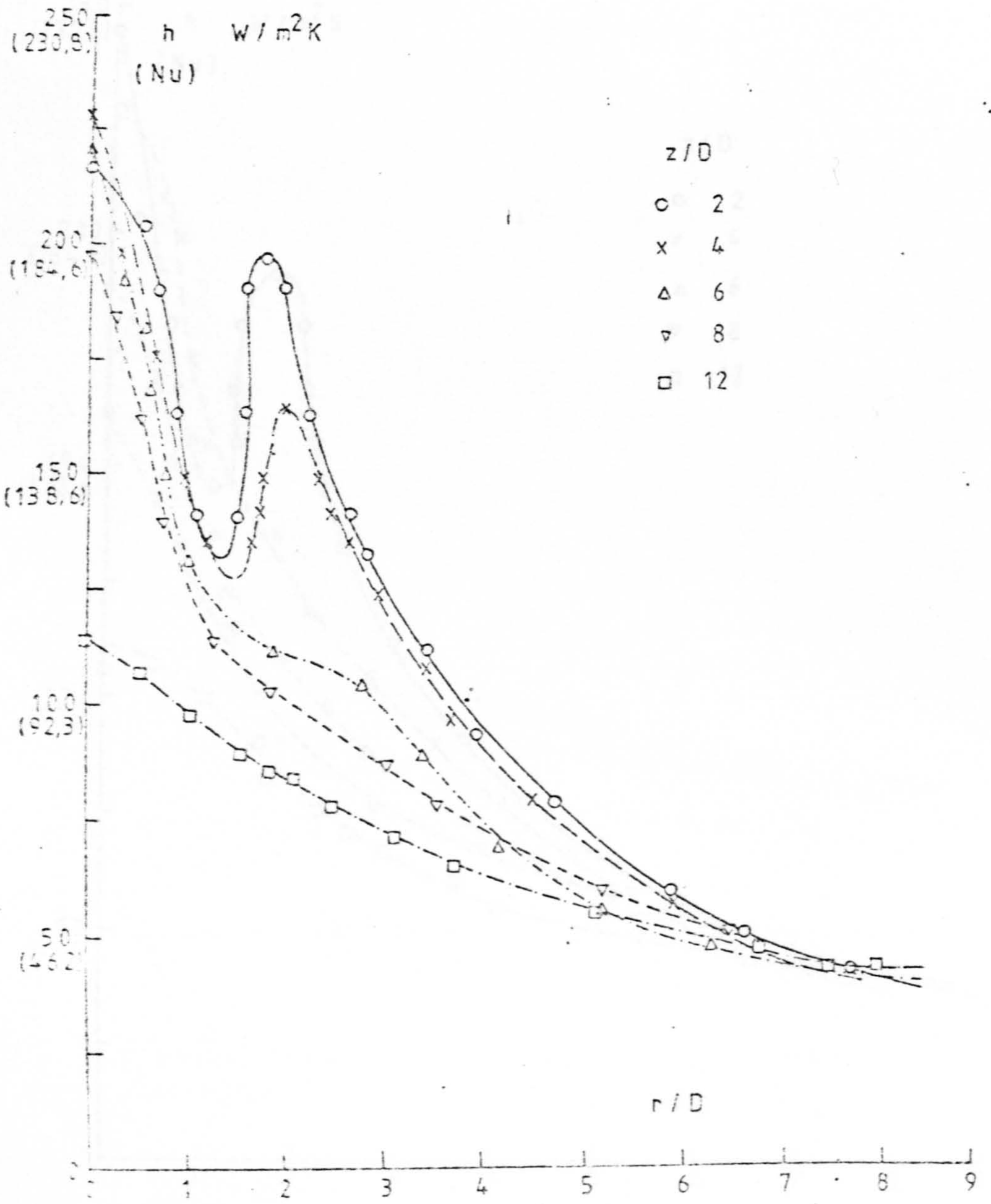

Fig 10,4 RADIAL VARIATION OF THE HEAT TRANSFER COEFFICIENT AT S = 0 FOR VARIOUS z/D's [Re_D = 32000]

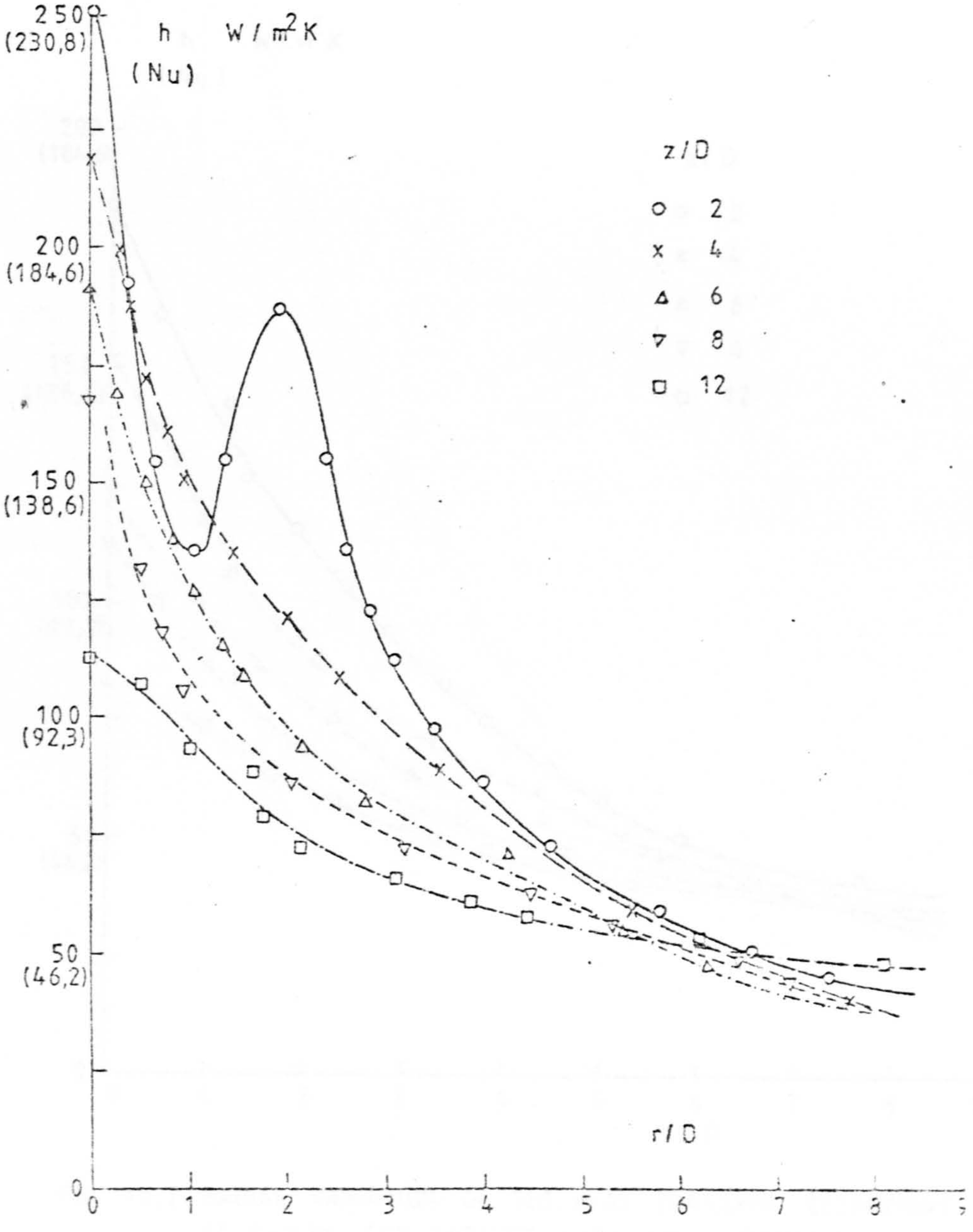

Fig 10,5 RADIAL VARIATION OF THE HEAT TRANSFER COEFFICIENT AT S = 0,12 FOR VARIOUS z/D's [Re_D = 32000]

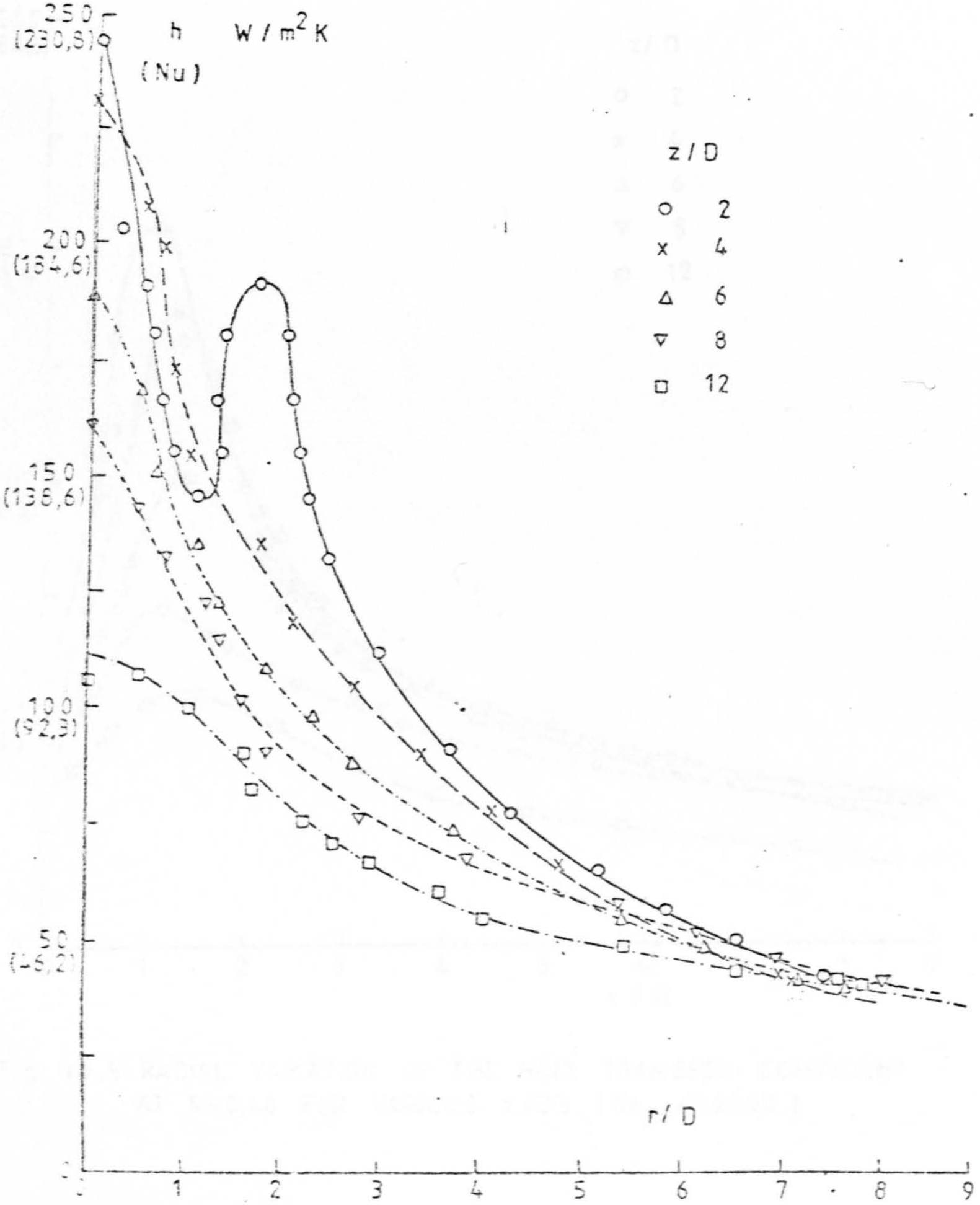

Fig 10,6 RADIAL VARIATION OF THE HEAT TRANSFER COEFFICIENT AT S = 0,24 FOR VARIOUS z/D's [Re_D = 32000]

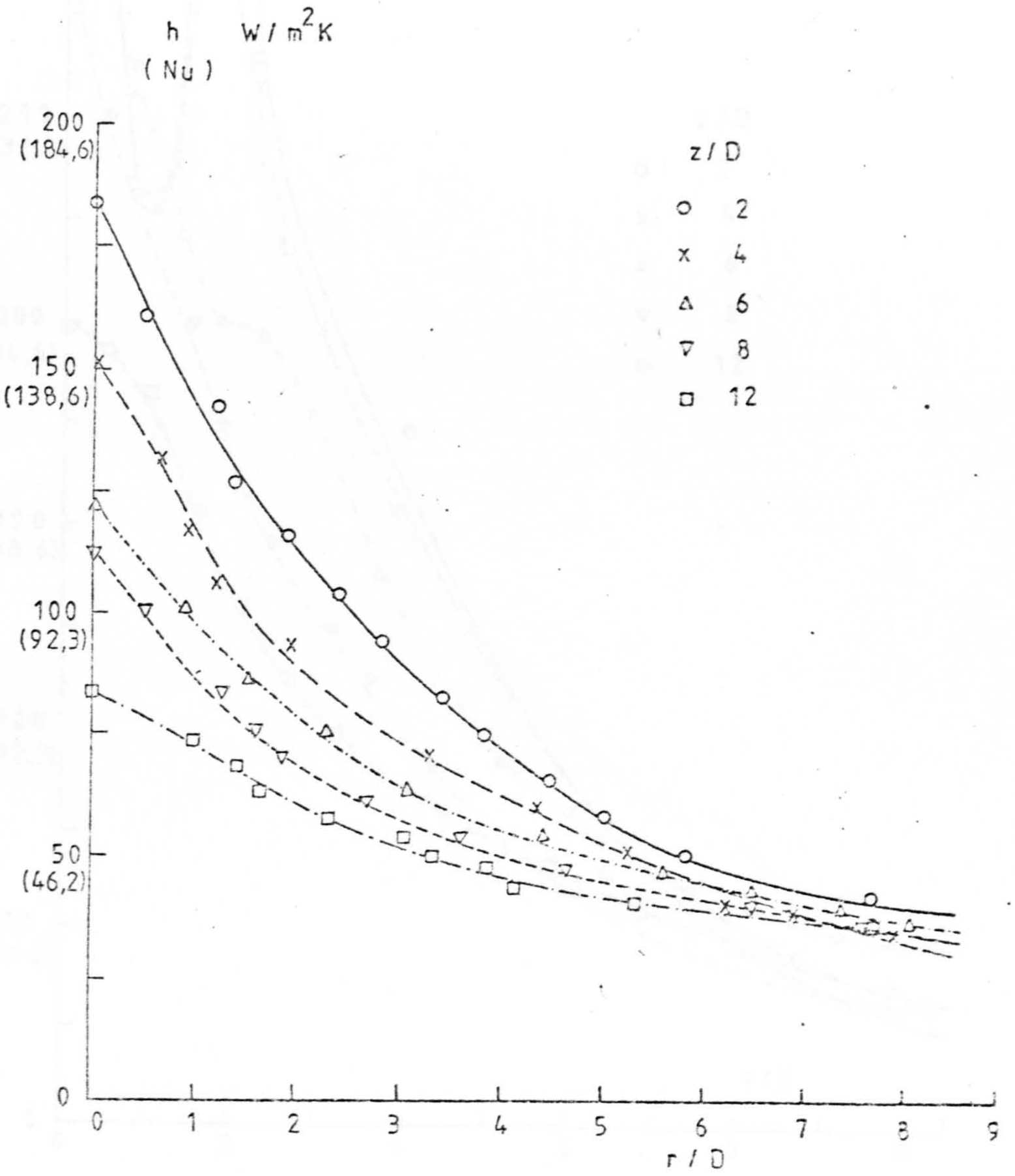

Fig 10,7 RADIAL VARIATION OF THE HEAT TRANSFER COEFFICIENT AT S = 0,36 FOR VARIOUS z/D's [Re_D = 32000]

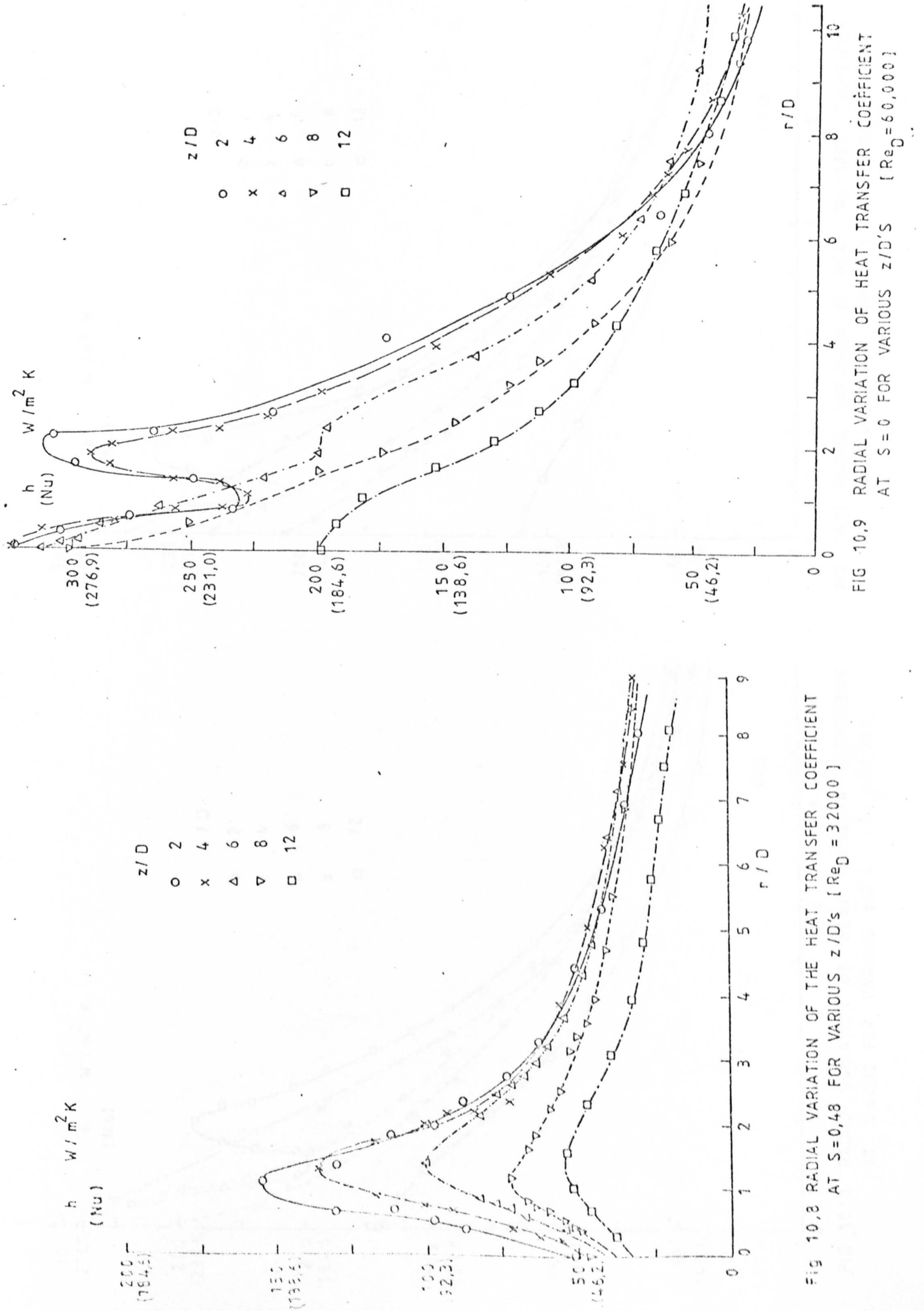

FIG 10,9 RADIAL VARIATION OF HEAT TRANSFER COEFFICIENT AT S = 0 FOR VARIOUS z/D'S [Re_D = 60,000]

FIG 10,8 RADIAL VARIATION OF THE HEAT TRANSFER COEFFICIENT AT S=0,48 FOR VARIOUS z/D's [Re_D = 32000]

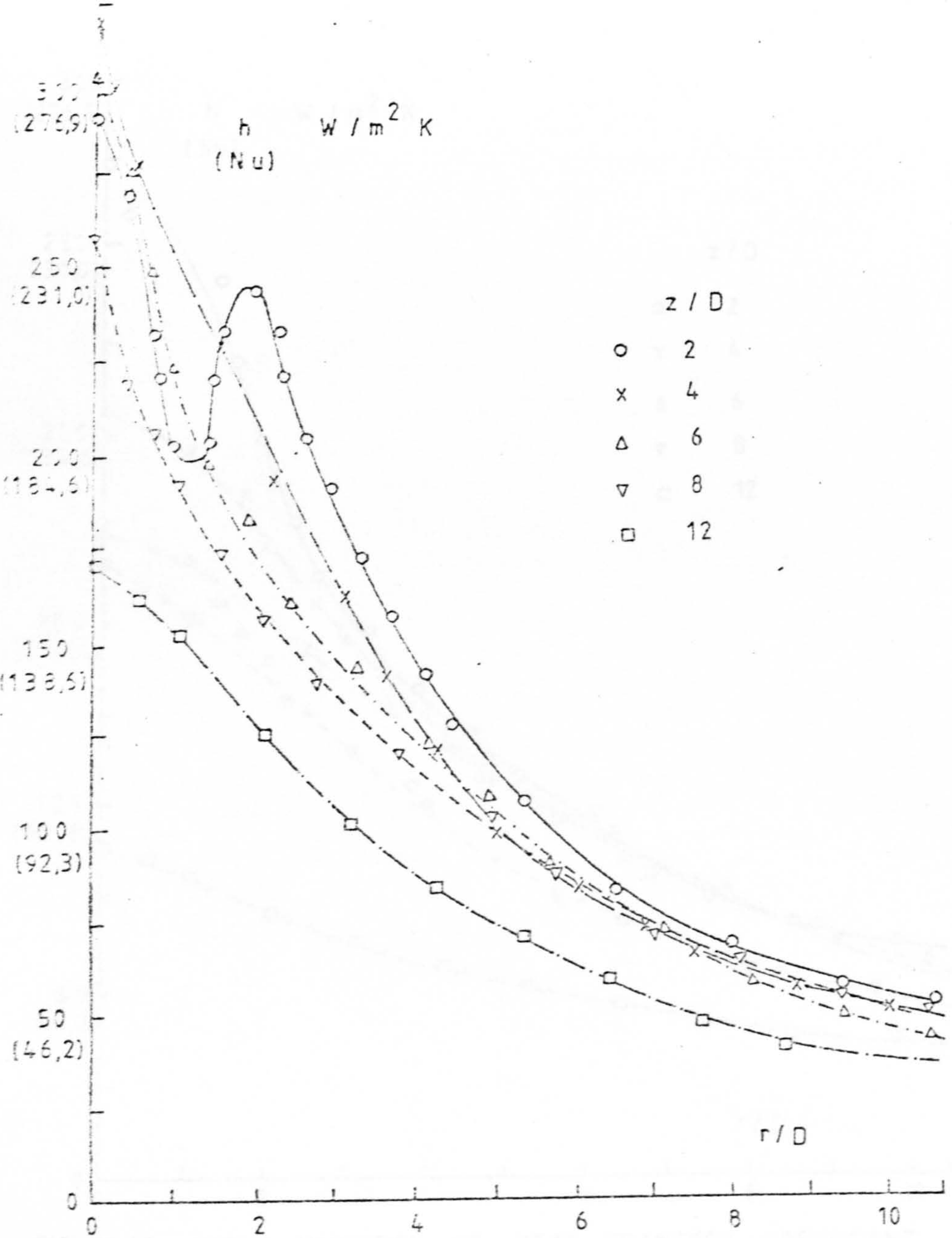

FIG 10,10 RADIAL VARIATION OF HEAT TRANSFER COEFFICIENT AT S = 0,12 FOR VARIOUS z/D'S [Re_D = 60,000]

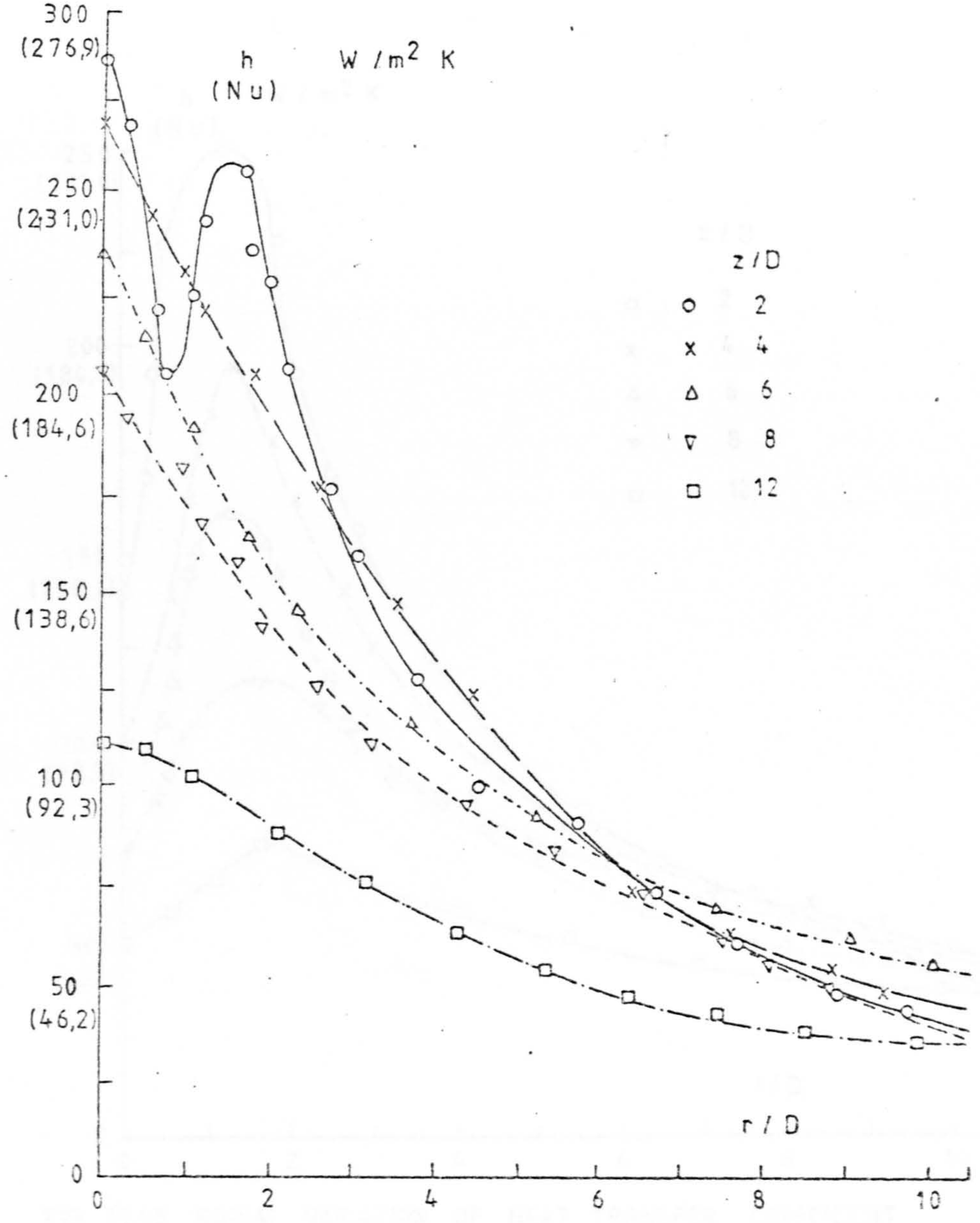

FIG 10,11 RADIAL VARIATION OF HEAT TRANSFER COEFFICIENT AT S = 0,24 FOR VARIOUS z/D'S [Re_D = 60,000]

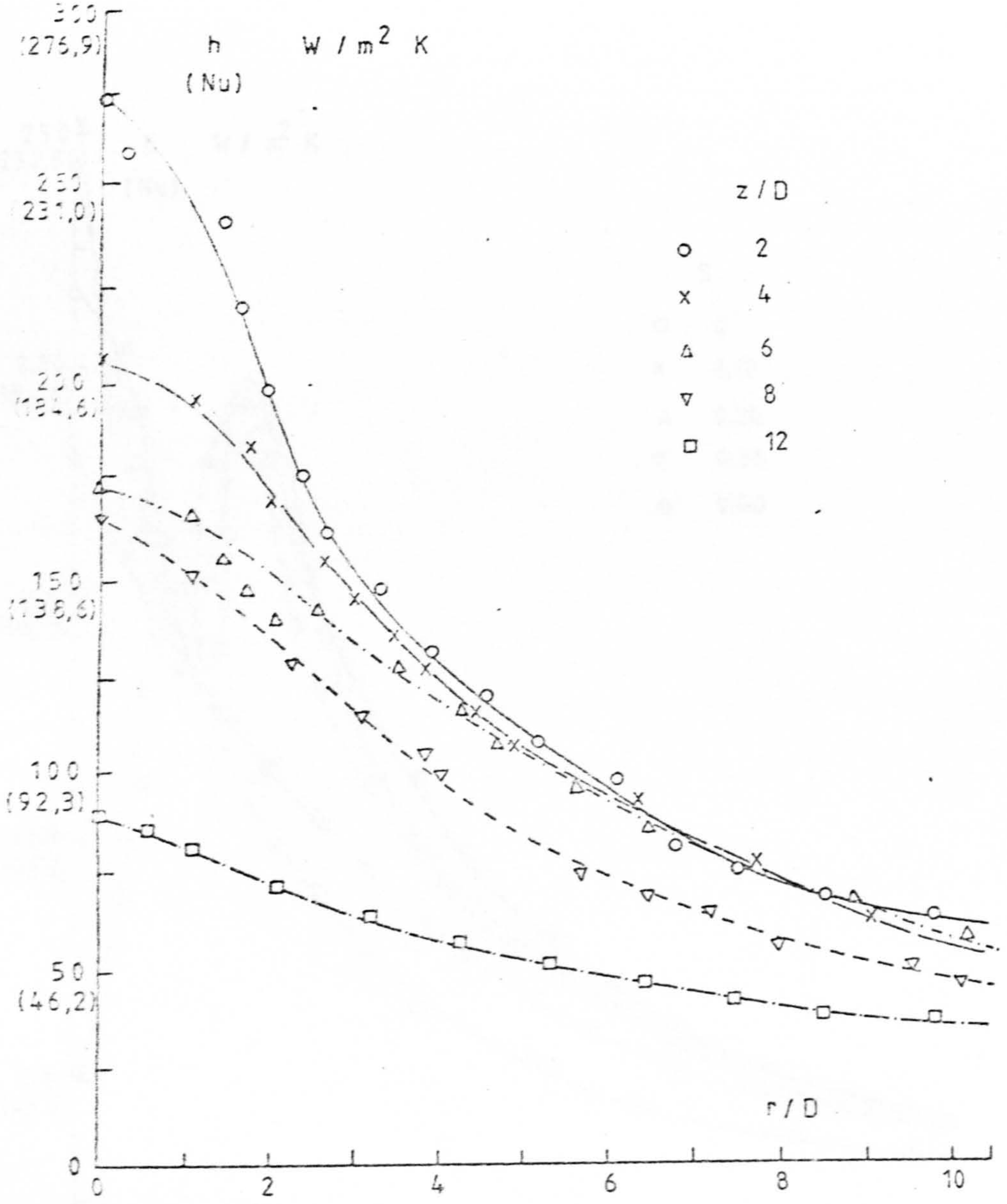

FIG 10,12 RADIAL VARIATION OF HEAT TRANSFER COEFFICIENT AT S = 0,36 FOR VARIOUS z/D'S [Re_D = 60,000]

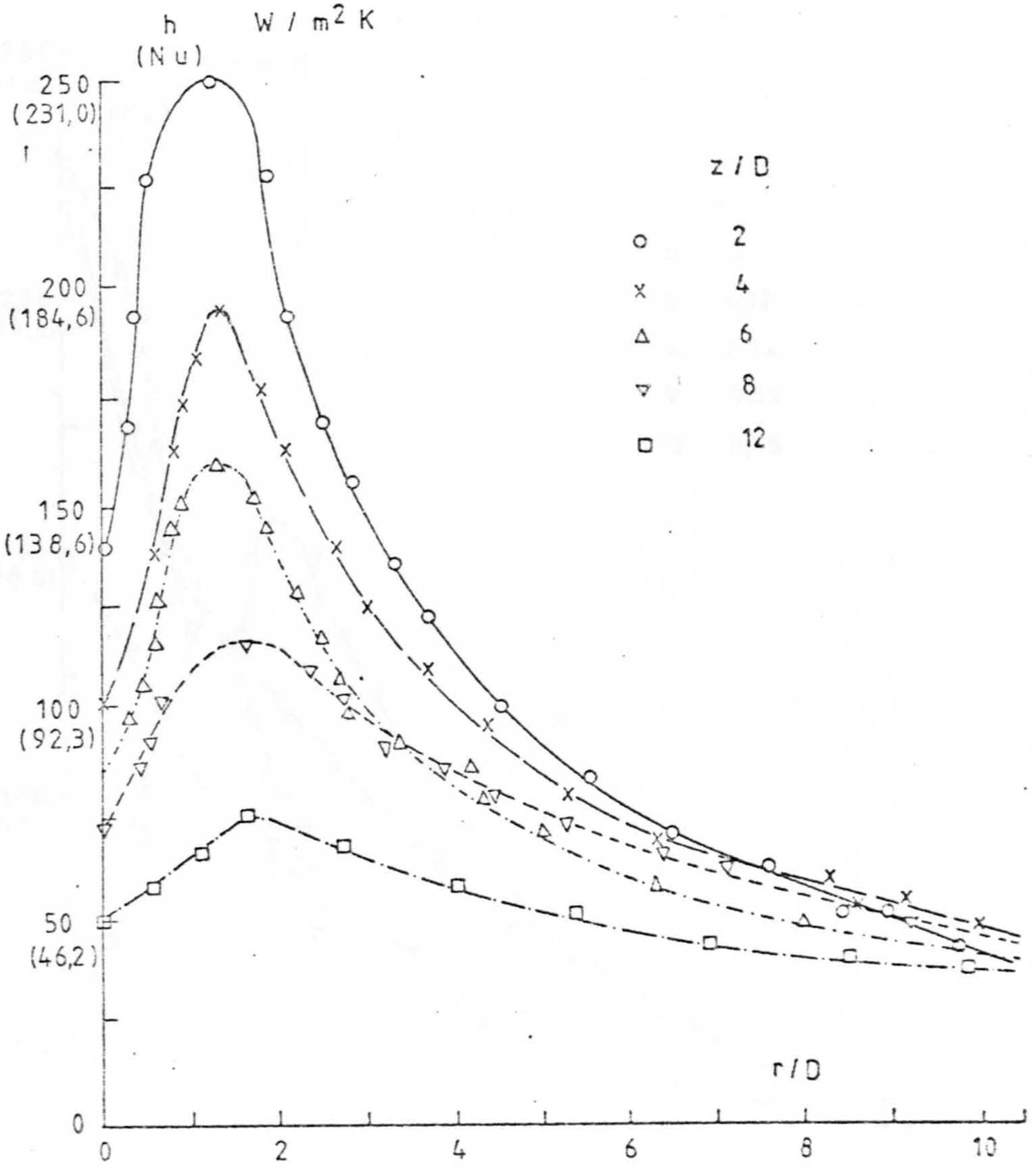

FIG 10,13 RADIAL VARIATION OF HEAT TRANSFER COEFFICIENT AT S = 0,48 FOR VARIOUS z/D'S [Re_D = 60,000]

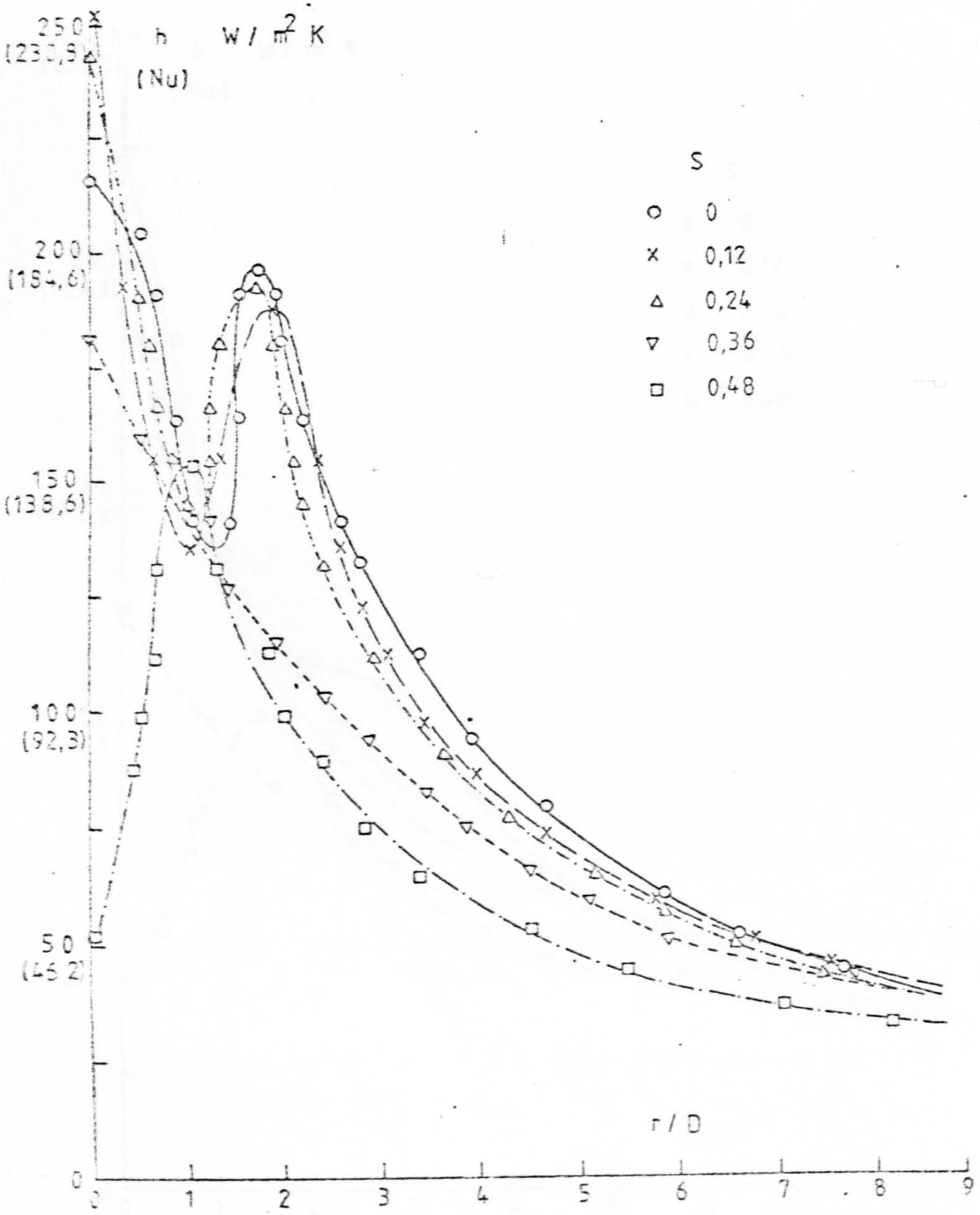

Fig 10,14 RADIAL VARIATION OF THE HEAT TRANSFER COEFFICIENT AT z/D 2 FOR VARIOUS SWIRLS [$Re_D = 32000$]

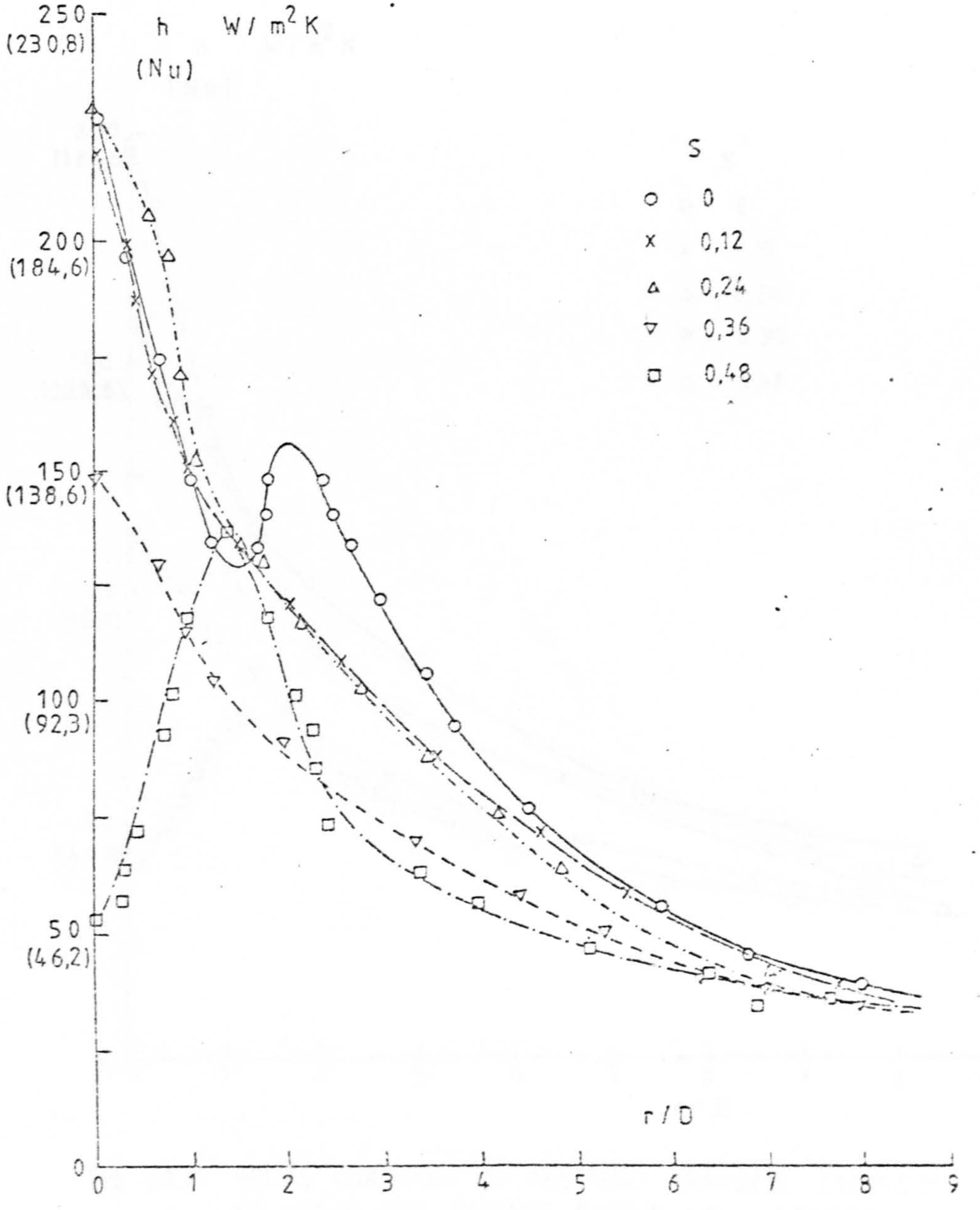

Fig 10,15 RADIAL VARIATION OF THE HEAT TRANSFER COEFFICIENT AT z/D=4 FOR VARIOUS SWIRLS [$Re_D = 32000$]

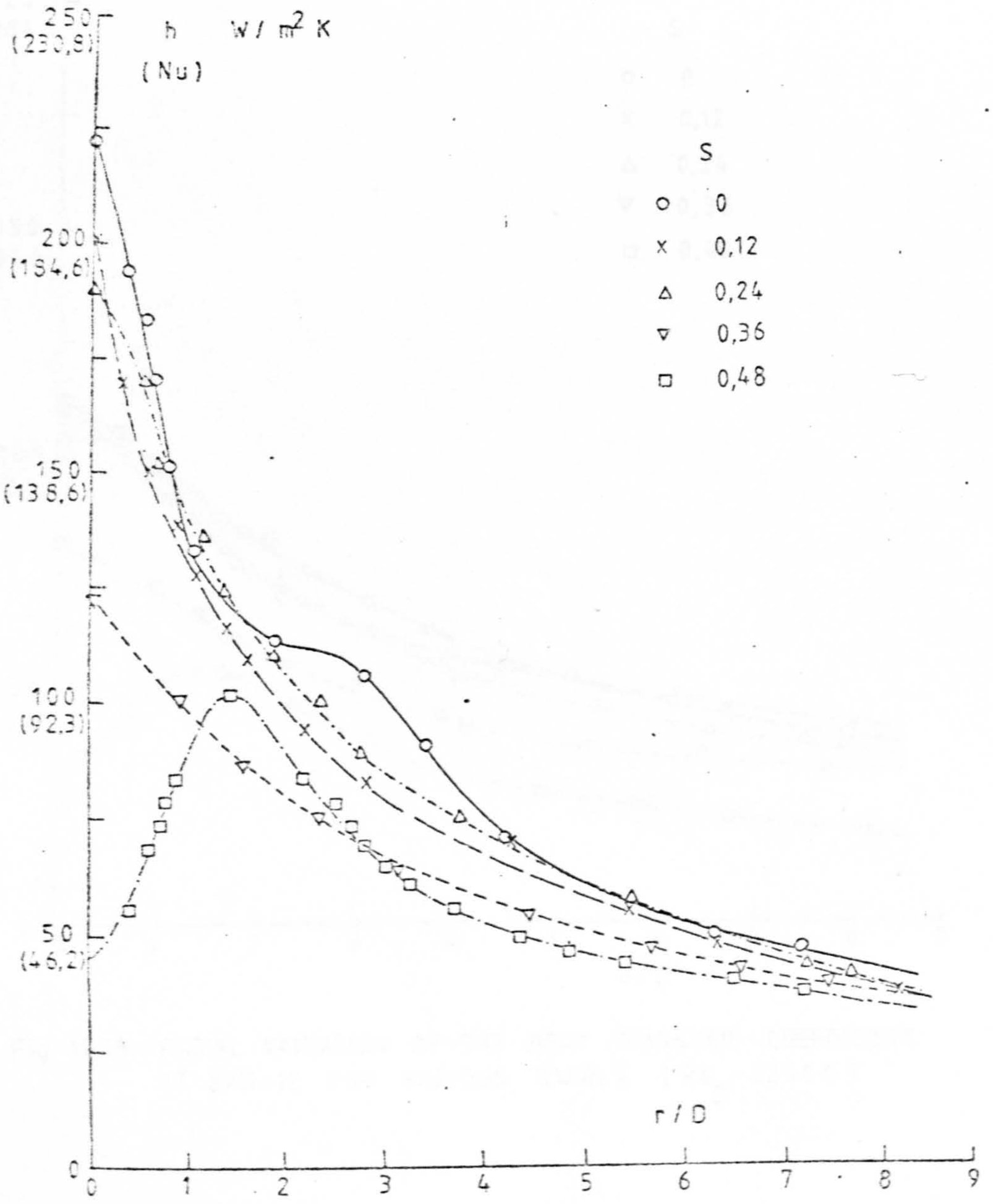

Fig 10,16 RADIAL VARIATION OF THE HEAT TRANSFER COEFFICIENT AT z/D= 6 FOR VARIOUS SWIRLS (Re_D = 32000)

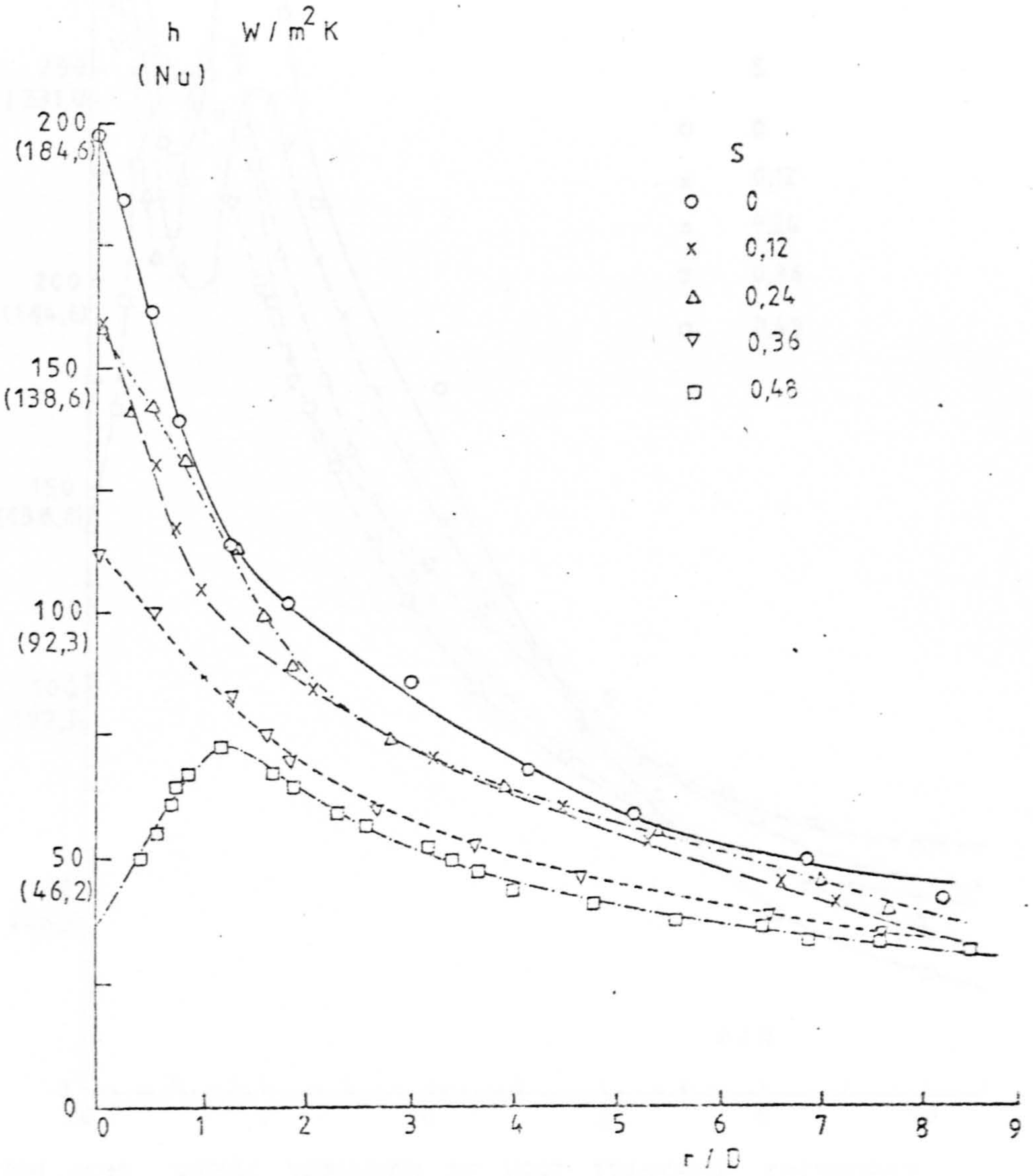

Fig 10,17 RADIAL VARIATION OF THE HEAT TRANSFER COEFFICIENT AT z/D= 8 FOR VARIOUS SWIRLS (Re_D = 32000)

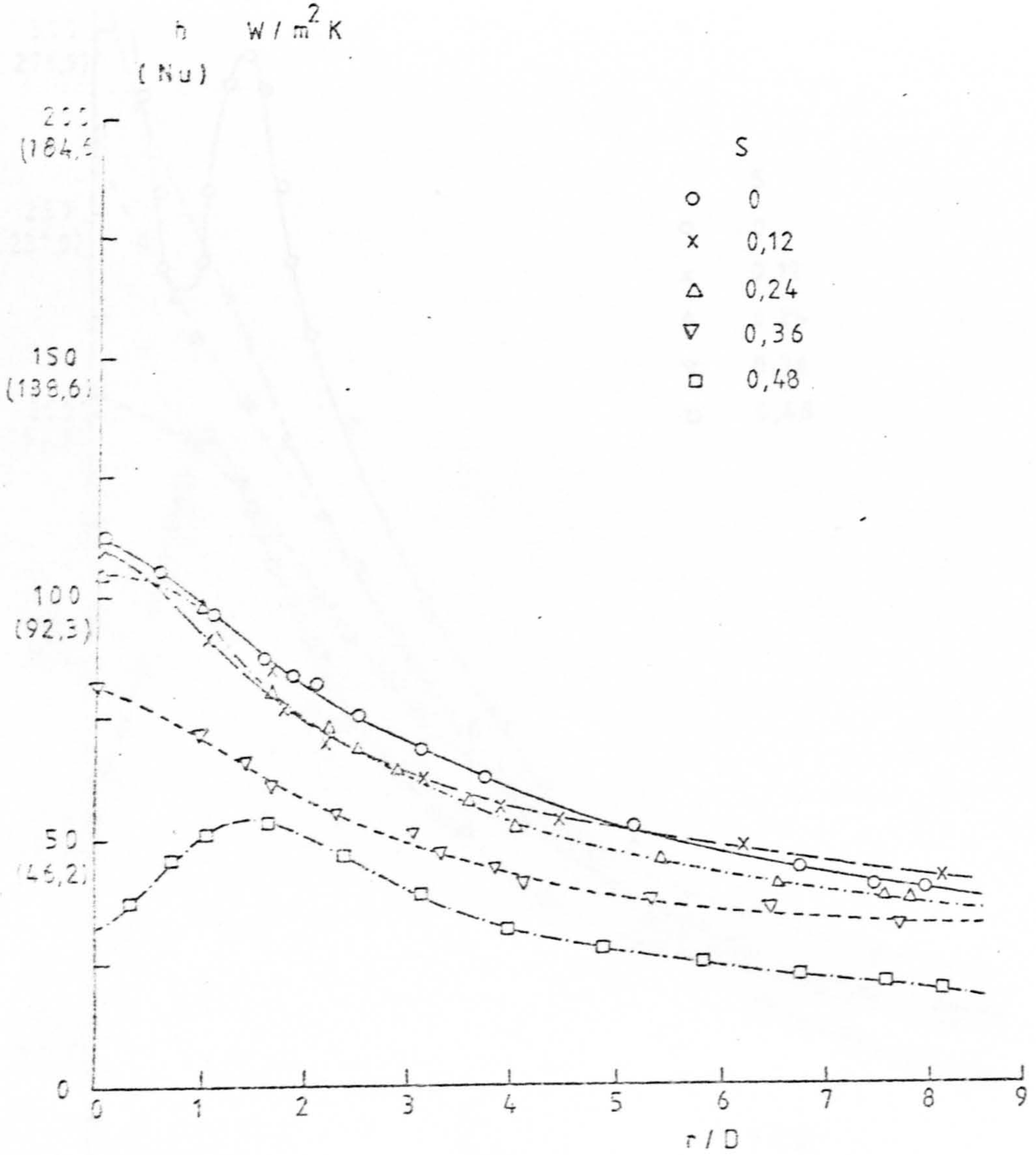

Fig 10,18 RADIAL VARIATION OF THE HEAT TRANSFER COEFFICIENT AT z/D=12 FOR VARIOUS SWIRLS [Re_D = 32000]

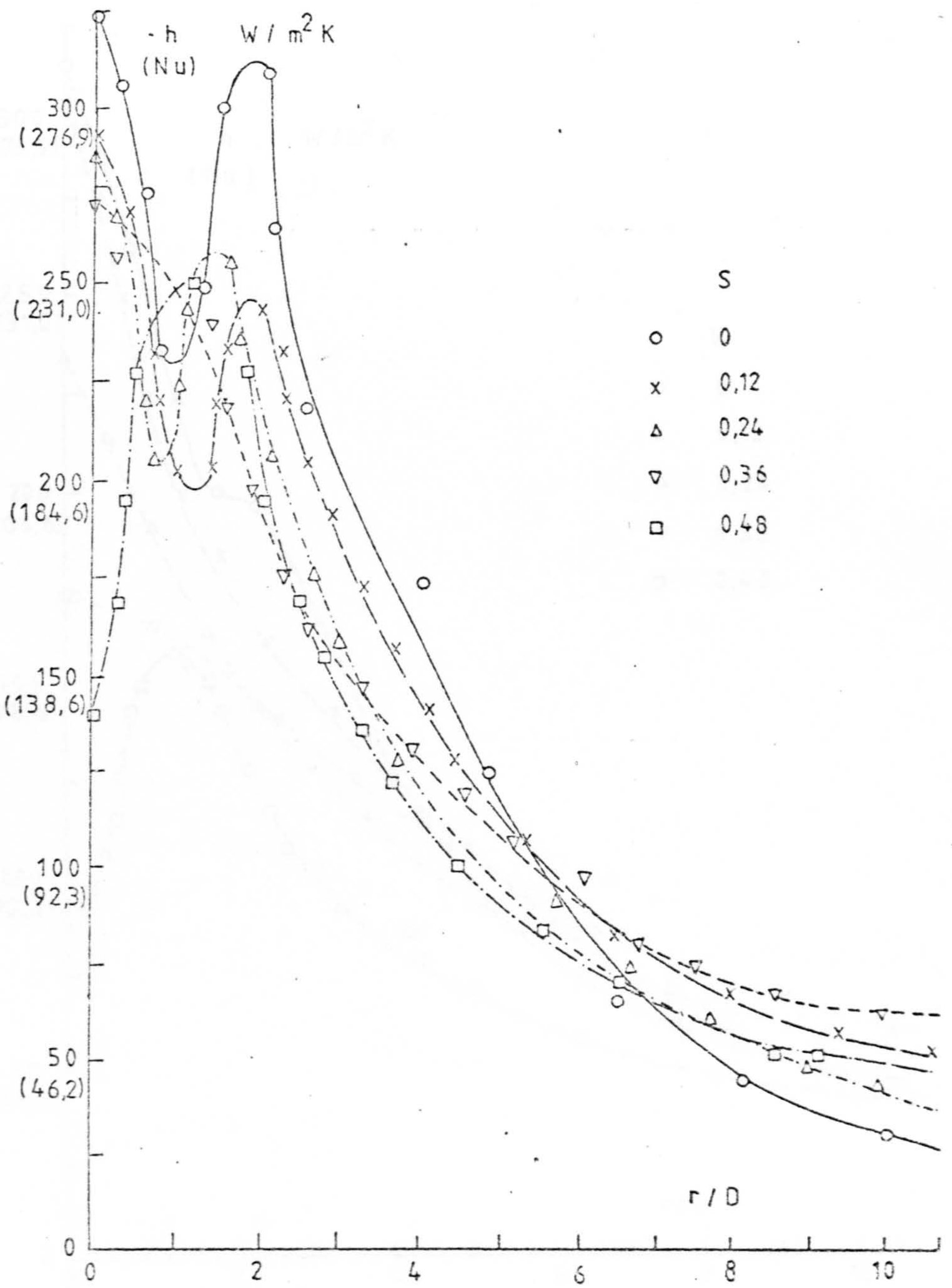

FIG 10,19 RADIAL VARIATION OF HEAT TRANSFER COEFFICIENT AT z/D = 2 FOR VARIOUS SWIRLS [Re_D = 60,000]

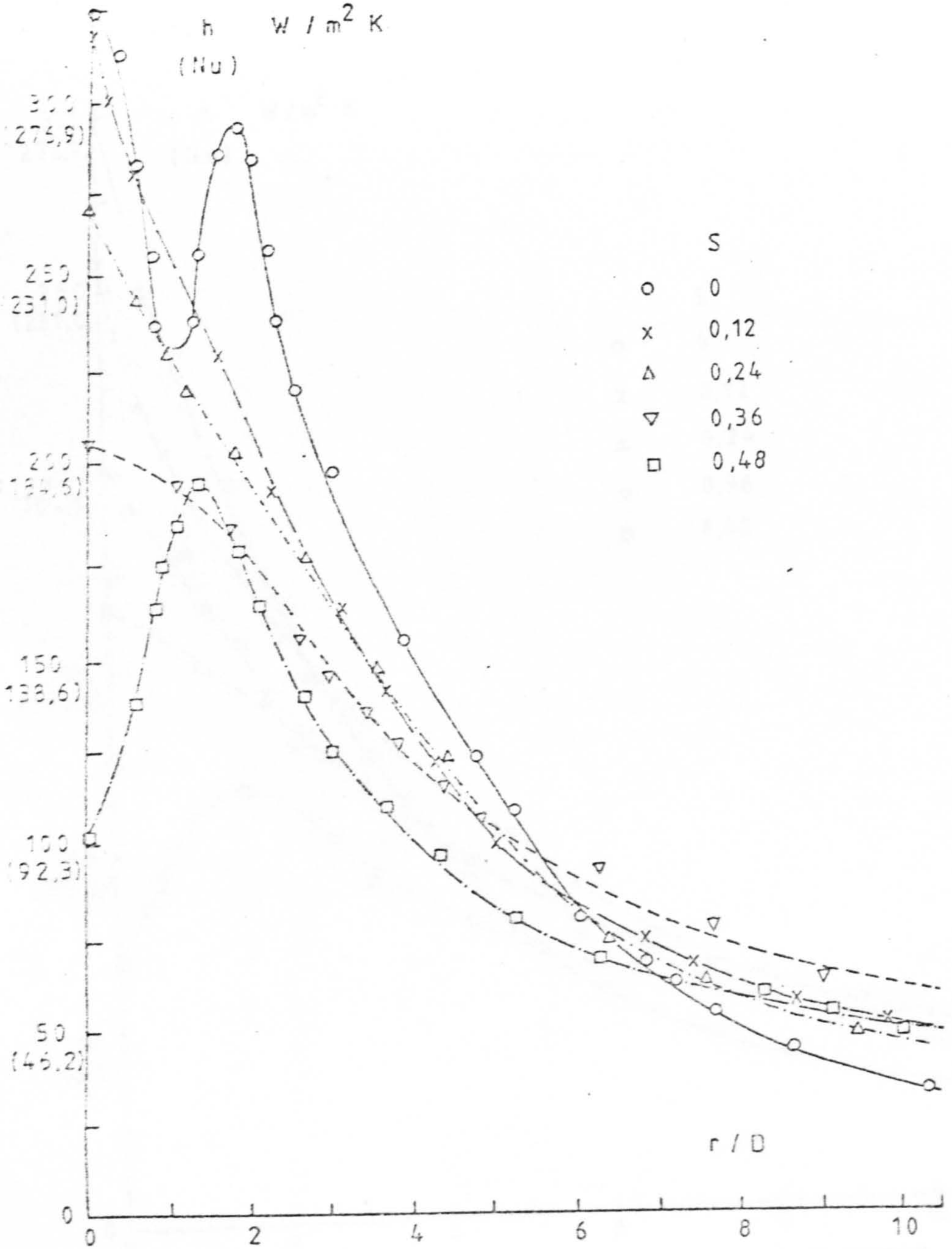

FIG 10,20 RADIAL VARIATION OF HEAT TRANSFER COEFFICIENT AT z/D=4 FOR VARIOUS SWIRLS [Re_D = 60,000]

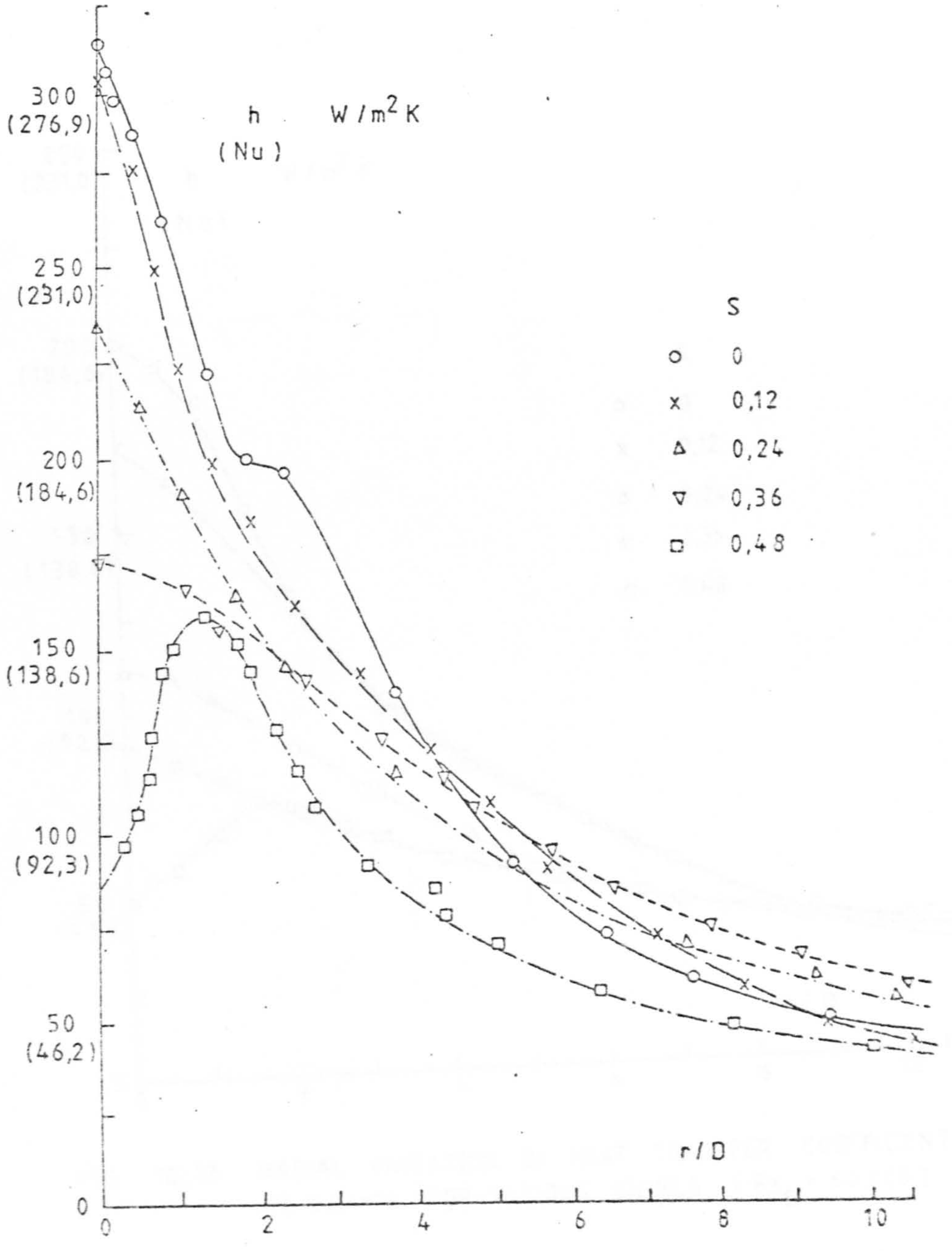

FIG 10,21 RADIAL VARIATION OF HEAT TRANSFER COEFFICIENT AT z/D = 6 FOR VARIOUS SWIRLS [Re_D = 60,000]

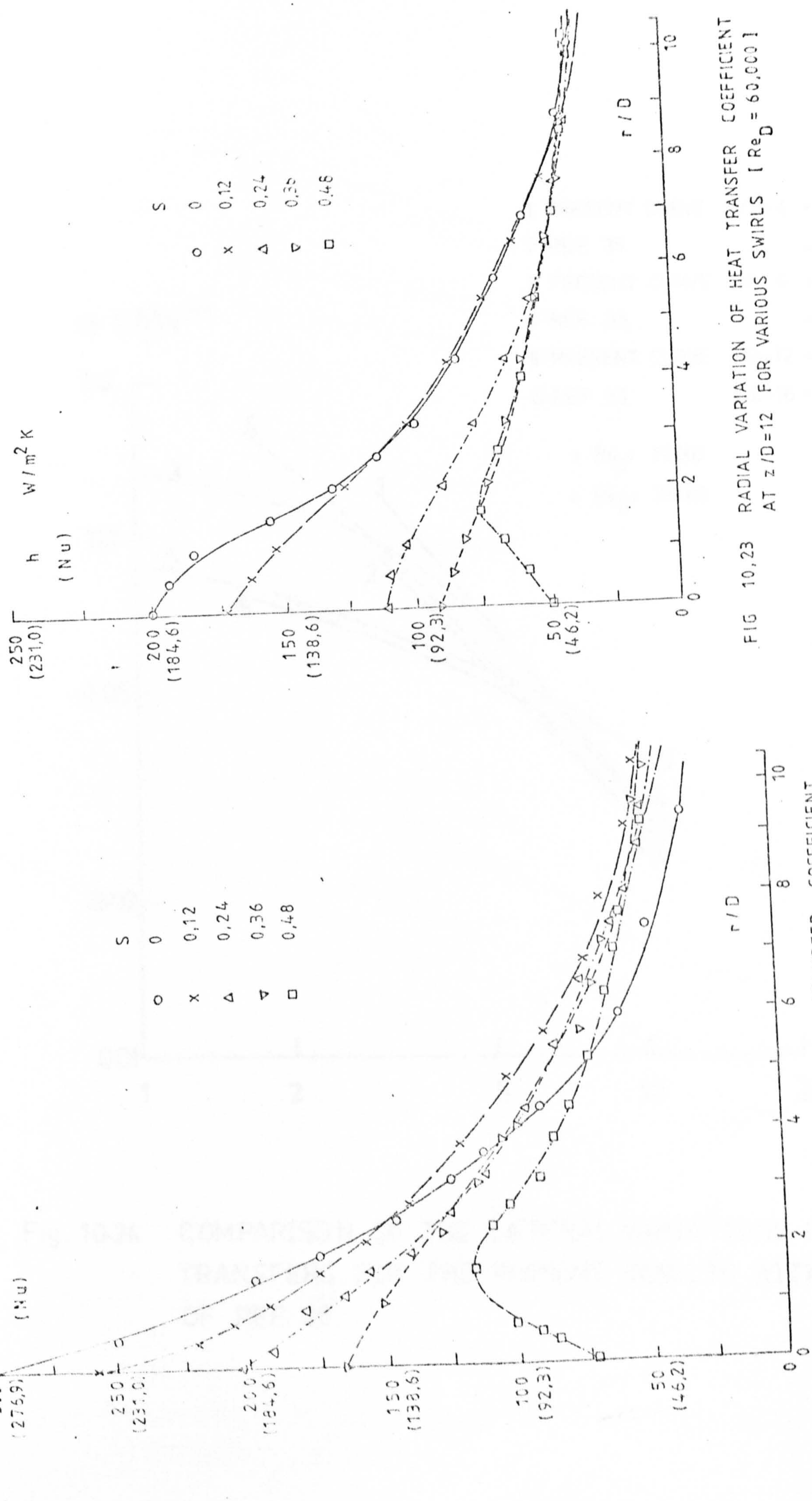

FIG 10,23 RADIAL VARIATION OF HEAT TRANSFER COEFFICIENT AT z/D=12 FOR VARIOUS SWIRLS [Re_D = 60,000]

FIG 10,22 RADIAL VARIATION OF HEAT TRANSFER COEFFICIENT AT z/D = 8 FOR VARIOUS SWIRLS [Re_D = 60,000]

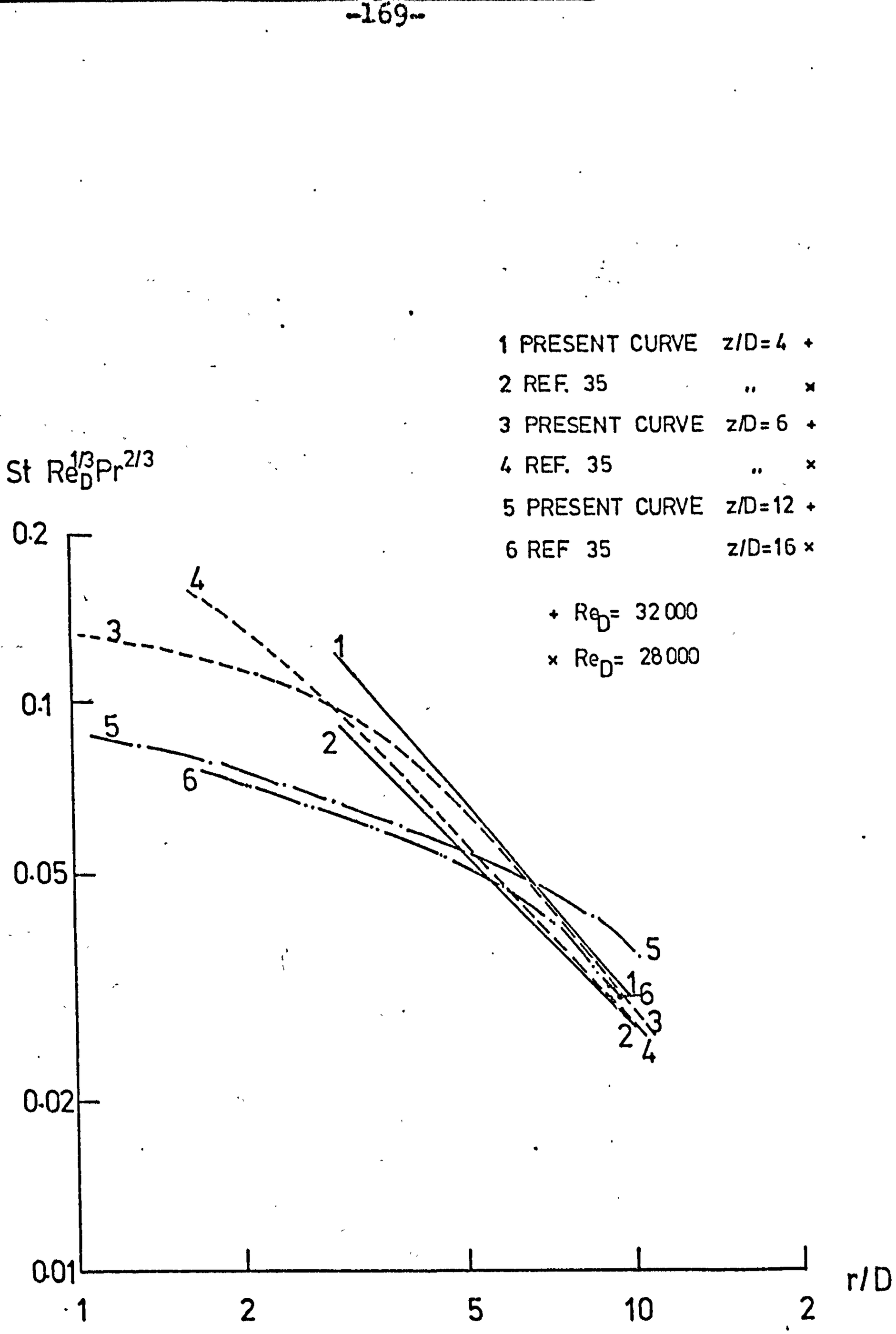

Fig. 10.24 COMPARISON OF THE LATERAL VARIATIONS OF HEAT TRANSFERS FOR THE PRESENT RESULTS WITH THOSE OF REF. 35.

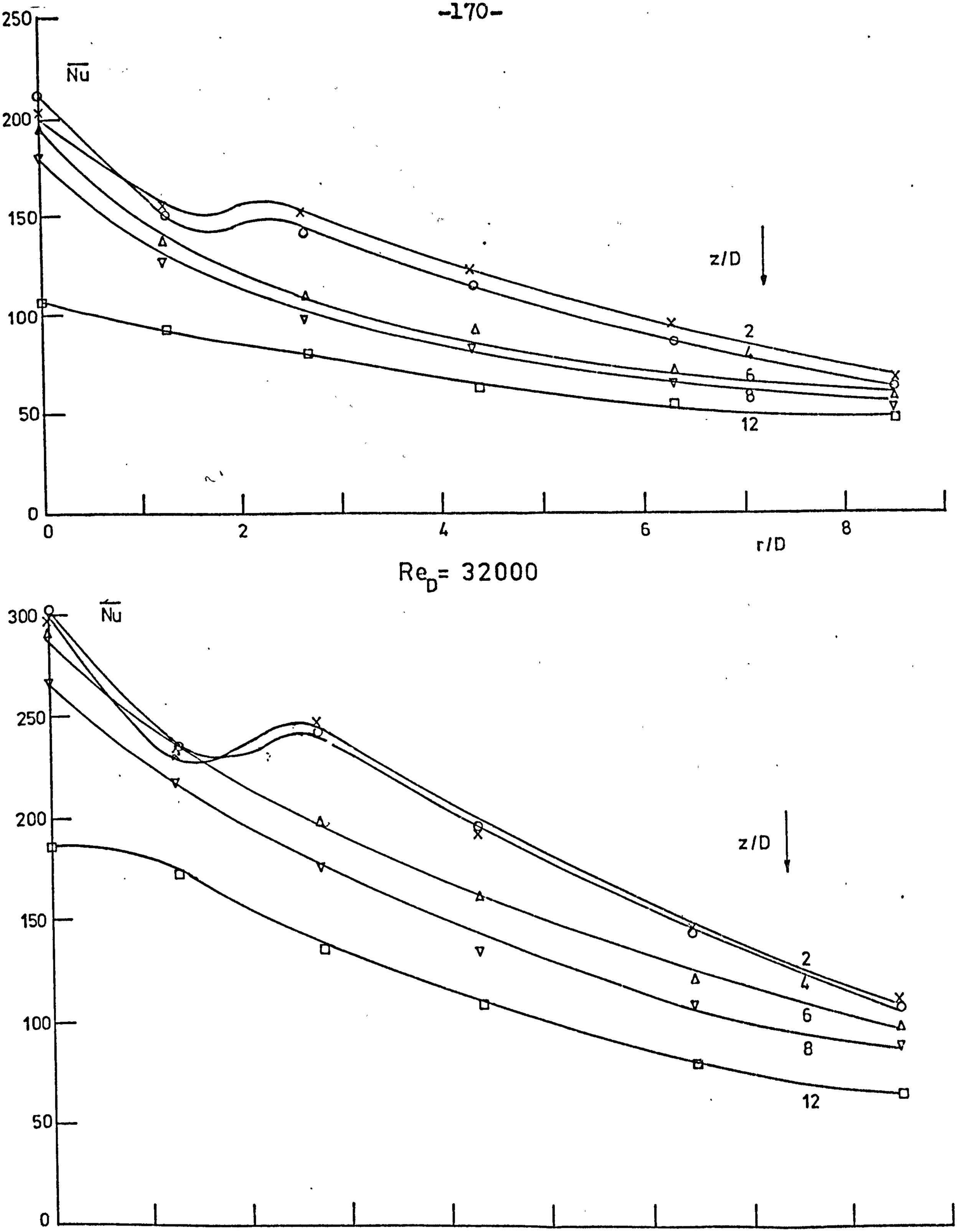

Fig. 10.25 VARIATION OF AVERAGE NUSSELT NUMBER WITH THE INTEGRATION AREA

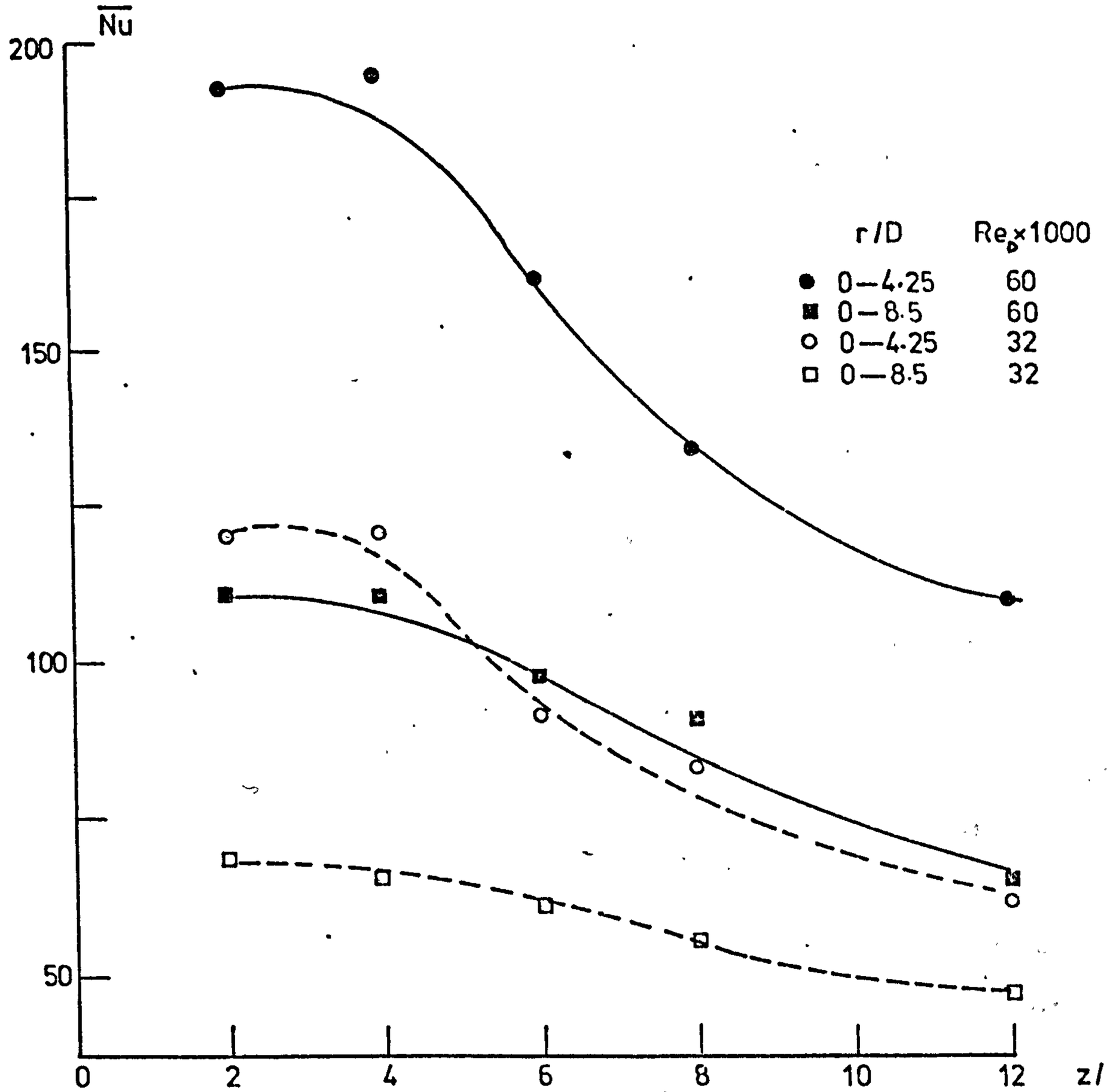

Fig.10.26 VARIATION OF AVERAGE NUSSELT NUMBER WITH z/D AT DIFFERENT INTEGRATION AREAS.

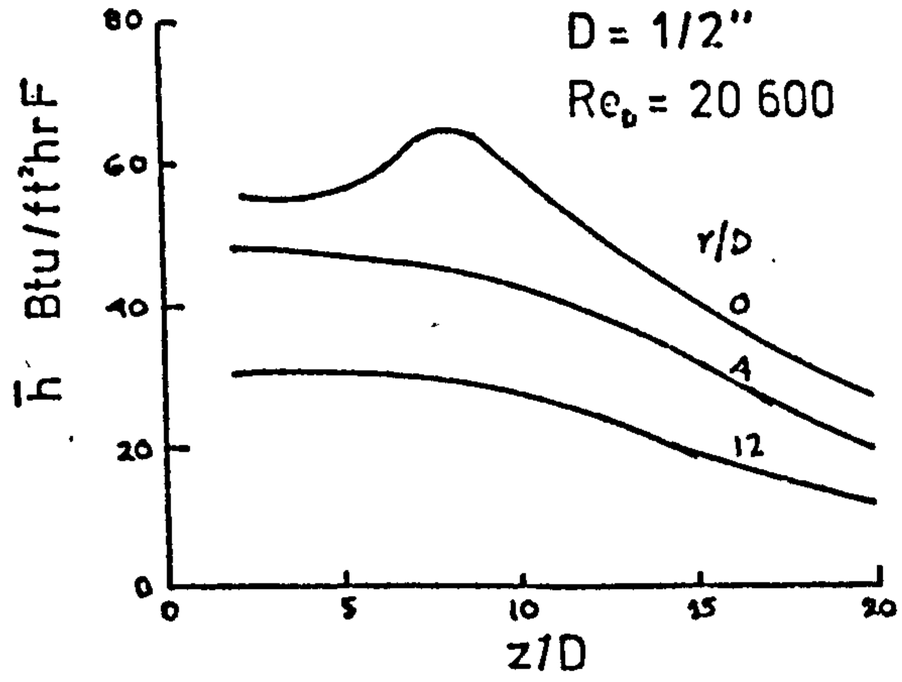

Fig. 10.27 AVERAGE HEAT TRANSFER COEFFICIENTS FOR AN AXISYMMETRIC AIR JET [REF. 38]

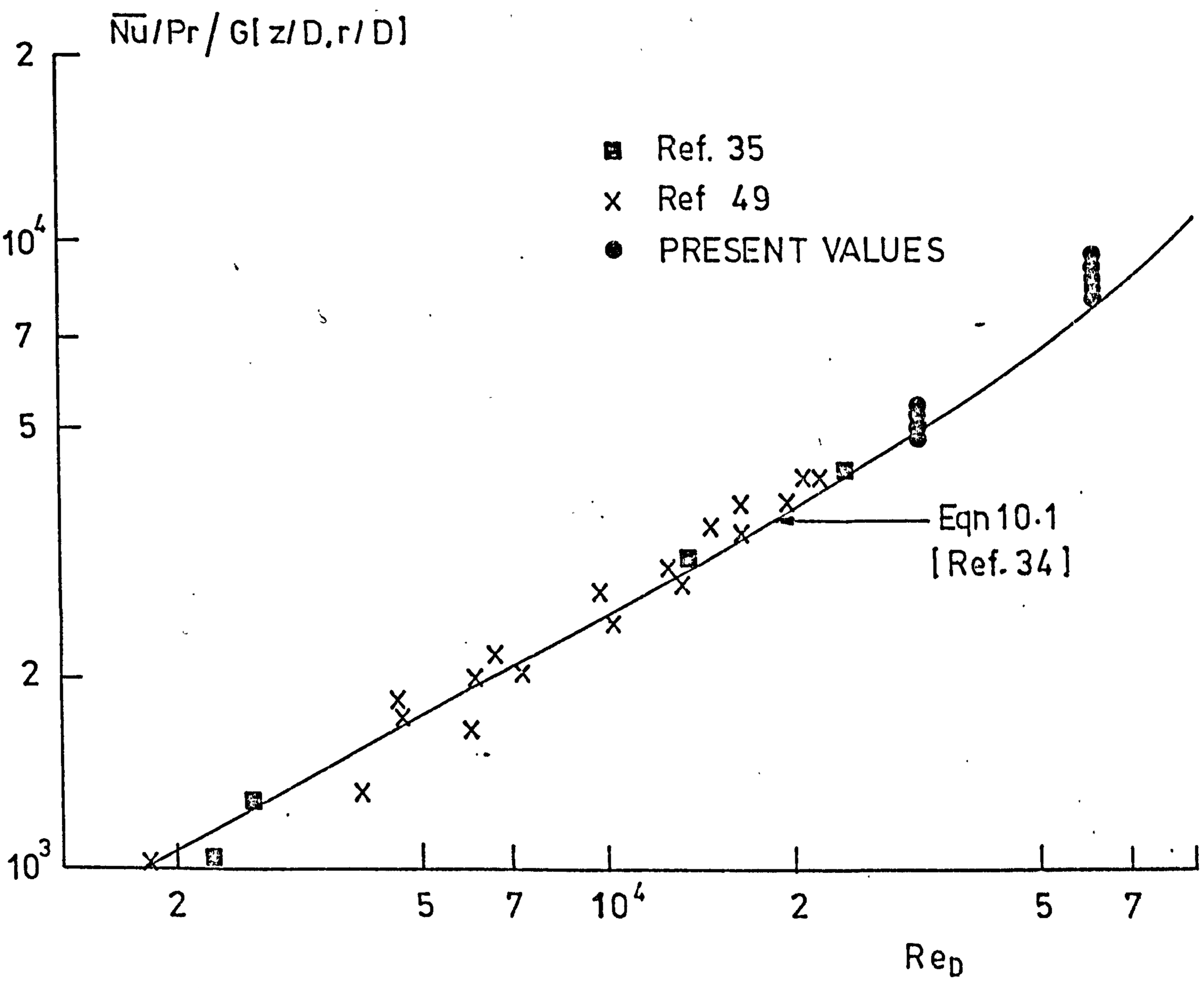

Fig.10·28 COMPARISON OF THE PRESENT RESULTS WITH EMPIRICAL CORRELATION QUOTED IN REFERENCE 34 FOR SINGLE NON-SWIRLING JETS.

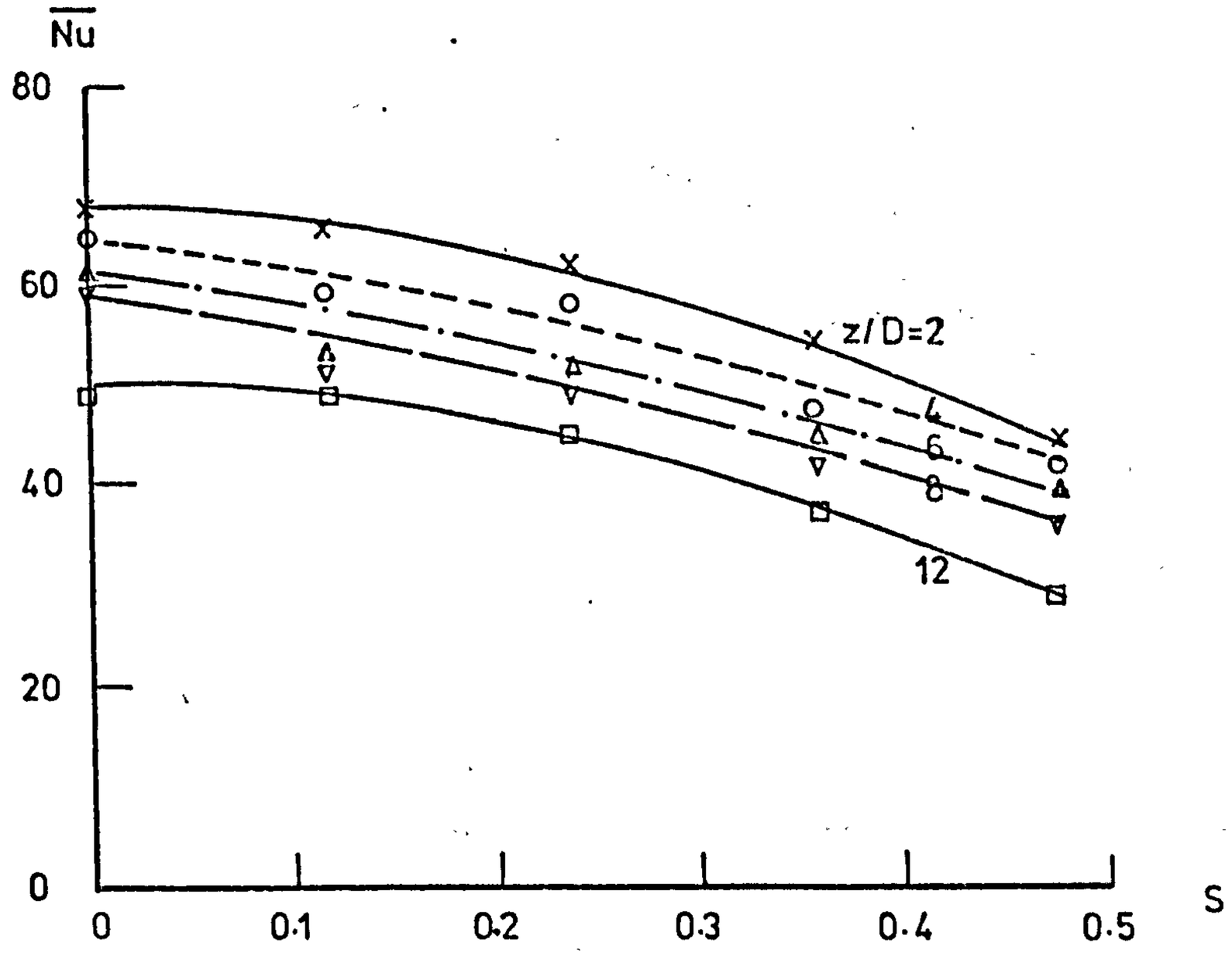

(a) Re_D= 32000

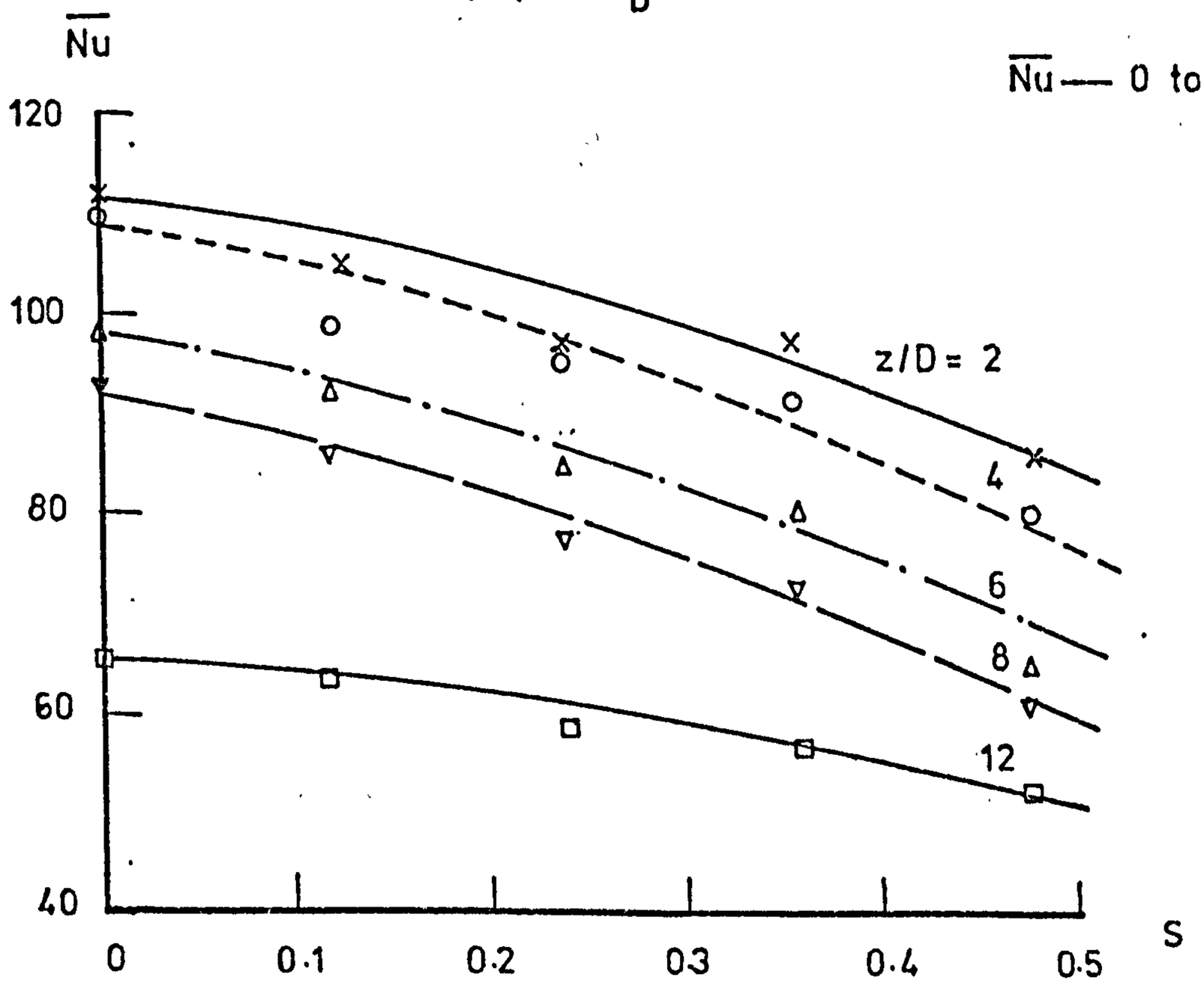

(b) Re_D= 60 000

Fig.10.29 VARIATION OF THE AVERAGE NUSSELT NUMBER WITH SWIRL NUMBER AT VARIOUS z/D's

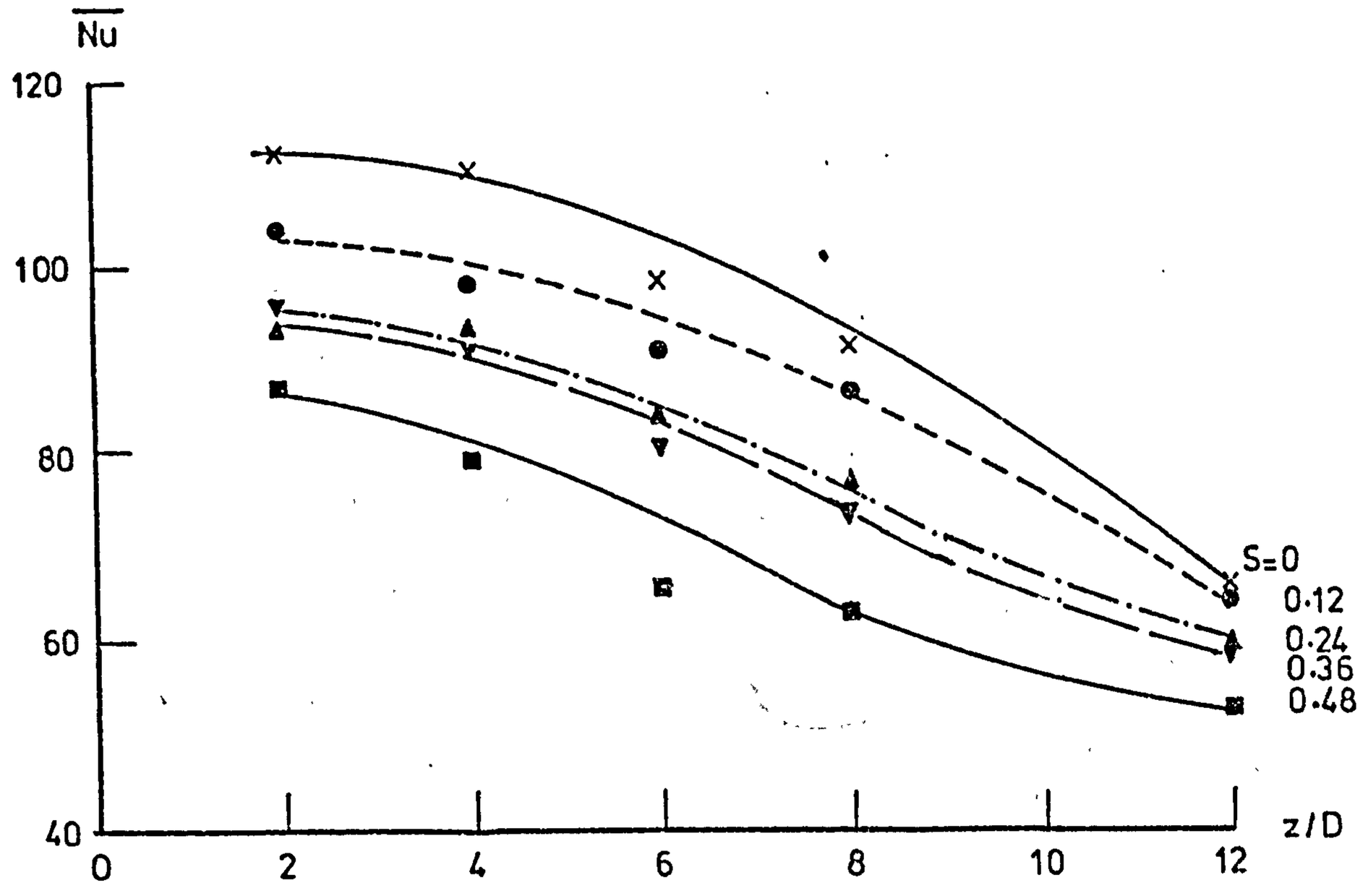

(a) Re_D= 32000

$\overline{Nu}$—0 to 8.5 r/D

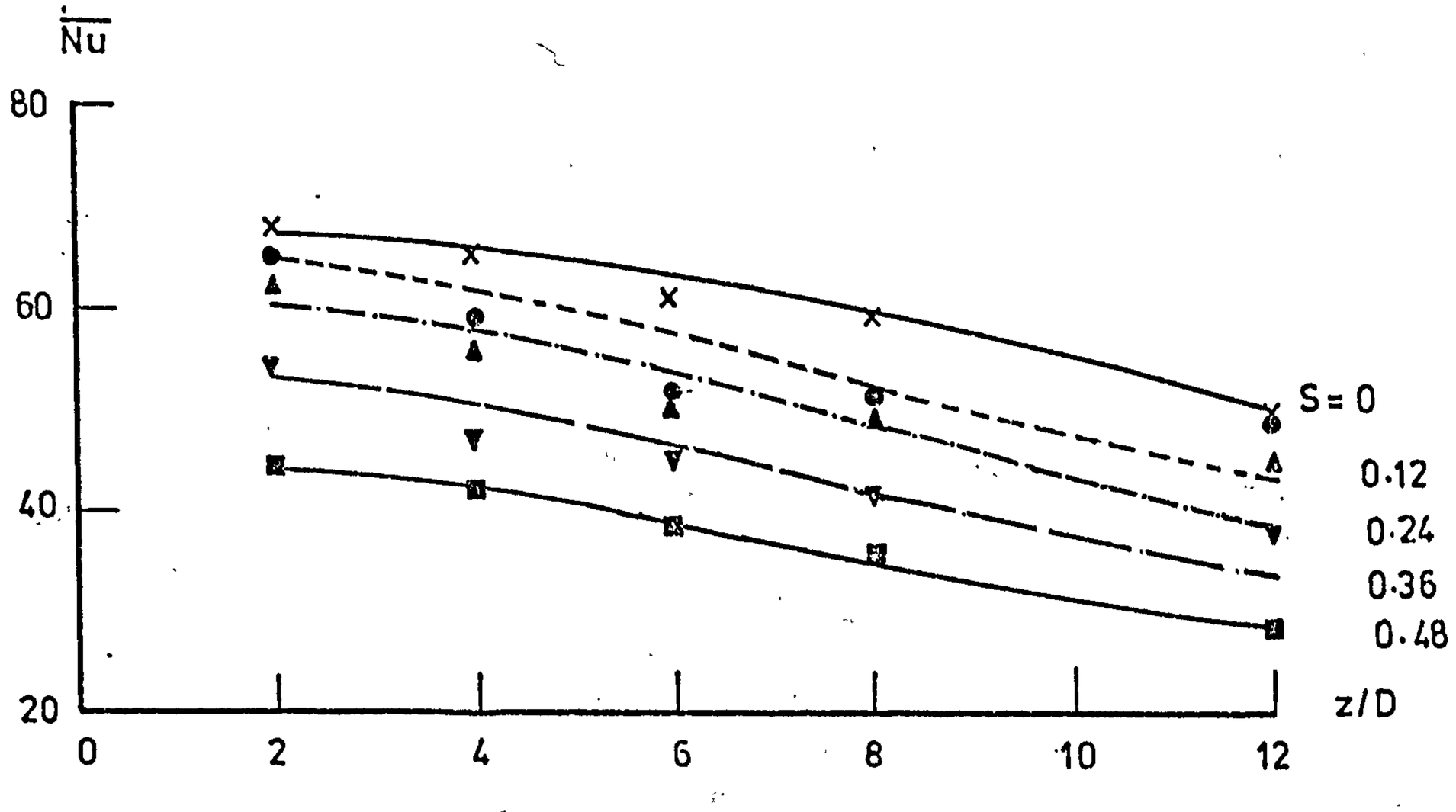

(b) Re_D= 60 000

Fig·10·30 VARIATION OF THE AVERAGE NUSSELT NUMBER WITH z/D AT VARIOUS SWIRLS

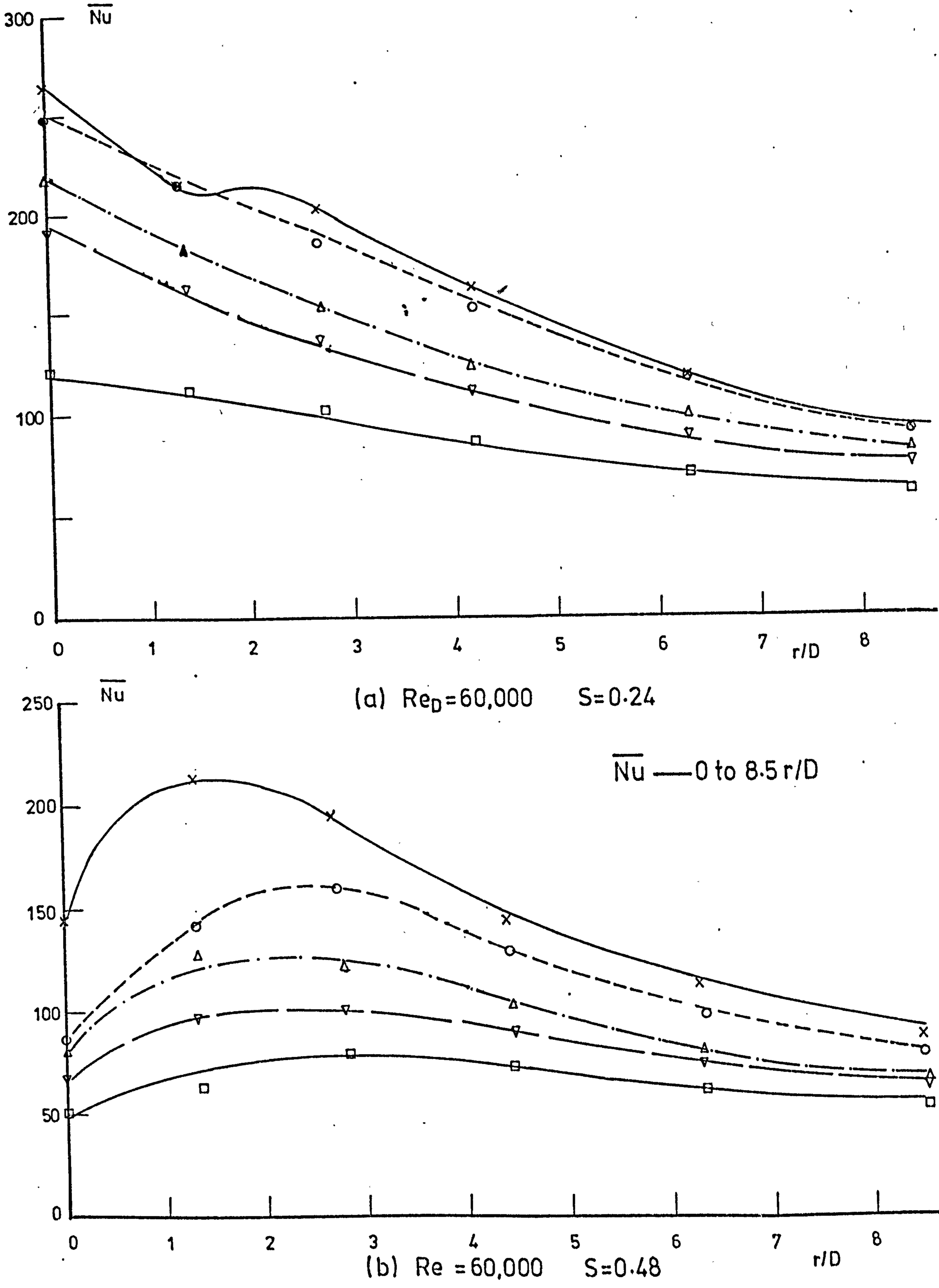

Fig.10.31 EFFECT OF THE AREA OF INTEGRATION ON $\overline{Nu}$ FOR SWIRLING JETS

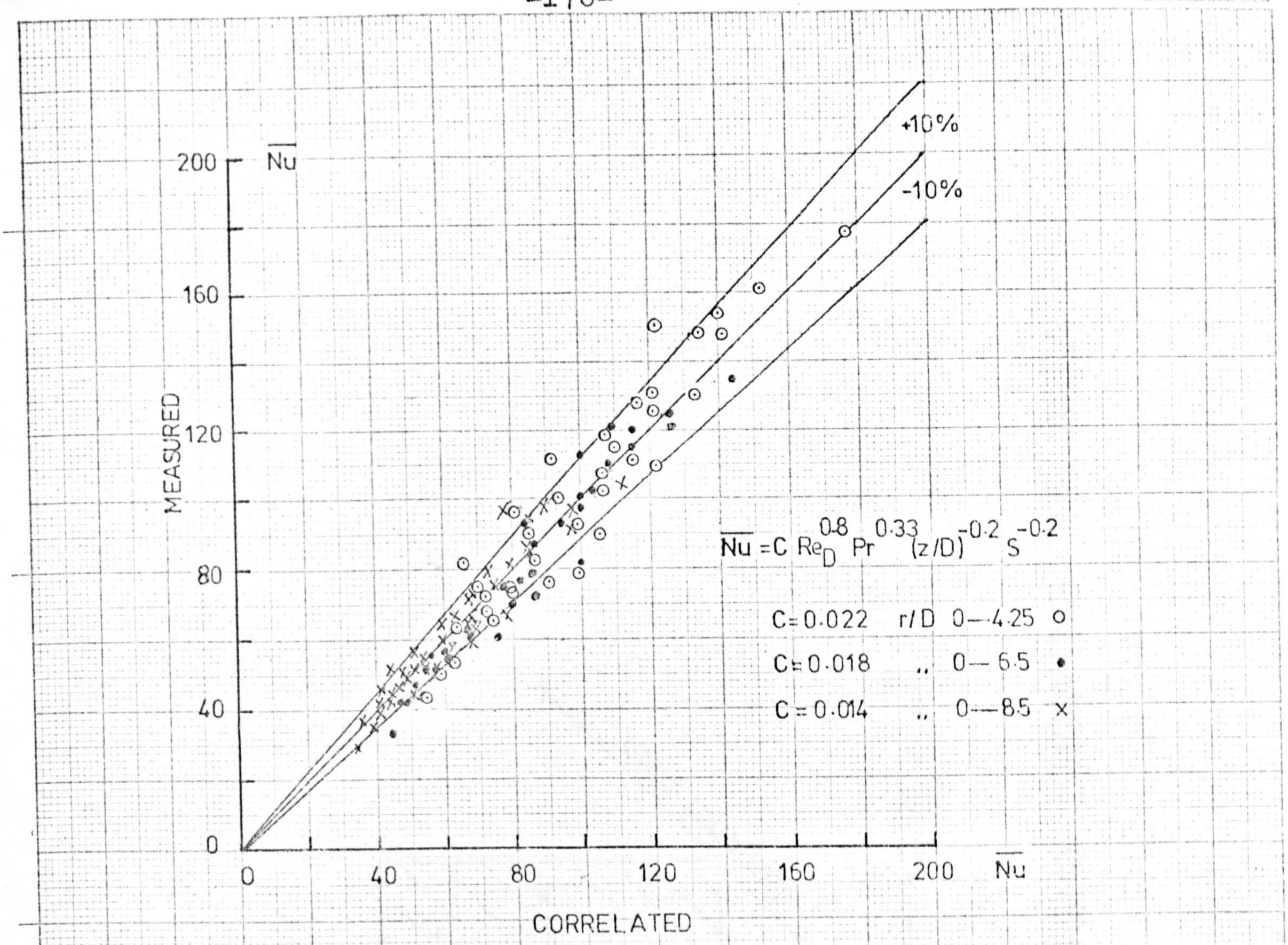

Fig 10,32 COMPARISON OF THE MEASURED & CORRELATED $\overline{Nu}$.

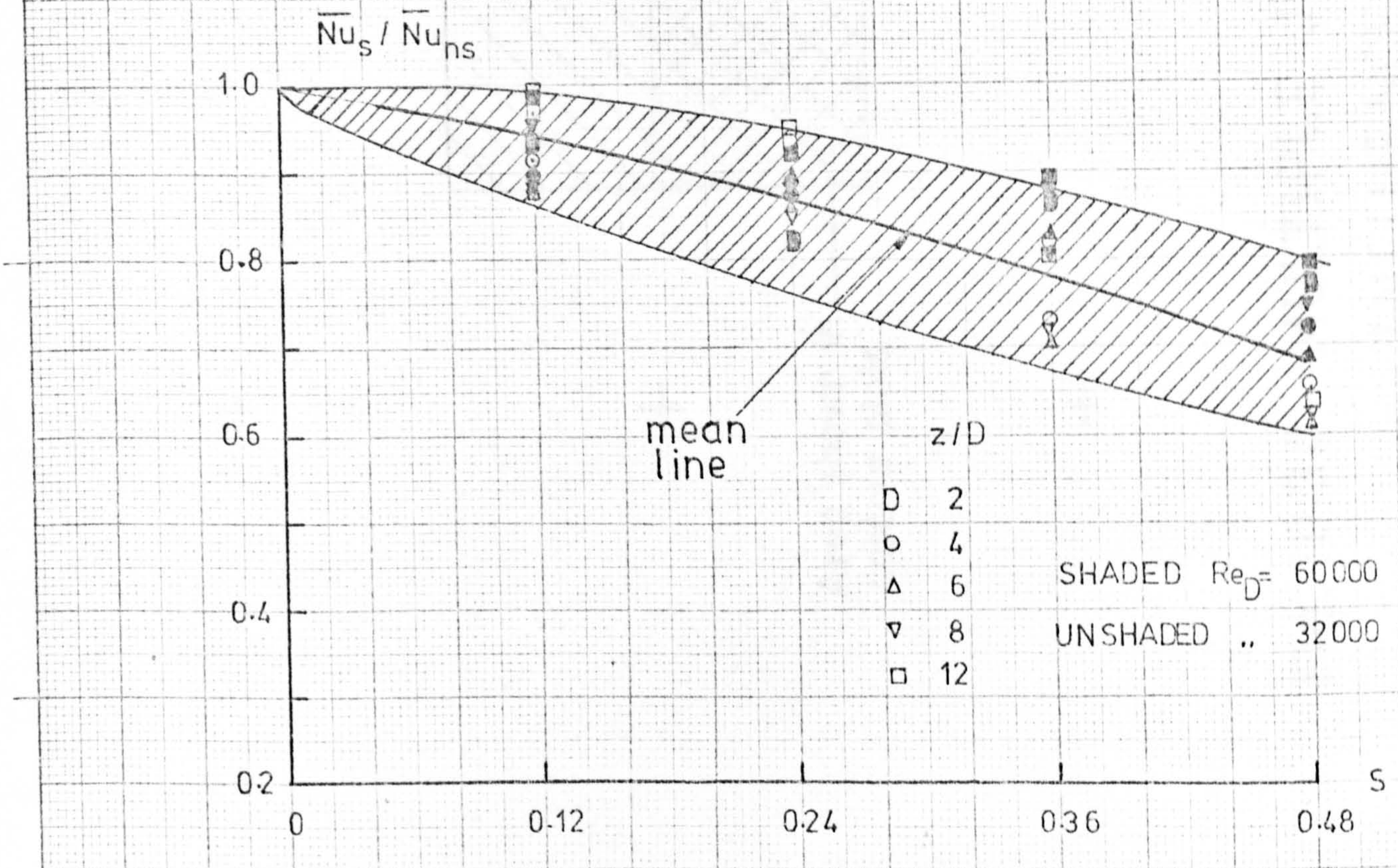

Fig.10,33 VARIATION OF Nu_s / Nu_{ns} AGAINST THE SWIRL NO.

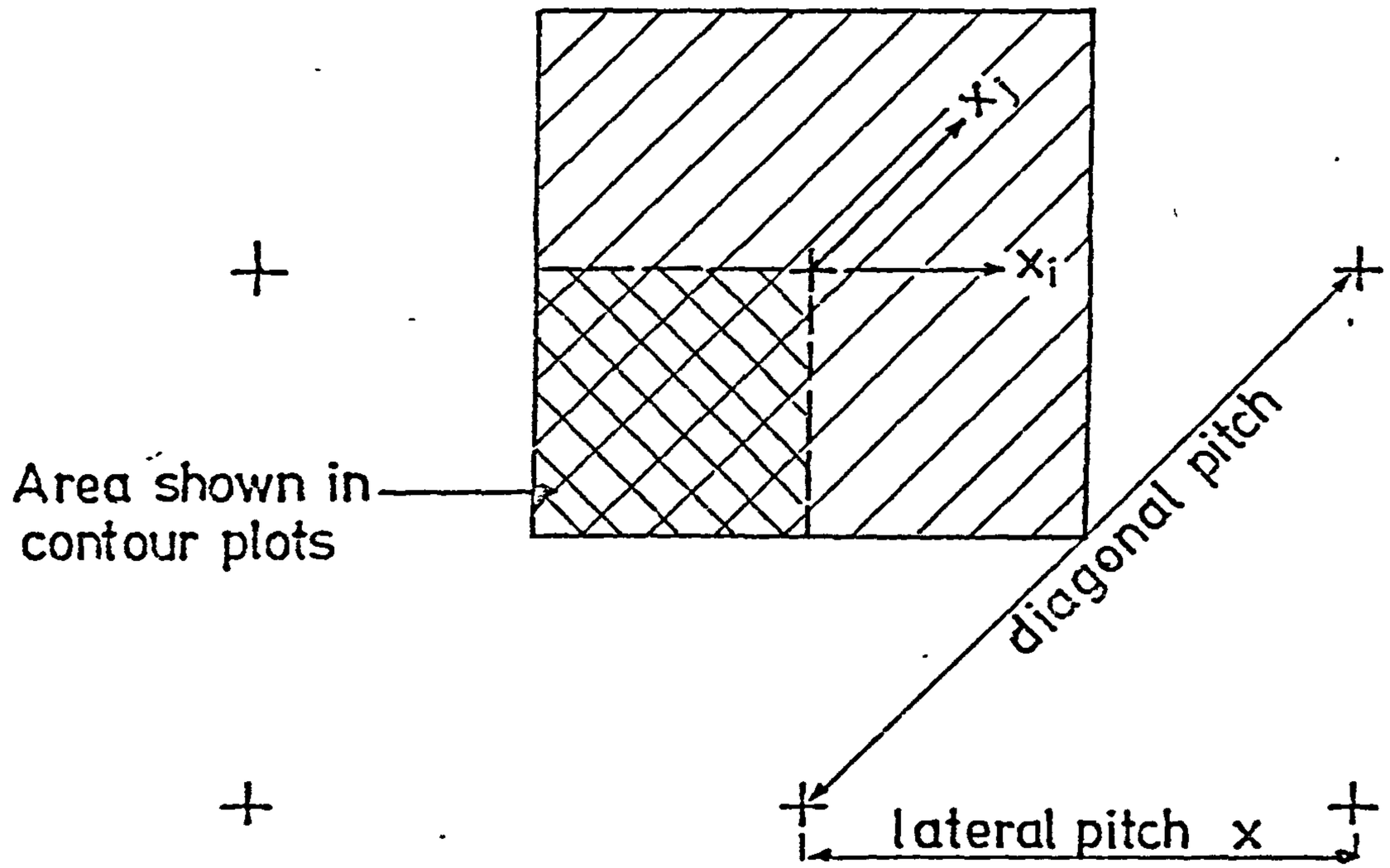

Fig. 10-34 MULTIPLE JET ARRAY SHOWING THE AREA INFLUENCED BY THE CENTRAL JET

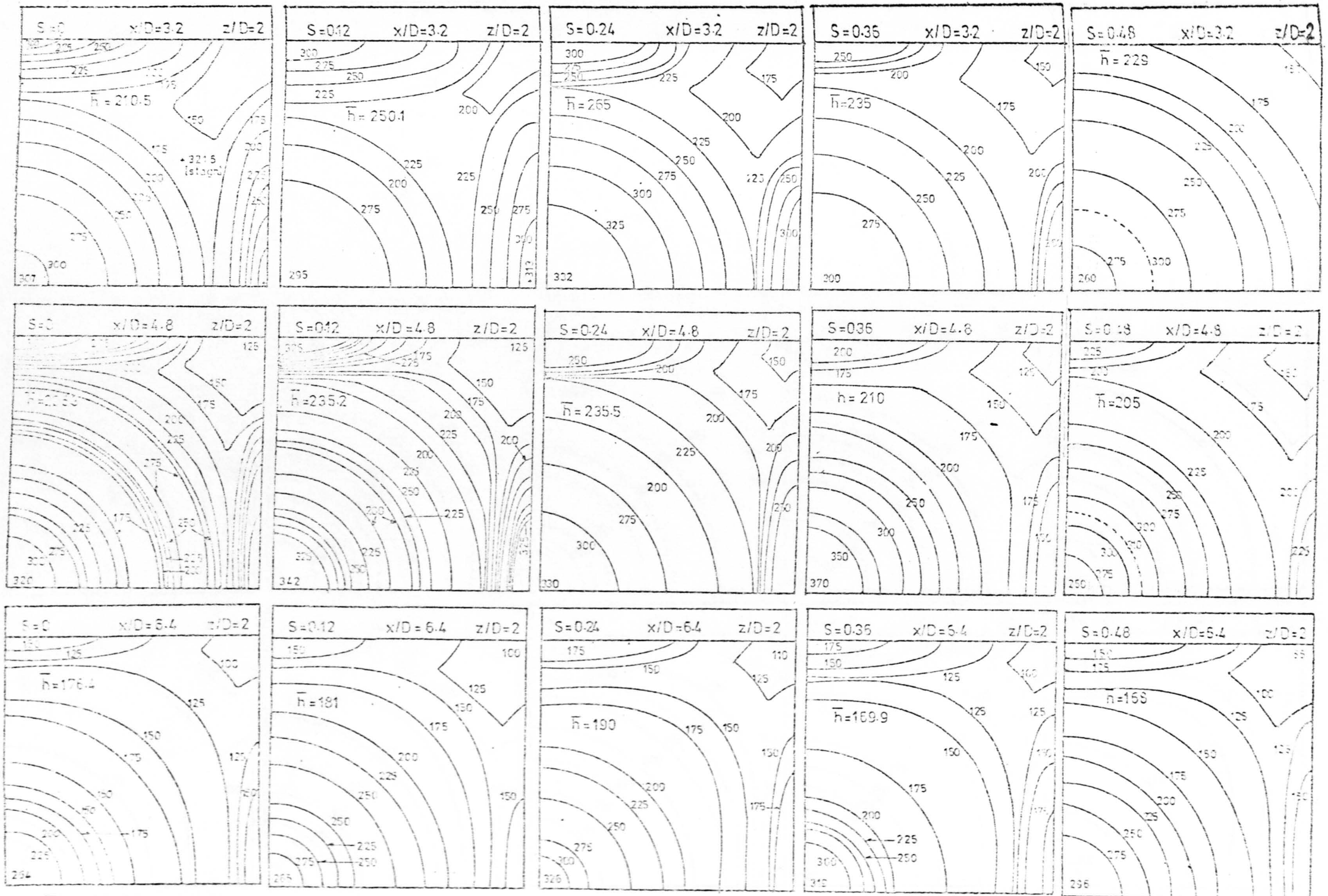

Fig 10,35 CONTOUR PLOTS OF h IN THE MULTIPLE JET ARRAYS FOR VARYING x/D & S (z/D= 2)

Fig 10.36 CONTOUR PLOTS OF h IN THE MULTIPLE JET ARRAYS FOR VARYING x/D & S[z/D]

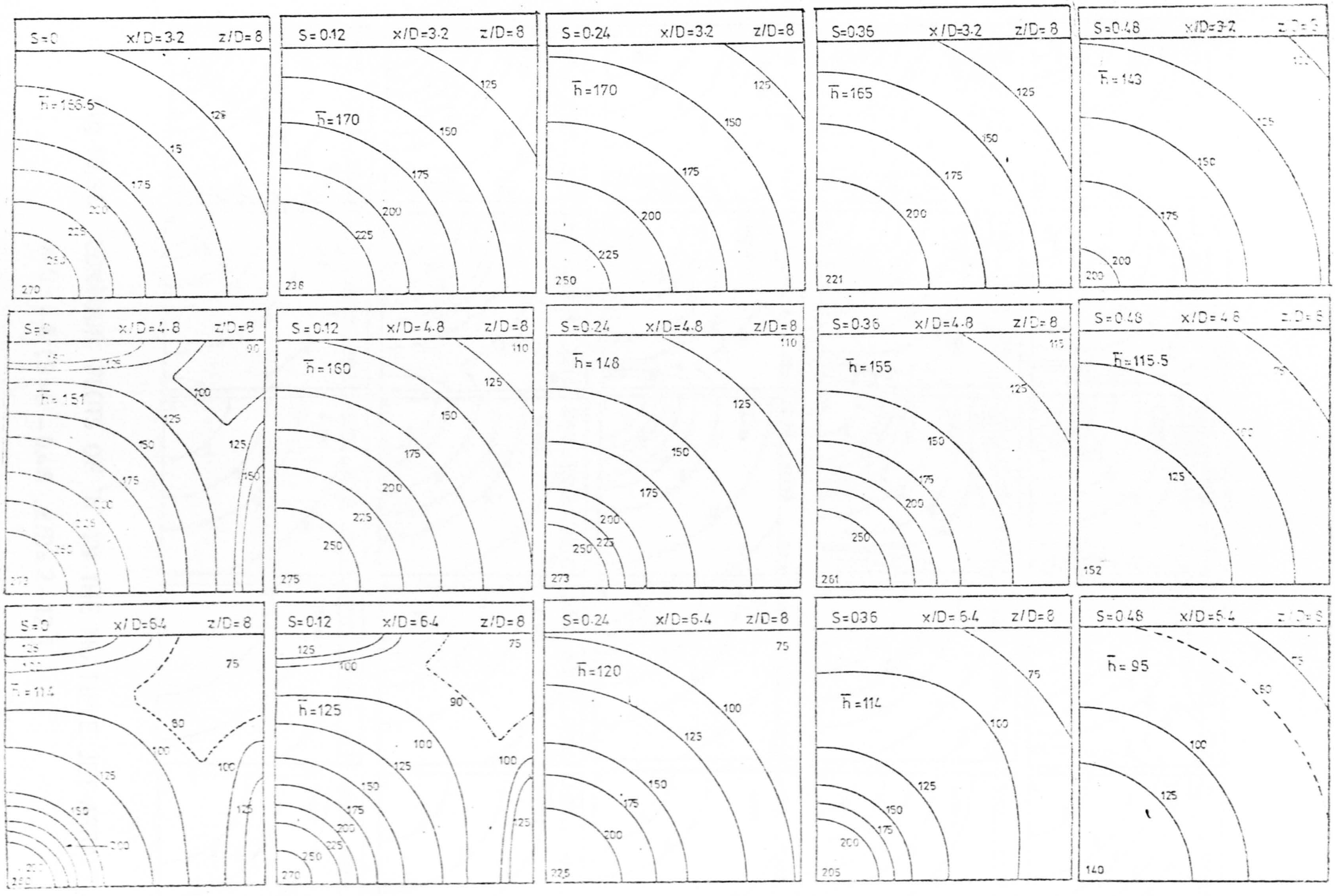

Fig 10.37 CONTOUR PLOTS OF h IN THE MULTIPLE JET ARRAYS FOR VARYING x/D & S [z/D]

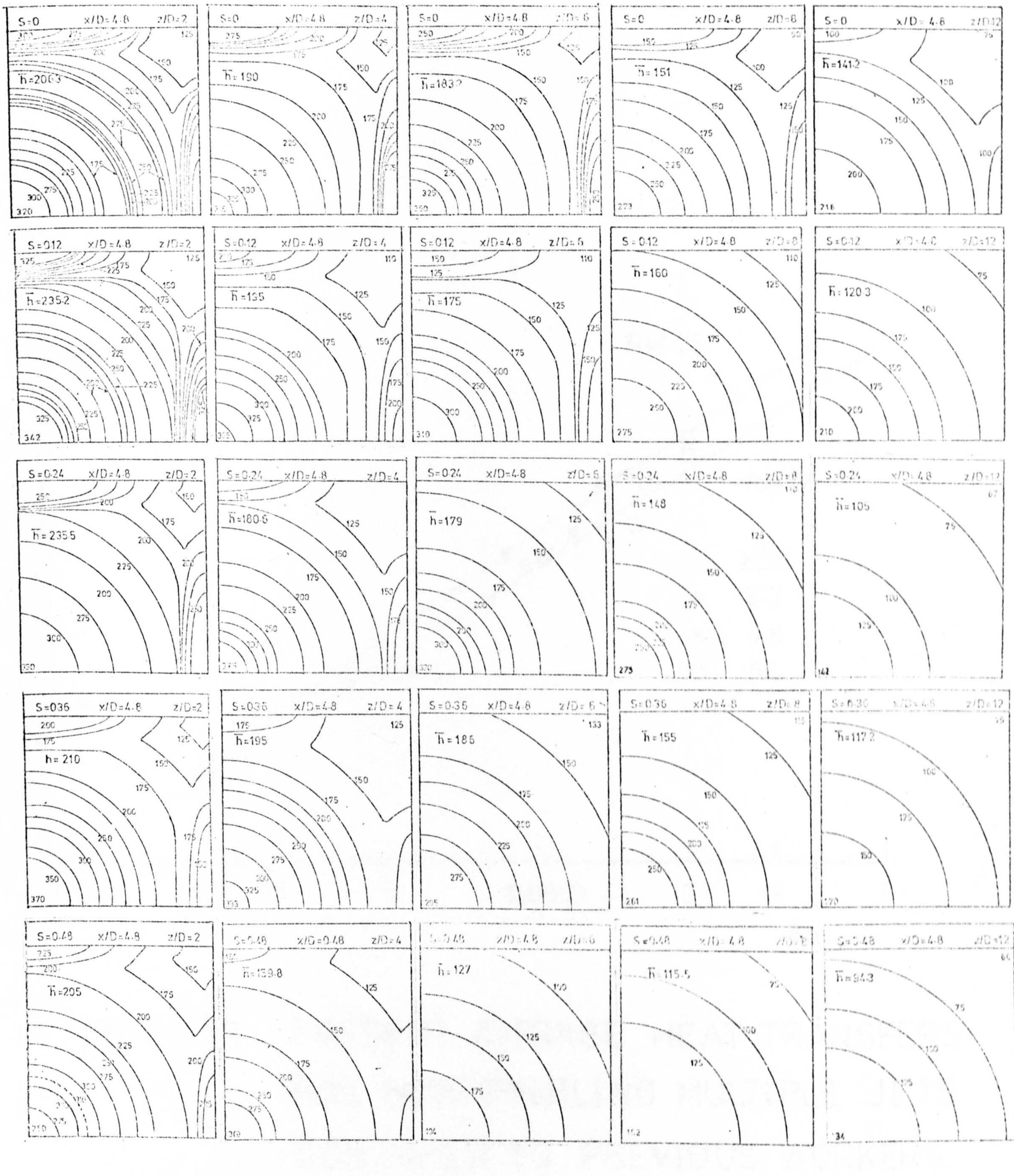

Fig.10,38 CONTOUR PLOTS OF 'h' IN THE MULTIPLE JET ARRAYS AT x/D = 4.8 (S = 0 — 0,48 , z/D = 2 — 12).

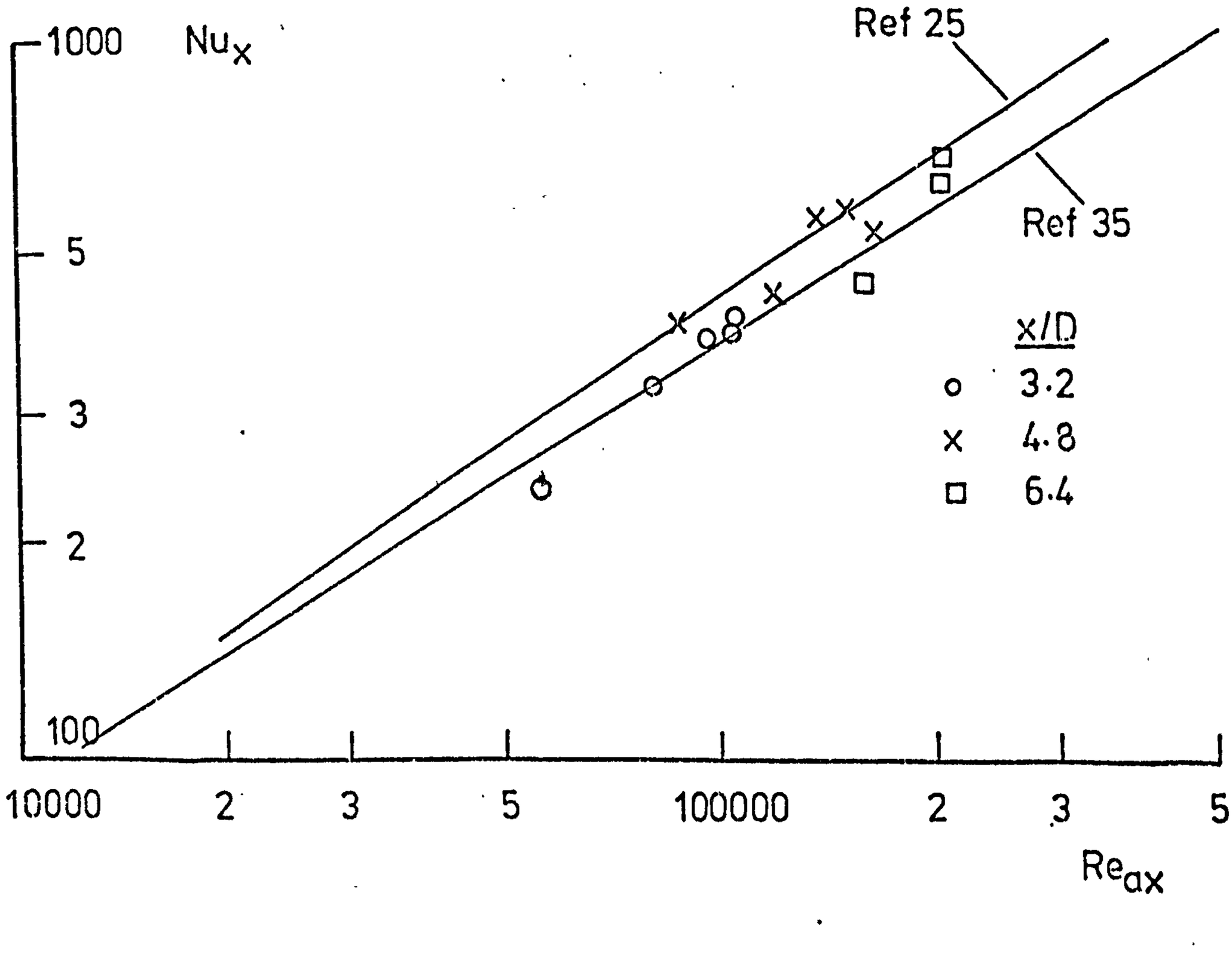

Fig. 10,39 PRESENT AVERAGE HEAT TRANSFERS FOR NON-SWIRLING MULTIPLE JETS COMPARED TO PREVIOUS WORKERS.

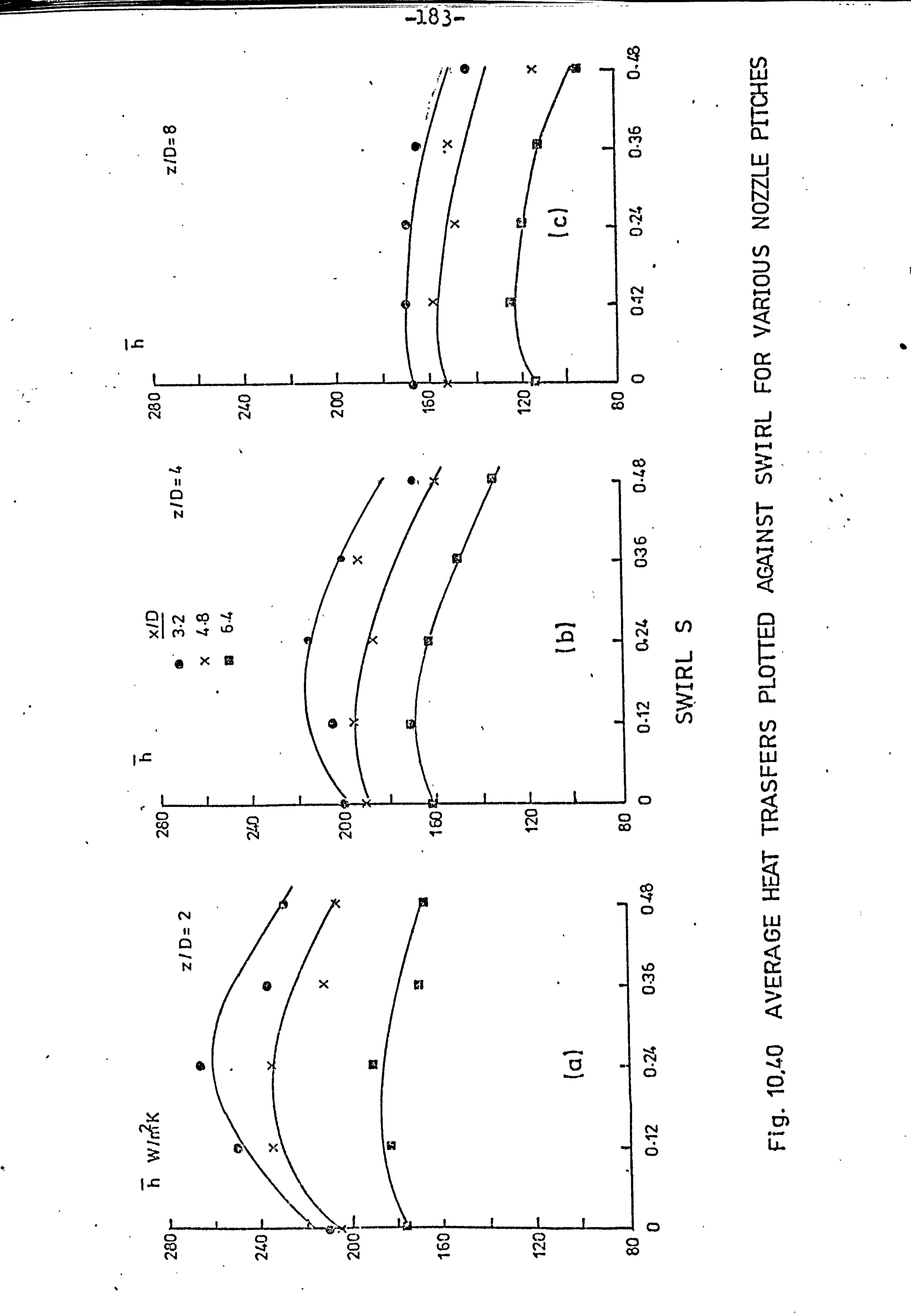

Fig. 10,40 AVERAGE HEAT TRASFERS PLOTTED AGAINST SWIRL FOR VARIOUS NOZZLE PITCHES

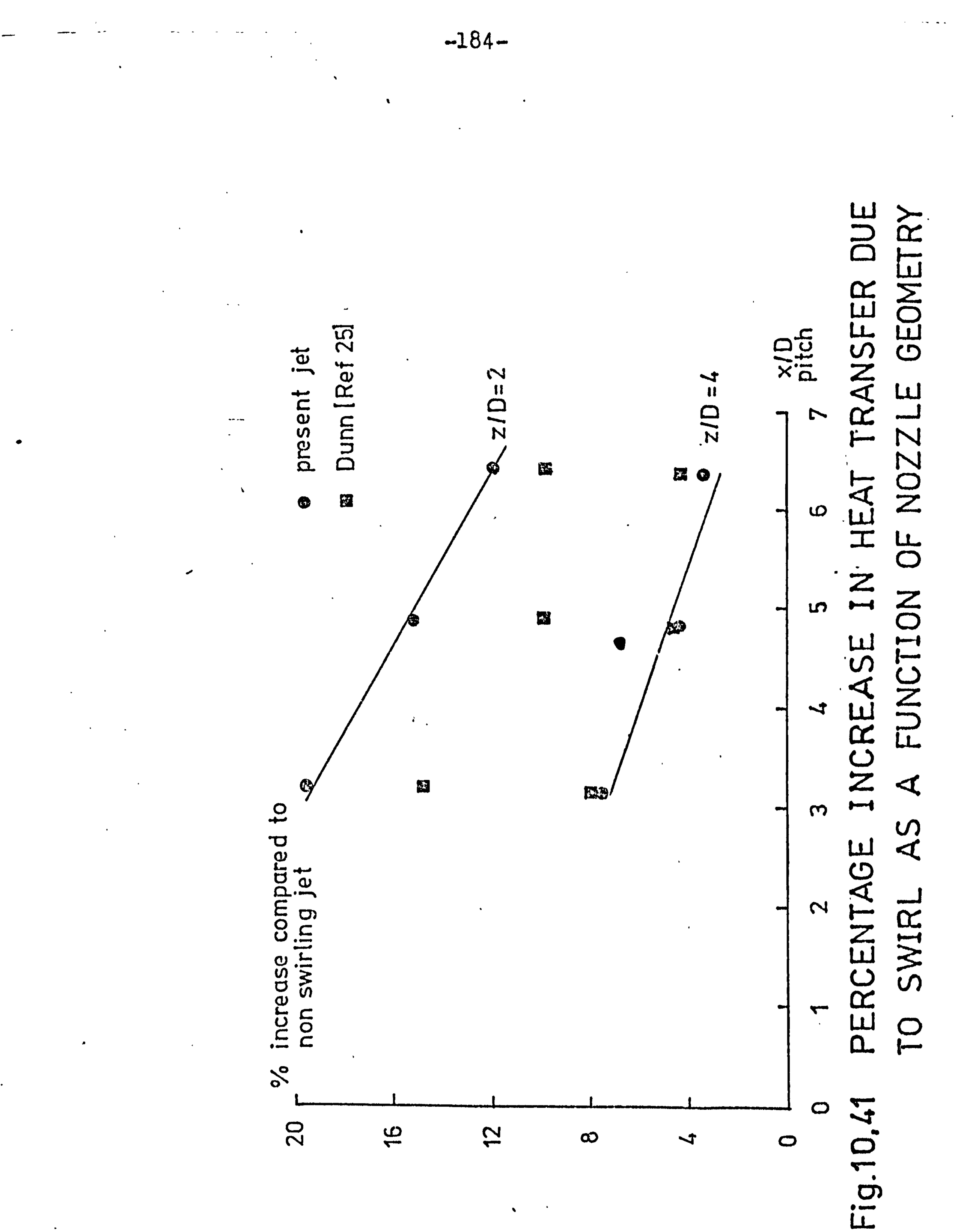

Fig.10.41 PERCENTAGE INCREASE IN HEAT TRANSFER DUE TO SWIRL AS A FUNCTION OF NOZZLE GEOMETRY

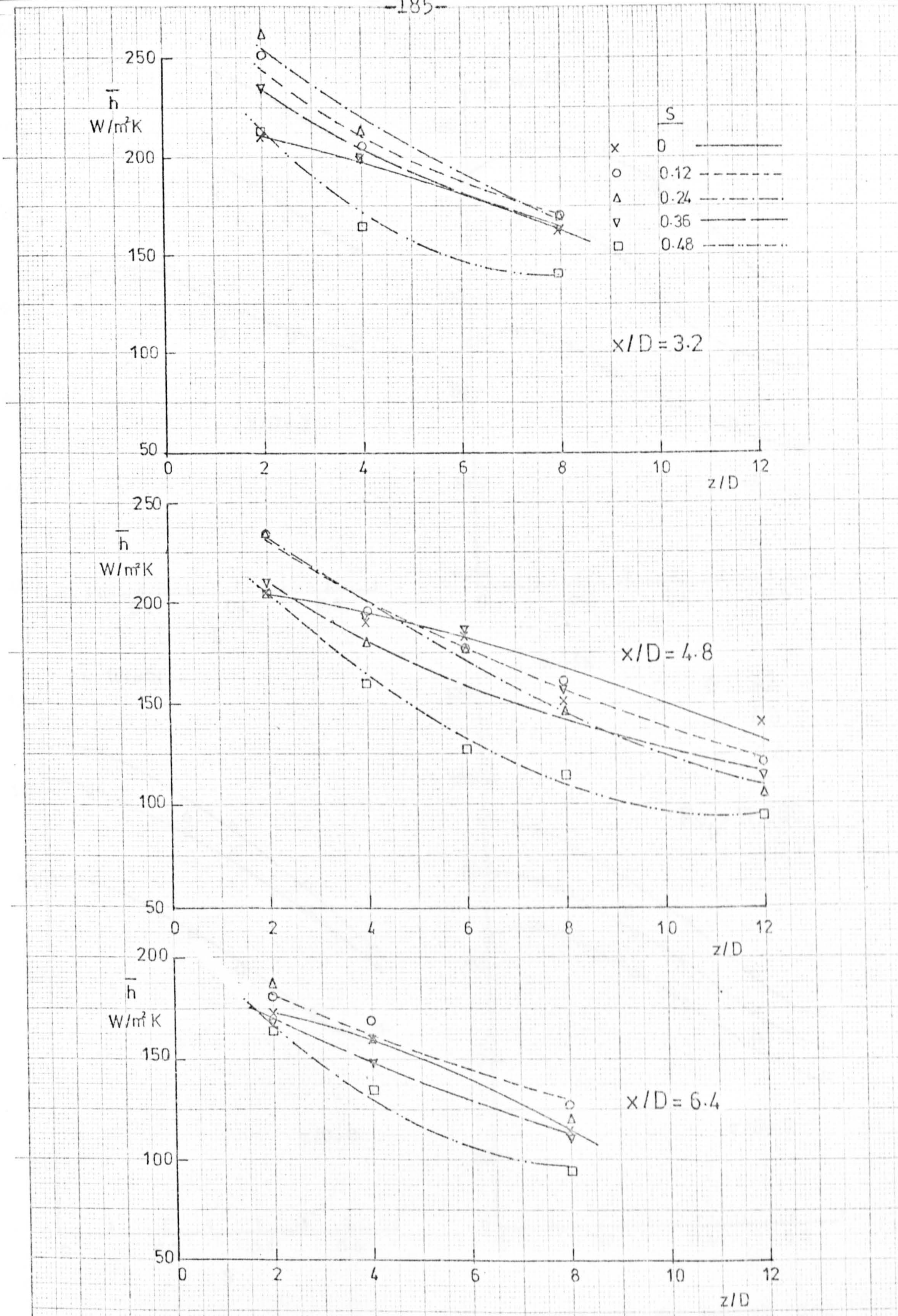

Fig 10.42 DECAY OF $\bar{h}$ WITH z/D AT VARIOUS SWIRLS FOR MULTIPLE JETS

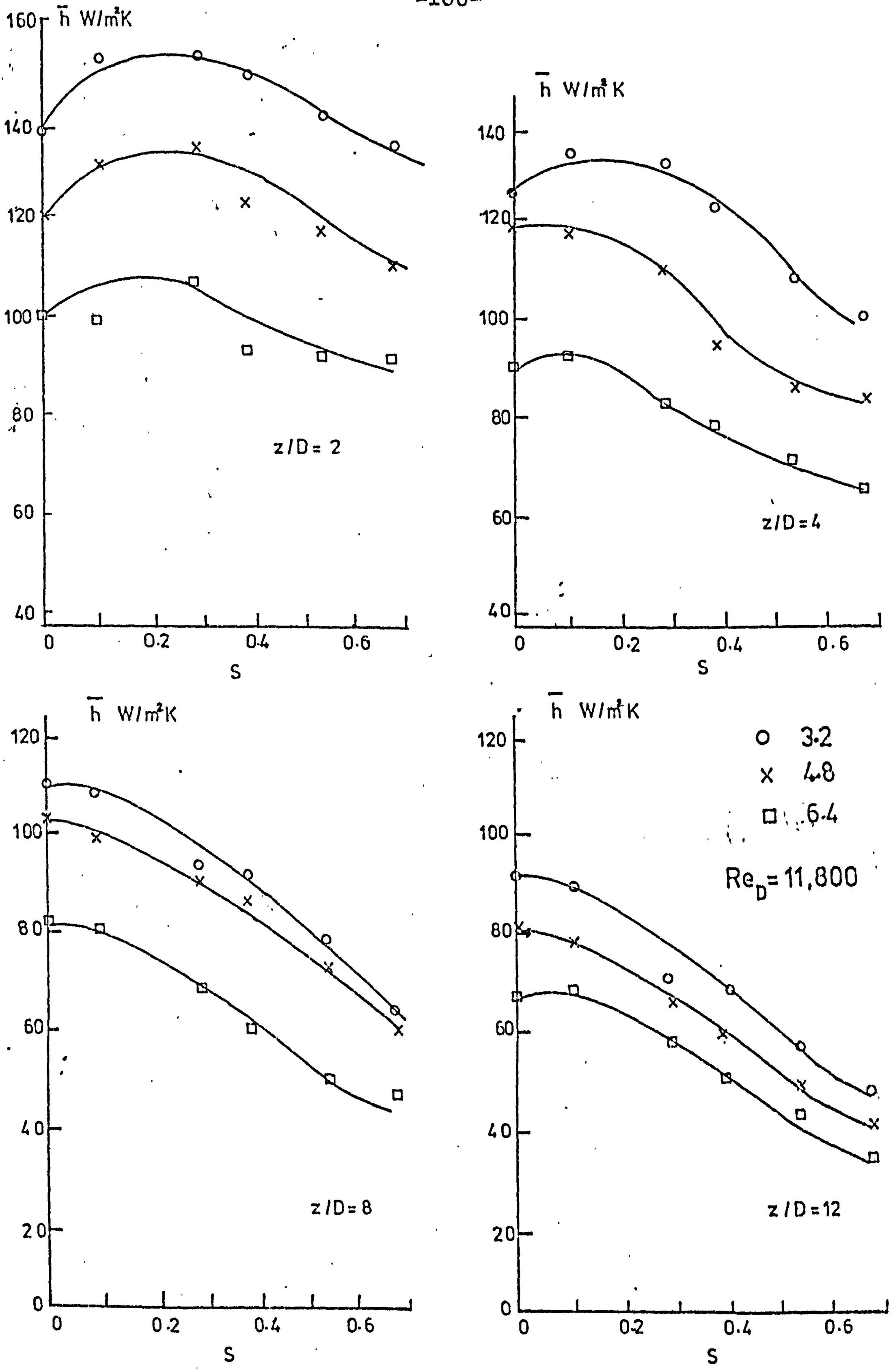

Fig 10,43 AVERAGE HEAT TRANSFER OBTAINED BY REF: 25 FOR VARIOUS DEGREES OF SWIRL & GEOMETRICAL PARAMETERS.

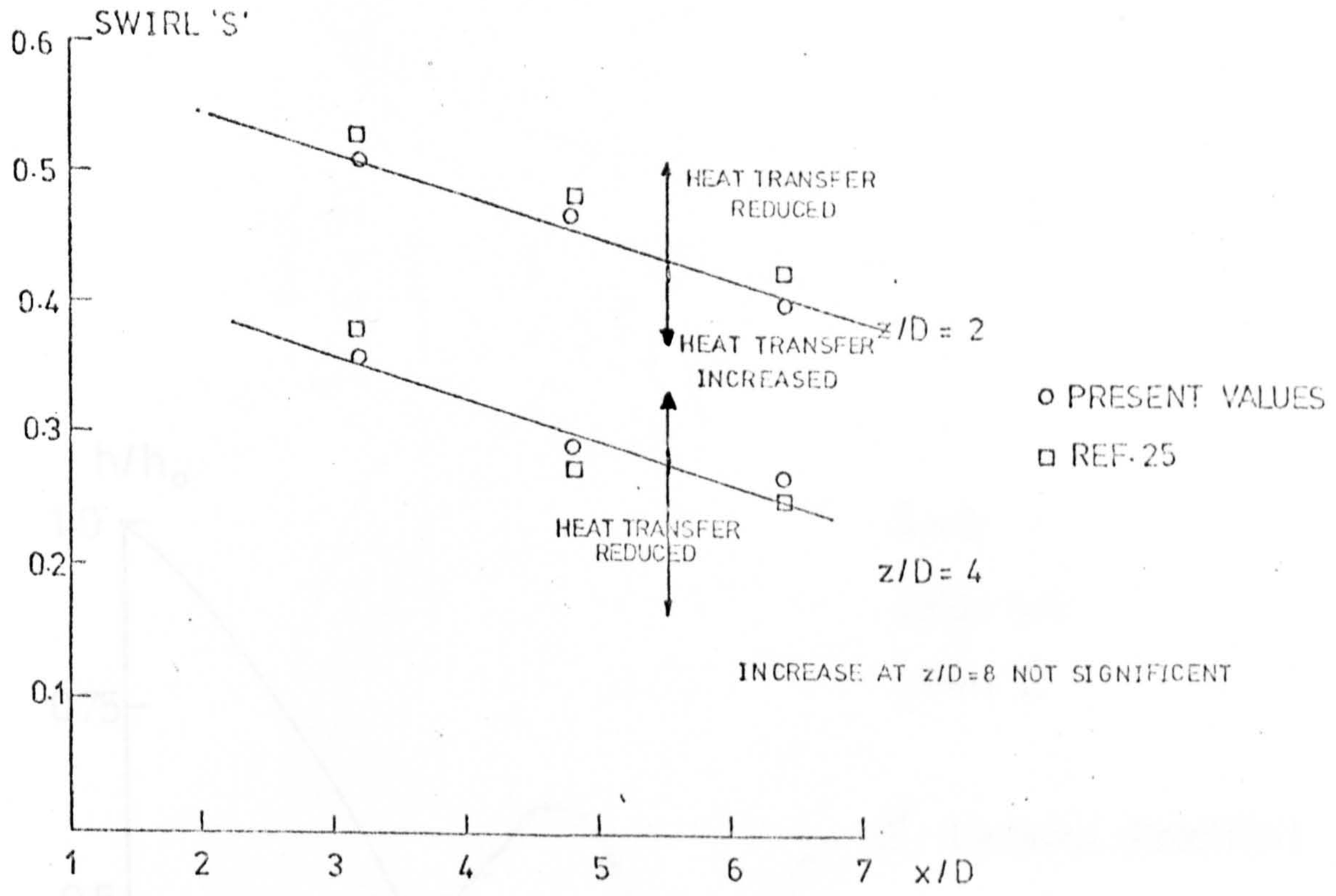

Fig. 10,44 EFFECTS OF THE GEOMETRICAL PARAMETERS (x/D, z/D) ON THE HEAT TRANSFER FROM THE SWIRLING JET

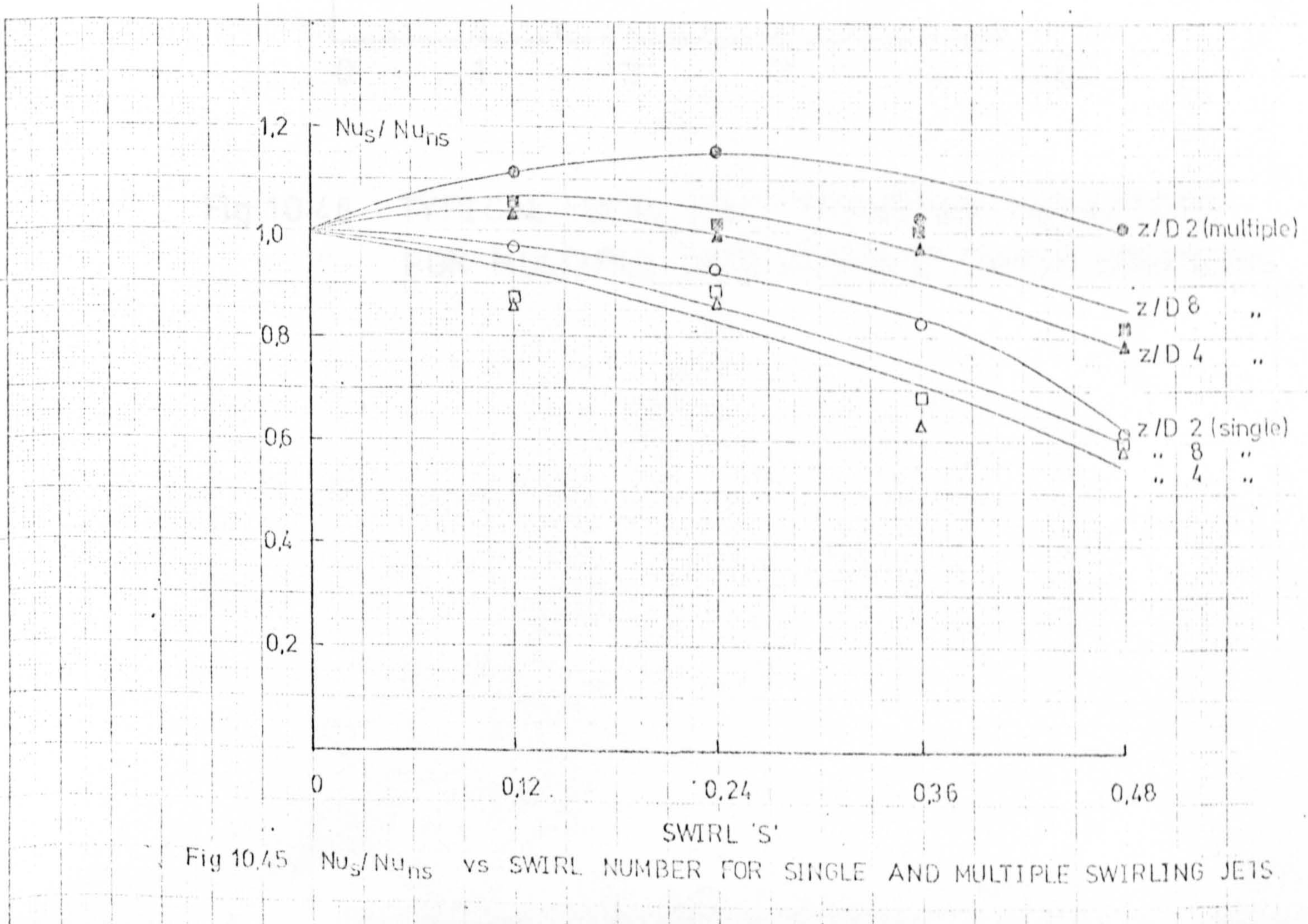

Fig 10,45 Nu_s / Nu_{ns} vs SWIRL NUMBER FOR SINGLE AND MULTIPLE SWIRLING JETS

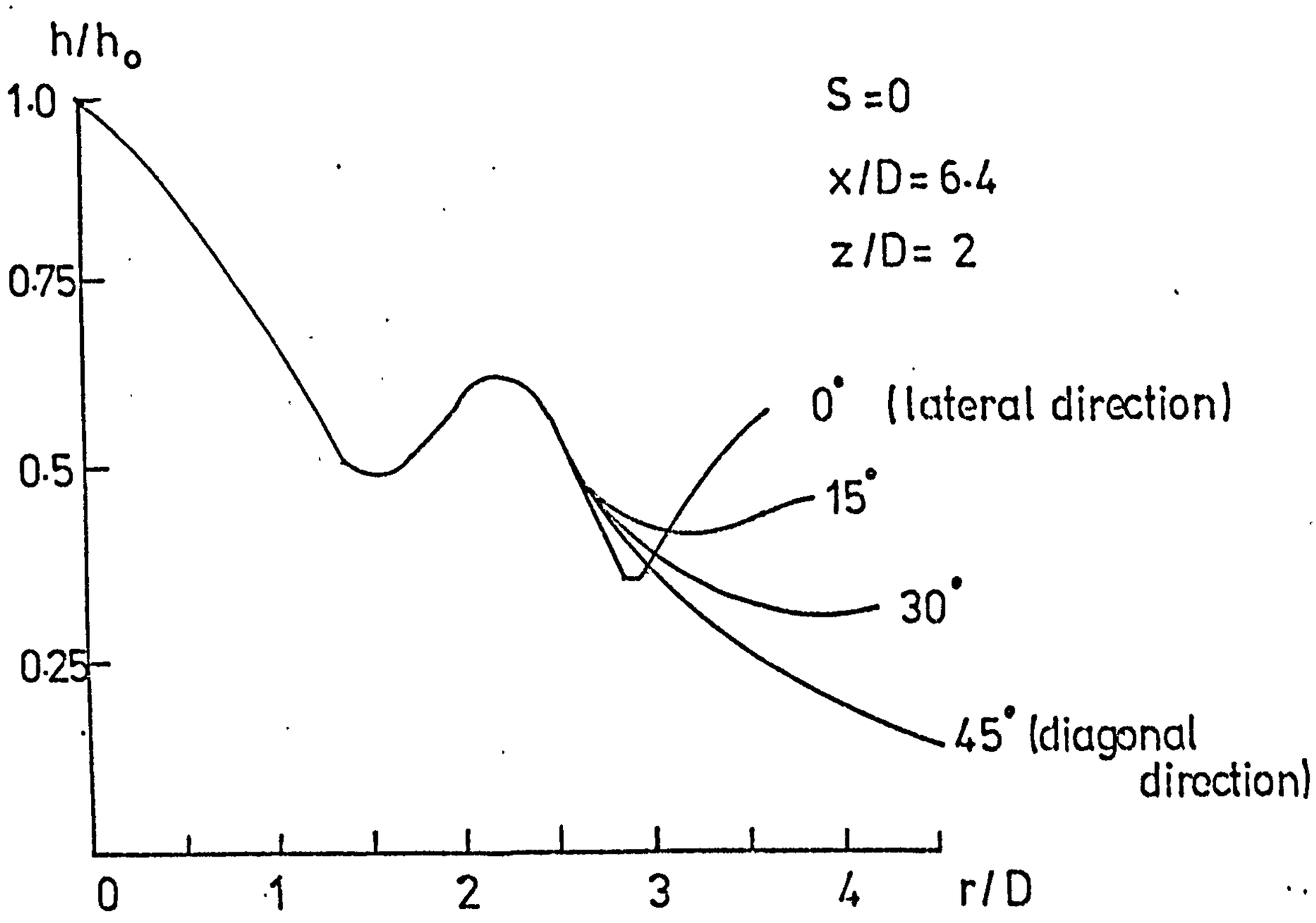

Fig 10.46 TYPICAL LOCAL HEAT TRANSFER VARIATIONS FOR MULTIPLE JETS ALONG DIFFERENT DIRECTIONS

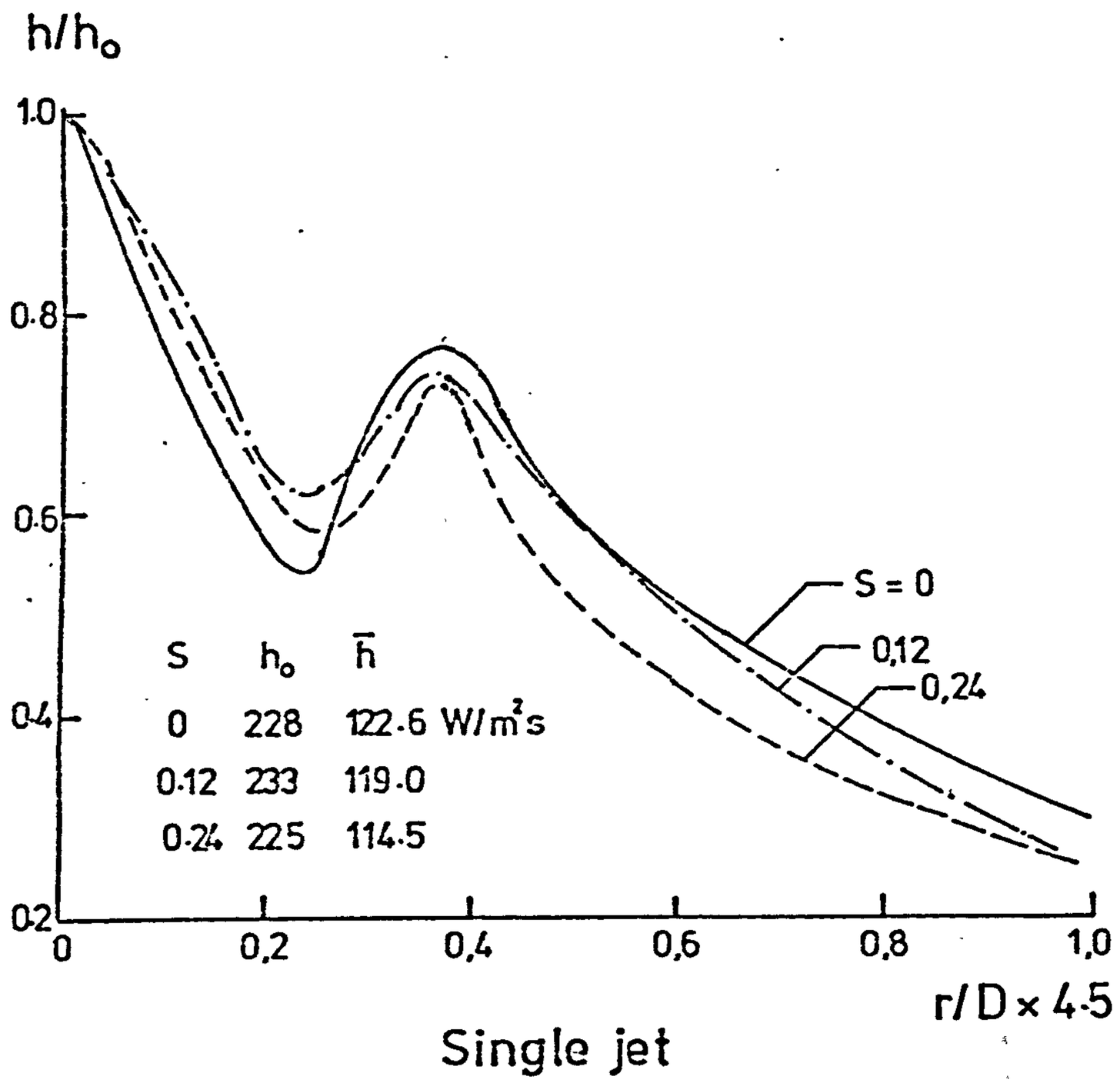

Single jet

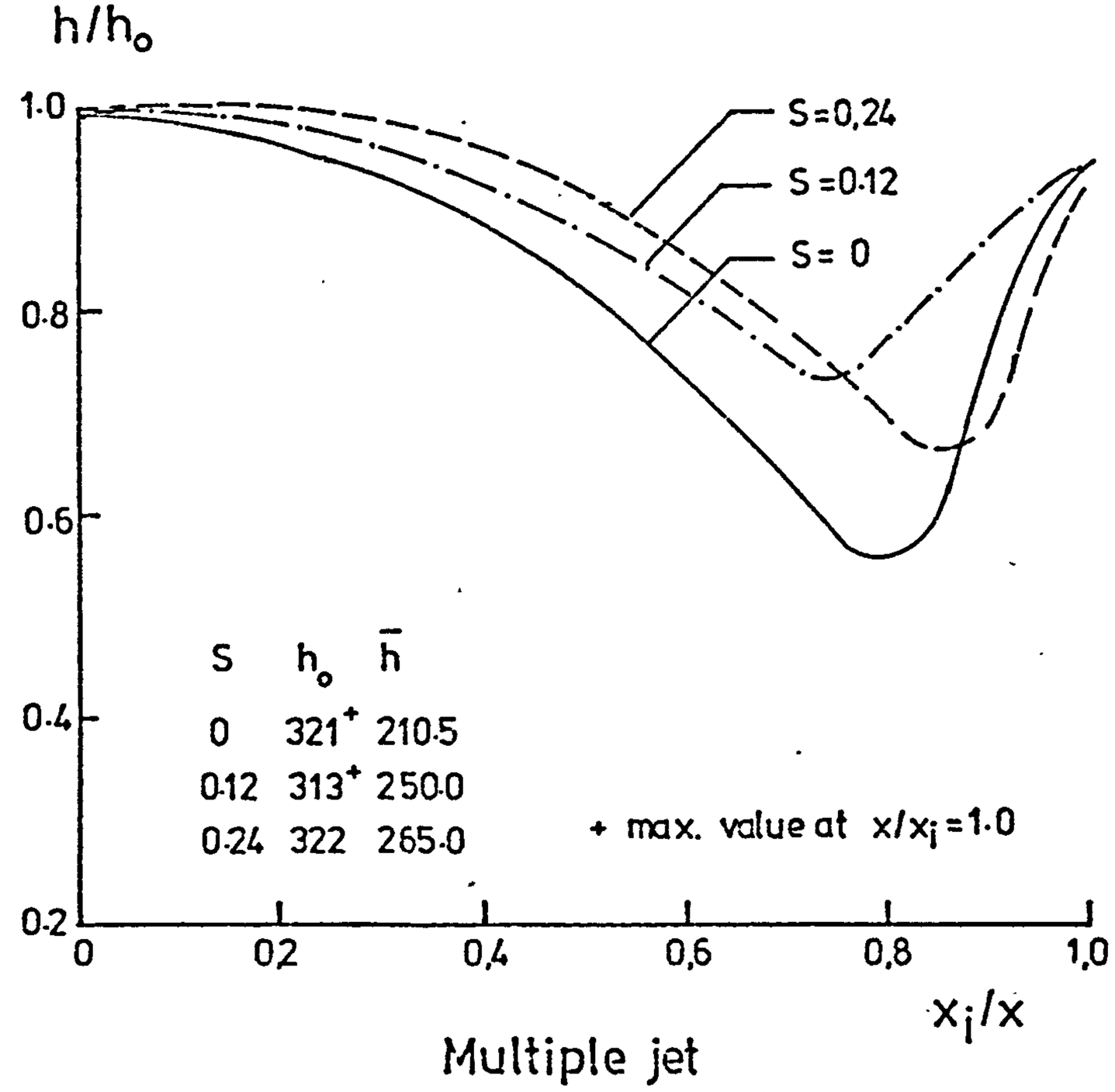

Multiple jet

Fig. 10,47 LOCAL HEAT TRANSFER DISTRIBUTIONS FOR SINGLE AND MULTIPLE JETS COMPARED AT VARIOUS SWIRLS (z/D=2).

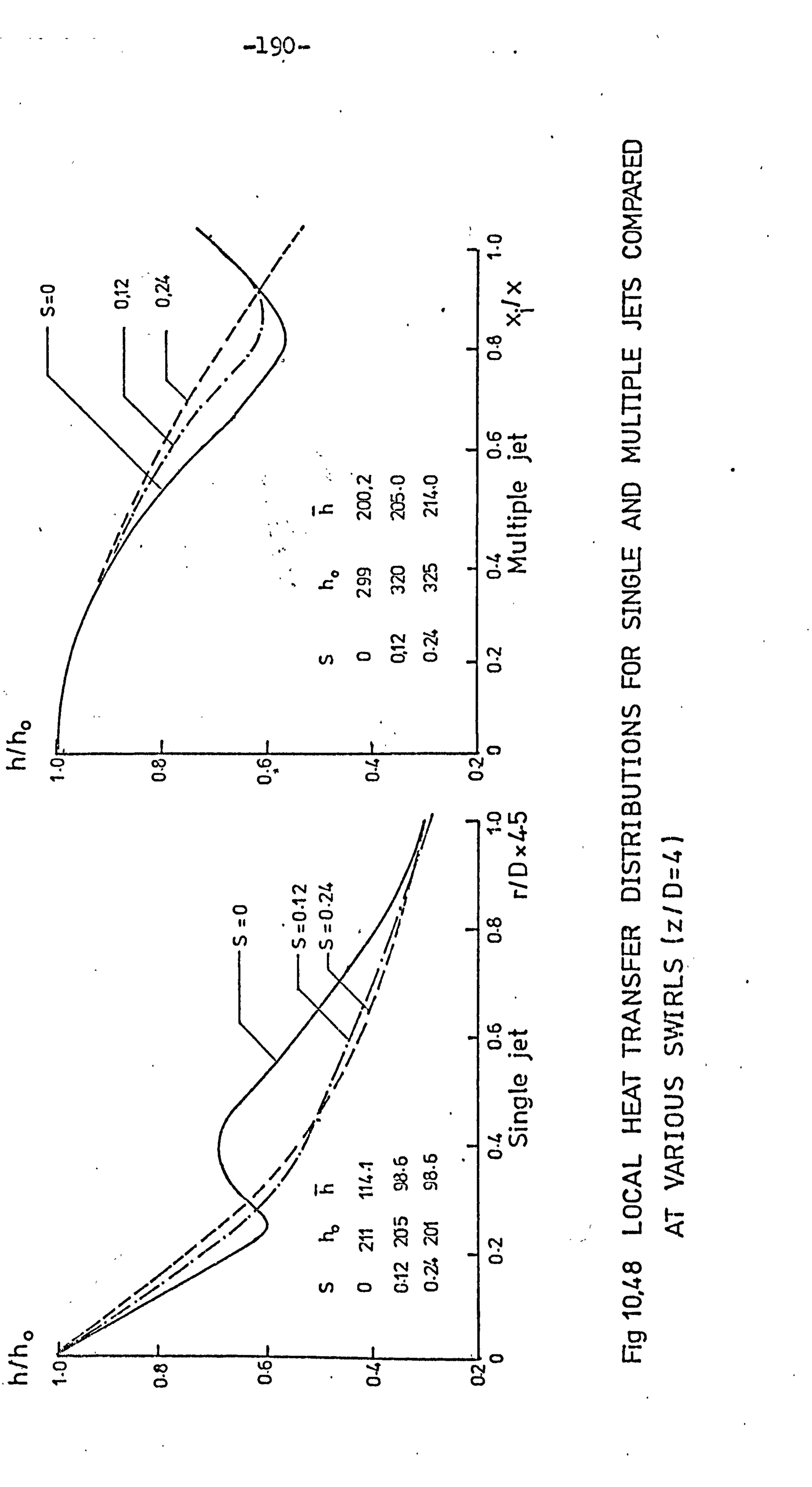

Fig 10,48 LOCAL HEAT TRANSFER DISTRIBUTIONS FOR SINGLE AND MULTIPLE JETS COMPARED AT VARIOUS SWIRLS (z/D=4)

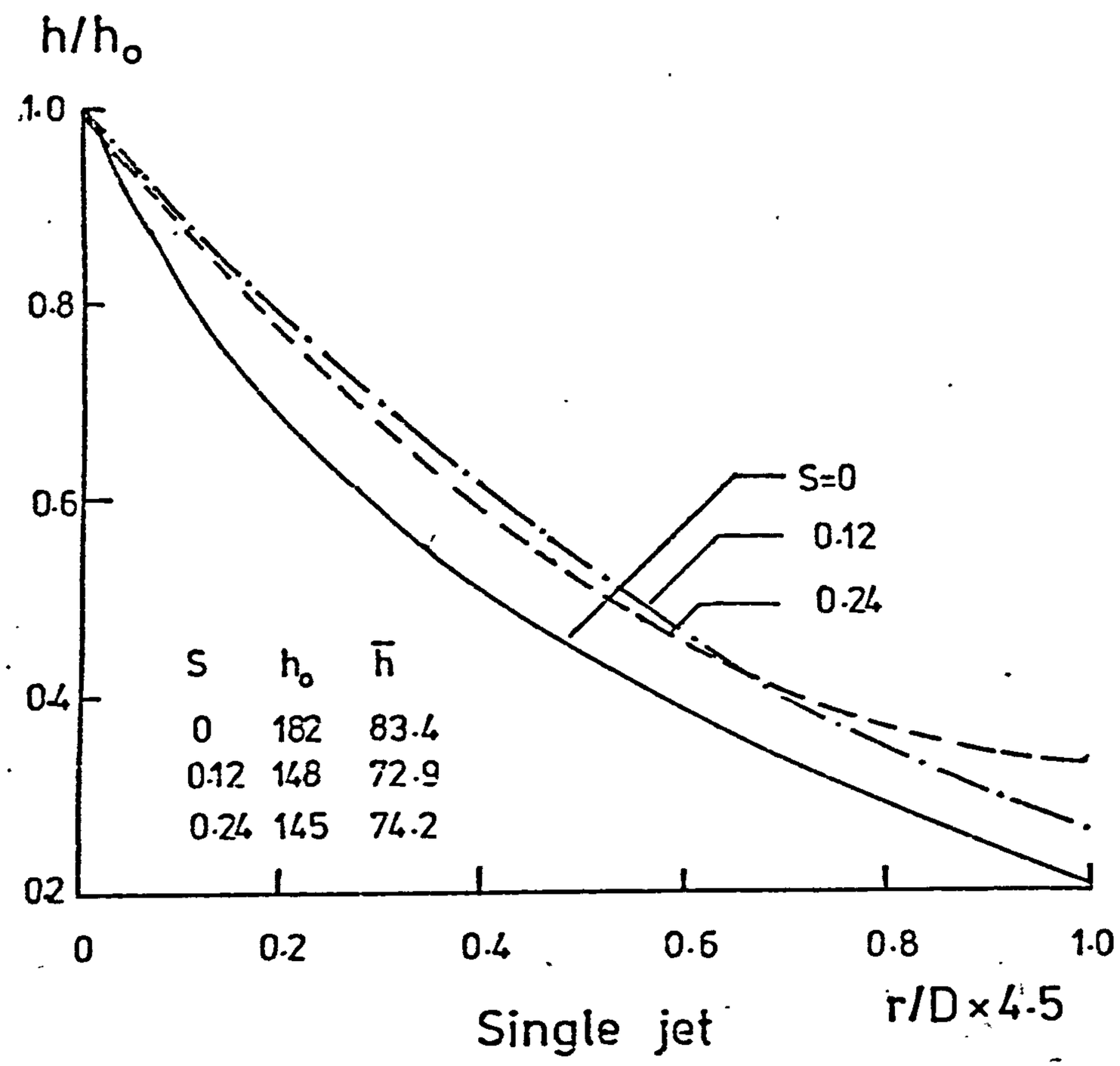

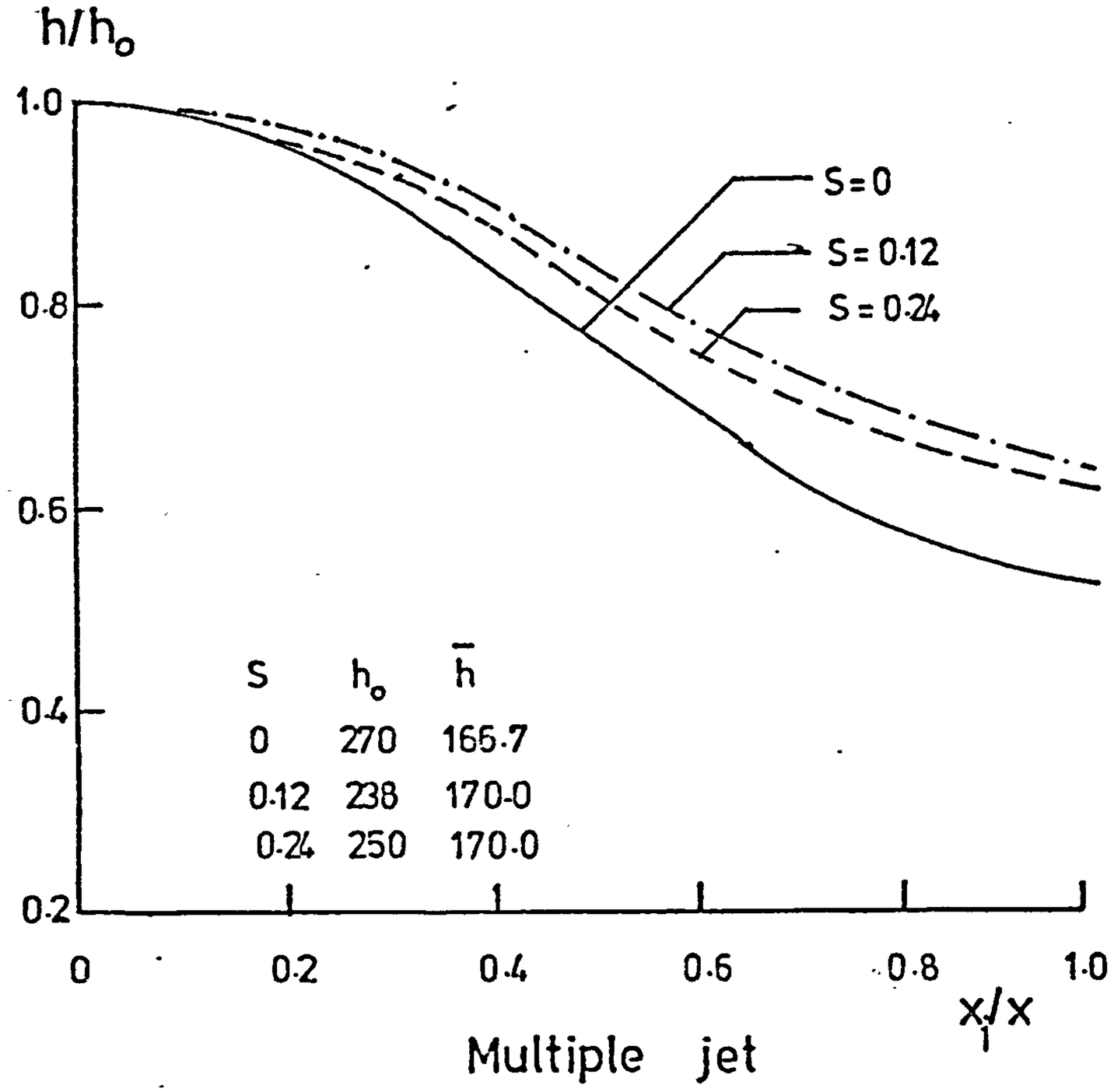

Fig.10.49 LOCAL HEAT TRANSFER DISTRIBUTIONS FOR SINGLE AND MULTIPLE JETS COMPARED AT VARIOUS SWIRLS (z/D=8)

CHAPTER 11

CONCLUSIONS AND RECOMMENDATIONS FOR FUTURE WORK

11.1 CONCLUSIONS

1. The 'thin-film' naphthalene mass transfer technique coupled with the Chilton-Colburn analogy appears to be an accurate and convenient method of determining local heat transfers from impinging jets. The technique is, however, less suitable for determining the heat transfers at and near the stagnation point.

2. The local and average heat transfer coefficients associated with impingement of a single free jet decrease as the degree of swirl applied to the jet is increased. However, the uniformity of heat transfers over the surface is improved at medium swirls.

3. The average heat transfer from a single impingement jet can be expressed by:-

$$\overline{Nu} = C\ Re_D^{0.8}\ Pr^{0.33}\ (z/D)^{-0.2}\ S^{-0.2}$$

where C depends on the 'target' area, e.g. C = 0.022, 0.018 and 0.014 for $0 \leqslant r/D \leqslant 4.25$, $0 \leqslant r/D \leqslant 6.5$ and $0 \leqslant r/D \leqslant 8.5$ respectively.

This equation is valid for S = 0.12 to 0.48, z/D = 2 to 12, and Re_D = 32,000 to 60,000. It represents the present data to approximately ± 10%.

4. At nozzle-to-target separations, $z/D \leqslant 8$, the average heat transfer coefficients associated with impingement from an array of circular jets increase initially as the degree of swirl applied to the jet is increased. The maximum heat transfer ensues at S = 0.24 approximately. Upon further increase in swirl, the heat transfer is reduced until eventually the performance of the swirling jet arrays becomes poorer than that of the non-swirling case. This characteristic of an initial increase in heat transfer is most marked at the nearest target spacing and nozzle pitch (i.e. z/D = 2 and x/D = 3.2).

5. The average heat transfer associated with an array of impinging jets (swirling and non-swirling) decreases as the distance between the nozzle exit and the impinging surface is increased. The rate of decay tends to increase with the degree of swirl. This can be attributed to simultaneous more rapid decay in the jet velocity.

6. The difference in the average heat transfer characteristics of single jet and arrays can be explained in terms of the modification of the local heat transfer distributions associated with the individual jets in the array.

11.2 FUTURE RECOMMENDATIONS

1. Further experiments are desirable to study more completely the range of swirls which provide an increase in the average heat transfer associated with the impingement of particular arrays of circular jets.

2. The effect of the adjacent jets rotating in opposite directions in an array should also be examined.

REFERENCES

1. Krieth, F. — Principles of Heat Transfer. International Textbook Company, Scranton, Pennsylvania, 1959.

2. Jones, R.E. — Hot Spot Formation in Rapid Heating Furnace Walls. MSc.Thesis. Cranfield Institute of Technology. 1974.

3. Mac, S.S. — Space-Average Heat Transfer in Rapid Heating. MSc.Thesis, Cranfield Institute of Technology. 1974.

4. Al-Mobarek, A.M.B. — Heat Transfer in a Billet Reheating Furnace. MSc.Thesis, Cranfield Institute of Technology. 1977.

5. Oladiran, M.T. — Local Heat Transfer in a Billet Reheating Furnace. MSc.Thesis, Cranfield Institute of Technology. 1977.

6. Kabari, L. — Flow and Heat Transfers Associated with Impinging Jets in Crossflows. PhD.Thesis, Cranfield Institute of Technology. 1977.

7. Chong, Y.K. — Two Dimensional Slot Jet Impingement in a Confined Crossflow Stream. MSc.Thesis, Cranfield Institute of Technology. 1979 (unpublished).

8. Perry, J., Winter, E.F. and Wilcock, R. — Rapid Heating of Steel for Hot Working. Steel Times. Vol.194, pp.761. 1964. Vol.195, pp.111, 1967, and Vol.195, pp.170, 1970.

9. Lucas, D.M. Masters, J. and Toth, H.E. — Predictions of the Performance of Rapid Heating Furnaces. J.Inst.Gas Eng., Vol.67, pp.397. 1969.

10. Cheetham, H.A. and Lanary, R.S. — Rapid Heating of Metals by Jet Impingement. Hamworthy Eng.Ltd., Poole, 1971.

11. Winter, E.F. — Jet Impingement - A Versatile Gas-Fired System for Process Heating of Metals.

Shell International Gas Ltd.,
Report No.SIG.71/7, 1971.

12. Duggan, A.P., Issac, J.G. and Thomas, J.R. — Convective Heating Investigations and Recent Developments. Slab Reheating Conference, Iron and Steel Inst. Bournemouth, June 1972.

13. Daane, R.A., and Han, S.T. — An Analysis of Air Impingement Drying. TAPPI, Vol.44, No.1, pp.73. 1961.

14. Arganbright, D.G. and Resch, H. — A Review of Basic Aspects of Heat Transfer under Impinging Air Jets. Wood Science and Technology. Vol.5, pp.73. 1971.

15. Chance, L.J. — Experimental Investigation of Air Impingement Heat Transfer under an Array of Round Jets. TAPPI, Vol.57, Part 6, pp.108. 1974.

16. Scheuter, K.R. and Dosdogru, G.A. — Investigation of Impinging Air Jet Dryers with Respect to Possible Automation. Tech.Assoc. of Graphic Arts (TAGA), Proc.224, 1971.

17. Hardisty, H. — Industrial Drying Using Impingement Air Jets - Part I. Report No.226. School of Mechanical Engineering, University of Bath, 1973.

18. Hardisty, H. — Industrial Drying using Impinging Air Jets - Part II. Report No. 227. School of Mechanical Engineering. University of Bath, 1973.

19. Black, J. and Hardisty, H. — Heat and Mass Transfer in Ink Drying and Infra-Red Dryness Measurements. Journal of Mech.Eng.Sc., Vol.18, pp.99. 1976.

20. Metzger, D.E., Yamashita, T., and Jenkins, C.W. — Impingement Cooling of Concave Surfaces with Lines of Circular Air Jets. Journal of Engg.for Power, Trans.ASME, Series A, Vol.91, No.3, pp.149. July 1969.

21. Chupp, R.E., Helms, H.E., McFadden, P.W. and Brown, T.R. — Evaluation of Interical Heat Transfer Coefficients for Impingement Cooled Turbine Airfoils. AIAA Paper No.GB.7564, June 1968.

22. Chigier, N.A. — Application of Model Results to the Design of Industrial Flames. 4th Symposium on Flames and Industry., Inst.of Fuel. 1972.

23. Beér, J.M. and Chigier, N.A. — Combustion Aerodynamics. Applied Science Publishers, London, 1972.

24. Perry, C.J. — Heat Transfer from Impinging Swirling Jets. MSc.Thesis, Cranfield Institute of Technology. 1975.

25. Dunn, A.R. — Heat Transfer from an Array of Swirling Jets. MSc.Thesis, Cranfield Institute of Technology, 1978.

26. Vickers, J.M.F. — Heat Transfer Coefficients between Fluid Jets and Normal Surfaces. Industrial Chem.Eng., Vol.51, No.8. pp.967. 1959.

27. Gauntner, J.W., Livingood, J.N.B. and Hrycak, P. — Survey of Literature on Flow Characteristics of a Single Turbulent Jet Impinging on a Flat Plate. Report No..NASA TN D-5652. February 1970.

28. Schrader, H. — Drying of Moist Surfaces by Means of Hot Air Jets. Flow Characteristics and Mass Transfer (In German). Forschungsh, Ver.Deutsch. Ing. 484, 1961.

29. Hoogendoorn, C.J. — The Effect of Turbulence on Heat Transfer at a Stagnation Point. Int.Journal Heat Mass Transfer. Vol.20, pp.1333, 1977.

30. Dawson, D.A. and Trass, O. — Mass Transfer in Turbulent Radial wall Jet. Canadian Journal Chem.Eng., Vol. 44, pp.121. 1966.

31. Schlünder, E.U. — Ubër die Ausbreitung Turbulenter Freistrahlen (The Expansion of Turbulent Free Jets). Zeitschrift fur Flugwissen-Schaften, Vol.19, pp.108. 1971.

32. Corrsin, S. — Investigation of Flow in an Axially Symmetrical Heated Jet of Air. NASA Wartime Report W-94. 1943.

33. Boguslawski, L. and Popiel, Cz.O. — Flow Structure of the Free Round Turbulent Jet in the Initial Region. Journal Fl.Mechanics. Vol.90, Pt.3, 531. 1979.

34. Martin, H. — Heat and Mass Transfer between Impinging Gas Jets and Solid Surfaces. Advances in Heat Transfer, Vol. 13, pp.1. Academic Press, London, 1977.

35. Gardon, R. and Cobonpue, J. — Heat Transfer between a Flat Plate and Jets of Air Impinging on it. International Developments in Heat Transfer. ASME, pp.454. 1962.

36. Gardon, R. and Akfirat, J.C. — Heat Transfer Characteristics of Impinging two-dimensional air jets. Trans.ASME. Journal Heat Transfer. Vol.88, pp.101. 1966.

37. Gardon, R. and Akfirat, J.C. — The Role of Turbulence in Determining the Heat Transfer Characteristics of Impinging Jets. Int.Journal Heat Mass Transfer. Vol.8. pp.1261. 1965.

38. Vallis, E.A., Patrick, M.A. and Wragg, A.A. — Radial Distribution of Convective Heat Transfer Coefficient between an Axisymmetric Turbulent Jet and a Flat Plate Held Normal to the Flow. Paper FC(b)-21, 6th Int.Heat Transfer Conference, Toronto, Canada, August 1978.

39. Huang, G.C. — Investigations of Heat Transfer Coefficients for Air Flow through Round Jets Impinging Normal to Heat Transfer Surface. Journal Heat Transfer, Vol.85, pp.237. 1963.

40. Sitharamayya, S. and Subba Raju, K. — Heat Transfer Between an Axisymmetric Jet and a Plate held Normal to the Flow. The Canadian Journal of Chem.Eng., Vol.47, pp.365. 1969.

41. Metzger, D.E. — Spot Cooling and Heating of Surface with High Velocity Impinging Air Jets. Technical Report No.52. Dept. of Mech.Eng., Stanford University. 1962.

42. Kercher, D.M. and Tabakoff, W. — Heat Transfer by a Square Array of Round Air Jets Impinging Perpendicular to a Flat Surface including the Effect of Spent Air. Trans.ASME., Journal of Engg. for Power. Vol.92, pp.73. 1970.

43. Metzger, D.E. and Korstad, R.J. — Effects of Crossflow on Impingement Heat Transfer. Trans.ASME. Journal of Engg.for Power. Vol.94, pp.35, 1972.

44. Metzger, D.E., Florschuetz, L.W. Takenchi, D.I., Behee, R.D. and Berry, R.A. — Heat Transfer Characteristics for Inline and Staggered Arrays of Inline Circular Jets with Crossflow of Spent Air. J. of Heat Transfer, Trans.ASME, Vol.101, pp.526-531, Aug.1979.

45. Perry, K.P. — Heat Transfer by Convection from a Hot Gas Jet to a Plane Surface. Proc. Inst.Mech.Engineers. London. Vol.168, pp.775. 1954.

46. Korger, M. and Krizek, F. — Verfahrenstechnik (Mainz). Vol.6, pp.223. 1972.

47. Freidman, S.J. and Mueller, C.A. — Heat Transfer to Flat Surfaces. Proc.General Discussion on Heat Transfer. Inst.of Mech.Engg., London. pp.138. 1951.

48. Thurlow, G.G. — Communication on Ref.45. Proc. Inst.of Mech.Engineers. Vol.168, pp.778. 1954.

49. Smirnov, V.A., Verevochkin, G.E. and Brdlick, P.M. — Heat Transfer Between a Jet and Plate held Normal to Flow. Int.Journal Heat Mass Transfer. Vol.2, pp.1. 1961.

50. Koopman, R.N. and Sparrow, E.M. — Local and Average Transfer Coefficients due to an Impinging Row of Jets. Int.Journal of Heat Mass Transfer. Vol.19, pp.673. 1976.

51. Hilgeroth, E.
Heat Exchange with Jet Streams Perpendicular to the Exchange Surface (German). Chem.Ing.Tech. Vol.37, pp.1264. 1965.

52. Ward, J., Ideriah, F.J.K., Probert, S.D. and Duggan, A.
Mass Transfer Technique for Investigation of Heat Transfer by Jet Impingement Systems. Journal Mech.Eng.Sci., Vol.14, No.6, pp.389. 1972.

53. Baines, W.D. and Keffer, J.F.
Shear Stress and Heat Transfer at a Stagnation Point. Int.Journal of Heat and Mass Transfer. Vol.19, pp.21. 1976.

54. Chigier, N.A.
Swirling Jets. Journal of Fuel Society. Vol 18. pp.16. 1967.

55. Mathur, M.L. and Maccallum, N.R.L.
Swirling Air Jets Issuing from Vane Swirlers. Part I : Free Jet. Journal of Inst.of Fuel. Vol.40, pp.214. 1967.

56. Kilik, E.
The Influence of Swirler Design Parameters on the Aerodynamics of the Downstream Recirculation Regions. PhD.Thesis, Cranfield Institute of Technology. 1976.

57. Chigier, N.A. and Beér, J.M.
Velocity and Static-Pressure Distributions in Swirling Air Jets Issuing from Annular and Divergent Nozzles. Trans.ASME. Series D. Vol.86. pp.788. 1964.

58. Chigier, N.A. and Chervinsky, A.
Experimental Investigations of Swirling Vortex Motion in Jets. Trans.ASME, Journal of Applied Mechanics. Vol.34, pp.443. 1967.

59. Watson, E.A. and Clarke, J.S.
Combustion and Combustion Equipment for Aero Gas Engine. Journal Inst.Fuel. Vol.21, pp.2. 1947.

60. Syred, N. and Beér, J.M.
Combustion in Swirling Flows. A Review. Combustion and Flame. Vol.23, pp.143. 1974.

61. Hartnett, J.P. and Eckert, E.R.G. — Experimental Study of the Velocity and Temperature Distribution in High Velocity Vortex-Type Flow. Trans.ASME, Vol.79. pp.751. 1957.

62. Rose, W.G. — A Swirling Round Turbulent Jet. Journal of Applied Mech., Trans ASME., Series E., Vol.84. pp.615. 1962.

63. Lee, J.C. and Ash, J.E. — A Three Dimensional Spherical Pitot Probe. Trans.ASME., Vol.78, pp.603. 1956.

64. Miller, R.D. and Comings, E.W. — Static Pressure Distribution in a Free Turbulent Jet. Journal of Fluid Mech., Vol.3. pp.1. 1957-58.

65. Loisyanskii, L.G. — The Propogation of a Twisted Jet in an Unbounded Space Filled with the same Fluid. Prikladanya Matematiza i Mekhanika, Vol.17, pp.3, 1953.

66. Görtler, H. — Decay of Swirl in an Axially Symmetrical Jet Far from the Orifice. Revista Matemática Hispano Americanas, Vol.14, Nos.4 and 5. pp.143. 1954.

67. Kerr, N.M. and Fraser, D. — Swirl, Part I : Effect on Axisymmetrixal Turbulent Jets. Journal Inst.of Fuel., Vol.38. No.299. pp.519. 1965.

68. Hiett, G.F. and Powell, G.E. — Three Dimensional Probe for Investigation of Flow Patterns. Engineer, London. Vol.213. pp.165. 1962.

69. Chigier, N.A. and Chervinsky, A. — Experimental and Theoretical Study of Turbulent Swirling Jets Issuing from a Round Orifice. TAE Report No.46, Dept. of Aero. Engg. Technion-Israel Inst.of Tech., Israel. Nov.1965.

70. Chigier, N.A. and Chervinsky, A. — Aerodynamic Study of Turbulent Burning Free Jets with Swirl. 11th International Symposium on Combustion. The Combustion Inst. pp.489. 1967.

71. Syred, N., Chigier, N.A. and Beér, J.M. — Turbulence Measurement in Swirling Recirculating Flows. Symposium on Internal Flow. Inst.of Mech.Engineers. London. held at University of Salford. Paper 13, 327-36. 1971.

72. Pratte, B.D. and Keffer, J.F. — The Swirling Turbulent Jet. Trans.ASME., Journal of Basic Engineering. Vol.94. pp.739. 1972.

73. Lilley, D.G. — Computing Strongly Swirling Flows with a Primitive Pressure-Velocity Code. 8th Fluid and Plasma Dynamics Conference. A.IAA., Hartford, Connecticut. June 1975.

74. Huang, B., Douglas, W.J.M. and Mujumdar, A.S. — Heat Transfer under a Laminar Swirling Impinging Jet - A Numerical Study. Paper FC(b)-23. 6th Int.Heat Transfer Conference, Toronto, Canada. August 1978.

75. British Standards Institute. — Methods of Measurement of Fluid Flow in Pipes. Part I : Orifice Plates, Nozzles and Venturi Tubes. British Standards Institute, London. 1964.

76. Bradshaw, P. — An Introduction to Turbulence and its Measurements. Pergamon Press, Oxford. 1971.

77. Maksoud, T.M.A. — A General Method for Investigating Blade to Blade Distribution of Flow Field Quantities inside a Turbomachinery. MSc.Thesis, Cranfield Institute of Technology, 1978.

78. King, L.V. — On the Convection of Heat from Small Cylinders in a Stream of Fluid. Phil.Trans.Royal Society, 214A. pp.373. 1914.

79. Siddall, R.G. and Davies, T.W. — An Improved Response Equation for Hot-Wire Anemometry. Int.Journal Heat and Mass Transfer. Vol.15, pp.367. 1972.

80. Klatt, F. — The X-Hotwire Probe in a Plane Flow Field.

DISA Information, No.8, July 1969.

81. Kjellstrom, B. and Hedberg, S. — Calibration of a DISA Hotwire Anemometer and Measurements in a Circular Channel for Confirmation of the Calibration. DISA Information, No.9. pp.8, February 1970.

82. Davies, T.W. — A Study of the Aerodynamics of the Recirculation Zone Formed in a Free Annular Air Jet. PhD. Thesis, Sheffield University, 1968.

83. Davies, P.O.A.L. — Recent Developments in Hotwire Anemometry. Int.Seminar on Heat and Mass Transfer, Hercey-Novi, Yugoslavia, 1969.

84. Hoffmeister, M. — Using a Single Hotwire Probe in Three-Dimensional Turbulent Flow Fields. DISA Information, No.13, pp. 26. May 1972.

85. (DISA) — Instruction and Service Manual for Type 55D01 Anemometer Unit.

86. Eckert, E.R.G. and Goldstein, R.J. — Measurements in Heat Transfer. Hemisphere Publishing Corp. Washington, 1976.

87. Taylor, J.F., Grimmet, H.L. and Comingo, E.W. — Isothermal Free Jets of Air Mixing with Air. Chem.Eng.Progress, Vol.47. pp.175, April 1951.

88. Reynolds, O. — On the Extent and Action of the Heating Surface of Steam Boilers. Scientific Papers of Osborne Reynolds, Cambridge, 1900.
Also, Proc.Manchester Lit. Phil.Soc. 14:7 (1874).

89. Prandtl, L. — Eine Beziehung Zwischen Wärmeaustaush und Strömungswiderstand der Flüssigkeiten. (A Relationship between Heat Transfer and Friction in the Fluids). Physik Z, Vol.11, pp.1072. 1910.

90. Taylor, G.I.
Conditions at the Surface of a Hot Body Exposed to the Wind.
Brit.Adv.Comm.Aeron. Rep. and Mem. 272, Vol.31, pp.423. 1916.

91. Von Kármán, T.
Analogy between Fluid Friction and Heat Transfer.
Trans.ASME., Vol.61, pp.705. 1939.

92. Colburn, A.P.
A Method of Correlating Forced Convection Heat Transfer Data and a Comparison with Fluid Friction.
Trans.Am.Inst.Chem.Engnrs. Vol.29, pp.174. 1933.

Also see, Relation between Mass Transfer (Absorbtion) and Fluid Friction.
Ind.Eng.Chem., Vol.22, pp.967, 1930.

93. Chilton, T.H. and Colburn, A.P.
Mass Transfer (Absorbtion) Coefficients.
Ind.Eng.Chem., Vol.26, pp.1183, 1934.

94. Lewis, J.S.
A Heat/Mass Transfer Analogy applied to Fully Developed Turbulent Flow in an Annulus.
J.Mech.Eng.Sci., Vol.13, No.4. pp.286. 1971.

95. Jayatillaka, C.V.L.
The Influence of Prandl Number and Surface Roughness on the Resistance of the Laminar Sub-layer to Momentum and Heat Transfer.
Progress in Heat and Mass Transfer. Vol.1, pp.193, Pergamon Press, Oxford, 1969.

96. Davies, R.M., Lucas, D.M., Moppet, B.E.(Mrs) and Galsworthy, R.A. (Mrs)
Isothermal Model Studies of Rapid Heating Furnaces.
Jnl. of the Inst.of Fuel. Vol.44, pp.453, 1971.

97. Simpson, R.L. and Field, R.L.
A Note on the Turbulent Schmidt and Lewis Numbers in a Boundary Layer.
Int. J.Heat and Mass Transfer. Vol.15, pp.177. 1972.

98. Mizushina, T. — The Electrochemical Method in Transport Phenomena. Advances in Heat Transfer, Vol. 7, pp.87, Academic Press. London, 1971.

99. Klein, V. — Dissertation, Tech.Hochsch, Hanover, 1933.

100. Winding, C.C. and Cheney, A.J. — Mass and Heat Transfer in Tube Banks. Ind.Eng.Chem., Vol.40, pp.1087. 1948.

101. Christian, W.J. and Kezios, S.D. — Experimental Investigations of Mass Transfer by Sublimation from Sharp-Edged Cylinders in Axisymmetric Flow with Laminar Boundary Layer. Heat Transfer and Fluid Mech. Institute, held at California Inst.of Tech., California 359, 1957.

102. Hinze, J.O. — Turbulence. McGraw Hill Book Co.Ltd. New York, 1959.

103. Wilkie, D and White, L. — Fuel Element Heat Transfer near Dimple Braces. Nucl.Engg., Vol.11, pp.596. 1966.

104. Neal, S.B.H.C., Northover, E.W. and Hitchcock, J.A. — The Development of a Technique for Applying Naphthalene to Surfaces for Mass Transfer Analogue Investigations. J.Physics E. Scientific Instrum. Vol.3, 636, 1970.

105. Neal, S.B.H.C. — The Development of the Thin-Film Naphthalene Mass Transfer Analogue Technique for the Direct Measurement of Heat Transfer Coefficients. Int.J.Heat and Mass Transfer, Vol.18, pp.559. 1975.

106. Wong, P.W. — Mass and Heat Transfer from Circular Finned Cylinders. Journal Inst.of Heating and Vent.Engnrs., Vol.34, pp.1. 1966.

107. Sherwood, T.K. and Bryant, H.S. — Mass Transfer through Compressible Boundary Layers.

Canadian Jnl.of Chem.Eng., Vol.35, pp.51, 1957.

108. - International Critical Tables. McGraw Hill Book Co.Inc. New York, Vol.3., pp.208. 1926.

109. - Handbook of Chemistry and Physics. 46th Edition. Chemical Rubber, Co.Cleveland, Ohio. 1965.

110. Sherwood, T.K. and Trass, O. Sublimation Mass Transfer through Compressible Boundary Layer on a Flat Plate. Trans.ASME., Jnl.Heat Transfer, Vol.82, pp.313, 1960.

111. Goldstein, R.J., Sparrow, E.M. and Jones, D.C. Natural Convection Mass Transfer Adjacent to Horizontal Plates. Inst.J.Heat Mass Transfer, Vol.16, 1025. 1973.

112. Oladiran, M.T. Private Communication. School of Mech.Eng., Cranfield Institute of Technology, Sept.1979.

113. Wolfshtein, M. Empirical Correlation for Evaluation of Stanton Number in Impinging Jets. ARC, Heat and Mass Transfer Sub-Committee, ARC 27613, 1966.

APPENDIX A

FIVE-HOLE PITOT PROBE - FURTHER NOTES

Evaluation of the Velocity Components and Pressure.

As mentioned in Section 5.2, the pressures are measured at each of the tappings when the pressures at tappings 4 and 5 are balanced (see Figure 5.1) The rotation of the probe to this station yields the yaw angle Φ. The pitch angle 'α', the flow velocity $\bar{V}$ and the static pressure can then be determined by using calibration curves supplied by the probe manufacturer (Figure A.1). The procedure is outlined below.

The factors $\frac{1}{2}\, k_1 k_2 k_3 k_4$ may be found from the formula:-

$$k_1 k_2 k_3 k_4 = \frac{H_3 - H_1}{H_2 - H_4}$$

where H_1, H_2, H_3 and H_4 are the pressures at tappings 1, 2 3 and 4 respectively.

The pitch angle 'α' can then be read for the appropriate value of $(\frac{1}{2} k_1 k_2 k_3 k_4)$ from the calibration chart. The velocity V and components u, v and w can be determined by knowing the values of 'α' and 'Φ' using the expressions already presented in Section 5.2.2. The static pressure may also be determined by a similar expression.

Determination of the Swirl Number.

The evaluation of the swirl number, S, from the velocity profiles is best illustrated by considering an example.

The curves for 'u' and 'w' for $Re_D = 60{,}000$ and $m_{tan}/m_{tot} = 0.74$ are presented in Figures 5.3 and 5.4. The swirl number $S = G\Phi/G_X R$, where:-

$$G\Phi = 2\pi\rho \int_0^R r^2 u\, w\, dr$$

$$G_X = 2\pi\rho \int_0^R r(u^2 - \tfrac{1}{2} w^2)\, dr$$

This later expression for G_X is an approximation, as suggested by Chigier and Chervinsky (Ref.58), which can be used for weak and medium swirls.

Table A.1 presents the components of the integrands tabulated at various radial stations. The integrated values can then be found using Simpson's rule.

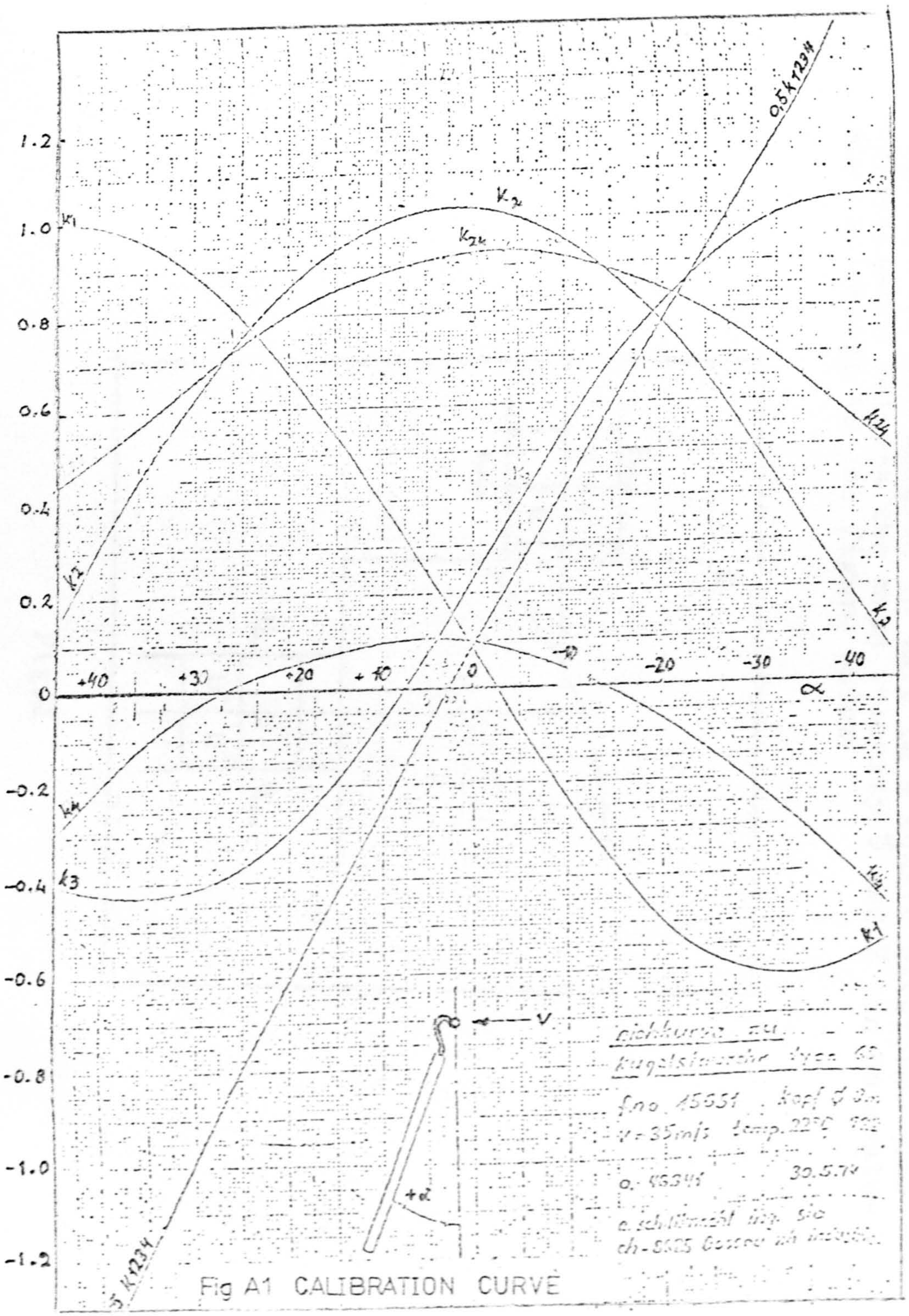

TABLE A.1

DETERMINATION OF SWIRL NUMBER

$r \times 10^2$ m	u m/s	w m/s	r^2uw	ru^2	$1/2rw^2$
0	34.6	0	0	0	0
0.159	34.5	3.50	0	1.893	0.010
0.318	34.1	5.75	0.002	3.698	0.053
0.476	33.3	6.85	0.005	5.278	0.112
0.635	32.1	8.00	0.010	6.543	0.203
0.794	30.5	8.50	0.016	7.386	0.287
0.952	28.5	8.50	0.022	7.733	0.344
1.111	26.3	8.20	0.027	7.685	0.374
1.270	24.0	7.60	0.029	7.315	0.367
1.430	21.5	7.00	0.031	6.610	0.350
1.590	18.8	6.25	0.030	5.620	0.311
1.740	16.3	5.63	0.028	4.623	0.276
1.910	13.5	4.75	0.023	3.481	0.216
2.060	11.0	4.00	0.019	2.493	0.165
2.222	8.5	3.00	0.013	1.605	0.100
2.350	5.8	2.25	0.007	0.777	0.060
2.540	3.0	1.00	0.002	0.229	0.013

$$G_\phi = 2\pi\rho \int_0^R r^2 uw\, dr = 2\pi\rho.(.00159/3)(0.692)$$

$$G_x = 2\pi\rho \int_0^R r(u^2 - \tfrac{1}{2}w^2)dr = 2\pi\rho(.00159/3)(209.473)$$

$$S = G_\phi/G_x R = (0.792)/(209.473)(.012) = 0.317$$

APPENDIX B

EVALUATION OF VELOCITY AND TURBULENCE INTENSITY USING A FOUR POINT MEASUREMENT TECHNIQUE WITH A SINGLE HOT-WIRE PROBE

The detailed procedure necessary to evaluate the velocity and turbulence intensity using this technique is given in Ref.23, but a brief description is presented in this Appendix for the sake of completeness. As previously discussed in Chapter 6, the hot-wire is initially calibrated in the 'u' direction and the constants in the King's law determined. The directionality constants G and K can also be found by calibration in the appropriate directions. The hot-wire is positioned such that the velocity 'u' is always perpendicular to it.

The instantaneous 'cooling' velocity is given by:-

$$U^2 = u^2 + G^2v^2 + K^2w^2 \qquad (1)$$

Since the calibration curve for the velocity is non-linear, the mean of the velocity fluctuations will not coincide with the mean of the voltage response. For the present case, the fluctuations are assumed to vary in a square waveform. The relationship between the mean velocity $\bar{U}$ and $\bar{E}$ can be evaluated referring to the figure below.

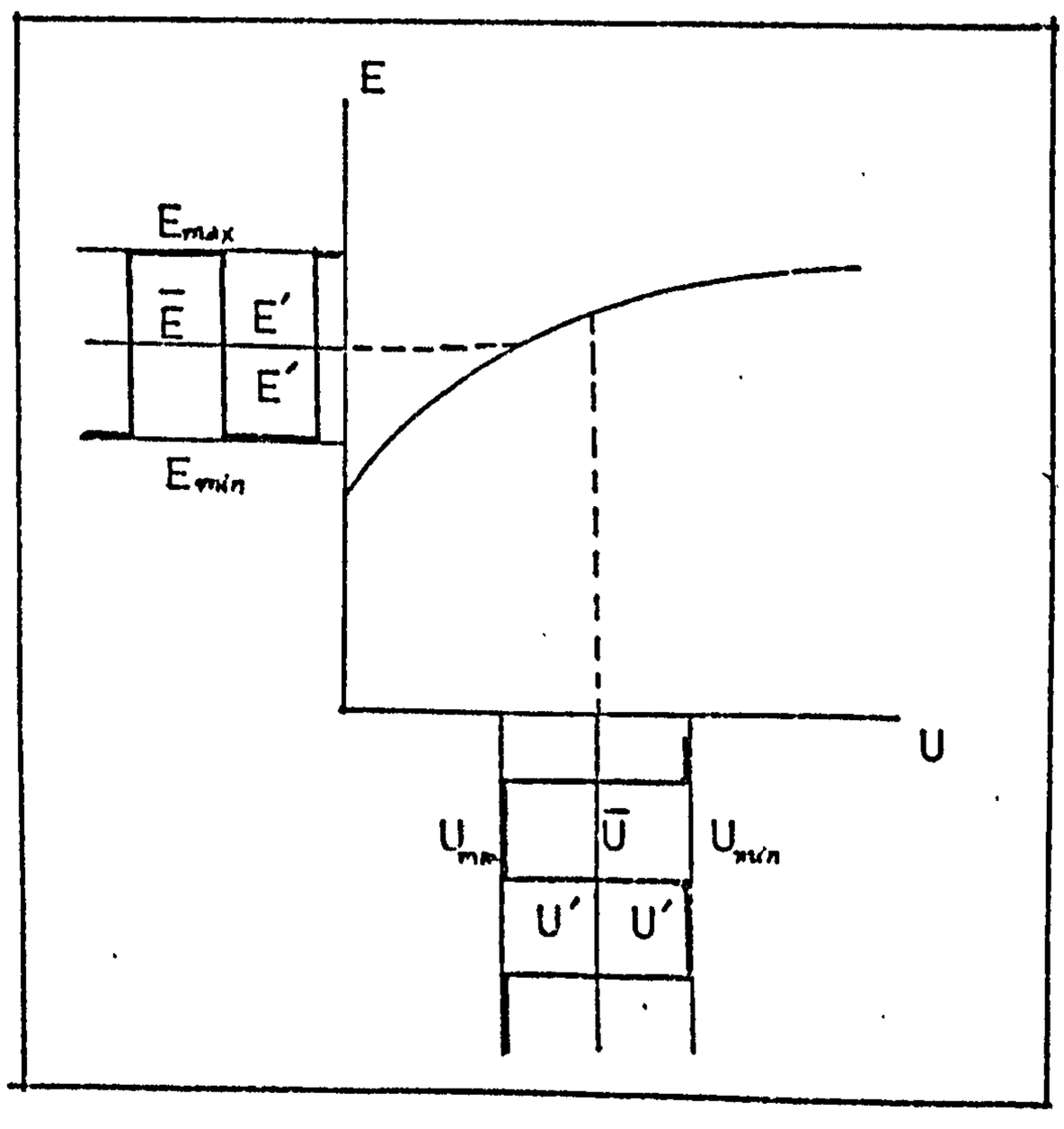

Fig.1

Assuming the King's law applies, the maximum and minimum velocities can be expressed by:-

$$U_{max} = \left[\frac{(\bar{E} + E)^2 - A'}{B'}\right]^2 \qquad (2)$$

$$U_{min} = \left[\frac{(\bar{E} - E)^2 - A'}{B'}\right]^2 \qquad (3)$$

B.1 Response Equations and Velocity Components.

The orientations of the wire and the directions of the three velocity components are related as shown in Figure 2.

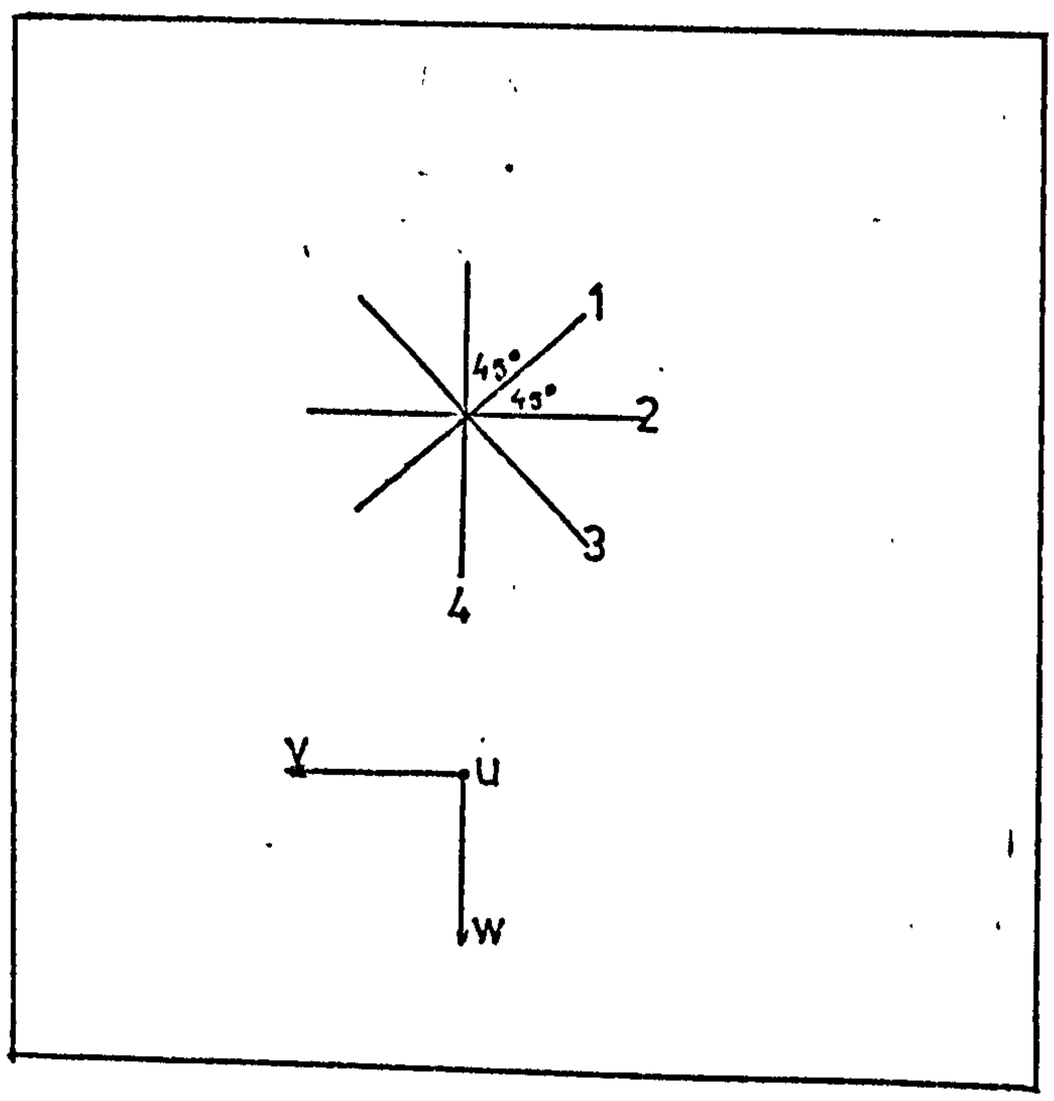

Fig.2

Velocity 'u' is perpendicular to the wire for all orientations, i.e. 'u' is perpendicular to the plane of the paper.

The response equations for each of the positions are found by reference to Equation (1), so that:-

$$U_1^2 = u^2 + G^2v^2 + K^2w^2 \qquad (4)$$

$$U_2^2 = u^2 + \frac{G^2}{2}(w + v)^2 + \frac{K^2}{2}(v-w)^2 \qquad (5)$$

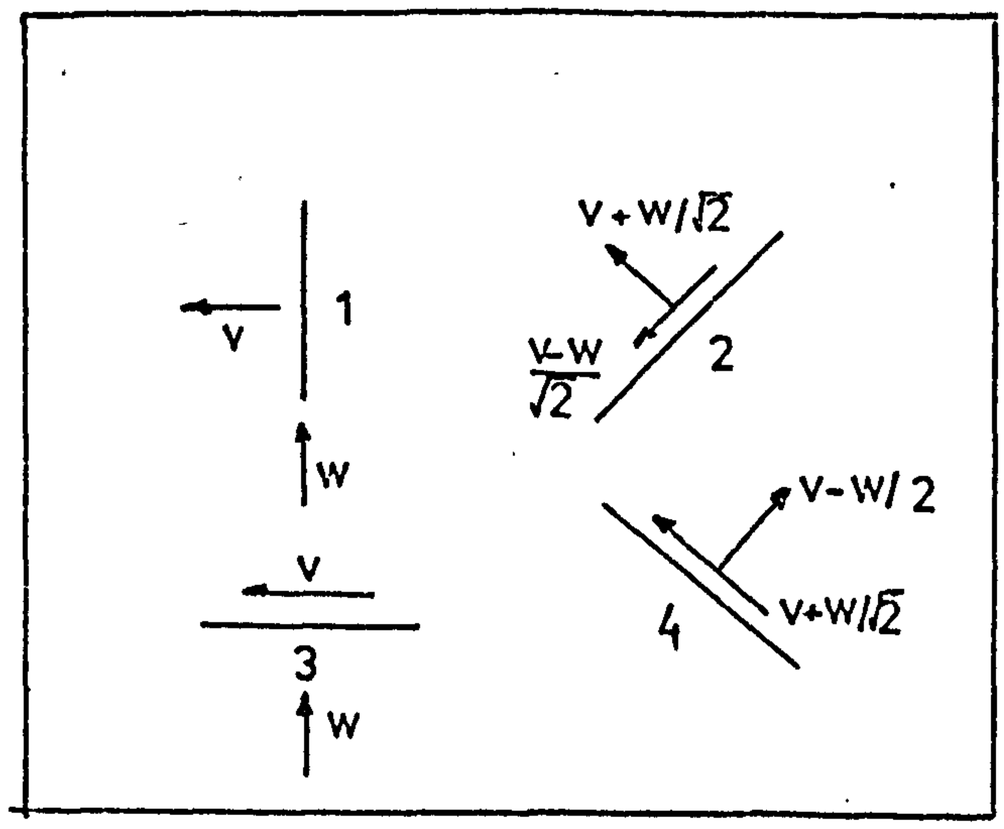

Fig.3

$$U_3^2 = u^2 + K^2v^2 + G^2w^2 \qquad (6)$$

$$U_4^2 = u^2 + \frac{G^2}{2}(v-w)^2 + \frac{K^2}{2}(w+v)^2 \qquad (7)$$

For all these above equations, 'G' and 'K' should be regarded as directionality constants perpendicular and along the wire rather than being associated with any direction.

Assuming 'w' to be the least significant component, the equations (5), (6) and (7) are chosen to solve for 'w', 'v' and 'u'. Subtracting (5) and (7) yields:-

$$U_2^2 - U_4^2 = (G^2 - K^2)\,2vw \qquad (8)$$

Adding (5) and (7), and subtracting (6) multiplied by 2 gives:-

$$U_2^2 + U_4^2 - 2U_3^2 = (G^2 - K^2)(w^2 - v^2) \qquad (9)$$

Equation (8) can be written as:-

$$u = \frac{1}{w}\left(\frac{U_2^2 - U_4^2}{2(G^2 - K^2)}\right) \qquad (10)$$

Substituting this value of 'v' into equation (9) yields:-

$$w^4 - w^2\left(\frac{U_2^2 + U_4^2 - 2U_3^2}{(G^2 - K^2)}\right) - \frac{1}{4}\frac{(U_2^2 - U_4^2)}{(G^2 - K^2)^2} = 0 \qquad (11)$$

This quadratic equation can be solved for 'w' so that:-

$$w = \sqrt{\frac{1}{2(G^2-K^2)}\ U_3^2 + U_4^2 - 2U_3^2 + \sqrt{(U_2^2 + U_4^2 - 2U_3^2)^2 + (U_2^2 - U_4^2)^2}} \qquad (12)$$

A similar expression for 'v' can be found by substitution of the above value for 'w' in Equation (10). Finally, 'u' is obtained by substituting both 'v' and 'w' in Equation (4). These expressions for 'u', 'v' and 'w' can be written as:-

$$w = h(U_2^2,\ U_3^2,\ U_4^2) \qquad (12)$$

$$v = g(U_2^2,\ U_3^2,\ U_4^2) \qquad (13)$$

$$u = f(U_2^2,\ U_3^2,\ U_4^2) \qquad (14)$$

The actual expressions for 'u', 'v' and 'w' are rather long; for example, compare Equation (12) for 'w', and they are not, therefore, presented here.

B.2 Evaluation of the Equations.

To evaluate the velocities and turbulence intensities from Equations (12), (13) and (14), it is necessary to assume that the three relevant voltages E_2, E_3 and E_4 are of similar shape and frequency distribution, see Figure 4.

It must also be assumed that E_2 and E_4 are in phase. To examine the validity of these assumptions, it is necessary to re-examine the Equations (4) to (7). The waveform and frequency of E is irrelevant. If, say, 'w' is small, then Equations (5), (6) and (7) are of very similar form and, hence, likely to be of similar shape and frequency distribution. Equations (5) and (7) would be virtually identical so that the 'in phase' assumption also seems to be reasonable.

The phase difference between equation (5) (or 7) and (6) is derived as follows:-

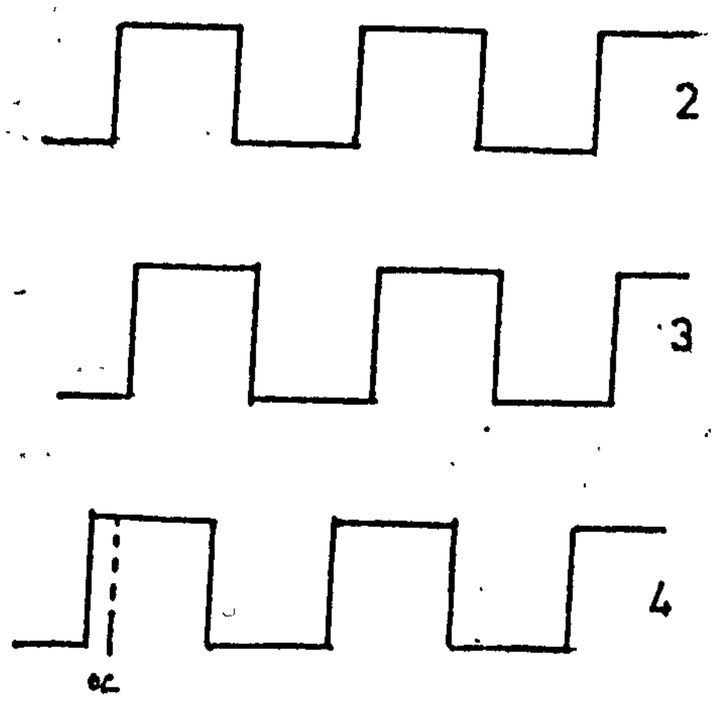

Fig.4

From equations (5), (6) and (7):-

$$U_2^2 + U_4^2 = 2U^2 + (G^2 + K^2)(v^2 + w^2) = U_1^2 + U_3^2 \qquad (15)$$

or $$U_1^2 = (U_2^2 + U_4^2 - U_3^2) \qquad (16)$$

If the time mean averages are taken on both sides of the equation (16), then:-

$$\bar{U}_1 = \overline{(U_2^2 + U_4^2 - U_3^2)^{\frac{1}{2}}} \qquad (17)$$

If the phase difference between U_2 (or U_4) and U_3 is 'α' and a square wave form is assumed, then:-

$$2\bar{U}_1 = \left[(U_{2\,max}^2 + U_{4\,max}^2 - U_{3\,max}^2)^{\frac{1}{2}} + (U_{2\,min}^2 + U_{4\,min}^2 - U_{3\,min}^2)^{\frac{1}{2}}\right] (1 - \alpha) + \left[(U_{2\,max}^2 + U_{4\,max}^2 - U_{3\,min}^2)^{\frac{1}{2}} + (U_{2\,min}^2 + U_{4\,min}^2 - U_{3\,max}^2)^{\frac{1}{2}}\right] \alpha \qquad (18)$$

This relation is derived by using the expression presented in equation (17) and relating it to Fig.4.

Re-writing (18) in terms of 'α',

$$\alpha = \frac{2\bar{U}_1 - (U_{2\,max}^2 + U_{4\,max}^2 - U_{3\,max}^2)^{\frac{1}{2}} - (U_{2\,min}^2 + U_{4\,min}^2 - U_{3\,min}^2)^{\frac{1}{2}}}{(U_{2\,max}^2 + U_{4\,max}^2 - U_{3\,min}^2)^{\frac{1}{2}} + (U_{2\,min}^2 + U_{3\,min}^2 - U_{3\,min}^2)^{\frac{1}{2}} - (U_{2\,min}^2 + U_{4\,min}^2 - U_{3\,min}^2)^{\frac{1}{2}}} \quad (19)$$

$\bar{U}_1$ can be determined by the expression:-

$$\bar{U}_1 = \frac{1}{2}(U_{1\,max} + U_{1\,min}) \quad (20)$$

The mean velocities are then evaluated as follows:-

$$\bar{u} = \frac{1}{T}\int_0^T f(U_2^2, U_3^2, U_4^2)\,dt \text{ from equation (14),}$$

where 'u' has been expressed as a functional relationship.

The time-mean average values for 'u' can be determined by solving the equation (14) for the four sets of values of U_2, U_3 and U_4 as given in the expressions below:-

$$\bar{u} = \frac{1}{2}\Big[f(U_{2\,max}^2, U_{3\,max}^2, U_{4\,max}^2) + f(U_{2\,min}^2, U_{3\,min}^2, U_{4\,min}^2) \quad (1-\alpha)$$
$$+ f(U_{2\,max}^2, U_{3\,min}^2, U_{4\,max}^2) + f(U_{2\,min}^2, U_{3\,max}^2, U_{4\,min}^2) \quad (\alpha_3)\Big] \quad (21)$$

Values for '$\bar{v}$' and '$\bar{w}$' are determined by solving equations (12) and (13) in a similar manner.

B.3 Evaluation of Turbulent Fluctuating Velocities.

From Ref.(102),

$$\overline{u}^2 = \overline{(u + u')^2} = \overline{u}^2 + \overline{u'^2}$$

It follows from equation (14):-

$$u^2 = \left[f(U_2^2, U_3^2, U_4^2)\right]^2$$

Hence, $$\overline{u'^2} = \overline{f(U_2^2, U_3^2, U_4^2)} - \bar{u}^2 \qquad (22)$$

$\overline{f(U_2^2, U_3^2, U_4^2)^2}$ may be evaluated in the same way as $\overline{f(U_2^2, U_3^2, U_4^2)}$:-

$$u'^2 = \frac{1}{2}\Big[f(U^2_{2\,max}, U^2_{3\,max}, U^2_{4\,max})^2 + f(U^2_{2\,min}, U^2_{3\,min}, U^2_{4\,min})^2 \ (1-\alpha)$$

$$+ \ f(U^2_{2\,max}, U^2_{3\,min}, U^2_{4\,max}) + f(U^2_{2\,min}, U^2_{3\,max}, U^2_{4\,min}) \ (\alpha)\Big] \qquad (23)$$

where $f(U_2^2, U_3^2, U_4^2)$ can be found squaring the expressions found for $f(U_2^2, U_3^2, U_4^2)$ earlier.

Similar results apply for $\overline{v'^2}$ and $\overline{w'^2}$

B.4 Summary

The complexity of the algebraic equations described in the previous section makes it difficult to offer a clear picture of the procedure so that in this section the method of obtaining the velocities and turbulence intensities is briefly summarised.

1. Four sets of voltages, mean $\bar{E}$ and fluctuating E, are obtained at each orientation and numbered 1, 2, 3 and 4 respectively.

2. These voltages are then converted to the maximum and minimum velocities using equations (2) and (3).

3. The difference in phase 'α' between the three velocities U_2, U_3 and U_4 is found by solving equation (19).

4. The velocities are then obtained by evaluating equations (12), (13) and (14), substituting the maximum or minimum values of U_2, U_3 and U_4 as appropriate, according to equation (21). For example, equation

(14) is first solved by substituting U_{2max}, U_{3min} and U_{4min} for U_2, U_3 and U_4 respectively: then U_{2min}, U_{3min} and U_{4min} etc. The four separate expressions in equation (21) are then derived and, since 'α' has also been found, it is possible to obtain the value of velocity component 'u'. The other components 'v' and 'w' are found similarly.

5. The turbulence intensities are obtained in a similar manner except that equation (23) is now solved for $f(U_2^2, U_3^2, U_4^2)^2$ for $\overline{u'^2}$.

APPENDIX C

PROPERTIES OF NAPHTHALENE

(a) General Information

Description : White crystalline solid with aromatic odour.

Chemical Formula : $C_{10}H_8$

Physical Properties

Molecular weight	:	128.16
Melting point	:	80.1C
Boiling point	:	217.9C
Flash point	:	86C
Density	:	1145 kg/m^3 at 20C.
Lower explosive limit in air	:	0.9% by volume.
Upper explosive limit in air	:	5.9% by volume.
Auto-ignition temperature	:	526C.
Gas constant Rv	:	64.7 J/kg K
Latent heat of sublimation	:	559 KJ/kg
Coefficient of volumetric expansion.	:	0.00028 / deg.K.

(b) Hazard Analysis

Toxic Hazard rating:

Acute local	:	Irritant - May involve both Ingestion reversible and irreversible changes not severe enough to cause permanent injury (moderate).
		Inhalation-Causes readily reversible changes which disappear after end of exposure (slight).

Acute Systematic	:	Ingestion Inhalation	- May involve both reversible and irreversible changes not severe enough to cause permanent damage.
Chronic Local	:	Irritant	- Causes readily reversible changes which disappear after end of exposure.
Chronic Systematic:		Ingestion Inhalation	- As above.
Toxicity	:		May be used as an insecticide.
Threshold Limit Values	:		- American Conference of Government and Industrial Hygienists (recommended) 10 parts per million of air; 50 milligrams per cubic meter of air.
Fire Hazard	:		- Moderate, when exposed to heat or flame; reacts with oxidising materials.
Spontaneous Heating:			- No.
Explosion Hazard	:		- Moderate, in the form of dust, when exposed to heat or flame.

Countermeasures:

To fight fire	:	Water, carbon dioxide, or carbon tetrachloride.
Personnel protection.	:	Respirator not usually needed.

(c) Saturation Vapour Pressure of Naphthalene

As mentioned previously in Section 7.5, several expressions have been suggested to obtain the vapour pressure of naphthalene. Four such expressions were plotted graphically in Figure 7.4 which shows the relative nearness

of all these expressions, especially at temperatures below 20C. These relationships include those proposed by:;

Sherwood and Bryant (Ref.107).

$$\log_{10} p_n = 11.5 - (3765/T_n)$$

Christian and Kezios (Ref.101).

$$\log_{10} p_n = 11.73 - (3825/T_n).$$

International Critical Tables (Ref.108).

$$\log_{10} p_n = A - (0.05223\,B/T_n),$$

where A = 11.45 and B = 71,401.

Handbook of Chemistry and Physics (Ref.109).

$$\log_{10} p_n = 11.45 - (3729/T_n).$$

In all these cases, the temperature is in degrees Kelvin while pressure is expressed in mm. of mercury. In the present case, the expression proposed by Sherwood and Bryant has been used since it gives a rather mean value of all the above expressions.

(d) Schmidt Number

Several values of Schmidt number can be found at a particular temperature using different sources. Lewis (Ref.94) has quoted several such references and may be referred to for details. An expression by Dawson and Trass (Ref.110) is quoted here:-

$$Sc = 7.00\ (T_n)^{-0.185}$$

T_n varies between 100 to 500 K.

In the present tests, the value of $(Sc/Pr)^{2/3}$ remains virtually constant and a value of 2.38 was used throughout the calculations.

APPENDIX D

CALCULATIONS INVOLVED TO DETERMINE FLOW RATES AND HEAT TRANSFERS.

D.1 Flow Rates

The amount of air flowing in both single and multiple jet test rigs was measured using sharp-edged orifice plates constructed and installed in the piping according to B.S. 1042 (Ref.75). Sample calculations to obtain the flow rates by measuring the pressure drops at the orifice plates may also be seen in the same reference.

In the present tests, the total mass flow rate of air, m_{tot}, at the nozzle exit was kept constant. In the case of single jet tests, this mass flow rate was 1.016×10^{-2} m^3/s and 1.771×10^{-2} m^3/s, and for multiple tests it was 5.46×10^{-2} m^3/s (for all nine nozzles). The fraction of the amount of air flowing in the tangential leg (or plenum for multiple jet rigs) can be varied from 0 (no swirl) to 1, allowing various swirls to be generated by the same swirler. The relationship between m_{tan}/m_{tot} and the swirl number is illustrated graphically in Figure 5.8 for the two types of swirler used in the present tests. For example, to generate $S = 0.36$ in the multiple jet swirlers, the ratio $m_{tan}/m_{tot} = 0.43$ and, therefore, the air flowing in the axial and the tangential plenum would be 0.0311 and 0.0235 m^3/s respectively, the total mass flow rate at the nozzle exit being 0.0546 m^3/s.

D.2 Reynolds Number

The Reynolds number, referred generally as 'Re_D' was based on the mean exit velocity, u_{mo}, for the non-swirling case and the nozzle diameter. This velocity is deduced by the relationship,

$$Q = \pi D^2 u_{mo}/4$$

where, Q is the volume flow rate.

In the case of single jet tests, two flow rates were employed with $u_{mo} = 20.56$ and 39.75 m/s, corresponding Reynolds numbers being 32,000 and 60,000. For multiple jets Re_D was kept constant at 32,000 ($u_{mo} = 30.63$ m/s).

In the test, reference has also been made to the Reynolds number based on the jet 'arrival velocity', u_a. This velocity can be determined by multiplying 'u_{mo}' with the appropriate factor depending on the nozzle-to-target distance. The relationship between this factor and z/D was determined experimentally by Ref.87, and has been presented in this Appendix, see Fig.D.1. For $z/D > 9$, the

relationship can also be expressed empirically as:-

$$u_a = 6.63\ u_{m_o}(z/D)^{-1} \qquad (D.1)$$

In many cases, the measured exit velocity for the non-swirling case, u_e, has been employed to non-dimensionalise the velocity plots. This velocity for Re_D = 60,000 was 41.3 m/s and 22.5 m/s for Re_D = 32,000.

D.3 Heat Transfer

As described earlier in Section 8.4.3, the photographic record of naphthalene clearance patterns was made for all the impingement tests. These clearance patterns were later employed to build up the local heat transfer variations on the target plate. The local distributions were integrated to yield the average heat transfer coefficients. In this Appendix, an example from the single jet tests has been chosen to demonstrate the calculations involved to determine the local heat transfer coefficients.

The procedure outlined is also applicable for the multiple jets except for slight differences which have been pointed out.

D.3.1 Determination of the Local Heat Transfer Coefficient.

The clearance pattern shown in Plate D.1 has been chosen from the set of photographs presented in Plate 5. The procedure to obtain the variation of the heat transfer coefficient on the plate can be divided into:-

(a) determination of the naphthalene spray density on the plate,

(b) the evaluation of the heat transfer coefficient from the time of a particular clearance, and

(c) the determination of the mean radial extent of the clearance from the stagnation point.

Data

General	:	Reynolds number Re_D = 60,000 Swirl, S = 0.12 Nozzle-to-plate spacing, z/D = 6
Spray	:	Five slides were positioned on the edge of the plate, as shown in Fig.D.2. Surface area of slide = 75 x 25 mm (1940 mm^2). Length of Plate sprayed = 40.6 cm. Spray time, t_1 = 3550s.

Time at first weighing of slides, t_2 = 4080 s.

Time at second weighing of slides, t_3 = 6645 s.

Weight of slides at t_2 = 44.6, 44.3, 41.2, 42.7 and 42.9 mg. (mean = 43.1 mg). 43.2

Weight of slides at t_3 = 40.0, 40.4, 37.5, 38.6 and 38.8 mg. (mean = 39.1 mg). 39

Impingement : Centre of the impinging jet at 200 mm from the slides, see Fig.D.2.

Impingement test started at 4920 s (t_4)

Temperature at the naphthalene surface during the test = 21.2C.

Calculations

Spray Density : Amount of naphthalene sprayed per unit area estimated by weighing the slides at 4080 s;

$$\frac{\text{Mean weight at 4080 s}}{\text{Surface area of the slide}} = \frac{43.1}{19.4} = 2.23 \text{ mg/cm}^2$$ 2.268

This figure represents the spray density on the plate for the position where the slides were fixed.

Loss due to natural convection:

$$\frac{\text{Mean Weight at } t_2 - \text{Mean Weight at } t_3}{(t_3 - t_2) \times \text{Surface area of the slide}}$$

$$= \frac{43.1 - 39.1}{(6645 - 4080) \times 19.4} = \frac{8.04 \times 10^{-5} \text{ mg/cm}^2\text{s}}{8.44 \times 10^{-5}}$$

Feed Rate of Plate:

Spray time/Length of plate sprayed

= 3550/40.6 = 87.4 s/cm.

Spray density at the time t = 0, i.e. weight of naphthalene initially sprayed:

2.23 mg/cms^2 + loss of naphthalene during t_2 secs.

= $2.23 + 8.04 \times 10^{-5} \times 4080$

= 2.56 mg/cm.^{2}

2.61

Spray Density on the plate at the intersection of the centre line of the nozzle.

Spray Density at t = 0 - (loss during the time rest of plate is sprayed, i.e. time to spray (41.3-20) cm.) - (loss during end of spraying, t = 3550s, and start of the impingement test, t = 4920s).

$2.56 - 21.3 \times 87.4 \times 8.04 \times 10^{-5} - (4920 - 3550)\ 8.04 \times 10^{-5} = 2.300$ mg/cm.^{2}.

2.337

This value of naphthalene spray density (m/A) can be used in the equation 7.16 to evaluate the heat transfer coefficient at the stagnation point or regions near the stagnation point. Since the amount of naphthalene varies on the plate because of the loss due to natural convection, this has to be accounted for in the calculations of the heat transfers at other positions.

Heat Transfer Coefficient : By using the Chilton-Colburn analogy, the relation between the heat transfer coefficient 'h' and the mass of naphthalene sublimated can be written as:-

$$h = \left(\frac{m}{A_n t}\right) \rho_a C_p \left(\frac{R_n T_n}{p_n}\right)\left(\frac{Sc}{Pr}\right)^{2/3} \qquad (7.16)$$

In the present example, T_n = 21.2C or 294.4K. The other temperature dependent properties at 21.2C are:-

Density of air, ρ_a = 1.199 kg/m^3.

Specific heat of air, C_p = 1.004 kJ/kg K.

Gas constant for naphthalene, R_n = 64.7 J/kg K.

Vapour pressure of naphthalene, p_n = 0.0577 mm of Hg. (7.592 N/m^2)

$(Sc/Pr)^{2/3}$ = 2.38 (1.577)

Thus,

$$h = \left(\frac{m}{A_n t}\right) \cdot \frac{1.199 \times 1.004 \times 10^3 \times 64.7 \times 294.4 \times 2.38}{7.592}$$

$$= \left(\frac{m}{A_n t}\right) \cdot 71{,}880 \ \frac{W}{m^2 K} \qquad (D.2)$$

where, $\frac{m}{A_n}$ is expressed as mg/cm.^{2}

In the present case, the estimated time for clearance at the stagnation point was 535s (first estimate) and 550s (second estimate). Therefore, ho = 304.6 and 297.6 w/m^{2}s for the two estimates respectively. (m/A_n) was found earlier to be 2.300 mg/cm.^{2} at the stagnation point. Thus, if the spray density is known for a particular clearance, the heat transfer coefficients can be found.

Size of the Radial Clearance : Since the naphthalene density varies over the plate surface, the shape of clearance shown in Plate D.1 is not circular. In this case, the 'mean' naphthalene density and radius of clearance was estimated as follows:- Twelve points were marked on the perimeter of the clearance and the distance (radial) from the stagnation point measured. These distances and the corresponding naphthalene densities (at the clearance) were tabulated along with the $(m/A_n \times r)$, see Table D.1.

Table D.1

ESTIMATE OF MEAN NAPHTHALENE DENSITY AND CLEARANCE RADIUS.

Point.	Radius 'r'	Naphthalene Densith m/A_n	$(m/A_n \times r)$
1	13.84	2.300	31.832
2	13.59	2.336	31.746
3	13.34	2.371	31.629
4	12.45	2.389	29.734
5	12.83	2.371	30.420
6	13.08	2.336	30.555
7	13.08	2.300	30.084
8	13.72	2.264	31.062
9	13.97	2.229	31.139
10	13.84	2.202	30.476
11	13.34	2.229	29.734
12	13.84	2.264	31.334

(N.B. Naphthalene spray density at various positions was found by using

the feed rate and natural convection loss).

Mean spray density of the clearance shown in Plate D.1 was defined as:-

$$(\overline{m/A_n}) = \Sigma(m/A_n).r / \Sigma r = 369.764/160.92$$

$$= 2.98 \text{ mg/cm}^2$$

$$\bar{r} = 160.92/12 = 13.41 \text{ cm.} \quad (5.3 \text{ inches}).$$

Thus, the heat transfer coefficient for this clearance pattern, photographed at 1840s after the commencement of impingement, is:-

$$h = 71,880 \times 2.298/1840$$

$$h = 89.77 \text{ W/m}^2\text{K}$$

Nusselt number, if required, can also be calculated by using the relationship,

$$Nu = hD/k,$$

where k, the thermal conductivity of air, at 20C = 0.0258 W/mK.

Therefore,

$$Nu = 0.923.h$$ for the single jet tests.

Similarly, the other eleven photographs of clearances for the present test were analysed to give a complete plot of the radial variation of the heat transfer coefficient over the plate.

Multiple Jets : In the case of multiple jets, since the heat transfer variations on the plate were not radially symmetrical and the target area associated with one of the jets was small, the naphthalene density at the stagnation point was assumed to be applicable for the whole area influenced by the central jet. Furthermore, only one-eighth of the area was analysed in the regions where the effects of the

adjacent jets caused the clearance pattern to depart from the initially circular shapes. These simplifications have negligible effect on the heat transfer variations while reducing the effort involved for the analysis considerably.

D.3.2 Average Heat Transfers.

The average heat transfers were obtained in the case of single jet tests by employing equation 2.8.

$$\bar{h} = 8/d^2 \int_0^{d/2} h.r\ dr \qquad (2.8)$$

Values of 'hr' were plotted against 'r' for all the measured points. The area under this curve was integrated by using Simpson's rule.

In the case of the multiple jets, the target area (in fact 1/4th of the total) was divided into a mesh of 8 x 8, i.e. 64 nodes. The size of mesh was found to be adequate for all the three pitches employed. The value of 'h' at each of the nodes was estimated from the contour plots.

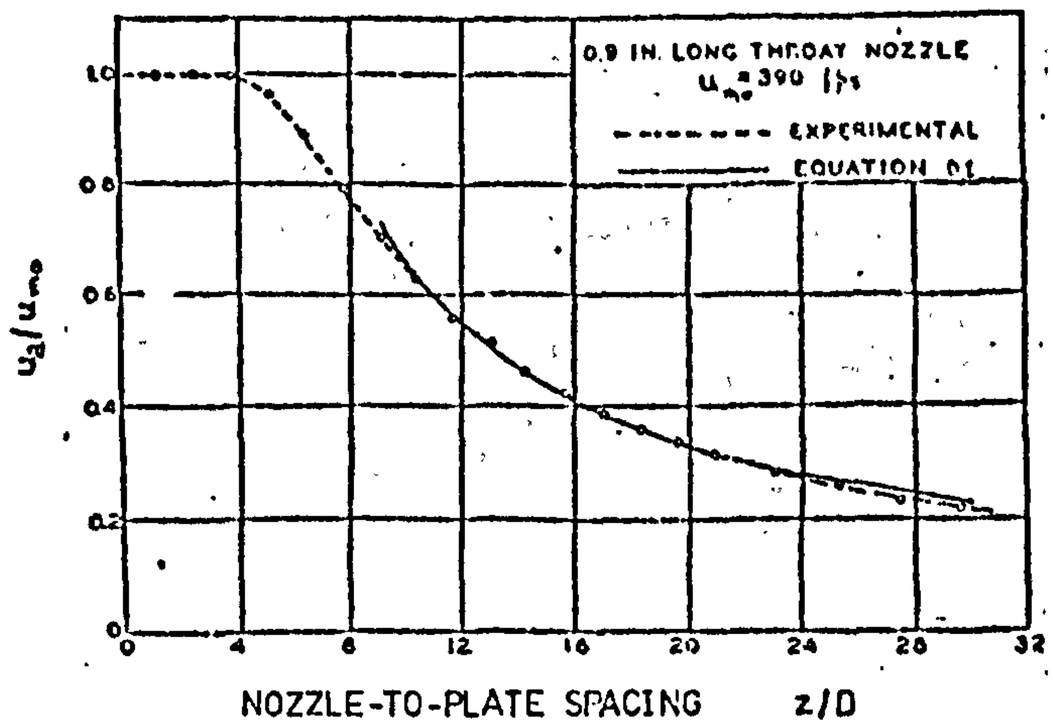

Fig. D1 AXIAL VARIATION OF ARRIVAL VELOCITY

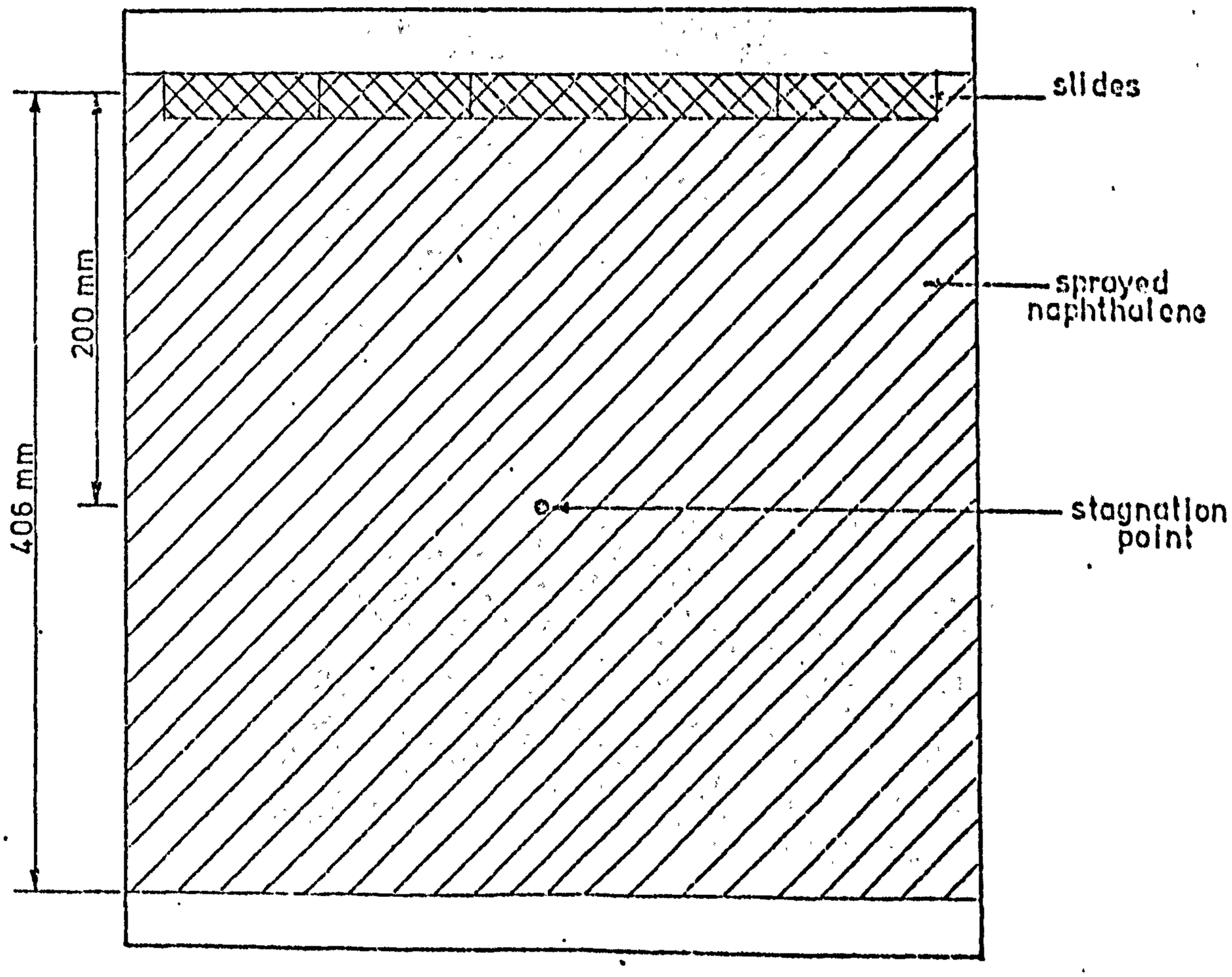

Fig. D2 TARGET PLATE SPRAYED WITH NAPHTHALENE

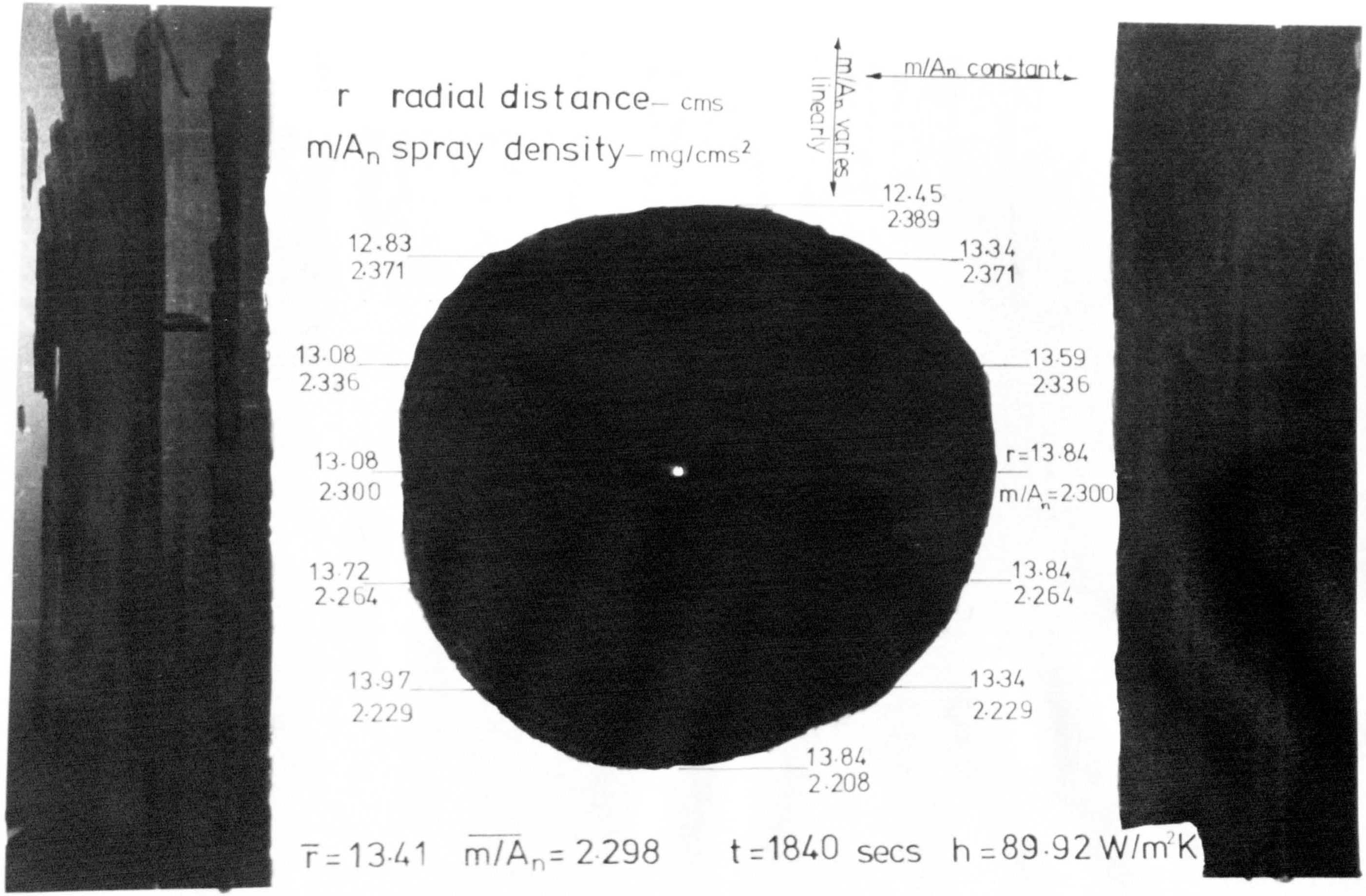

PLATE D1 DETERMINATION OF THE HEAT TRANSFER COEFFICIENT FROM A CLEARANCE PATTERN.

APPENDIX E

AN ANALYSIS OF THE FACTORS AFFECTING THE ACCURACY OF THE MASS/HEAT TRANSFER MEASUREMENTS

As discussed earlier in Chapter 9, the mass transfer results were particularly affected by the consistency of the naphthalene film sprayed onto the plate, the prediction of the specific mass of this coating, and the estimation of the temperature at the mass transfer surface during the test. Moreover, errors in the measurement of the air flow rates were also important. Evaluation of the absolute magnitude of these errors is difficult. Thus, to demonstrate that the technique provides essentially self-consistent and repeatable results, a set of three tests was carried out under nominally identical conditions. Good agreement was obtained for these tests (see Figure 10.1). Further comparison of the present results for non-swirling jets with published data from a variety of other workers also demonstrated the validity of the naphthalene thin-film technique.

This Appendix has been included, however, to amplify the discussions introduced earlier in Chapter 9 concerning the accuracy and repeatability of the experiments. The individual measurements which form part of the technique are discussed separately.

(a) Measurement of the Clearance Radius, r

To facilitate accurate assessment of r, the target plates were scribed with a square grid (12.5 x 12.5mm for single jet tests and 6.25 x 6.25mm for the multiple jets). The clearance patterns for d < 12.5mm were still difficult to measure. This is illustrated by the scatter shown in Figure 10.1 for $r/D \leq 0.25$ (also see part (d)).

(b) 'Clearance Time'

The digital timer was used in the present tests to determine the time for clearance at a particular station. Typically, the minimum difference between consecutive measurements (i.e. making photographic records) in a test was at least 100s, and an error of 0.1s contributes only ± 0.1%

In most of the cases the time for a clearance was far more than 100s and, therefore, the error in the measurement of time is negligible.

(c) Weighing of Slides

The slides were weighed on a balance which could be read to 0.1mg. The weight of an unsprayed slide was 540mg and the weight of naphthalene sprayed on a single

slide was at least 30mg. Thus, the measured weights were far in excess of the minimum resolution. In order to find out the reproducibility of the weighing procedure, an unsprayed clean slide was weighed fifteen times and the scatter in these readings observed. The coefficient of variation for these measurements was found to be 0.00053. Thus, the errors due to the process of weighing can be neglected.

(d) Consistency of the Naphthalene Coating.

As mentioned in Section 9.2, a comparison of the weights of twelve slides sprayed under similar conditions (i.e. equal naphthalene concentration and flow rates) was also made. These weights were:- 30.5, 29.6, 30.2, 30.9, 30.7, 29.7, 29.5, 29.8, 29.6, 30.3, 29.4 and 31.0 mg. The mean of these was found to be 30.2mg and the scatter of this sample is within ± 3% of the mean. However, it may be recalled that in the actual tests only five to six slides were fixed onto the plate. Therefore, a scatter in the mean of this population was also found by randomly selecting fifteen sets of any five slides. The mean of these sets was found to be 30.16mg with the standard deviation σ = 0.18 and the coefficient of variation = 0.006. Thus, it may be concluded that a minimum of five slides are sufficient to evaluate the mass of naphthalene sprayed. This observation, together with the preliminary test quoted in Section 9.2(b) comparing the weights of the slides sprayed on the same plate fixed at two different positions, shows that the spraying was acceptably consistent over the spray surface.

Table D.1 (in Appendix D) illustrates the method to determine the 'mean naphthalene density' and 'mean clearance radius'. The variation in the factor $(m/A_n \times r)$ tabulated in Table D.1 is either due to the value of 'r' or the estimate of m/A_n on various positions on the plate which involves (in addition to the sprayed weight of naphthalene) the loss rate of naphthalene due to the natural convection. The values of the factor $(m/A_n \times r)$ in Table D.1 are within ± 3.3% of the mean.

(e) Stagnation Point Mass Transfer

As discussed earlier in Section 9.4, 'clearance' stagnation points were particularly difficult to estimate. Two methods were employed to determine clearance at this point. In the first case, two readings were taken, one corresponding to the earliest estimate, i.e. clearance commencing, and the other later estimate when a definite cleared area was established. The mean of these values was then used. Alternatively, in some tests photographs were obtained at frequent intervals as the near stagnation regions cleared and these mass transfer results were extrapolated to the stagnation point value. The first of these methods was more satisfactory, e.g. for the clearance pattern shown in Plate 5, the two of h_o were 304.6 and 297.6 W/m^2K. This is, however, parti-

cularly good because in most cases the difference between the two estimates lay between 5 - 10%.

(f) Air Flow Measurements

For both the single and multiple jet arrangements, orifice plates (constructed according to B.S.1042) were employed to measure the flow rates. The tolerance on the calibration of the orifice plates is about 1.5%. Errors in measuring the pressure difference were reduced by ensuring that the difference in height of the two columns in the manometer was at least 150mm. If smaller differences occurred, an inclined alcohol manometer was substituted for the standard water-filled manometer.

(g) Temperature Measurements

As discussed earlier, the estimation of the naphthalene surface temperature is generally simplified by measuring the temperature of the impinging jet. In the present tests, the temperature measurements posed a more serious problem in the multiple jet arrangement. The individual temperatures measured at the surface of the plate varied by 0.3C, see Section 9.5 for details. This difference in temperatures can cause an error of about 3% (in the temperature range of the present tests, i.e. 17 - 22C) in the values of the vapour pressure.

(h) Schmidt Number, Sc.

The variation of the Schmidt number with temperature can be determined by using the expression quoted in Appendix C. In the present tests, the temperature varied from 17 to 22C and, for this range, the Sc can be treated as a constant. For example, at 15C, the Schmidt number is 2.455 and at 25C, Sc = 2.439.

(i) Overall Accuracy

A general estimate of the overall accuracy for the heat transfer coefficient can be obtained by considering individual factors in equation 7.16, i.e.

$$h = (m/A_n t)\ \rho_a C_p .(R_n.T_n/p_n)\ (Sc/Pr)^{2/3}$$

From the above discussions, it is fair to assume that the errors due to the time t, density of air ρ_a, specific heat of air C_p, gas constant R_n, temperature T_n and the Schmidt/Prandtl numbers are negligible compared to errors in m/A_n and p_n. In the case of 'm/A_n", an estimated error of ± 3% and for 'p_n' ± 1.5% can be quoted. Thus, the overall accuracy could be approximately quoted as ± 5%, assuming that the other factors contribute about half a percent of this figure.